A new SiC/HfB_2 based micro hotplate for metal oxide gassensors

Florian Solzbacher

A new SiC/HfB_2 based micro hotplate for metal oxide gassensors

vorgelegt von
Diplomingenieur
Florian Solzbacher
aus Saarbrücken

Der Fakultät Elektrotechnik und Informationstechnik
der Technischen Universität Ilmenau
zur Erlangung des akademischen Grades

Doktoringenieur
- Dr.-Ing. -

vorgelegte Dissertation

Berichterstatter:

Vertr.-Prof. Dr.-Ing. habil. T. Doll
Univ.-Prof. Dr.-Ing. habil. W. Buff
Univ.-Prof. Dr. rer. nat. A. Schütze
Univ.-Prof. Dr. M. Vellekoop

Eingereicht am: 13.05.2003
Verteidigt am: 28.11.2003

Ilmenau 2003

Abstract

Solzbacher, Florian

A new SiC/HfB_2 based modular concept of micro hotplates for metal oxide gassensors

Im Rahmen dieser Arbeit wurde ein neuer SiC/HfB_2-basierter Mikroheizer mit niedrigster Leistungsaufnahme für die Anwendung in Metalloxid-Gassensoren entwickelt und demonstriert. Erstmals wurden Siliziumkarbid (SiC) und Hafniumdiborid (HfB_2) als Werkstoffe für einen Mikroheizer eingesetzt. Durch geringe Modifikation der Herstellungsprozesse lässt sich der Heizer so variieren, dass der Einsatz sowohl für den automobilen Anwendungsbereich (12V-24V) als auch für tragbare Geräte (1V-2V) für eine Vielzahl unterschiedlicher Messgase möglich ist. Es ist der erste Mikroheizer für Gassensoren überhaupt, der den Batteriebetrieb bei nur 1-2 V erlaubt. Der modulare Fertigungsansatz ermöglicht die Reduzierung der Entwicklungs- und Fertigungskosten für die unterschiedlichen Anwendungsbereiche. Aus der Marktentwicklung in der Sensorik, den industriellen Anforderungen und den zu den Metalloxid-Gassensoren im Wettbewerb stehenden alternativen Technologien ergeben sich das Anforderungsprofil des Sensors. Die Wahl der Materialien spielt eine Schlüsselrolle für die Heizereigenschaften.

Der Mikroheizer besteht aus einer 1 μm dicken, an 150 μm langen und 10 bis 40 μm breiten Stegen aufgehängten Membran mit Außenmaßen von 100 μm x 100 μm. Alternativ kommen eine HfB_2 – Dünnfilm-Widerstandsheizung oder ein dotierter SiC-Heizer zum Einsatz. Mit Leistungsaufnahmen von 32 mW werden Temperaturen von 600°C erreicht, was einer Effizienz von ca. 19 K/mW entspricht. Die verwendeten hexagonalen Strukturen ermöglichen dichtes Packen der Sensoren in Arrays bei hoher mechanischer Stabilität. Erste NO_2 Sensoren mit gassensitiver In_2O_3 Schicht konnten gezeigt werden.

Abstract

Solzbacher, Florian

A new SiC/HfB_2 based modular concept of micro hotplates for metal oxide gassensors

A new SiC/HfB_2-based micro hotplate with ultra low power consumption for the application in metal oxide micro gas sensors is developed and demonstrated. For the first time, silicon carbide (SiC) and Hafniumdiboride (HfB_2) are used as materials for a micro hotplate structure. Using only slight modifications of the fabrication process, the device can be used either for automotive applications with operating voltages of 12V-24V or for battery operated handheld detectors with operating voltages of 1V-2V for a variety of different gases. It is the first micro hotplate device ever designed to work for low battery voltages of 1V-2V. The modular approach towards the processing allows easy modification for a variety of application fields and thus also reduces market entrance barriers. Based on the market development of micro sensors, the industrial requirements, and competing metal oxide gas sensors using alternative technologies, technical specifications for the hotplate as well as the state of the art's limits are determined. The new material choice plays a key role in the device properties.

The micro hotplate consists of a 100 μm x 100 μm membrane supported by thin beams of 1 μm thickness, 150 μm length and 10 to 40 μm width. Alternatively, an HfB_2 – thin film resistive heater or a doped SiC heater are used. Temperatures of 600°C are achieved using a power consumption of only 32 mW resulting in a thermal heater efficiency of ~19 K/mW. The hexagonal geometry allows close packing of the hotplates in array structures with high mechanical strength. NO_2 sensors with gas sensitive In_2O_3 layer are presented.

Table of contents

Table of symbols

Symbol	Description	Unit
α	Thermal expansion coefficient	1/K
ε	Emissivity	-
η	Heat source density	W/m
κ	Thermal diffusivity	m^2/s
λ	Thermal conductivity	W/(m K)
μ	Charge carrier mobility	m^2 / (Vs)
ν	Kinematic viscosity	m^2/s
π	3.1415...	-
ρ	Density	Kg/m^3
σ	Stefan-Boltzmann constant, $5.670\ 400 \times 10^{-8}$	$W/(m^2 K^4)$
σ	Electrical conductivity (chapter 2)	Ωm
σ_c	Effective cross sectional area of a gas atom	m^2
τ	Time constant	s
υ	Temperature / °C	°C
ω	Frequency ($\omega=2\pi f$)	1/s
$\Delta\rho$	Change in density	Kg/m^3
λ_{Au}	Thermal conductivity of Au	W/(m K)
σ_c	Effective cross sectional area of a He-atom	m^2
τ_{off}	Time constant upon switching off	S
τ_{on}	Time constant upon switching on	S
λ_{SiC}	Thermal conductivity of SiC	W/(m K)
a_{therm}	Temperature coefficient of resistivity of the temperature sensor	K^{-1}
A_{heater}	Temperature coefficient of resistivity of the HfB_2 heater	K^{-1}
A	Area	m^2
A_{bridge}	Cross sectional area of micro bridge	m^2
A_{leads}	Cross sectional area of Au leads on micro bridge	m^2
c	Heat capacity	J/(kg K)
C	Specific heat	J/K

C_l	Longitudinal coefficient	-
C_p	Thermal capacitance at constant pressure	J / (kg K)
E	Energy	J
E_A	Activation energy	J
E_I	Energy for ionisation	J
G_D	Gibbs energy	J
g	Gravitational acceleration constant (9,81 m/s^2)	m/s^2
h	Convection coefficient	W/m^2
H	Enthalpy	J
J_{th} , j	Thermal current density	W/m^2
K(T)	Thermal conductivity as function of temperature	W/(mK)
l	Effective length	m
l	Mean free path (chapter 7)	m
L_c	Characteristic length	m
n	Number of molecules per unit volume	$1 / m^3$
n_i	Charge carrier density (index i)	cm^{-3}
Nu	Nusselt Number	-
Nu_l	Longitudinal Nusselt Number	-
Nu_t	Transversal Nusselt Number	-
p	Pressure	Pa
P	Power	W
Pr	Prandtl Number	-
q_i	Charge (index i)	C
r	Radius	m
Ra	Rayleigh Number	-
$R_{Air, cond.}$	Thermal resistance of ambient air through conduction	K/W
$R_{Air, conv.}$	Thermal resistance of ambient air through convection	K/W
$R_{Rad.}$	Equivalent thermal resistance of power losses through radiation	K/W
$R_{SiC, cond.}$	Thermal resistance of SiC bridges through conduction	K/W
R_{th}	Thermal resistance	K/W
T	Temperature	K
T_a	Temperature at a	K
T_{max}	Maximum Temperature	K
T_r	Temperature at radius r	K

T_R	Temperature at radius R	K
T_w	Temperature at w	K
U	Voltage	V
V	Volume	M^3
x	Length	m
x,y,z	Cartesian coordinates	-

Table of acronyms

α-SiC	All single crystal SiC polytypes, except for the cubic polytype.
β-SiC	Cubic 3C-SiC polytype
2D	Two Dimensional
3D	Three Dimensional
ChemFET	Chemically sensitive Field Effect Transistor
CVD	Chemical Vapour Deposition
DIP	Dual Inline Package
DLC	Diamond like Carbon
DRIE	Deep Reactive Ion Etching
FCC	Face Centred Cubic
FEA	Finite Element Analysis
FET	Field Effect Transistor
IDE	Interdigital Electrodes
IDS	Interdigital (Electrode Comb) Structure
IR	Infrared
LED	Light Emitting Diode
LPCVD	Low Pressure Chemical Vapour Deposition
LPE	Liquid Phase Epitaxy
MAK	Maximale Arbeitsplatz-Konzentration (Maximum Workplace Concentration, according to German Law)
MBE	Molecular Beam Epitaxy
MEMS	Micro Electro-Mechanical Systems
PECVD	Plasma Enhanced Chemical Vapour Deposition
RIE	Reactive Ion Etching
RTD	Resistance Temperature Detector
SCCM	Standard Cubic Centimeter per Minute
SGFET	Suspended Gate Field Effect Transistor
SOI	Silicon on Insulator
TCR	Temperature Coefficient of Resistance

Acknowledgements

The work described in this thesis was done at the Microsensor and Actuator Technology Center of the Technical University Berlin and finished at the Faculty for Electrical Engineering and Information Technology at the Technical University Ilmenau. Financial support from the German Ministry of Education and Research (BMBF) through the LEGUAN (Low Power Mikrogassensoren für energietechnische und umweltrelevante Anwendungen) project is gratefully acknowledged.

I would like to thank both, Prof. Dr.-Ing. habil. T. Doll for supervising, discussing and helping to shape the final version of the dissertation as well as participating in the examination committee and Prof. Dr.-Ing. E. Obermeier for giving me the opportunity to do this work and for support and fruitful discussions.
This work would not have been possible without the help of many, whom I would like thank for their support, help and discussions:

Prof. Dr.-Ing. habil. W. Buff, Prof. Dr. M Vellekoop, Prof. Dr. rer. nat. A. Schütze, Prof. Dr.-Ing. habil. C. Knedlik and Prof. Dr.-Ing. habil. H. Wurmus for participating in the examination committee,

our partners in the LEGUAN project – in particular, Dr. J. Sonntag from HL-Planartechnik, Dortmund- for discussions and information on the device specification,

M. Eickhoff at DaimlerChrysler, Munich for supplying me with the SiC-layers without which the realisation of my devices would not have been possible,

Dr. W. Skorupa at Forschungszentrum Rossendorf, Dresden, for performing the implantation and annealing process for the SiC-heater device version,

Dipl.-Phys. O. Ehrmann and C. Meinherz for letting me use their sputtering system and performing many runs on my samples in “next-to-no-time”,

my colleagues from the Microsensor and Actuator Technology Center: especially, Dr.-Ing. C. Imawan and Dr.-Ing. H. Steffes for being great colleagues throughout the whole project. Dipl.-Phys. E. Jansen for many discussions on the origin of thermal phenomena, Dr.-Ing. S. Zappe and Dr.-Ing. J. v. Berg for introducing me to the simulation tools and to bowling, Dipl.-Ing. R. Ziermann for discussions on SiC and support (and bowling), Dipl.-Phys. P. Krause and Dipl.-Ing. T. Diepold for “knowing-it-all” and always being there in case of technological trouble, Dipl.-Phys. V. Schlichting for helping and repairing every breakable thing in the cleanroom laboratory and for introducing me to the equipment.
I would like to thank Dipl.-Ing. S. Ganzlin for carrying out the transient simulations as part of his diploma-thesis.

Also, I am especially thankful to our team at First Sensor Technology GmbH who – despite the tremendous amount of work to be done during the construction and building of FST – have left me the time and space, as well as all time support to finish my thesis and work at the TUB, properly. They have become dear friends.

Finally, all of this wouldn’t have been possible without the never-ending encouragement and support of Anne Lücke, who also did part of the manuscript proofreading.

Summary

This work presents the development of a new SiC/HfB_2 based micro hotplate for metal oxide gas sensors with ultra low power consumption and high long-term stability. In order to achieve this, the performance of current micro gas sensor solutions is analysed, focussing on design and materials used. Based on the analysis, sensor specifications are set in close co-operation with industrial partners, leading to a new design and material choice. For the first time ever, silicon carbide (SiC) and hafnium diboride (HfB_2) are used as micro hotplate materials. Small modifications of the fabrication processes allow the variation of the hotplate for the use with an automotive power supply (12V–24V) or in a battery operated environment (1V-2V) for a variety of different gases.

Current market trends show a strong growth potential for micro gas sensors. In mass products, different technological approaches with their specific advantages and disadvantages are competing against each other. Micromachined metal oxide gas sensors appear to be the most promising approach towards simple, low cost, mass producible devices, but they require high development and technological infrastructure expenses. Since today, the production volumes required for gas sensors are still comparably small, a large range of application fields has to be covered with one basic sensor in order to achieve sufficient production volumes justifying the high development expenses.

The gas sensitive and solid state properties of the metal oxide films used in these sensors are shown to require the operation at elevated temperatures of between 200 °C and 450 °C. Fast thermal response of the heater is necessary in order to allow pulsing of the sensor for reduced power consumption and operation in specific measurement modes like e.g. temperature pulsed desorption.

The technical requirements compiled for the new micro gas sensor are: lower power consumption than current solutions (<50 mW), faster thermal response

(~1 ms), good long-term stability, small size (heater dimensions < 100 μm x 100 μm) and high versatility.

Based on these requirements, a micro hotplate design is derived, consisting of a front and backside micromachined membrane supported by thin beams with maximum thermal insulation from the surrounding substrate material. A buried heater with electrically insulating heat-spreader top layer allows high temperature uniformity across the gas sensitive layer.

The material choice of the substrate and heater plays a key role in the determination of the device performance. Commonly available semiconductor materials like SiO_2 and Si_3N_4 are compared to silicon carbide polytypes (3C, 4H, 6H) and diamond like carbon (DLC) for their suitability as supporting membrane. 3C-SiC thin film layers on silicon substrates are chosen, since they combine compatibility with standard silicon based micromachining processes with outstanding mechanical, thermal and chemical strength.

Two different heater materials are necessary to allow the generation of sufficient heater power during operation with 1V-2V or 12V-24V. Thus, the design has to facilitate the use of a metal thin film heater for the low voltage and a semiconductor heater for the high voltage version.

For the metal heater, a variety of standard CMOS and MEMS materials are compared leading to the use of HfB_2 as heater material with the highest melting point (3250 °C) and very high resistivity (253 μΩcm).

For the semiconductor heater, N_2-doping of the underlying 3C-SiC substrate across the heater area is employed yielding a high resistivity heater (> 6 kΩ at room temperature). Ti:TiWN:Au serves as very low resistivity, high temperature compatible (up to 600 °C) metallisation layer for both hotplate versions.

Theoretical modelling is used prior to simulation in order to estimate the device properties and to set the boundary conditions for the simulation. Finite element analysis is used to optimise the device's thermal, thermo-mechanical and electrical static and transient properties.

The resulting micro hotplate consists of a SiC-membrane of 1 μm thickness and 100 μm x 100 μm lateral extension, supported by SiC beams of 1 μm thickness, 150 μm length and 10 μm to 40 μm width. Alternatively, an HfB_2 resistive thin film heater or a doped SiC resistive heater can be used. The buried heater is electrically insulated from the electrodes contacting the gas sensitive layer by a covering Si_3N_4 PECVD layer. The complete micro hotplate is placed within a 1 μm thick SiC diaphragm allowing the close placement of adjacent hotplates with little thermal crosstalk.

Single heater devices and arrays are fabricated and characterised. Theoretical, simulation and actual properties are in good agreement. A power efficiency of up to 19 K/mW is achieved yielding to operating temperatures of more than 600°C at 32 mW power consumption. Thermal time constants of about 1 ms are obtained. By using the device as a Pirani vacuum gauge the validity of the used theoretical model can be shown and the thermal conductivity of the SiC micro bridges can be determined.

Finally, an NO_2 sensor for the application in the MAK-range (5 ppm: maximum workplace concentration range, according to German law) is fabricated and tested. Using In_2O_3 thin film layers with (211) surface texture, good sensitivity, reproducibility and acceptable time constants can be achieved.

The results of this work show the feasibility of the concept and can be used as base for the development of new low power micro gassensor devices. The use of SiC however currently limits the use in commercial applications, until new progress has been made in the field of commercially available SiC-on-Si substrates.

1. Introduction

The increasing presence of computerised aids and tools in all parts of life triggers the development of their "senses", which gain more and more attention from researchers and industry. Sensors are of vital importance to any controlled operation of automated devices.

Physical sensors still constitute by far the greater market share compared to chemical sensors [1.1]. The increasing demand for chemical sensors in low-cost applications in household and (personal) environmental monitoring systems however will, according to new market analyses [1.1] cause the biggest relative market volume growth of all sensors in the next decade.

This growth is also promoted by new regulations and laws calling for improving monitoring of toxic or environmentally harmful gaseous species [1.2]. The increasing environmental and health concern in the population of industrialised countries gives additional momentum to this development. The growing public environmental awareness yields a huge market for small, portable, personal monitoring devices for environmental and medical surveillance purposes.

Despite the vast number of working principles for gas detection and concentration measurements, which have been shown in the past three decades, only few have been brought to application use by industrial sensor manufacturers. These principles range from chemical tracing, electrochemical cells, catalytic sensors and optical methods to conductivity based gas sensors.

Commercially available methods used for gas detection and concentration measurement depend very much on the application field. E.g. environmental and climate monitoring stations mainly use chemical and electrochemical tracing methods, gas chromatography and spectrometry requiring high technical and financial efforts [1.3]. The very high resolution and accuracy required for these monitoring station measurements (ppb-range) however up to date leave only little choice in the detection principles and sensors. Optical methods can be

used e.g. for the detection of CO_2 in exhaust gas control and medical analysis [1.4], since the specific IR-absorption of CO_2 makes this an ideal detection principle for CO_2. Sometimes, specific physical properties of some gases can be used as well: e.g. the paramagnetism of O_2 is used in equipment for the measurement of O_2 concentrations in sports medicine and breathing and metabolism analysis. Most of these methods are highly accurate (gas concentration detection levels < ppb), but require highly sophisticated technical equipment, making the equipment large, expensive and complex to service. Furthermore, they are difficult to use in practical applications and frequently do not directly yield an electrical signal which can be used for the electronic processing of the data.

The new application fields opening today require cheap, miniaturised sensors with low power consumption for the use in portable gas detection and measurement devices. None of these properties is satisfied by the classical gas measurement methods.

Micro gas sensors have the potential to fill this market gap. They come as mass sensitive, optical, catalytic heat sensitive or metal oxide based conductivity sensors. Micro gas sensors can be of simple design and use technologies suitable for mass production (semiconductor and thin film / thick film technology). These sensors are moderately cheap and yield an electrical output signal with mostly acceptable accuracy. Among these sensors, the metal oxide based conductivity gas sensors and catalytic heat sensitive gas sensors are the cheapest type [1.5].

One of the commercially most successful (and best known) examples of this type is the “Figaro” sensor based on the Taguchi sensing principle [1.6] marketed by Figaro since 1968. Ts has proven to be a simple and inexpensive sensor with, for many applications sufficient accuracy for many applications. It is also available for a fairly large variety of gaseous compounds. The Figaro sensor had become an unofficial “standard” every new (micro-)gas sensor had to

measure up to. Its main drawback is its unspecific response to a large variety of gases and the insufficient long term stability. In recent years the company UST GmbH (Gschwenda), an East-German automotive supplier, has replaced Figaro as market leader in micro gas sensors.
None of the micro sensors currently available however are capable of covering a wide variety of applications and requirements set upon them (i.e. testing gases, gas concentrations, operating temperatures) satisfactorily. The main drawbacks lie in their selectivity, high power consumption and insufficient long term stability (except for optical sensors) and their limitation to specific applications, as will be described in detail in chapter 2.

Future devices have to be small, inexpensive, moderately accurate sensors with low power consumption and a reasonably long lifetime covering as wide as possible a range of application fields.

Hence, the need for new improved micro gas sensor devices is obvious. Metal oxide based gas sensors have despite of their known disadvantages (low selectivity, sensor poisoning and high operating temperature) been very successfully used in the past decades. Metal oxides continue to be a very tempting group of materials for this application. The growing variety of metal oxides available, which all feature different gas sensitivity and selectivity has put them into the focus of many researchers.
Since the metal oxides require elevated operating temperatures, they have to be heated for proper operation. Micro heaters with integrated contact electrodes for the gas sensitive material have been demonstrated and used in many variations, as will be discussed in chapter 2.
Current trends in the development of these devices lead towards sensor arrays, small size and low power consumption. Apart from ceramics (Al_2O_3) based chips and various membrane type chips for gas sensor applications, micro

hotplates have appeared in recent literature [2.34-2.50] as an approach to reduce the size and power consumption of the resulting sensors. They are commonly based on standard MEMS-compatible processes and material systems and have a power consumption between 60 mW and 250 mW. They consist of a thin membrane, a resistive heater and contacts for the contacting of one particular gas sensitive layer. The long term stability, temperature range and versatility of these devices is however very limited.

This work introduces a new very low power micro gas sensor using a new set of materials, a simple basic structure and a system of modular processing blocks to build different sensor variations with little modification of the fabrication process. Its particular modularity results from the interchangeable metal and semiconductor on-chip heater. Furthermore, the two new high temperature materials, Silicon Carbide (SiC) and Hafnium-Diboride (HfB_2) are used to overcome problems inherent to the measurement in gaseous species: long term stability in aggressive and corrosive media and at high operating temperatures.
Starting from an overview over common approaches, their advantages and drawbacks, the necessity for new materials and designs are shown. The new materials' properties are stated and the device design, realisation and characterisation of the new modular SiC-based micro hotplates is explained. The application of the new micro hotplate in metal oxide gas sensors shows the advantages of the new approach.

2. Micro gas sensors

In this chapter the major types and properties of micro gas sensors will be presented. Since metal oxide based micro gas sensors constitute the largest group of these, the principles of metal oxide – gas interaction and the use of metal oxides as gas sensitive material are explained. Finally, due to the fact that the need for smaller power consumption and size has brought up micro hotplate based gas sensors, an overview of the state-of-the-art of the these devices is given. The main drawbacks and disadvantages of these devices lead to the requirements on the new micro hotplate device presented in this work.

Of the many concepts used for gas detection only a few are used for micro gas sensors. Presently, micro gas sensors come as mass-sensitive, optical, calorimetric, FET-based and conductivity devices (Fig. 2.1).

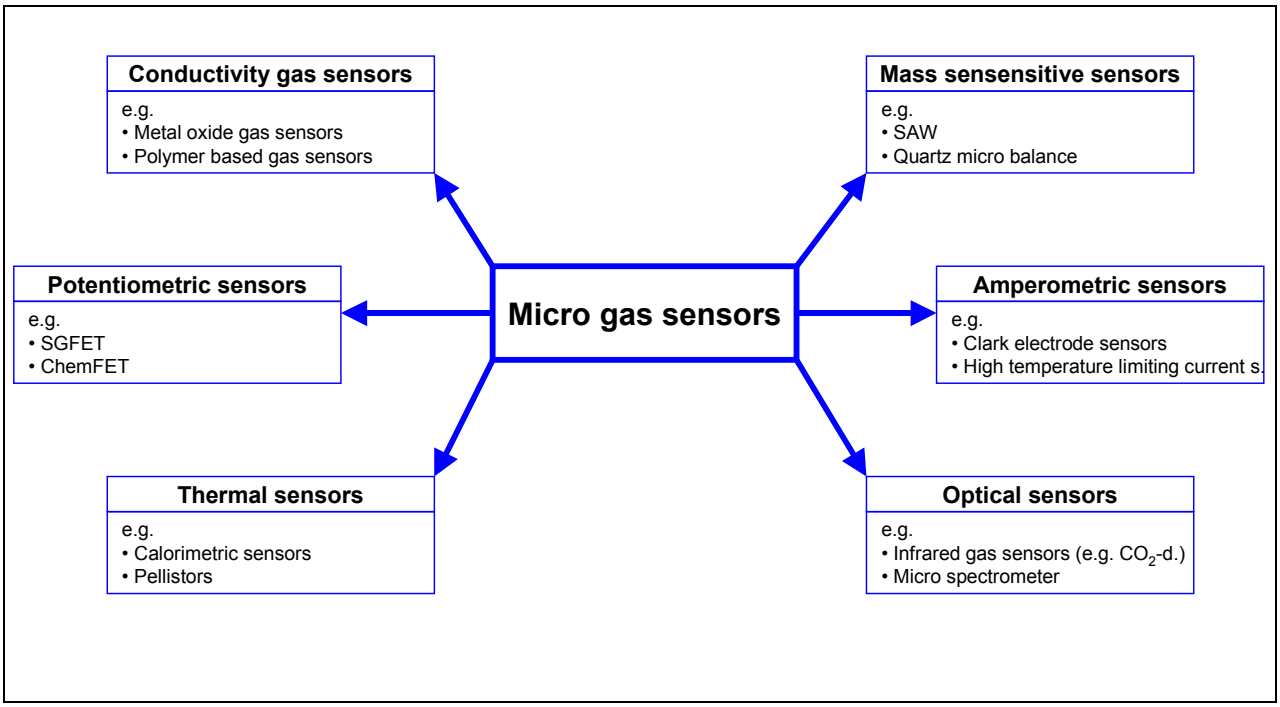

Fig. 2.1: Micro gas sensors: main groups [2.1]

2.1 Overview of micro gas sensors

This chapter summarizes the main features of the most common micro gas sensor devices.

2.1.1 Mass sensitive micro gas sensors

Mass sensitive micro gas sensors can be surface acoustic wave devices (SAW), quartz micro balances (QMB), Love Wave Devices or Flexural Plate Wave (FPW or plate-mode oscillators) devices [2.2-2.5]. They all use a similar operating principle: A thin membrane (e.g. FPW, love wave) or the whole device (e.g. quartz micro balance) is excited to oscillate at resonant frequency. The change in mass of (part of the) device results in a change in oscillation amplitude, frequency or phase, which can be detected in a variety of ways.

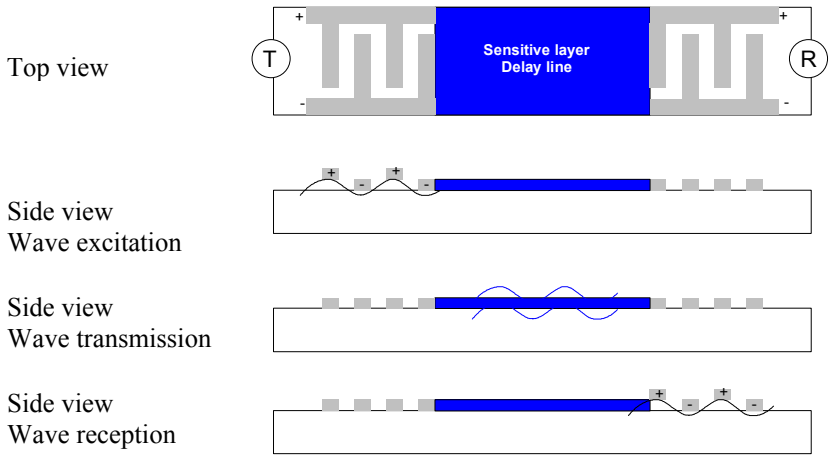

Fig. 2.2: Schematic drawing of SAW device with Transmitter (T). Receiver (R) and sensitive layer.

Metal oxide thin films or organic compounds are used as sensitive films on top of the resonator. The resonator is frequently made from ST-cut stress- and temperature compensated) quartz or $LiNbO_3$ which has a large piezoelectric coefficient [2.1] Gas molecules from the surrounding gas atmosphere adsorb or absorb on these layers thereby changing the mass and thus the frequency of the

oscillator. Usually, the change in resonant frequency with changing gas concentration is used as a measure for the gas concentration. The relation between frequency change and added mass of the adsorbed molecules is generally described using the Sauerbrey equation [2.1].

Mass sensors are usually simple in construction and operation and have a high sensitivity. Frequently a sensor delay line is used in parallel to a reference line in order to measure the phase shift between the reference and the sensor during gas exposure. They feature a low power consumption and light weight. Furthermore, the frequently used piezo crystals are cheap and readily available.

FPW or plate-mode oscillators use the same operating principles as SAW devices. However, in FPW, the thickness of the plate is comparable to the wavelength λ and the whole plate becomes involved in the periodic motion. The resulting Lamb waves can be symmetric or anti-symmetric. The key advantage of FPW over SAW lies in the lower velocity of the lowest order anti-symmetric mode, allowing measurements in liquids, which can decrease below the velocity of the compressional wave in the liquid. Due to this effect, the energy loss in the normal direction decreases [2.1].

The main drawbacks of both SAW and FPW devices are inherent to the operating principle. They are vulnerable to interferences and the selectivity is poor, since it is impossible to distinguish between different gases in gas mixtures by measuring the mass of the adsorbed gas atoms [2.2]. Since the adsorption of the gas molecules requires the active sensitive film to be in contact with the gas atmosphere, the sensor is usually saturated at a surface coverage of adsorbed gas molecules of $\Theta=1$ [2.3]. The gas concentration measuring range thus is limited. Frequently, heat pulses have to be employed to enact desorption. Even more significantly, the complexity of the electronics required to read out and interpret the signal data is considerably higher than for other detection principles. A low frequency counter or accurate lock-in-amplifiers in the case of a frequency signal (SAW) or capacitance meters in the case of a capacitive

signal (FPW) [2.4, 2.5] are necessary to detect the change in resonant frequency or capacitance with increasing gas concentration. One of the key problems is the lacking of suitable key-lock layers and the low sensitivity for light gas molecules [2.6]. Carbowaxes (polethylene glycols, their esters and related polyethers) as sensitive coatings have gained importance in industrial applications for aromatic, aliphatic and halogenated hydrocarbons [2.7].

2.1.2 Optical micro gas sensors

Optical micro gas sensors use the change in light absorption or diffraction due to a change in gas concentration or composition [2.8]. They typically use IR-laser diodes for the emission of light and photodiodes for the detection of the altered signal (signal amplitude, phase shift or polarisation).

The great advantage of these devices is their outstanding long term stability, since they do not require direct contact of the active semiconductor with the gas media. No gas sensitive layer is needed. Furthermore the photo and IR-diodes are available as standard semiconductor devices. Their power consumption can however exceed several watts. Long absorption paths using multiple mirrors are required for the detection of low gas concentrations, which have so far not been realised in MEMS technology. The alignment of the diodes is difficult making the optical gas sensor expensive in mass production. Their application can thus more frequently be found in industrial and process control. The interpretation of the obtained data can be very difficult due to the many side effects influencing the signal amplitude, phase and polarisation [2.8]. Using neuronal networks, however, screening of test gas mixtures is possible using a micro spectrometer.

2.1.3 Thermal/Calorimetric micro gas sensors

Thermal micro gas sensors make use of heat of adsorption/combustion as sensing principle. They come as thermistors, pyroelectric sensors or catalytic gas sensors and were amongst the first sensors available as micro gas sensors since the early 1960's. Using a catalytic layer (e.g. noble metal catalysts or metal oxides) they detect the heat caused by a chemical reaction of the gas (usually, oxidation) in the presence of the catalyst. Subsequently, the heat causes a change in device temperature which results in a detectable change in resistance of the device or a metal resistor placed in it.

Calorimetric sensors together with the metal oxide based conductivity sensors are amongst the cheapest sensors available. The reproducibility of their electrical and gas sensitive properties can be very high, if the fabrication parameters are carefully controlled and the device design is very simple. The power consumption of these devices is usually of the order of a few hundred milliwatts. The sensors can however be poisoned during operation and have to be cleaned using heat pulses [2.1]. Also, the catalytic effect can undergo ageing requiring re-conditioning before use, after storage [2.1].

2.1.4 Potentiometric gas sensors

Potentiometric gas sensors work on the principle of charge transfer between an electrode and a second phase. Under condition of zero current flow they yield a gas concentration dependent voltage. Micro gas sensors using this operating principle are mostly solid state devices, i.e. FET or workfunction sensors.

Field-effect-transistor based devices use a transistor with gas sensitive gate (e.g. SGFET (Suspended Gate FET)). Using a gas sensitive metal oxide as gate yields a variation of transistor behaviour (U_{SD}, U_{GS}, Workfunction, etc.) with change in

gas concentration due to band bending caused by physisorption or due to changes in electron affinity caused by adsorbed dipoles [2.1].
The availability of FET in standard semiconductor technology is of great advantage when considering high production volumes and low fabrication prices. The lack of suitable inert reference layers however causes device poisoning causing signal drifting during long term exposure.

2.1.5 Amperometric sensors

Amperometric sensors, just as potentiometric sensors are electrochemical devices. They yield a gas concentration related current signal. The main disadvantage of these sensors lies in the time variation of the signal at constant concentration. For very small electrodes, however, a steady current sufficient for measuring purposes state can be reached. The material consumption requires a liquid ion reservoir which can so far not be realised in MEMS technology.
Fuel cell type amperometric sensors and high temperature limiting-current sensors (e.g. yttrium-stabilized zirconia (ZrO_2-Y_2O_3)) are the only solid-state based micro gas sensors of this type [2.8], but require high driving power in present configurations, necessitated by a high defect mobility in the bulk material.

2.1.6 Conductivity micro gas sensors

Conductivity micro gas sensors measure the change of the electrical conductivity of a semiconducting metal oxide with a change in ambient atmosphere gas concentration. They constitute the largest group of gas sensor devices. Their working principle is explained in more detail in chapter 2.2. They usually need to be operated at elevated temperatures between 150 °C and

1100 °C [2.10] thus requiring an integrated or external heat source. There are a number of types known today:

- Polymers
- Chemiresistors (e.g. Au-thin films, semiconductors)
- Semiconducting oxide gas sensors:
  - Thin and thick film devices on semiconductor or ceramic substrates
  - Membrane heater with Interdigital Capacitor Electrodes (IDE)
  - Spider-type micro hotplate in surface or bulk micro machining
  - Heated micro bridge similar to Pellet-type gas sensors

As previously mentioned, one of their advantages is that they are amongst the cheapest and most commonly used micro gas sensor devices available. The reproducibility of the gas sensitive properties and the fabrication process control is very good for the device structure but of only moderate quality for the sensitive layers. Today, many years of experience and a large number of sensors available for different gases are an indication of the commercial success of this sensor type. Dominantly, SnO_2 metal oxide films are used as gas sensitive layer, being the most well known and commercially most successful sensor of this type. The large variety of metal oxides available with significantly differing gas sensitive properties offers vast possibilities to choose and modify the gas sensitive layer material to suit a particular application and test gas.

The drawbacks of these sensors lay in the usually high influence of humidity on the sensor signal, the cross-sensitivity to other gases, the long term drift and frequently the slow response (30 s < τ_{Gas} < 180 s) [2.11]. More recently, new binary and ternary metal oxides and the use of additional promoters or dopants have shown significant improvements of these properties [2.12].

2.1.7 Summary

Table 2.1 summarises the major properties, advantages and disadvantages of the micro gas sensors presented. Clearly, the majority of micro gas sensors is metal oxide based. Since every single application leads to a very specific set of requirements and specifications, technological expenses and long term stability are impossible to compare in other than a crude manner, as done in table 2.1. A true comparison of the available technologies would always have to take into account the specific sensor application (i.e. quantities, accuracy, testing gas, measurement environment, end user, etc.).

Table 2.1: Some significant properties of optical-, semiconductor- and CHEMFET-type gas sensors in comparison [2.12, 2.13, 2.14]. Ranking: ++ (excellent) to – (poor),

Property	**Mass sensitive sensors**	**Calori-metric sensors**	**Ampero-metric sensors**	**Optical systems**	**Conducti -vity gas sensors**	**Poten-tiometric sensors**
Expenses for technological infrastructure	- (high)	+ (low)	o (medium)	- (high)	++ (low: thick film) - (high: thin film)	- (high: FET) + (low: thick film)
Long term stability	-	o	o	++ (no reaction)	o	o
Availability of technology for mass production	+	++	o	o	++	o..+
Power consumption	o	-	o	-..+ (~W ..100 mW)	-..++ (~W ..~10 mW)	+
Price	o	++	--	o	++ (thick film) o..+ (thin film)	o
Selectivity	o	o..+	+..++	++	o..+	o
Sensitivity	+	o	++	+	o..+	o..+
Screening	--	-	-	+ (micro spectro-meter)	o	o
Size	+	-	-	o	+ (thick film) ++ (thin film)	+

2.2 Metal oxides as gas sensitive material

Metal oxide based gas sensors use the change in electrical conductivity with changing ambient air gas concentration as function of temperature. The origin of the electrical conductivity of metal oxides and the gas depending change in electrical conductivity can be explained using a variety of theoretical models. The understanding of the actual reaction processes causing the sensor response is however difficult. This does not hinder the development of gas sensitive metal oxide layers with specific properties in a heuristic manner.

2.2.1 Electrical conductivity of metal oxides

The charge carriers contributing to the electrical conductivity of a material are electrons, holes and ions. The overall scalar electrical conductivity is thus given by:

$\sigma = \Sigma_i n_i q_i \mu_i$. (n_i – carrier density, q_i – carrier charge, μ_i – mobility)

In intrinsic semiconducting metal oxides, the charge carriers are created by point defects in the bulk crystal lattice. These point defects are created by the non-stoichiometry of the metal oxide. The defects in the crystal can be Frenkel or Schottky defects [2.16]. Frenkel defects are caused by atoms moving their lattice positions into interstitial positions, whereas Schottky defects result from the diffusion of atoms to the semiconductor surface where they enter the gaseous phase leaving a void in the crystal. Depending on the predominant effects in the particular material, one finds oxygen voids $V_O^{\bullet}$ or interstitial metal atoms M_I' (annotation according to Krüger/Fink). Excess oxygen yields a p-type semiconductor with mobile defect electrons (holes), excess metal an n-type semiconductor with mobile electrons. The charge carrier concentration thus

increases with increasing proportion of oxygen (p-type) or metal (n-type) in the lattice.

The creation and equilibrium of the crystal defects is temperature dependant [2.17]. While at room temperature and up to several hundred degrees Celcius, the defect equilibrium is frozen, at high temperatures –depending on the metal oxide used (e.g. ~800°C for Ga_2O_3)- the lattice oxygen is in thermodynamic equilibrium with the ambient air oxygen partial pressure p_{O2} .

The ionisation of the crystal defects is also temperature dependent. The free charge carrier concentration thus depends on the energy required for defect formation (Gibbs energy G_D) and for ionisation E_I .

A hopping mechanism can be used to explain the electrical conductivity of semiconductors with low charge carrier mobility and high bandgap [2.12, 2.18]. I.e. in a p-type metal oxide the conductivity results from carrier dissociation or phonon induced hopping of holes from one void to another requiring a hopping activation energy. We thus obtain a temperature dependant carrier mobility $\mu(T)$. For n-type metal oxides similar hopping mechanisms have been postulated, where the electron hopping is hindered by defect potential barriers [2.18]. The defect concentration is again temperature dependant. At high defect concentrations electron tunneling through the potential barriers is possible.

For all metal oxides we do however obtain an electrical conductivity following:

$$\sigma \cong \exp (E_A / k_B T)$$

E_A being the activation energy consisting of the energy required for defect creation, the energy required for ionisation of the charge carriers and the temperature dependant hopping energy [2.19].

2.2.2 Metal oxide – gas interaction

The electrical conductivity of the metal oxide can change drastically with change in gas atmosphere. This behaviour can be caused by either volume or surface effects.

Volume effects are based on the thermodynamic equilibrium at high temperatures between the oxygen partial pressure in the surrounding gas atmosphere and the lattice oxygen in the semiconductor as previously described in chapter 2.2.1. Using a defect model one can find a proportionality relation between the carrier concentration n and the oxygen partial pressure p_{O2}, which - assuming the mobility and ionisation energy not to be affected by the oxygen partial pressure - leads to a proportionality between the electrical conductivity and the oxygen partial pressure [2.19].

Since most metal oxide gas sensors are operated at medium temperatures (150°C - 650°C) the defects are almost frozen or only slowly varying and surface effects are usually predominant. Some metal oxides with lower melting temperature (e.g. MoO_3) however feature a strong exchange of oxygen with the lattice oxygen already at lower temperatures, prohibiting the adsorption of oxygen on the surface [2.20].

The surface bound oxygen and its bonding type plays a major role in surface effects of the gas – metal oxide interaction [2.12, 2.21] (Fig.2.3).

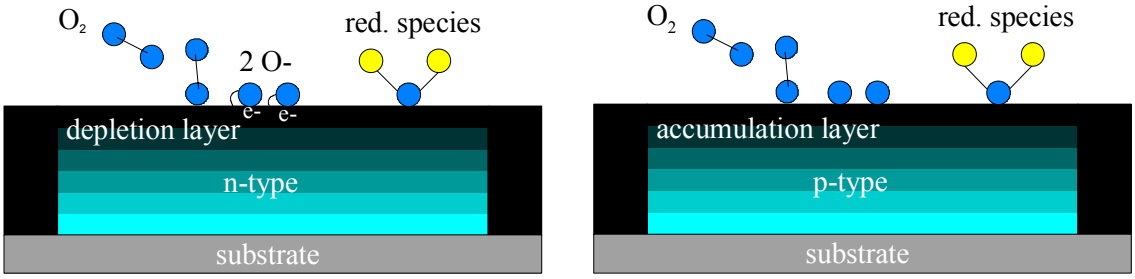

Fig. 2.3: Surface bound oxygen on n-type and p-type metal oxide causing a depletion or accumulation layer.

At the interface between the semiconductor and the gas, the gas atoms are first physisorbed. Weak Van-der-Waals forces bind the gas atoms to the surface with low binding energies (<0.1 eV). Since no electrons are exchanged in this type of bond, no influence on the metal oxide conductance and thus the sensitive behaviour is expected in the CTM.

Physisorption is in equilibrium with chemisorption, where the adsorbed species is chemically bonded. Chemisorption can in some cases be associated with a dissociation of the adsorbed molecules. Since adsorbens and semiconductor exchange electrons, the number of free charge carriers at the surface is changed. Subsequently, the electrical conductivity at the surface changes, too. The bonding types range from a covalent bond to ionisorption with bonding energies between around 0.6 eV to 1 eV [2.11-2.18].

Chemisorption is usually explained using the Lennard-Jones-Model. Fig. 2.4 shows the energy of a molecule approaching the semiconductor surface from the gas phase.

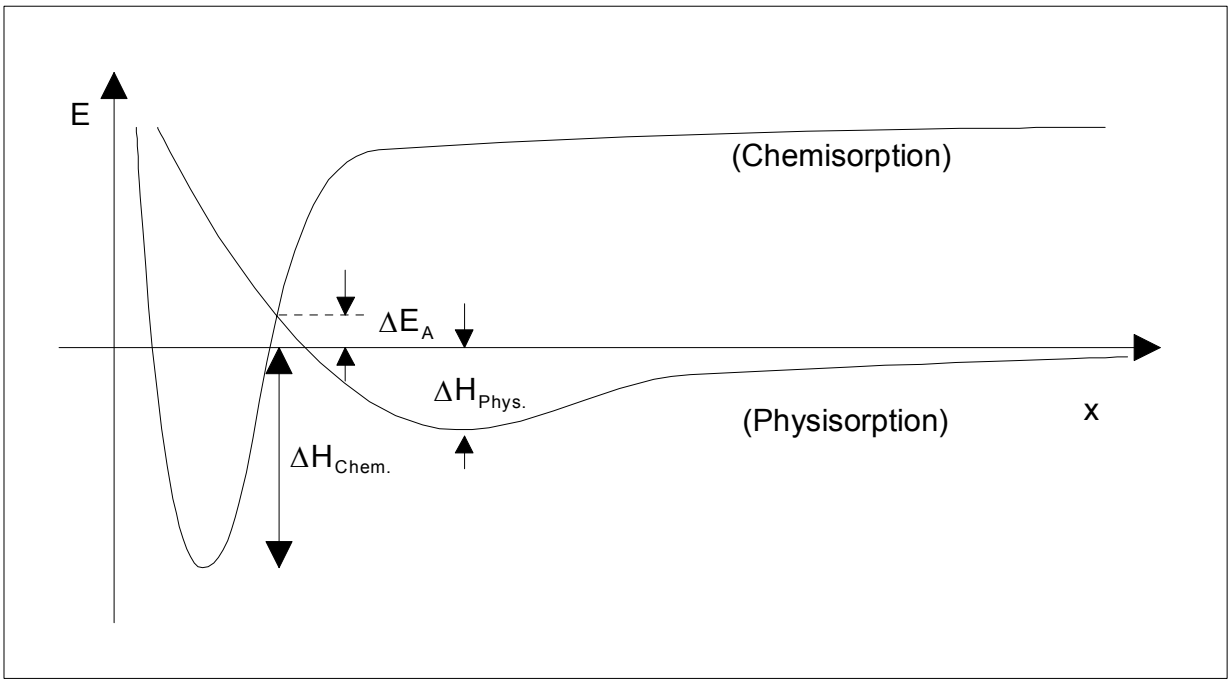

Fig. 2.4: Lennard-Jones model of physisorption and chemisorption of molecules on a solid surface [2.22].

In the Charge Transfer Model, the molecule can be physisorbed without activation energy. $\Delta H_{Phys.}$ and $\Delta H_{Chem.}$ are the bonding enthalpies of physisorption and chemisorption of the molecule. In the CTM, an activation energy ΔE_A can be necessary for the physisorbed molecule to become chemisorbed, obviously depending on the relative position and shape of the potential curves. Since ΔE_A is thermally induced, the gas-semiconductor interaction is temperature dependant. Simplified, the binding energy for chemisorption is much higher, since the energy state is lower than for the physisorbed molecule. For a molecule or atom to leave this state, a much higher energy is needed (i.e. much higher temperatures). These particles will not remain in the energy minimum, but desorb. Clearly, chemisorbtion based gas sensitivity is limited to a medium temperature range. Fig. 2.5 shows a typical thermo-desorption spectrum and the contributions from physisorption, chemisorption and desorption.

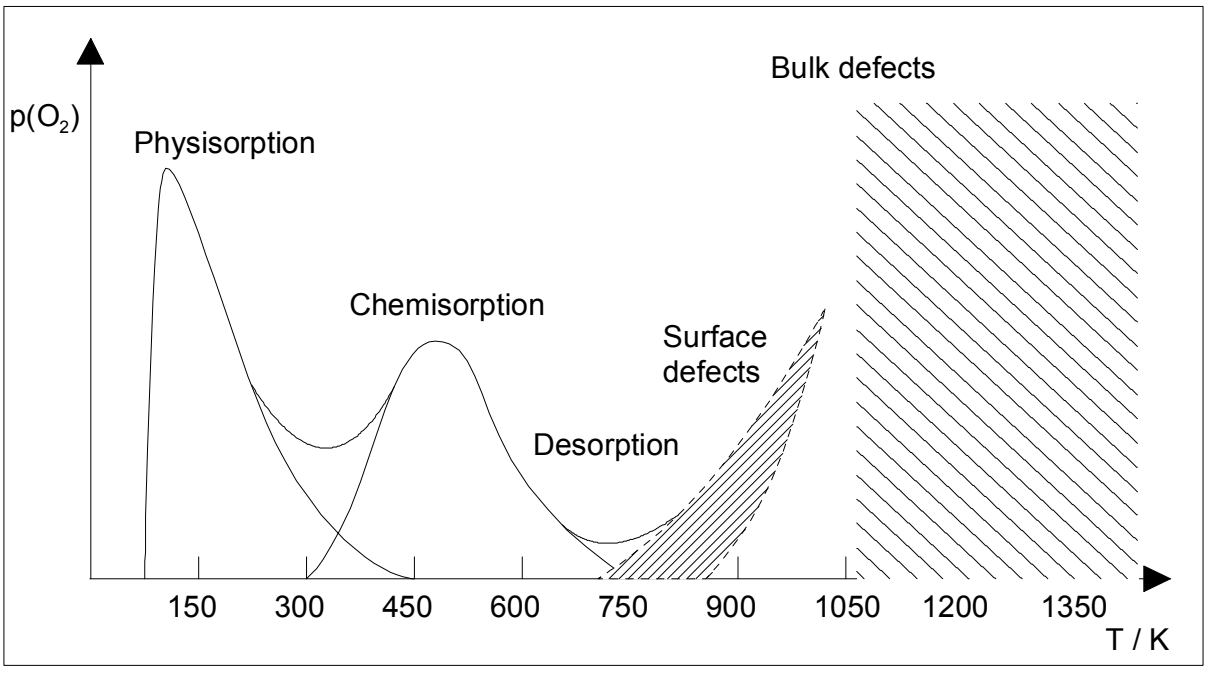

Fig. 2.5: Thermal desorption spectrum of O_2 on a [100] single crystal ZnO surface [2.23, 2.24] indicating the temperature regimes and contributions resulting from for physisorption, chemisorption, desorption and surface and bulk defects.

The temperature ranges for the different phenomena depend strongly on the material combination. The temperature range can therefore yield a first measure to control the gas sensitive behaviour of the metal oxide.

The charge transfer model is the most commonly used model to explain the interaction between metal oxide and gas [2.25]. Starting with a clean semiconductor surface, every surface can be seen as a disruption of the lattice structure periodicity. The dangling bonds at the surface often lay in the energy band gap thereby acting as surface donor or aceptor. The charge transfer between the surface states and the bulk material produces a space charge region with subsequent bending of the energy bands at the surface (surface potential V_S). The surface potential can be found by solving the poisson equation.

The chemisorption of gas molecules introduces an alteration of the surface state density, thereby changing the band bending and the space charge region depth and thus influencing the surface electrical conductivity. The effect of chemisorption on the space charge region is however energetically limited by the Weisz-limit (additional band bending can only occur when the surface states are in the vicinity of the Fermi-energy level without a reverse charge transfer, preventing further ionisation of the surface states). This limit is fairly low (at 10^{-4} cm^{-2} “physisorbed” O_2, in the CTM) , resulting in a normally O_2-saturated surface.

The electrical conductivity can thus be explained by the surface state density and subsequently the coverage of the semiconductor surface with O_2-molecules. The surface coverage is pressure dependant [2.26]. The relation between the actual gas partial pressure and the surface coverage can be described using adsorption-isotherms like e.g. the Langmuir-isotherm.

Technically fabricated metal oxides are usually polycrystalline rather than single crystal. The grain size and the relation of the grain size and debye length further influence the gas sensitive mechanisms of the metal oxides [2.27]. Dopants and

promotors can be used to alter the bulk electrical conductivity, the grain size and lattice constant, the depth of the space charge region and act as catalysts for electron spill-over or fermi-level pinning at the semiconductor surface. The details of these phenomena are described in literature [2.16, 2.17, 2.27, 2.28].
Finally, one has to consider the variety of reaction paths upon dissociation of the gas molecules at the metal oxide surface which are depending on the materials and gases used, the partial pressures and the temperature.

2.2.4 Summary

The electrical conductivity of the bulk metal oxide, the defect creation and carrier ionisation, the physisorption and chemisorption effects at the metal oxide surface and the chemical reaction path of the measured species at the metal oxide surface are all temperature dependant. The choice and control of a sensors' operating temperature is therefore a key to the design of a multi-versatile gas sensor or a gas sensor product family. The operating temperature for measuring will in most cases be somewhere in the medium temperature region (150°C-650°C) where chemisorption occurs. For cleaning desorption pulses, operation in temperature programmed desorption mode or operation using the bulk effects, the metal oxide must be operated at 800 °C-1100 °C. For fast changes between modes of sensor operation and the measurement of Temperature Programmed Desorption (TPD), very fast temperature cycles and thus, short thermal response times are required.

2.3 Micro hotplates in gas sensor applications

The use of metal oxides as gas sensitive materials clearly requires the operation at elevated temperatures between 150°C and 1100°C as well as a good control of the operating temperature (chapter 2.2).

Two possible solutions for this problem are either a passive (indirect) or active heating of the metal oxide. In the passive case, the gas is heated to a certain temperature by an external heat source and passing the gas sensor thereby heating the whole sensor to its operating temperature. An example is the measurement of exhaust gases from combustion engines or fires (e.g. power plants), where the gas is heated up to several hundred degrees Celcius. The advantage of this approach lies in the simplicity of the sensor design, since no integrated heating and no heater control system is needed. The sensor is, however, required to operate only in the particular application mode it was designed for. Variations in gas temperature (e.g. due to changing fuel quality) will change the sensor signal.

The active heating of the metal oxide is far more common. In this case the gas sensor features an integrated heating to keep its operating temperature constant irrespective of the environmental conditions. Furthermore, most of the new application fields for new micro sensors require measurements in gas environments at about room temperature, i.e. heating the sensor for a proper operation of the metal oxide sensing element is essential.

The heaters used for these purposes are exclusively resistive heaters, despite efforts towards new miniature power supplied and alternative energy sources on a micromechanical level. The resistive heaters can be made out of a metal film or a semiconductor resistor.

2.3.1 Present micro heater solutions

The manufacturing technologies for micro gas sensors used today are pellet, thick film, thin film and (silicon-)semiconductor technology. Pellets can be as small as 2 mm and use a simple wire (e.g. platinum) covered with a porous metal oxide bead [2.29]. Running a current through the wire heats the sensor to

its operating temperature. Their power consumption is in the order of a few hundred mW. The thermal time constants are of the order of a few seconds (10s) [2.30]. Compared to recent developments these sensors are far from being truly “micro” in size, but despite their very basic technology, they are amongst the most commonly used in industrial applications.

Thick film gas sensors mostly use a ceramic substrate (e.g. Al_2O_3, AlN) and screen printed metal oxide pastes as gas sensitive layers. The heater, the contact electrodes to the metal oxide and the connecting leads are frequently screen printed using AgPd, or Au-pastes. Alternatively, the electrodes and heater can be sputter deposited, while the metal oxide is screen printed. In order to ensure a homogeneous heat distribution across the metal oxide layer and in order to reduce the device size, the heater is frequently positioned on the backside of the substrate. Sometimes, a resistive temperature sensor is additionally integrated. The power consumption of these devices is in the order of a few watts. Newer devices achieve down to 1 W for operating temperatures around 600 °C. This reduction is primarily due to scaling effects, i.e. the reduction in size. The thermal response time of these devices can be as low as 1 s [2.30]. The time constant of the gas sensitive response varies strongly with test gas, concentration, temperature and metal oxide used, but is usually between 0.5 min and 3 min.

Thin film gas sensors work similarly to the thick film devices. They use ceramic and semiconductor substrates. The gas sensitive layers as well as the metallisation system (heater, electrodes, etc.) are deposited by thin film techniques like sputtering or evaporation. The main advantages of these devices are high structural resolution compared to thick film gas sensors, high reproducibility of the fabrication parameters [2.31] and MEMS-compatibility of the fabrication processes.

The most up-to-date micro gas sensor and hotplate devices in research make use of standard semiconductor substrates and processes. To a large extent, silicon substrates with standard MEMS layers (passivation and metallisation) are used for the fabrication of the heater, temperature sensor, sensing electrodes, and metal oxide layer. Forced by technological requirements and market demand, the trend in gas sensor development in the past decade has been towards a reduction in size, lower power consumption (improved thermal efficiency), short thermal and gas sensitive response and better device long term stability.

There has been a multitude of technological attempts to solve this task, starting at simple Si-membranes to the most recent micro hotplates. As a first type, thin membranes (1-10 μm thickness) were used as substrate for the heater and sensitive layer in order to improve the thermal insulation of the active sensor part and thereby reduce its power consumption. The choice of MEMS-materials with low thermal conductivity (e.g. Si_3N_4/SiO_2) for the membrane further reduces the power losses. The main problem with this approach is to generate a mechanically stable membrane with excellent thermal insulation which sustains the thermally induced mechanical stress.

The advantage of these devices is that they can be fabricated similarly to other micromachined Silicon sensors. The technology necessary for the fabrication is well controlled giving good fabrication reproducibility. They have a power consumption of a few hundred milliwatts and thermal time constants of around 0.1 seconds (table.2.2).

The second, more advanced type, uses front side bulk micromachining to produce a small hotplate supported by beams. The hotplates are between 100 μm x 100 μm and 500 μm x 500 μm in size and are hanging about 200 μm above the substrate. This approach produces a significant advance in thermal heater efficiency, despite the still close distance to the thermally highly conductive Si-substrate. Power consumptions around and below 50 mW (heater efficiencies of up to 9 mW/K) are possible. The small size and fragile design, however, has its

drawbacks when it comes to the long term stability of the devices, the maximum operating temperature and the variation freedom for the design of the sensitive electrode structures, all of which are limited (table. 2.2). The geometry of the electrodes has to be adjusted to the metal oxide used due to the large range of electrical conductivity covered by metal oxides. Fig. 2.6 gives a schematic view of the back and front side micromachined device types.

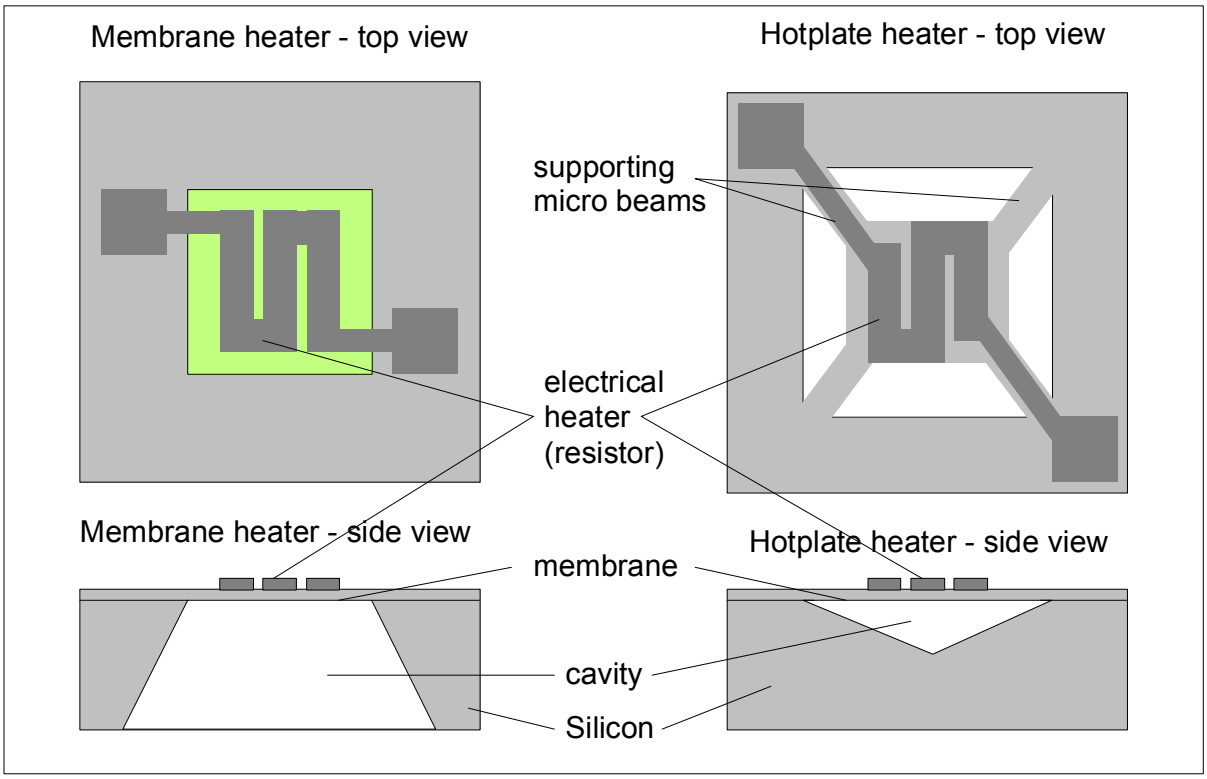

Fig. 2.6: Schematic view of micro membrane and micro hotplate heater.

Both types use SiO_2, Si_3N_4, SiO_2/Si_3N_4 sandwich or SiON membranes. SiO_2 has the lowest thermal conductivity (~ 2 $Wm^{-1}K^{-1}$ at RT) [2.32] of the available CMOS materials, but tends to exhibit compressive stress on Silicon substrates, preventing the use for membranes (buckling and cracking/fracture due to compressive stress). Si_3N_4 has a thermal conductivity more than one order of magnitude larger than SiO_2 (~ 20 $Wm^{-1}K^{-1}$ at RT), but tends to be under tensile stress on Silicon substrates, making it an ideal material for the use as membrane or diaphragm. For these reasons, most present devices use a sandwich

combination of both materials in order to combine the mechanical suitability of Si_3N_4 and thermal conductivity properties of SiO_2 to prevent rupture of the membrane structure.

Recently, hot micro-filaments have been demonstrated using a similar set up as the pellets described earlier [2.33]. They consist of a free standing Pt-wire realised by removing a sacrificial layer underneath it and covering it using Micro-CVD. For deposition of the sensitive layer, the heater is operated under gas flow of metal organic compounds resulting in the deposition of metal oxide on the Pt wire, if the thermodynamic equilibrium of the reaction process is considered properly.

In all cases, the actual heater element is either a semiconductor resistor (Polysilicon) or a metal thin film resistor (e.g. Pt-meander). Obviously, the non-linear behaviour of the semiconductor resistor is less favourable when considering the temperature control circuit design. Digital signal processors, however, make the requirement for a linear signal characteristic more and more "obsolete". The advantage of the semiconductor resistor is its availability in standard semiconductor processing lines, compared to non-standard metal thin films like Platinum, Molybdenum or Tungsten, which are used as thin film heaters. Metal thin film heaters have a linear resistance characteristic, allowing easy temperature control. Some, like e.g. Pt can be used up to temperatures of 1000°C, which is a clear advantage compared to e.g. implanted Si-heaters.

High temperatures on a semiconductor device cause a number of problems. Due to the difference in thermal expansion coefficients of the materials used, large thermally induced mechanical stress occurs in the surface layers of the device. These can lead to immediate failure (breaking of membrane material or metal leads) or continuous drifting of the device properties and reduced lifetime through accelerated ageing of the material combinations used. The short response times of the micro hotplates allow pulsed operation of the device in order to further reduce the power consumption or to operate the device in a

temperature programmed desorption mode. This heat cycling, however, increases the mechanical ageing effect further, thus reducing the device lifetime.
Depending on the temperature range and materials used, oxidation (mostly metal thin films) or diffusion of oxygen (or aggressive gases) can occur, changing the material properties thereby destroying the device properties' stability.
In order to reduce the above stated effects, a number of measures is taken. Finite Element Simulation is used to optimise the device layout, such that the different thermal expansion of the materials result in as little mechanical stress as possible. Thick passivation layers of Si_3N_4 or SiO_2 are deposited on top of the device (except for the metal oxide) to prevent the direct contact of the metallisation or substrate with the surrounding gas atmosphere.
Despite these efforts the limits of present devices are set around 450°C maximum operating temperature. In present literature, device life times are only rarely stated. Typically, 50 h in continuous operation at maximum operating temperature appear to be the ultimate [2.34]. Recent papers [2.52] state lifetimes in excess of 200 hours at 500 °C, but remain unclear as to whether this refers to the sensitive layer only or the complete device. Compared to the life time and stability of commercially available thick film gas sensors, this is far from satisfying.
None of the present devices has tried to address these problems by choosing new materials which are better suited for operation at high temperatures in oxidising gaseous media like, e.g. 20% O_2.
Table 2.2 gives an overview of recently presented micro heaters and micro hotplates for gas sensor applications.

Table 2.2: Summary of micro hotplate specifications in literature. Stated are the active heater membrane / hotplate dimension, the power consumption at maximum operating temperature, the maximum operating temperature, the materials used for membrane and heater and whether the device was only simulated (S) or fabricated (D).

Heater lateral dimensions / µm	P / mW	T / °C	τ / ms thermal	Type (membrane-M, spider – S)	Materials used	FEA (S) / Device (D)	Reference
900	130	500	10	M		D	[2.34]
100 (200)	47	320		S	SiO_2/Si_3N_4	D	[2.35]
	67	500	0.6		Poly-Si heater Al-contacts		
200	50	425	2	S	Poly-Si heater, SiO_2	D	[2.36]
100	50	550	1	S	Poly-Si heater	D	[2.37]
100	20	350	4	S	SiO_2 Porous Si as sacrificial layer	D	[2.38]
150	60	500	200	Pellet		D	[2.39]
500	60	225		M	Pt-heater	S / D	[2.40]
	85	345			Poly-heater		
500	85	450		M	SiO_2/Si_3N_4	S	[2.41]
120	23.4	320.. 400		S	SiO_2/Si_3N_4	S	[2.42]
100	7.5 K/mW			S	SiO_2/Si_3N_4 Poly-Si heater Al-contacts Ta, Ti/Au, Ti/Pt coating	D	[2.43]
1000	100	400	20	M		D	[2.44]
100x10	35	560	0.2	Micro bridge		D	[2.45]
200					Poly-Si heater with Pt- film	D	[2.46]
1600x1600	80	270		M	Poly-Si heater, Au-pads	S/D	[2.46]
1350x370	250	500		M	Pt-heater, Au electrode pads	S/D	[2.48]
300x700	50	600		S	Poly-Si heater, SiO_2/Si_3N_4 membrane	S	[2.49]
110	100	400		S (surface micro machined)	Poly-Si membrane	S	[2.50]
100 x 100	5	300		M	SOI membrane, CMOS FET heater (n-type and p-type	S	[2.51]
200 x 200	10						
300 x 300	25 (FEA data only)						

2.3.2 Discussion

Categories of micro heaters include:

- Pellets
- Thick film and thin film devices on ceramic or semiconducting substrates
- Semiconductor based micromachined devices (micro hotplates, etc.)

Keeping in mind the motivation and applications fields aimed at, the only devices with the potential to reach very low power consumptions are clearly the semiconductor based micro membrane and micro hotplate heater devices. These can be categorized into

- Backside micro machined membrane heaters
- Front side micro machined micro hotplates
- Micro-Filament devices

All these devices have a number of major drawbacks in common:

1. The power consumption at sufficiently high temperatures is in most cases still too high (60mW-100mW) for the use in battery powered devices. Reasons for this can be found in the device designs underlying some limitation from the materials employed.

2. Small devices with lower power consumption use very simple contact electrodes, rather than interdigital electrodes. A varying number of electrode pairs and electrode spacing is not possible and thus no adjustment to varying metal oxide specific resistances can be made.

3. Standard MEMS materials are used in the device fabrication (membrane and heater) in order to ensure reduced development expenses (cost and time) and fabrication cost. They are widely used and easily available in every

semiconductor fabrication facility. Standard MEMS materials are however not designed for the use in oxidizing high temperature gas atmospheres. The device long term stability and lifetime is therefore very limited compared to thick film devices on ceramic substrates.

4. The operating temperature ranges are small ($T_{max.}$ < 450 °C). Many devices do not feature a separate on-chip temperature sensor, which allows a more precise control of the operating temperature than by the measurement of the heater resistance.

5. The device designs are limited to specific applications rather than allowing the flexibility to use the wide variety of metal oxides with strongly varying operating temperature and specific resistance. The main advantage of metal oxide based gas sensors is thus not used: the huge variety of possible material combinations. Not only does this approach cause development costs for almost every new gas sensitive metal oxide used, the number of devices needed for a single application is usually too small to justify mass production oriented MEMS devices.

Arrays of micro gas sensors have been proposed and demonstrated to improve the selectivity and distinguish between different gases in gas mixtures. They usually consist of several single gas sensors thereby wasting space and increasing the power consumption. Attempts to integrate several micro hotplates and subsequently gas sensors into one micro membrane are not presented in literature. The only array type getting close to anything like an integrated micro hotplate array are the front side micromachined hotplates presented by NIST [2.35]. These hotplates however, are not placed within one thin substrate membrane, but each feature micro bridges in direct contact with the bulk material.

These key problems of present devices constitute the bases for the requirements set on new improved micro hotplates for the use with metal oxide thin films in gas sensor applications.

2.4 Perspectives and requirements for future devices

The requirements for a new gas sensor device for the use in portable applications include the combination of:

- The stability, lifetime and low cost of simple thick film technology and pellet based gas sensors
- A lower power consumption, and shorter thermal and gas sensitive response as well as a smaller size than state of the art micro hotplate based devices.
- Battery powered operation for portable devices, not exceeding 2 V of operating voltage (1.5 V, 750 mAh as typical values for a AAA size cell)
- The possibility of integration of several micro hotplates/sensor arrays on one chip

The criteria for the requirements for a new micro hotplate gas sensor can be derived from the drawbacks of present state of the art devices in research and industrial use (chapter 2.3). In order to ensure a high relevance to industrial applications, a questionnaire on the sensor requirements was answered by a number of representative industrial users ranging from small and medium size enterprises (SME's) to large global players. The combination of both information sources lead to the new sensor design specifications and design goals. I.e. the design task is twofold: fulfilment of the technical requirements and the expanding of the limits of state of the art in research.

Clearly, a new micro hotplate must have lower power consumption, higher operating temperature, shorter thermal response time, better long term stability, improved gas sensitive response and smaller size than state of the art devices.

Further, it must be usable in as many gas sensor applications as possible. Hence, it must work in the largest possible temperature range, with short thermal response times, to allow different modes of operation. It must also facilitate the use of a large bandwidth of different metal oxides with different specific resistances. Therefore it has to provide enough space for a proper interdigital electrode structure for contacting of the metal oxide. For the same reason, the device must allow operation with different supply voltages. Since the metal oxide characteristics vary with temperature (chapter 2.), the temperature variation across the gas sensitive metal oxide layer should not exceed 5 K to 10 K.

Finally, a new design should facilitate the integration of multiple array structures on a single chip. These criteria are crucial for the use in portable and handheld gas measurement and detection devices. The combination of these properties leads to a new generation of micro hotplate devices for micro gassensors beyond the limitations of current industrial and research devices. Table 2.3 summarizes quantitatively the minimum requirements set on a novel micro hotplate gas sensor device.

The requirements constitute a significant expansion of state of the art micro hotplate research devices on the one hand and industrial thick film gas sensors on the other hand. The power consumption and geometry is reduced below state of the art hotplates, while allowing operating temperatures beyond state of the art hotplates and close to current thick film gas sensor devices. Furthermore, no device working with only 1-2 V operating voltage has been presented in literature before, as is required for the new micro hotplate.

Tab. 2.3: Requirements for the novel micro hotplate device. Lower power consumption, battery operation capabilities and higher operating temperatures compared to state of the art micro hotplates are combined.

Property		**Quantity**	**Unit**	**Comment**
Heater efficiency		> 9	K/mW	
Power consumption		< 50	mW	
Operating temperature range		RT..T..450 (650)	°C	
Thermal response time		< 100	ms	
Temperature variance across metal oxide		± 5…10	°C	
Heater long term stability at maximum operating temperature (continuous operation)		>> 50	h	The long term stability is a property depending strongly on the application and requirements of the industrial user
Gas sensitive response time		< 30	s	Gas sensitive response is mainly controlled by the characteristics of the gas sensitive layers
Size	Chip	≤ 2 x 2	mm^2	
	Heater	≤ 100 x 100	μm^2	
	Array-heater	-	-	
Operating voltage		1-2	V	(two ranges)
		12-24	V	
Sensing electrode structure		flexible/IDE		
Array integration		On-chip		

3. Sensor concept

In this chapter, based upon the specifications compiled in the previous paragraph, the sensor concept is developed and explained. Where possible, alternative solutions are compared, leading to the final sensor concept. First, the general design (i.e. rough shape, geometry and layer design) is developed. A new front and backside micromachined design of sandwiched supporting, heating and insulating layers, allowing very close packing of several hotplates into one array is proposed. Then, suitable materials for the mechanical structure and heater metallisation are presented, compared and selected.

The micro gas sensor detection principle is based on measuring the gas dependant change in electrical conductivity of metal oxide thin films. When using this operation principle, three components are needed on a device: a heater for the operation at elevated temperatures (preferably a resistive temperature sensor for temperature control), contact electrodes and a metal oxide thin film for gas detection.

The sensitivity of metal oxide gas characteristics towards temperature changes require a homogeneous temperature distribution across the sensitive layer (chapter 2). A sandwich structure of substrate, heater, electrodes and metal oxide placed on top of each other allows a simple device design with a homogeneous temperature distribution across the sensitive metal oxide layer. The lateral extension of such a device (Fig. 3.1) is smaller than a comparable device with heater, sensitive layer and temperature sensor placed adjacent to each other.

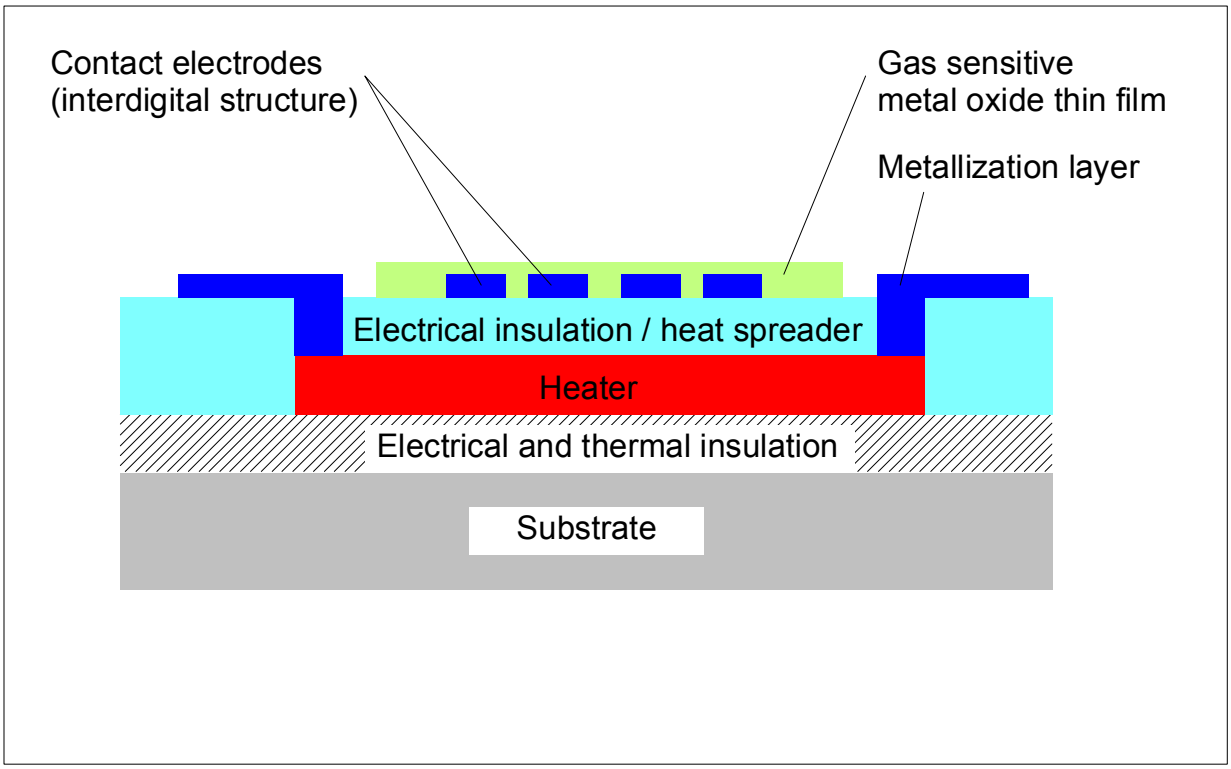

Fig. 3.1: Sandwich structure of substrate, heater, electrodes, metal oxide and insulating layers. An additional temperature sensor can be implemented at heater or metallisation layer level.

Insulation layers are placed between substrate and heater as well as between heater and electrodes to prevent leakage currents and short circuits between heater and sensing electrodes. The metallisation layer includes the connecting leads, the heater supply contacts, the sensing electrodes and a resistive temperature sensor in one layer. This reduces the number of layers and processing steps and thus the fabrication cost. Furthermore, placing the sensing electrodes and the temperature sensor in close proximity to each other insures reliable information on the actual temperature at the metal oxide layer. The sensing electrodes are designed as interdigital comb structure. This way, the metal oxide thin film resistance is split into several smaller resistances switched in parallel, thereby reducing the usually high resistances (e.g. $\rho_{MoO3} = 10^5$ ..

10^{10} Ωcm [3.1, 3.2]). By adjusting the number of finger pairs in the comb structure, the resistance range for the applicable metal oxides can be modified.

3.1 The new micro hotplate concept

Present devices use either a backside bulk micromachined membrane type heater or a "front side" surface micromachined supported membrane ("spider"-type). The new micro hotplate combines both into a front and backside micromachined device consisting of a thin membrane "containing" a variable amount of supported heaters (Fig. 3.1 (left)).

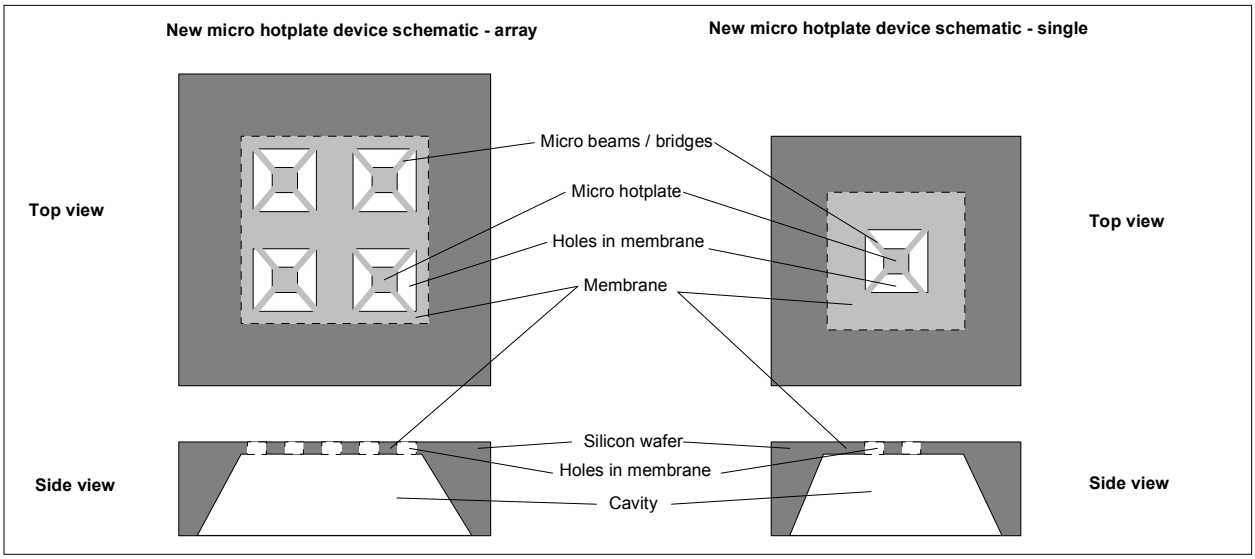

Fig. 3.1: Schematic of new micro hotplate concept with back and front side micromachined membrane.

The advantage of this approach is a twofold thermal one: integrating the supported membranes into a larger membrane reduces the thermal losses through the substrate compared to the surface micromachined devices where the supporting micro bridges are in direct contact with the substrate. Furthermore, this design avoids the small air gap between heater and underlying substrate (between 2 μm and 150 μm deep). At such short distances between heater and

thermally highly conductive silicon substrate (acting as a thermal ground/mass), the thermal conduction through the air does become a significant factor.
In order to give a preliminary estimate for the correctness of this assumption, we assume a simplified model with a heated area of 100 μm x 100 μm at 500 K above ambient air temperature. Assuming average air gap depths of between 2 μm and 100 μm depth (as approximate average value underneath the hotplate for the pyramid shaped 150 μm deep pit of the surface micromachined devices) , we obtain (using λ_{air} = 0.02 $Wm^{-1}K^{-1}$) power losses of ($P = -\lambda_{air} A_{heater} \Delta T / \Delta x$) 1 mW (at 100 μm gap) to 50 mW (at 2μm gap). Considering the power consumption of the whole device is to be between 30 and 50 mW this is a very significant source of thermal loss. A new design will therefore have to avoid creating a small air gap between heater and substrate, but rather remove all the material beneath the heater through bulk micromachining. A detailed model analysis and simulation of the device's thermal properties will be presented later in this work.
Finally, the device design integrating small supported membranes in a bigger one gives a larger amount of freedom in placing several micro hotplates close to each other in one membrane and on one chip.

3.2 The new material choice

Apart from the device design, the material choice is of utmost importance to the device properties. The materials used for micro gassensor devices today typically originate from MEMS technology.

As previously stated, the material choice in present devices is one of the main causes for poor device properties. The necessity of new materials for the use in micro hotplate gas sensors is obvious, when trying to improve upon the device properties. A new material combination has to sustain higher operating

temperatures and corrosive media and feature better mechanical strength to allow new designs and higher thermally induced stress (i.e. higher operating temperatures). At the same time it must have a reasonably low thermal conductivity to prevent high thermal losses and allow standard semiconductor processing.

When looking at the material choice, we have to distinguish between the materials used for the membrane structure and the materials used for the metallisation. SiO_2, Si_3N_4, SiO_xN_y, SiC and DLC (Diamond-like-Carbon) are materials available and principally suitable for membranes in MEMS processing technology (Tab. 3.1).

Tab. 3.1: Properties of selected materials [3.3, 3.4, 3.5, 3.6, 3.7, 3.8, 3.9, 3.10, 3.11]

Material	**SiO_2**	**Si_3N_4**	**SiC**	**DLC**
Melting Point T_m / °C	1600	1480	Sublimes >1800	>4000°C
Young's Modulus/GPa	46-92	104-380	700-2000	150-800
Intrinsic stress / MPa	(compressive)	(tensile)	200-1000 (tensile)	(tensile)
Specific resistivity / Ωcm	$10^{14} – 10^{16}$	10^{14}	10^{12}-10^{14}	-
Structuring	Wet etch (HF, NH_4F)	Dry etch (SF_6)	Dry etch (SF_6:O_2)	-
Thermal expansion coefficient / C^{-1}	$5 * 10^{-7}$	$2.8 * 10^{-6}$	$8.9 * 10^{-6}$	-
Thermal conductivity / $Wm^{-1}K^{-1}$	1.4	20	500	1000

SiO_2 membranes almost always exhibit compressive stress causing buckling of the membrane. Si_3N_4 is amongst the most frequently used materials for thin heater membranes today due to its intrinsic tensile stress producing flat membranes. The mechanical stress of these membranes as well as the high oxidation rate at elevated temperatures are drawbacks to their mechanical and chemical stability. SiO_xN_y membranes and sandwich structures of both materials try to combine the lower oxidation rate and lower thermal conductivity of the SiO_2 layer with the tensile stress of the Si_3N_4 layer. In practice, these types are

used almost as often as the pure Si_3N_4 membranes. The different thermal expansion of the layers however induces thermo-mechanical stress which can lead to cracking of the membrane.

DLC certainly exposes highest thermal, mechanical and chemical strength, but the rare availability of the material itself as well as suitable processes needed for the structuring of the material make it unsuitable for a cheap gas sensor device. Furthermore, its thermal conductivity is exceptionally high, obviously making it unsuitable as membrane material when aiming for high thermal insulation.

SiC comes in a number of polytypes (polycrystalline on SiO_2, 3C, 4H, 6H) and features very high mechanical strength and chemical and thermal resistivity while being more and more available as "standard" material in MEMS. Its oxidation rate is one order of magnitude smaller compared to most other silicon-compounds. Its material properties and processing technology has reached a sufficient level to allow construction of sensor devices from this material. SiC is best suited to satisfy the requirements set upon the new sensor device. Its properties will be described in more detail in chapter 3.2.1.

For the metallisation layer, a variety of CMOS and MEMS materials are known today. To name a few: Al (AlSi), Au, Pt, TaN, TiW, TiWN, WC, TaC, TiC, HfB_2 and Mo are amongst the most prominent ones used today (Tab. 3.2).

Tab. 3.2: Material properties for selected metallisations [2.1, 3.4]

Material	**Al**	**Au**	**Pt**	**Mo**	**HfB_2**
Density [kg/m^3]	19300	2700	21500	10200	11200
Thermal conductivity λ [W/mK]	237	317	71.6	138	41.8
Melting point T_m / °C	660	1000	1768.4	2623	3250
Specific heat capacity [J/KgK]	897	129	133	251	25.1
Specific resistance / μΩcm	2.4	2.2	9.6	4.85	253 ± 5
Passivation required	Si_3N_4/ SiO_2	-	-	Si_3N_4/ SiO_2	Si_3N_4/ SiO_2/TaN
Contact layer / diffusion barrier required on Si and SOI substrates	Ti / TiWN	Ti / TiWN	Ti	-	-

Al-metallisations are most frequently used with a limit in operation temperature at about 1/3 of the melting point of Al. Also, a suitable passivation, like e.g. Si_3N_4 has to protect the Al from oxidizing.

Au thin films feature high sublimation and diffusion rates at elevated temperatures. Diffusion barrier layers are necessary to prevent the diffusion of the Au into the underlying (Si-)substrate. The Au melting point is however far higher compared to Al. Also, the electrical conductivity is the highest of all metallisation layers available today. Layers of this type have been shown to operate up to temperatures of 650°C.

Pt-layers exhibit a very large maximum operating temperature up to about 1000°C and are practically inert against most aggressive media. The specific electrical conductivity of Pt is comparably low for a metal thin film layer. Pt is therefore frequently used as heater or in thick film technology, where the layer thickness compensates for the low specific conductivity. Thin film Pt-layers usually have to be structured using physical processes like sputter etching, making their processing difficult and expensive.

TaN/TaC is used as protective coating in inkjet printhead heaters but exhibits rather poor electrical conductivity. Ti, TiW, TiWN, WC and a number of other combinations are used as contact metals or diffusion barriers between substrates and Au-based metallisations. Mo exhibits a very linear U-I relation even at temperatures of about 600°C. It is however difficult to structure, requires a protective passivation layer and features a medium electrical conductivity.

HfB_2 has the highest resistivity and highest melting point (>3200 °C) of all metals available as thin film metallisation layers and is used in inkjet printhead heaters [3.18]. It can easily be structured using wet etching processes. A passivation layer is however required to prevent deterioration of the layer through oxidation processes. Its properties are described in more detail in chapter 3.2.2.

The heater metallisation as well as the electrical contacts have to sustain sufficiently high temperatures. The sandwich design of the device and the required simple heater geometry necessitate a very high resistance metallisation with high melting point. The contact metallisation has to exhibit the lowest possible resistance in order to reduce power losses.

The resulting concept thus suggests using an HfB_2 heater protected by an insulating passivation layer (sandwich design) with a potential to operate up to 1000°C. On a separate note, it must clearly be said at this stage, that thin film layer properties after processing can differ largely from the bulk material properties. I.e. even though there is the potential for HfB_2 to open up a new temperature range for thin film heater elements, technical realisation will impose some limitations. The heater will be supported by a SiC-membrane structure, which can easily sustain extremely high temperatures. On an additional note, indicating the right material choice, it may be stated here that current NASA research focuses on HfB_2:SiC compounds for thermal shielding, which can sustain temperatures up to 5000°C [3.12].

SiC is known for its excellent chemical durability, mechanical strength and sustaining of high temperatures while keeping semiconducting electrical properties [3.6, 3.7, 3.8, 3.9]. HfB_2 is investigated for thermal shielding [3.12, 3.17] in combination with SiC and has also come to the attention of researchers through its application as heater in inkjet-printheads [3.18]. The following chapters gives a brief summary of the deposition and growth techniques as well as the relevant material properties in comparison to presently used standard (semiconductor) materials for both SiC and HfB_2.

3.2.1 Silicon carbide properties

SiC is a stoichiometric compound semiconductor made of Si and C atoms, which comes in various lattice configurations or polytypes. The 3C-polytype has a zincblende structure, i.e. it consists of two face-centred-cubic (fcc) lattices – one made of Si, one made of C – displaced by one quarter of the lattice constant. Furthermore, there are 2H (Wurtzite structure), 4H and 6H (hexagonal structure), 15R and 21R (rhombohedral structure) polytypes [3.12]. Whereas the rhombohedral forms are used in non-electronic applications (e.g. surface coatings, abrasives), the 3C, 4H and 6H forms are used for electronic and micromechanical devices. 3C-SiC has a higher electron mobility and isotropy than 4H and 6H-SiC. 4H-SiC has an isotropic, but lower electron mobility than 6H material. The electron mobility in the 6H-polytype varies with crystal direction. 4H single crystal material wafer, 6H single crystal material (wafer), polycrystalline and amorphous (thin films by CVD-deposition) material can be readily bought from commercial sources. Some of the most relevant material properties of 6H, polycrystalline and amorphous SiC are summarised in Table 3.1.

Table 3.1: Some important properties of single crystal, poly-crystalline and amorphous SiC [3.20..3.25] at 300 K

Property	**Single crystal SiC**		**Poly-crystalline SiC thin films**	**Amorphous SiC Thin films**
	3C	**6H/4H**	**3C**	
Bandgap [eV]	2.3	2.9	-	-
Lattice parameter [A]	4.348	a=3.0806 c=15.117	-	-
Density [g/cm^3]	3.166-3.210	3.211-3.249	-	-
Dielectric constant	9.72	9.66 ⊥ 10.03 ||	-	42
Electron mobility [cm^2/Vs]	1000	600		
Hole mobility [cm^2/Vs]	40	40		

Property	Single crystal SiC		Poly-crystalline SiC thin films	Amorphous SiC Thin films
	3C	6H/4H	3C	
Breakdown field E_B [V/cm]	$4 \cdot 10^6$	$2.5 \cdot 10^6$		2.2
Thermal conductivity [W/mK]	500	500	90-210	130-160
Melting point [°C]	Sublimes >1800	Sublimes >1800	Sublimes >1800	Sublimes >1800
Mohs' hardness	≈ 9	≈ 9	≈ 9	
Coeff. of thermal linear expansion [10^{-6} K^{-1}] (at 300K)	8.9	8.9	3.7	
Saturation electron drift velocity [cm/s]	$2.5 \cdot 10^7$	$2 \cdot 10^7$		
Young's modulus [GPa]	250-350	700	440	$8.5\ 10^6$ (ceramic at room temperature)
Poisson ratio	0.05-0.3		0.16	
Intrinsic mechanical stress σ_{max} [MPa]			200-400 (tensile)	200-900 (compressive, as-deposited, tensile, after anneal)
Tensile strength [GPa]		21		725-2900 (at 25 °C)
Deposition temperature	1000 °C – 1500 °C		600°C-750 °C	300°C-400°C

SiC fabrication techniques vary with the SiC application field. Material for non-electronic applications is mostly made by the Acheson process (bulk material) [3.25] or deposited by CVD or sputtering (surface coating). The impurity of this material makes it non-suitable for electronic applications.

The use of SiC in electronic or micromechanical devices requires the fabrication of high purity SiC thin films and wafers. 4H and 6H-SiC is available as bulk and thin film material, 3C-SiC can so far only be fabricated as thin film on Si or α-SiC.

Bulk SiC can be grown from vapor (e.g. Van-Arkel, Lely, sublimation method)[3.26]. SiC-thin films can be deposited in homoepitaxy (on SiC substrates) using Liquid Phase Epitaxy (LPE), Molecular Beam Epitaxy (MBE), Chemical Vapor Deposition (CVD) and the sublimation method. Heteroepitaxial films (e.g. on Si or SOI) can be produced by CVD [3.26].

The single crystal material features all the properties making SiC so attractive: high mechanical strength, high thermal conductivity, ability to operate at high temperatures, excellent chemical inertness, high bandgap. Drawbacks are the high thin film deposition temperatures (1000°C - 1500°C) and complex fabrication processes, despite the remarkable progress in recent years. Poly-SiC thin films have been demonstrated by various authors with deposition temperatures around 650°C – 750 °C [3.27..3.29]. The structuring of these layers and the etch selectivity towards Si and SiO_2 is still challenging. The Al-mask frequently used during SF_6:O_2 RIE-etching of the SiC can impose contamination problems for following processes [3.17].

Since a large proportion of the MEMS applications of SiC require only the mechanical, thermal and chemical properties of SiC, PECVD-grown polycrystalline and amorphous 3C-SiC layers on standard Si-wafers and other non-Si substrates gain increasing attention of researchers [3.30..3.33]. Among their advantages are a more homogeneous thickness distribution, lower deposition temperatures (300°C-400°C compared to 1000°C-1500°C, therefore less damage to the underlying Si-crystal) and the availability of layers on large area substrates up to 6 inch diameter. Also, the layer parameters (stress, Young's modulus) can be tuned adapting them to the specific needs of the particular device [3.33].

In summary, the choice of the right SiC type depends very much on the application. Whereas all electronics and many sensor applications (e.g. SiC-piezoresistors for high-temperature pressure and force sensors) require single crystal material, most MEMS devices only need the SiC as protective coating, masking and mechanical support. These applications are more likely to use amorphous PECVD material, which satisfies all the requirements without the

necessity of a complex high temperature deposition process. The thermal conductivity of these layers is considerably lower than of single crystal material.

3.2.2 Hafnium diboride properties

Hafnium diboride is a metal alloy. Hafnium was only separated from its closest chemical neighbour Zirconium in the 1950's[3.34]. Since then, the fabrication and number of available compounds of which Hafnium carbide and Hafnium diboride are the most common has continously increased [3.34]. Research in high temperature compatible materials for thermal shielding [3.12, 3.16] studies HfB_2 due to its high melting point.
In MEMS technology, HfB_2 has been applied in inkjet printheads as heating element with a TaN protective coating [3.18]. The available data of its material properties is very limited and summarised in Table 3.2.

Hafnium Diboride is available as powder or in sintered form. HfB_2 thin films can be deposited by sputtering. Hafnium as a pure element is known to be highly resistant to concentrated alkalis. At elevated temperature, however, it reacts quickly with O_2, N_2, C, B, S and Si. It oxidises quickly, building a Hafnia (HfO_2) layer on the surface [3.34]. Corrosive liquids and fumes destroy the HfB_2 thin films very quickly. As many acids (e.g. HCl, HNO_3, H_2SO_4) attack HfB_2 easily, the key to structuring these layers lies in a clean etching process that can be controlled accurately as will be described in chapter 6.

3.3 Discussion

The new sensor concept uses supported micro hotplates in a thin membrane for improved thermal insulation and application flexibility. These micro hotplates

are fabricated using front and backside micromachining. A sandwich structure placing heater, sensing electrodes and metal oxide layer on top of each other onto the substrate is used. SiC and HfB_2 are used as new material combination to overcome the problems inherent to present devices' materials. A challenging task will of course be the deposition of the sensitive metal oxide layers onto the micro membrane heater without regular photolithography processes.

The advantages of this concept are:

- Combined front and backside micromachining: the subsequent small size and minimal amount of space needed for each device lead to advantages in power consumption and array design.
- The sandwich structure with mechanically strong SiC membrane, heater and electrode structure placed on top of each other, thereby limiting the size, power consumption and temperature inhomogeneity across the hotplate and subsequently the metal oxide layer.
- The material choice: SiC and HfB_2 has the potential to break the limits of conventional MEMS-type materials by far, allowing a much larger operating temperature range and mechanical stress and thus a larger device design flexibility. Technological and processing requirements are expected to have an impact on the material performance.

Fig. 3.2 outlines the design and development process of the micro hotplate. Following the basic design concept including the materials used, the geometry of the supporting structure, hotplate, electrodes and contact leads will be decided and optimised towards achievement of the technical specifications.

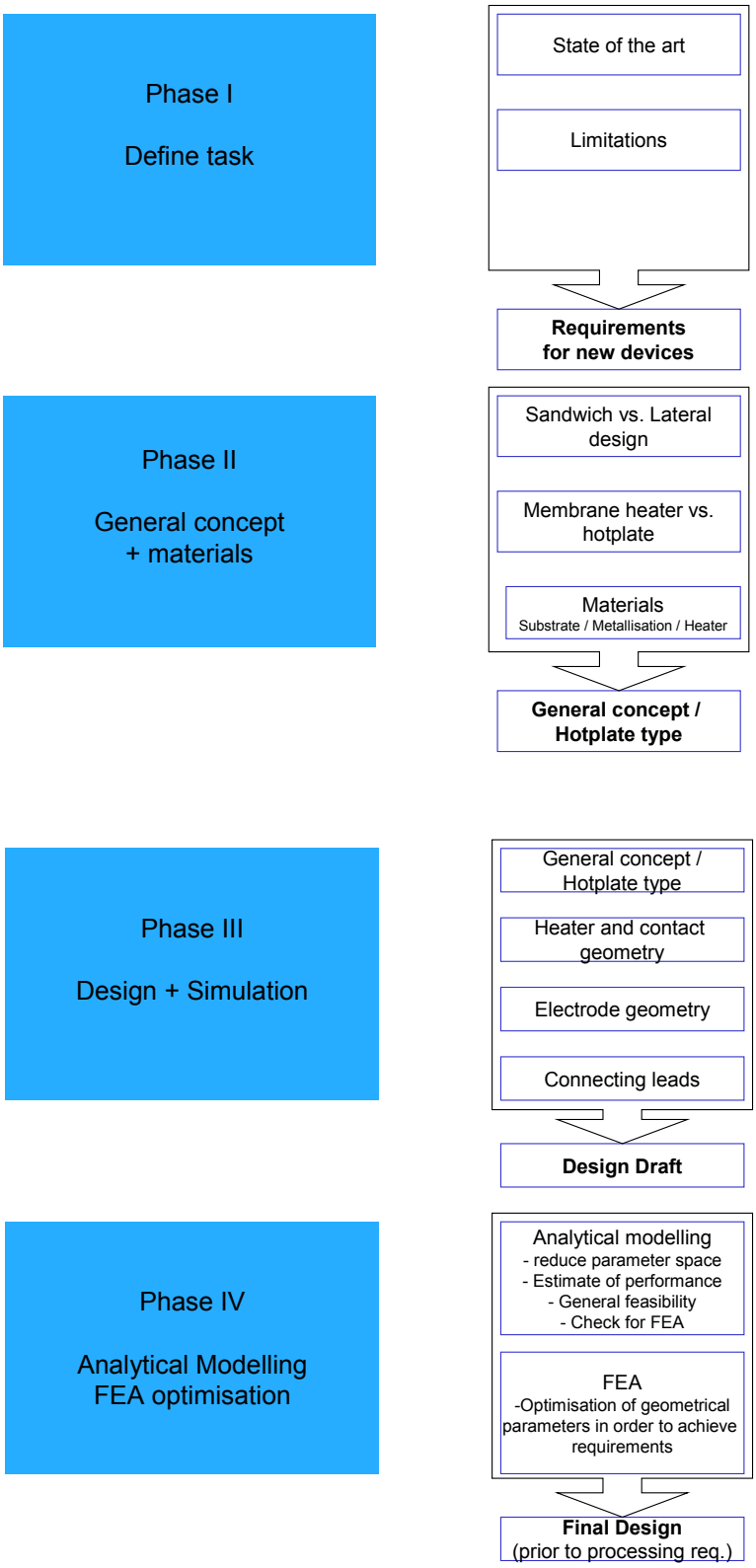

Fig. 3.2: Sensor development phases. At this stage, the general concept has been decided. Based on the concept the design draft is developed and optimised.

4. Design and simulation

In chapter 4, the general device concept from chapter 3 is developed further into a complete device design. The designing process is partitioned into the micro hotplate, the sensing electrodes and temperature sensor and the geometrical properties of the supporting structure. Partially, Finite Element Analysis (FEA) is used to compare alternative solutions. The final modelling and FEA of the complete device can be found in chapter 5.

Designing the new micro hotplate device includes the actual heater, the temperature sensor, the electrode structure, the insulating layers and the supporting structure geometry of the membrane. Since all components are mutually influencing each other in design and operation, the design of each component has to take the boundary conditions imposed by the other components into account.
The design process starts with the heater, followed by the resistive temperature sensor for temperature control, the sensing electrode structure, the insulating layers and the supporting structure geometry.

4.1 Integrated micro heater

The heater has to heat the gas sensitive layer to its operating temperature, which depends on the metal oxide, operation mode and gas species. It must fulfil the following specifications (tab. 2.3):

- Minimum operating temperature range from 100°C to 500 °C. Preferably, up to 1000 °C for pulsing / cleaning
- Maximum heater power consumption below 100 mW; Heater efficiency better than 9 K / mW

- Lateral extension fitting on a 100 µm x 100 µm hotplate
- Good temperature uniformity ($\Delta T = \pm 10$ K)
- Two operating voltage ranges (1-2V, 12-24 V)

4.1.1 Micro heater design

The heater has to be able to generate a maximum of around 100 to 200 mW in heater power in order to keep a power "buffer" for operation well above the required 500 °C maximum operating temperature. Considering the two operating voltage ranges of 1-2 V and 12-24 V we thus obtain heater resistances of around 10 Ω and a few kΩ for the respective ranges. These can be obtained by using a metal thin film resistive heater for the low voltage and a semiconductor resistive heater for the high voltage range.

Hafnium diboride has been chosen as metal thin film heater material due to its outstanding thermal properties and its specific resistance of 256±15 µΩcm. Silicon carbide is used for the semiconductor heater. Its outstanding thermal and corrosive properties are obvious.

The rough dimensions of the heater are given through the industrial demand and physical requirements (chapter 2). Principally, the resistive heater shape can be a meander type or a simple rectangular heater (Fig. 4.1).

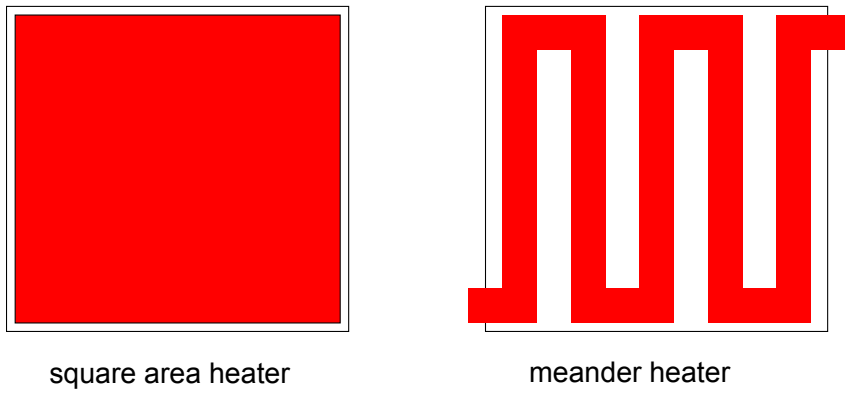

Fig. 4.1: Design decision between a square area heater and a meander shaped heater. Temperature uniformity across the heater and technological design considerations (i.e. lateral lithography resolution) favour the square heater.

The square area heater has a parabolic temperature profile with maximum in the center. The shape of the parabola is however strongly dependant on the heater environment (i.e. surrounding heat sinks, like e.g. supporting beams or the substrate). A meander structure can consist of serial or parallel resistors and allows fine tuning of the power and heat density across the heated surface for better temperature uniformity. Frequently, an additional heat spreader layer has to be used to smooth the temperature profile. The temperature profiles obtained this way can be more uniform than simple rectangular heater profiles [4.1]. The design and fabrication effort (meander precision and additional layers for heat spreading) is considerably higher than for rectangular heaters, thus causing additional cost factors for series production.

Finally, the limitations of the available technology have to be taken into account. A lateral resolution of 2.5 μm is the limit on a perfectly flat substrate surface using the available technical equipment at the Technical University Berlin. Considering the groves and surface roughness through front and backside micromachining of the device, experience tells that 5 μm is the maximum possible lateral resolution. I.e. every line on the surface needs a 10 μm wide corridor. Considering the small size of the hotplate, a meander shape is not advisable. Furthermore, an insulation layer will be needed between heater and sensing electrodes, whose lateral extension has to fit between the hotplate outer extensions and the resistive heater, in order to cover it completely, while additionally keeping in mind the lateral resolution. Hence, a square area heater of 80 μm x 80 μm was chosen (maximum size possible). The next step is to decide on the geometry of the electrical contacts for the heater.

4.1.2 Influence of the electrical heater contacts on the heater current density distribution

When using a square area heater, the shape and size of the electrical heater contacts is very important in determining the electrical current distribution across the heater. Assuming a constant sheet resistance, the current distribution is a direct measure of the heat power density.

For the achievement of a uniform temperature distribution, a uniform power density across the active IDE-area of the heater is of utmost importance. Guaranteeing a homogeneous current distribution in the heater resistor can yield such a distribution. When using a square pattern for the resistor area and assuming the resistor sheet resistance to be uniform, the widths of the connections on either side of the heater control the current distribution (Fig. 4.2).

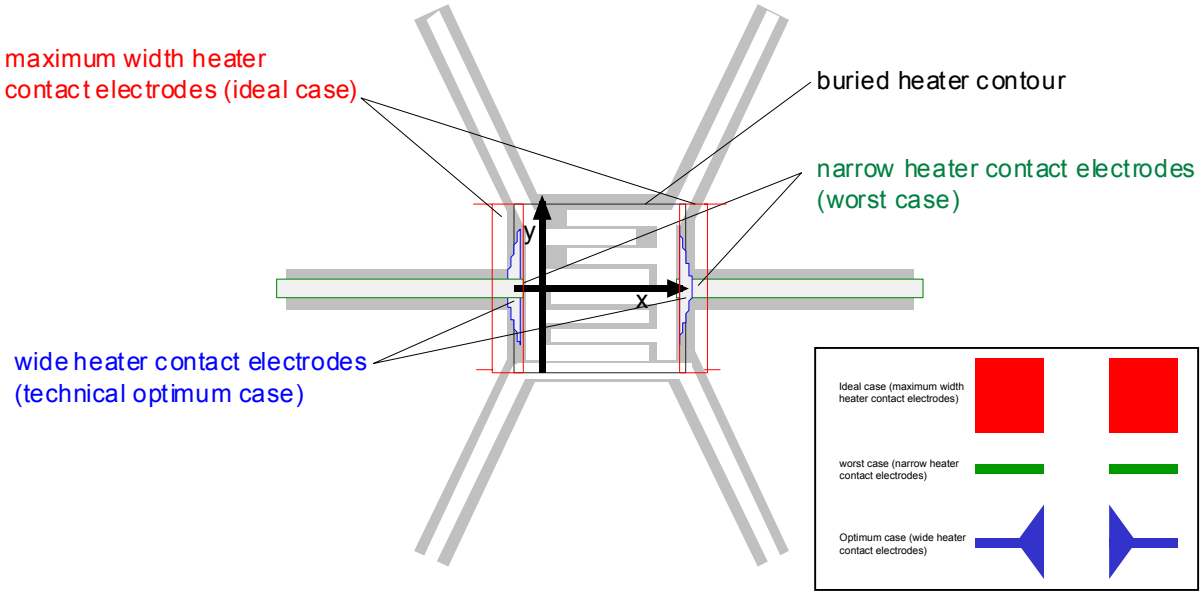

Fig. 4.2: Comparison of possible heater contact electrode shapes. For a homogeneous current distribution across the heater, the electrodes contacting the buried heater ought to be as wide as possible. This ideal case is limited by a combination of geometrical and technological restraints. The blue fan shaped electrodes indicate the optimum case.

A design using only the 10 µm wide Au-leads was compared to fan-shaped electrodes of about ¾ the width of the resistor. This limitation was given by the geometry of the heater and IDE. The positioning of the leads for the IDE and the temperature measurement resistor prevent the use of wider electrodes.

A Finite Element Analysis (FEA), using a three dimensional model of the hotplate and supporting beams, was performed to determine the difference between the two heater contacts. Only the relative difference between the two versions is important, so no further detail on the material data assumed is given here. More detailed information can be derived from appendix D. In the simulation model a constant voltage was applied at the contacts. The electrical conductivity of the materials used was assumed to be constant as well. A heater lateral extension of 80 µm x 80 µm with heater contacts of 10 µm and alternatively 60 µm width were used as geometrical constraints.

Clearly, the current density is almost constant in the case of the wide electrodes and has high peaks on either side of the heater in the case of the small electrodes (Fig. 4.3, Fig. 4.4).

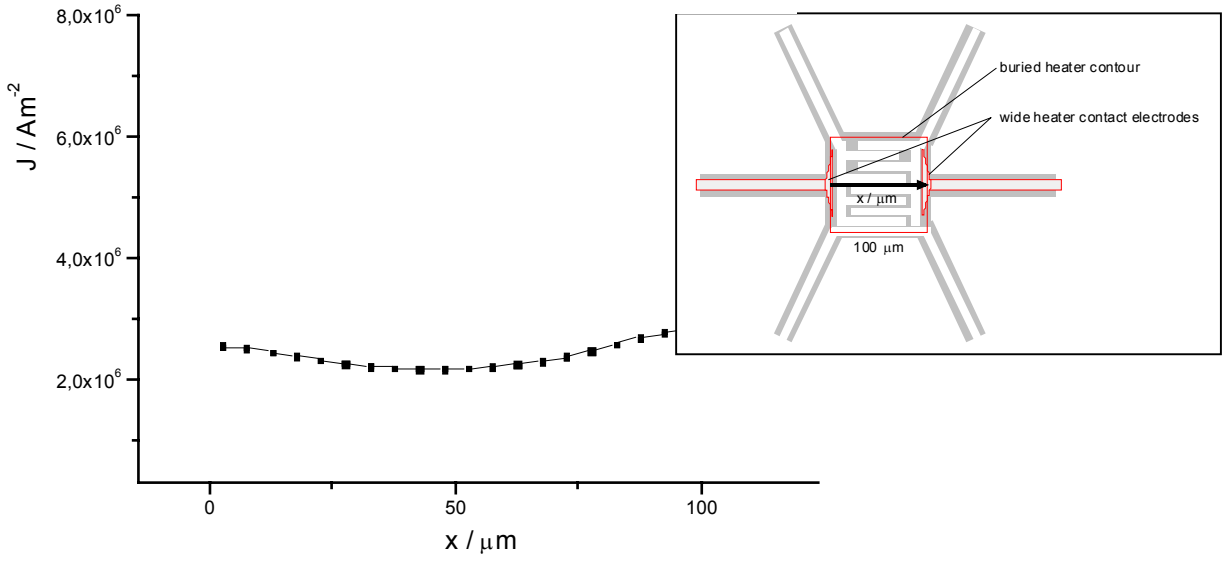

Fig. 4.3: Current density in direction of the current flow across the heater membrane using wide electrodes (¾ of the heater width) (Supporting beam of 10µm width and 150 µm length). A fairly flat profile can be observed.

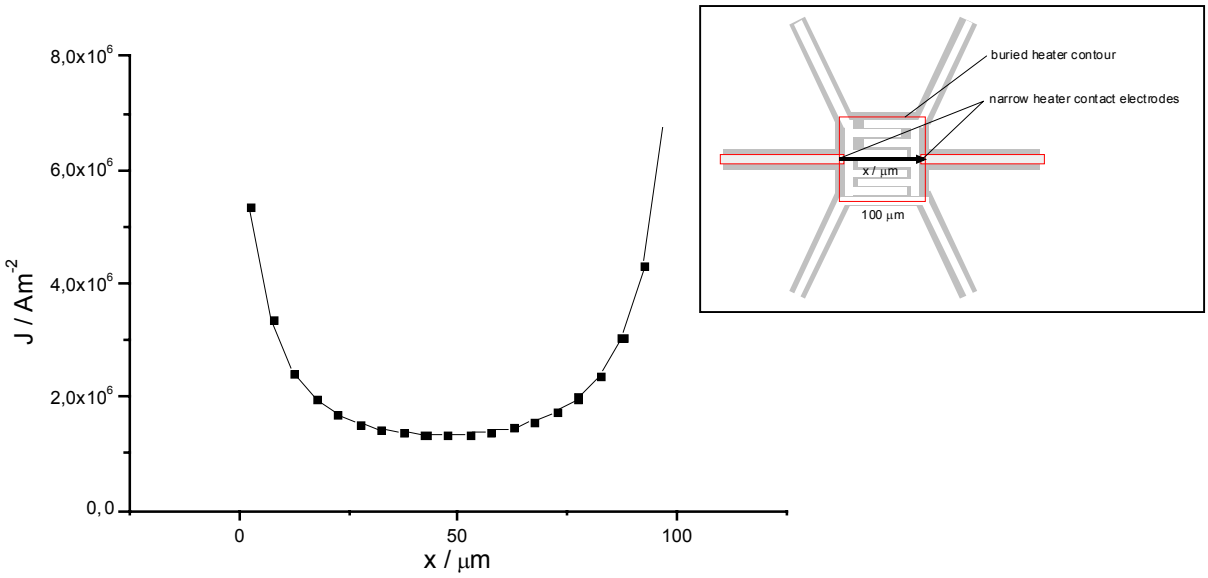

Fig. 4.4: Current density in direction of the current flow across the heater membrane using small electrodes (10 µm wide) (Supporting beam of 10µm width and 150 µm length). Peaks can be observed on either side of the heater where the contact electrodes are placed.

These peaks would cause temperature peaks at the corresponding positions on the heater and increase material deterioration through corrosion, oxidation and migration/diffusion originating from the high temperature and current through a system of metallisations (TiWN/Au leads, HfB_2 heater) whose characteristics under such circumstances are unknown.

The power differential dP is given by the current density J multiplied with the voltage drop dU along an infinitesimal volume increment dV, leading to:

$$dP = J\,A\,dU \tag{5.1}$$

$$\frac{dP}{A\,dx} = J\frac{dU}{dx} \quad \text{(simplification as linear case)} \tag{5.2}$$

$$\frac{dP}{dV} = const. \cdot \frac{dU}{dx} \quad \text{(assuming J = constant, A = constant)} \tag{5.3}$$

Thus, for a constant power density, a constant potential gradient along the x-axis is required. As can be seen from Fig. 4.5 the wide electrode heater version clearly produces a linear voltage profile, i.e. a constant voltage gradient, compared to the tan(x) - behaviour when using the narrow electrodes (Fig.5.19).

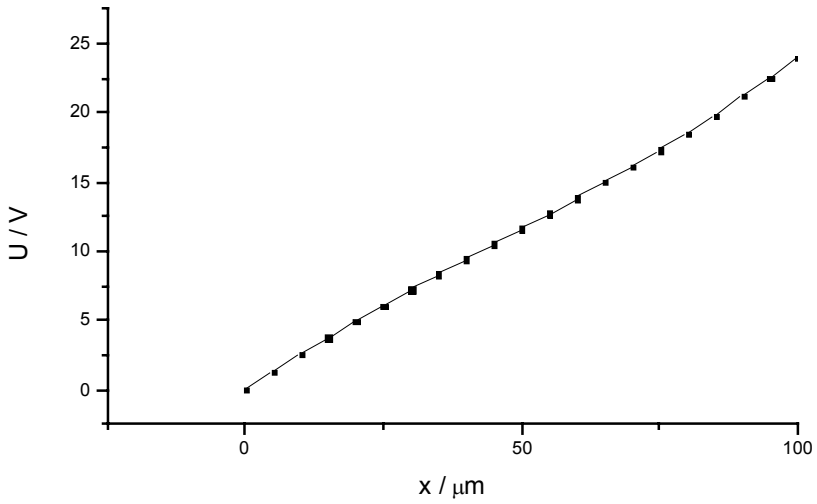

Fig. 4.5: Voltage drop in the direction of the current flow across the heater membrane (wide electrodes, supporting beam of 10μm width and 150 μm length)

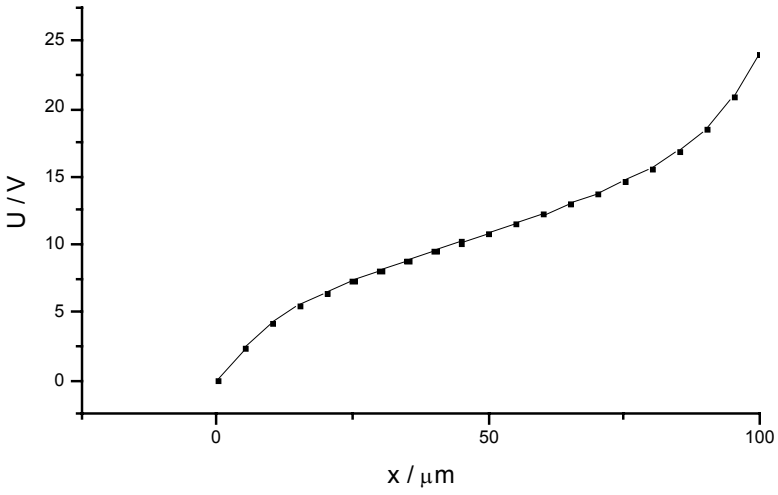

Fig. 4.6: Voltage drop in the direction of the current flow across the heater membrane (small electrodes, supporting beam of 10μm width and 150 μm length)

The wider electrodes naturally constitute the more favourable design. Ideally, the electrodes would have the complete width of the heater. As previously mentioned, geometrical limitations prevent the use of electrodes covering the complete heater width. Hence, heater contact electrodes of 60 μm width (3/4 of the heater width) were chosen to guarantee uniform current distribution and a

constant potential gradient leading to a constant heater power density across the heater area. This constant heater power density can be used in later simulations of the actual device in order to predict and optimise its behaviour.

4.2 Designing the interdigital contact electrodes and the resistive temperature sensor

As described earlier (chapter 3, chapter 2) the flexibility of the device for the application with a wide variety of metal oxides and operation modes requires a variable design of the electrodes contacting the metal oxide and a resistive temperature sensor to allow accurate temperature control of the heater. For simplicity in fabrication processing both the temperature sensor and the electrodes are integrated in one metallisation layer.

Interdigital electrodes (IDE) allow easy adjustment of the measured resistance ranges of the metal oxide layers covering them by changing the number of electrode finger pairs and the distance between them. Easier estimation of the expected sensor thin film resistance and the square shape of the heater in combination with technological considerations lead to the choice of a square IDE geometry. A large number of metal oxides have a very high resistivity requiring the reduction in measured resistance of the layer by turning it into smaller “parallel” resistors. With a heater area of 80 μm by 80 μm in size, the electrodes will have to be placed within this area to prevent large temperature gradients across the contacted metal oxides for the reasons stated earlier on (chapter 2). Technological limitations (chapter 4.1.1) allow a minimum structure width of 2.5 μm. A maximum of eight electrode finger pairs can thus be integrated on the heater area.

In order to cover the largest possible variety in metal oxide layer resistance, two variations of the IDE were chosen: one with only a single pair of electrodes for

low resistance layers and one with four pairs of electrodes for high resistance layers (Fig. 4.7). All electrodes feature a structure width of 5 µm.

Since only one metallisation layer is used for heater contacts, temperature sensor and metal oxide electrodes, the resistor for the temperature measurements has to be placed next to the IDE. It has to be placed as close to the heater and IDE as possible in order to measure the temperature at the metal oxide thin film precisely. The minimum distance to the IDE of 5 µm is determined by technological limitations. The influence of the distance of the resistor to the actual IDE and center of the heater on the measured temperature will be determined later in this chapter, once the hotplate geometry is fixed. The four electrode pairs use 75 µm of the available 80 µm heater width. The temperature sensor can therefore only be placed at the edge of the hotplate parallel to the heater (Fig. 4.7). Its resistance is determined by the sheet resistance of the metallisation layer.

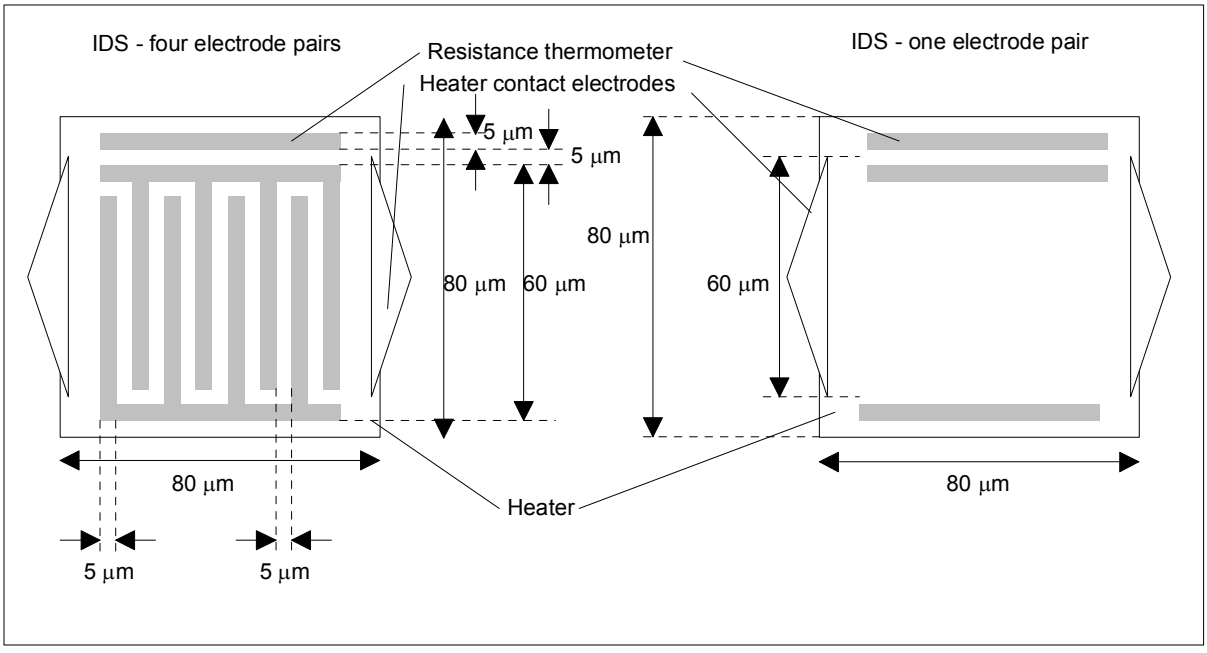

Fig. 4.7: IDE structure for four pair and single pair electrodes.

The design of the IDE and temperature sensor is governed by the small size of the hotplate in combination with technological limitations. Four electrical contacts are necessary for IDE and temperature sensor.

4.3 Connecting leads, hotplate shape and geometry

The sandwich structure consisting of heater, IDE, temperature sensor and insulating layers (chapter 3) rests on a thin free standing membrane supported by micro beams. The structure has to carry the active parts of the device, ensure a uniform heat distribution across the heater and thermally insulate the heater from the substrate. Six connecting leads are required to contact the heater, IDE and temperature sensor. All leads are placed in one metallisation layer. Therefore, six supporting beams are used, each carrying one lead (Fig. 4.8).

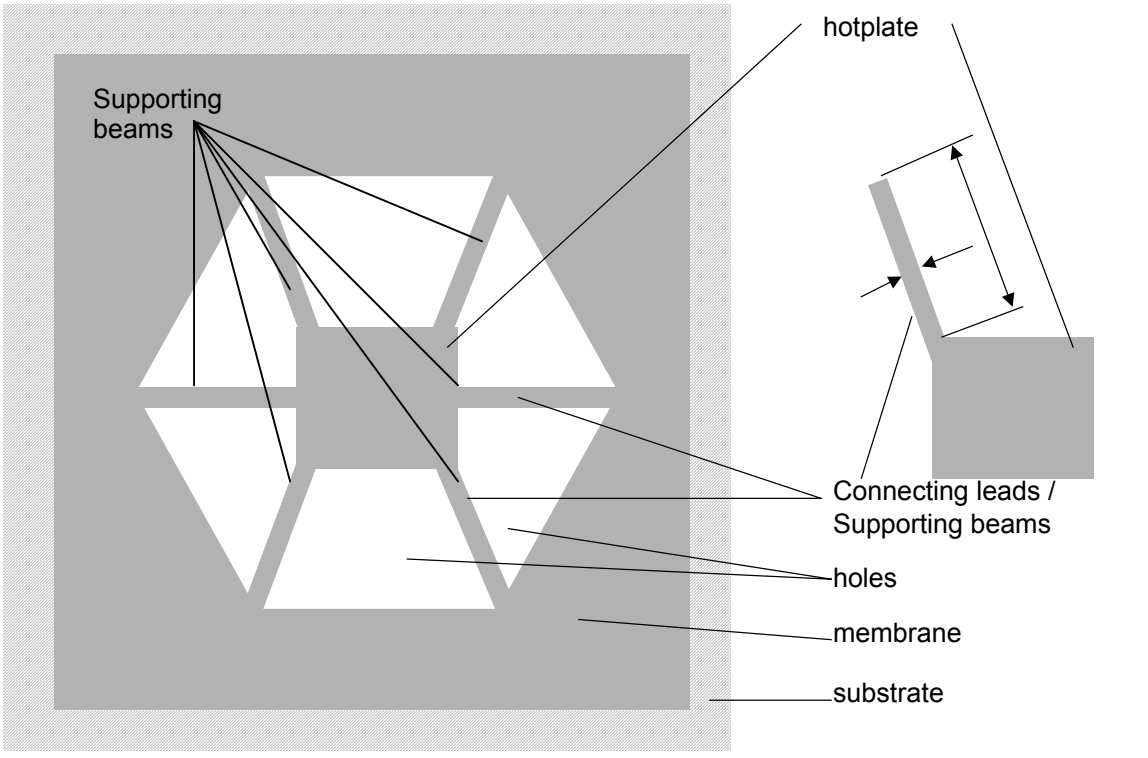

Fig. 4.8: Hotplate shape and geometry (hexagonal design) and dimensions of supporting beams as parameters for hotplate optimisation.

This approach gives greater freedom in thermal design by placing the heat sinks (i.e. the beams) around the hotplate, such that the temperature profile across the heater and the sensing metal oxide can be influenced. Since the space (width) required for the leads remains unchanged irrespective of the beam design, the overall thermal power losses through the beams are not affected. Furthermore, the electrical insulation or disturbances of the signals through electrical crosstalk is minimized, by placing each lead on a separate beam. The hotplate geometry could either be of circular or square shape considering the small dimensions required.

Finite element simulations were performed in order to compare the temperature distribution of a circular hotplate relative to a square hotplate, assuming six beams to be holding the hotplate. The geometrical constraints are –as before- a heater of 80 μm x 80 μm lateral extension, a hotplate diameter or side length of 100 μm and a uniform temperature dependant thermal conductivity of the supporting SiC membrane and beams. In order to achieve a satisfying uniformity across the active area of the heater and IDE, the square membrane was compared to a circular membrane (Fig. 4.9, Fig. 4.10). Both membranes have supporting beams distributed at about 60 ° angle to each other. The square membrane proved to have a more homogeneous distribution of isotherms at over 720 °C (60 mW heater power) giving a “square”-shaped profile, than the round membrane at only 420 °C (40 mW heater power), even though one might expect a higher temperature gradient for the square membrane due to the higher operating temperature. This simplifies the shape of the IDE positioned on top of the heater to a simple square. The circular membrane, which initially must seem as the naturally more homogeneous shape, does not yield the more homogeneous temperature distribution. The micro bridges act as heat sinks causing a narrow strip of high temperature in the centre of the membrane.

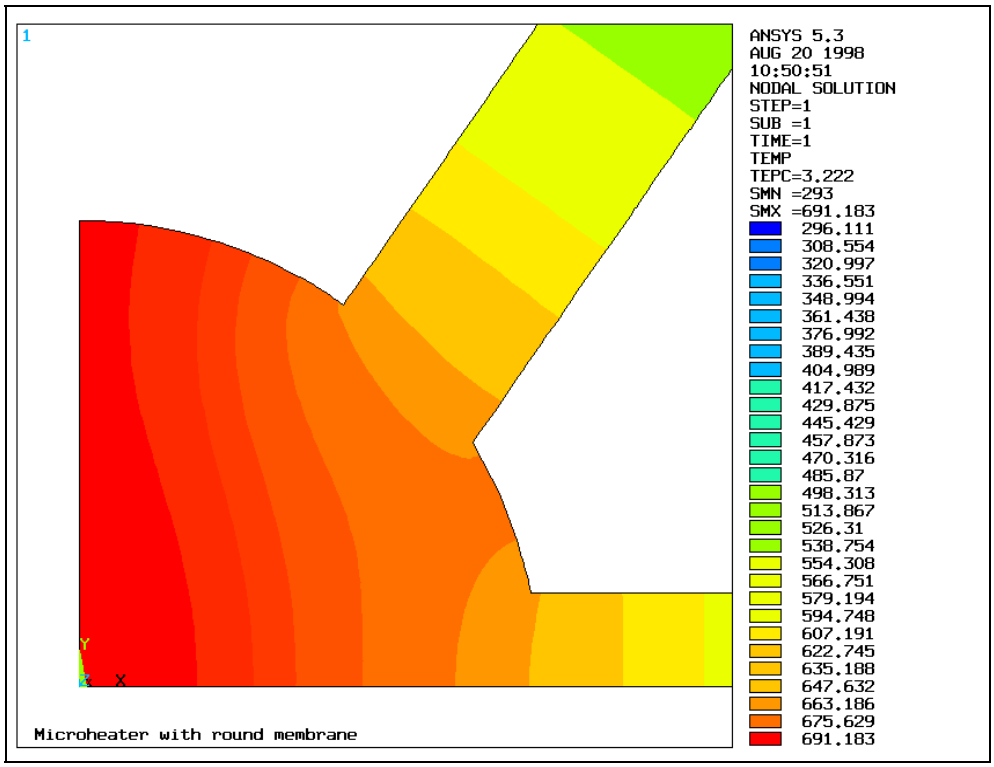

Fig. 4.9: Temperature distribution on a circular heater membrane at 40 mW heater power and operating temperatures around 690 K (420 °C). A narrow strip of high temperature remains in the centre.

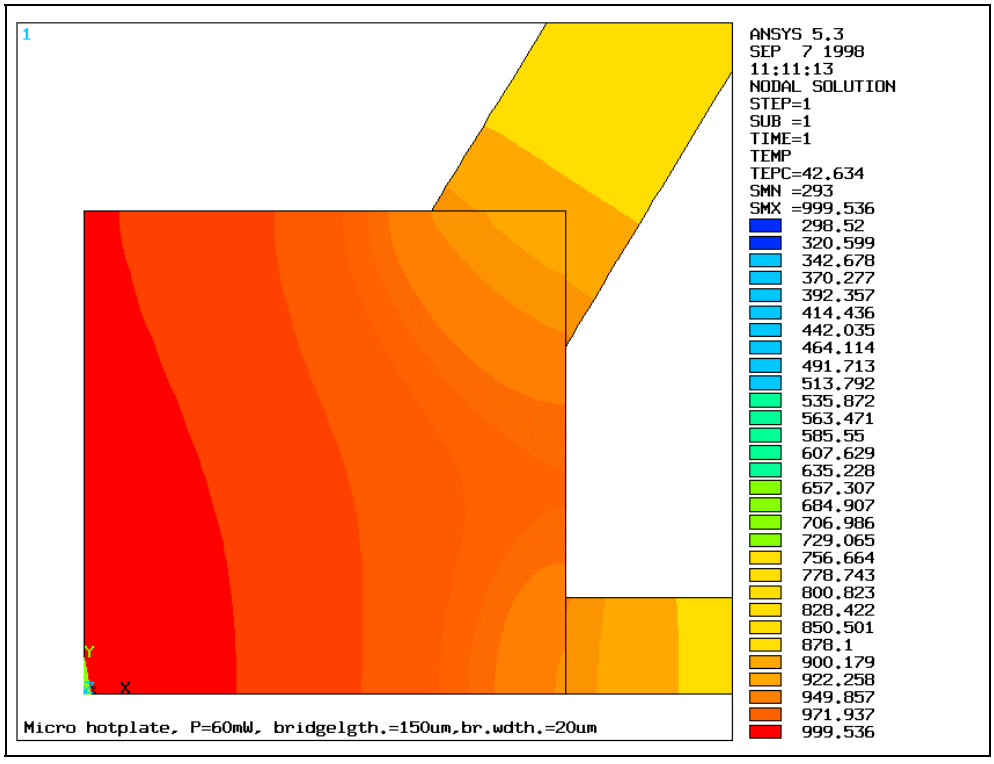

Fig. 4.10: Temperature distribution on a square heater membrane at 60 mW heater power and operating temperatures around 995 K (720 °C)

The main reason for the better temperature distribution on the surface of the square membrane lies in the fact that, with the square membrane the micro bridges at the corners - and subsequently the heat sinks - are placed further away from the centre of the membrane compared to the one with circular shape. The closer position of the heat sinks to the centre „compresses“ and deforms the isotherms, causing a higher temperature gradient and a smaller strip of high temperature.

Similarly to the comparison of the two heater contact widths in the previous chapter, the purpose of the FEA is only to determine the relative difference between a circular and a square hotplate shape, prior to a detailed FEA analysis presented later in this work.

4.4 Hotplate – array structures

With the general design of the sandwich structure, hotplate, heater, IDE, temperature sensor and number of beams given, the outer shape of the hotplate structure has to be considered when designing hotplate arrays.

All array structures presented to date use square structures with four beams reaching to the suspended hotplate from each corner of the square. The new hotplate features six beams of identical width and length carrying the six leads to heater, the IDE and the temperature sensor. As previously mentioned, an advantage of this approach is that the heat sinks (beams) can be evenly distributed around the heater for a uniform temperature distribution (i.e. at roughly 60 ° angle to each other). The six identical beams clearly suggest a

hexagonal structure shape. Principally, however, a free shape may be chosen. The constraints given are a minimal amount of used surface area and high mechanical strength, while allowing close packing of the micro hotplates in one membrane.

The thermal behaviour of the hotplate is independent of the structure shape, assuming the thermal resistance of the beams to be high enough to prevent thermal crosstalk between the hotplates.

4.5 Summary

The design for the micro hotplate evolving from the above considerations is therefore a sandwich structure consisting of a silicon carbide membrane, a thermal and electrical insulation layer (SiO_2), a rectangular heater made from a HfB_2 thin film (low voltage version) or by doping the silicon carbide (high voltage version), a further insulation layer and the metallisation layer building the electrical contacts and the IDE. The actual hotplate measures 100 μm x 100 μm with heater dimensions of 80 μm x 80 μm. Six identical SiC beams support the free standing hotplate within the SiC membrane building a hexagonally shaped structure (Fig. 4.11). Fig. 4.12 gives a three dimensional view of the model for clarification.

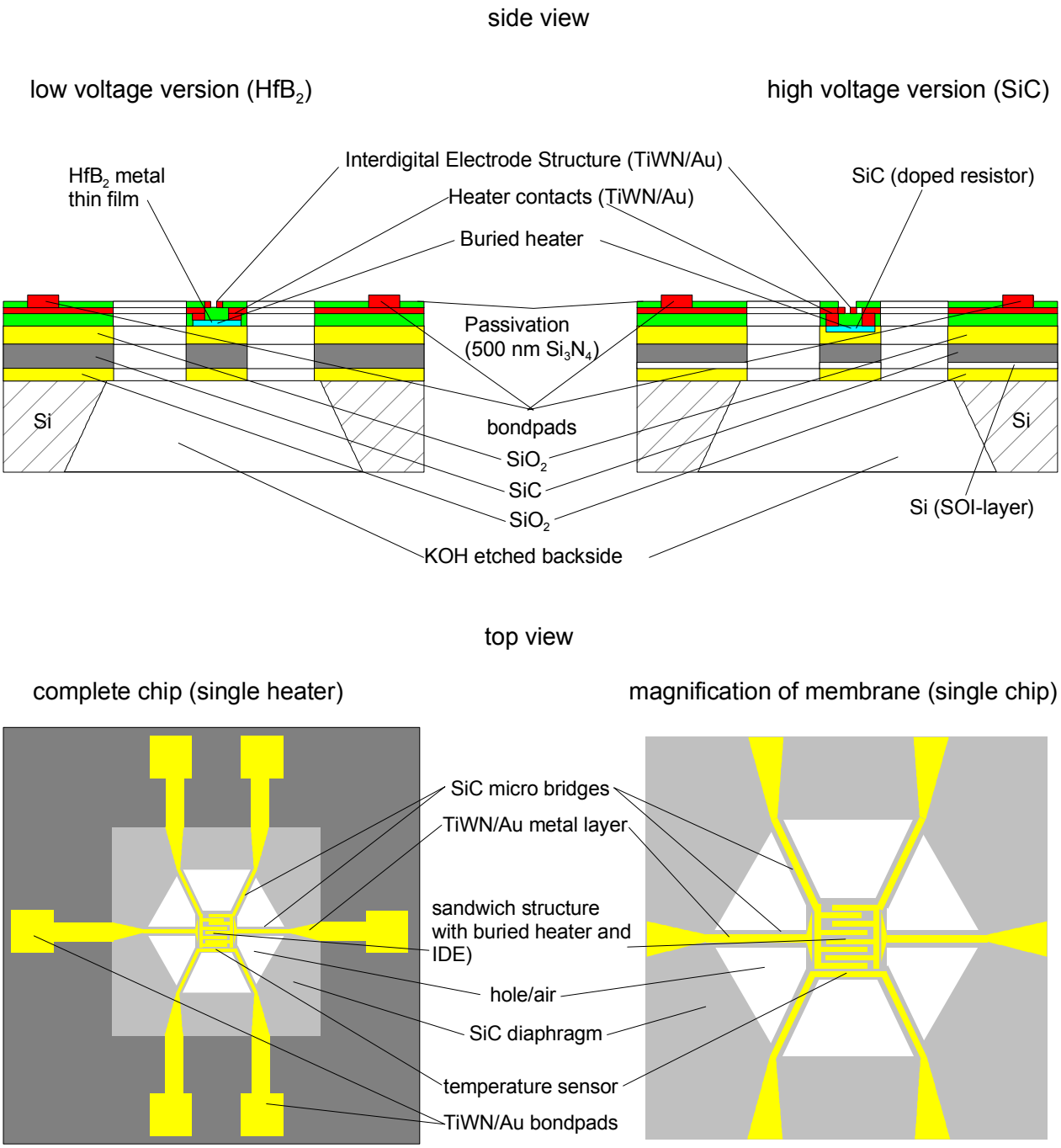

Fig. 4.11: Hexagonal shape of the micro heater design (schematic)

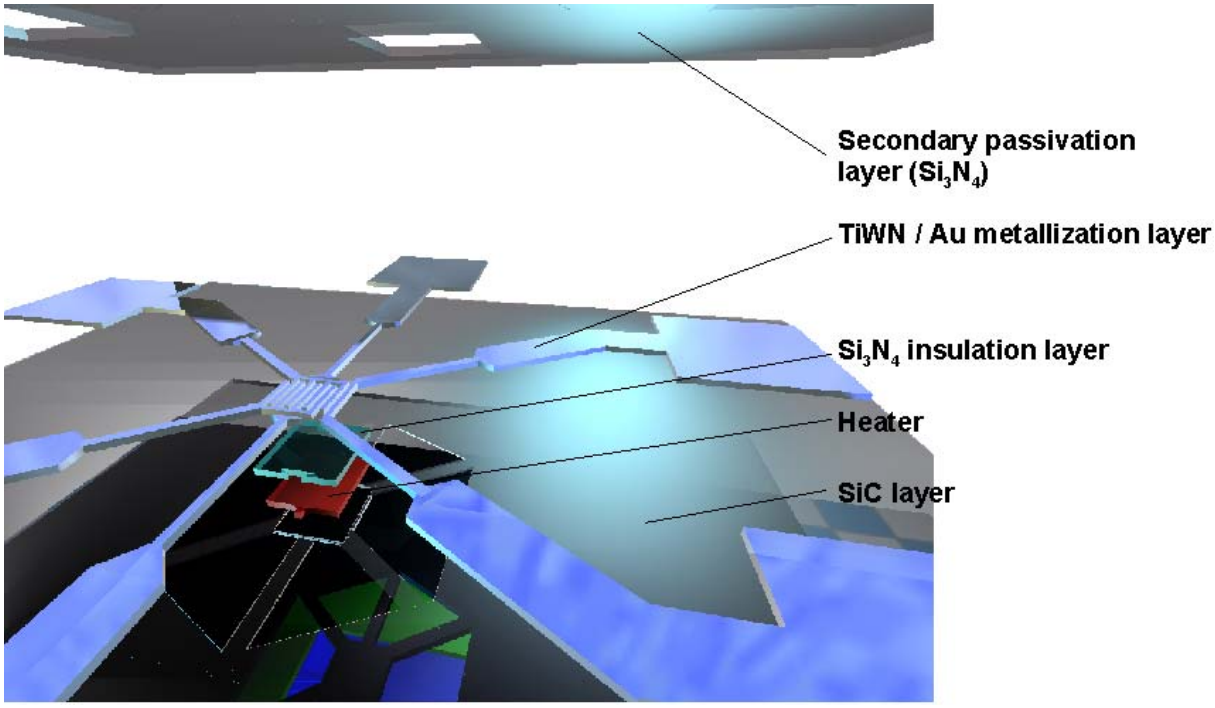

Fig. 4.12: Close view of schematic heater design (expanded view)

The gas sensor device consists of three modular building blocks: the mechanical structure, the heater and the sensitive element (i.e. the gas sensitive layer). By exchanging only single process steps in the fabrication process, the device can be adapted to its operating environment, thereby reducing the development expenses.

5. Modelling and finite element analysis

Chapter 5 describes and optimises the model of the micro hotplate device with respect to power consumption, mechanical stability and thermal response times. Thus, first of all, a simple analytical model of the hotplate is generated for three purposes: to achieve a rough estimate of the device performance and feasibility prior to simulation, to have a first check on the validity of the subsequent simulations and to set the boundary conditions required in the simulation. Physical phenomena which only affect the specified device properties in a negligible (i.e. 2^{nd} or 3^{rd} order) way can be omitted in the simulation allowing simpler and thus more reliable and faster modelling. Secondly, FEA simulations are performed to optimise the device properties and to yield an estimation of the expected device characteristics.

Thermo-mechanical, static and transient thermal as well as electrical simulations were performed to optimise the sensor design with respect to low power losses, uniform temperature distribution, uniform current distribution in the heater, small response times and prevention of stress singularities leading to thermally induced mechanical failure of the structure.
A commercially available program package, “ANSYS Release 5.3” was used. A brief description of the simulation procedure is given here, prior to explaining and analysing the FEA results.
The general procedure when modelling a device using FEA always covers three main steps [5.1]: the generation of the model including the application of loads, the solving of the linear system of differential equations and the post-processing (compilation and read-out of data). The model generation includes the construction of a two- or three-dimensional structure using the Ansys programming language, followed by the generation of a “mesh”, where the structure is partitioned into small elements. These have “nodes” which

communicate with the other elements' nodes on the bases of the material properties given to the respective elements. For reasons of symmetry the modelling of a quarter of the complete heater membrane is sufficient thereby reducing the number of elements and calculation time needed.
The boundary conditions that have to be applied to produce a stable solvable model depend on the number of degrees of freedom in the system. The solution is done automatically using the Ansys built-in solver and written into results-files. Post-processing includes the extraction of data from the results-files to yield the information expected, like temperature over position (x, y, z). In this paragraph we will only discuss the main results extracted from the FEA. A complete list of all the simulations undertaken can be derived from appendix C.

5.1 Modelling the sensor

In order to meet the specification, it is necessary to optimise the sensor geometry and the general sensor design. A simplified analytical model is created to estimate the relevant physical effects prior to creating a Finite-Element-Analysis model. The complexity of the device geometry prohibits the exact analytical solution of the differential equations describing the thermal, mechanical and electrical behaviour of the total system: "micro-hotplate". Numerical analysis using FEA simulations allows a detailed investigation of the estimated device properties before technological realisation.
The analytical model only describes an estimate of the static and transient thermal properties and lays a fundament for the boundary conditions and the complexity of the thermal FEA-model. The resulting mechanical properties (induced stress) are evaluated only by FEA, based on the thermal FEA solution.
The electrical properties of the heater are evaluated in a separate FEA model.

5.1.1 Analytical modelling of the thermal characteristics

Thermally, the heater and its surroundings can be described as a network of thermal resistors and a heat current density **J** or temperature **T** source (Fig. 5.1). The thermal resistance can be defined as [5.2]:

$$R_{th} = \frac{dT}{J\,dA} = \frac{dT}{dP} \qquad [R_{th}] = 1\ K / W \qquad (5.1)$$

The effects to be considered are conduction, convection and radiation. Stationary and transient case will be examined separately.

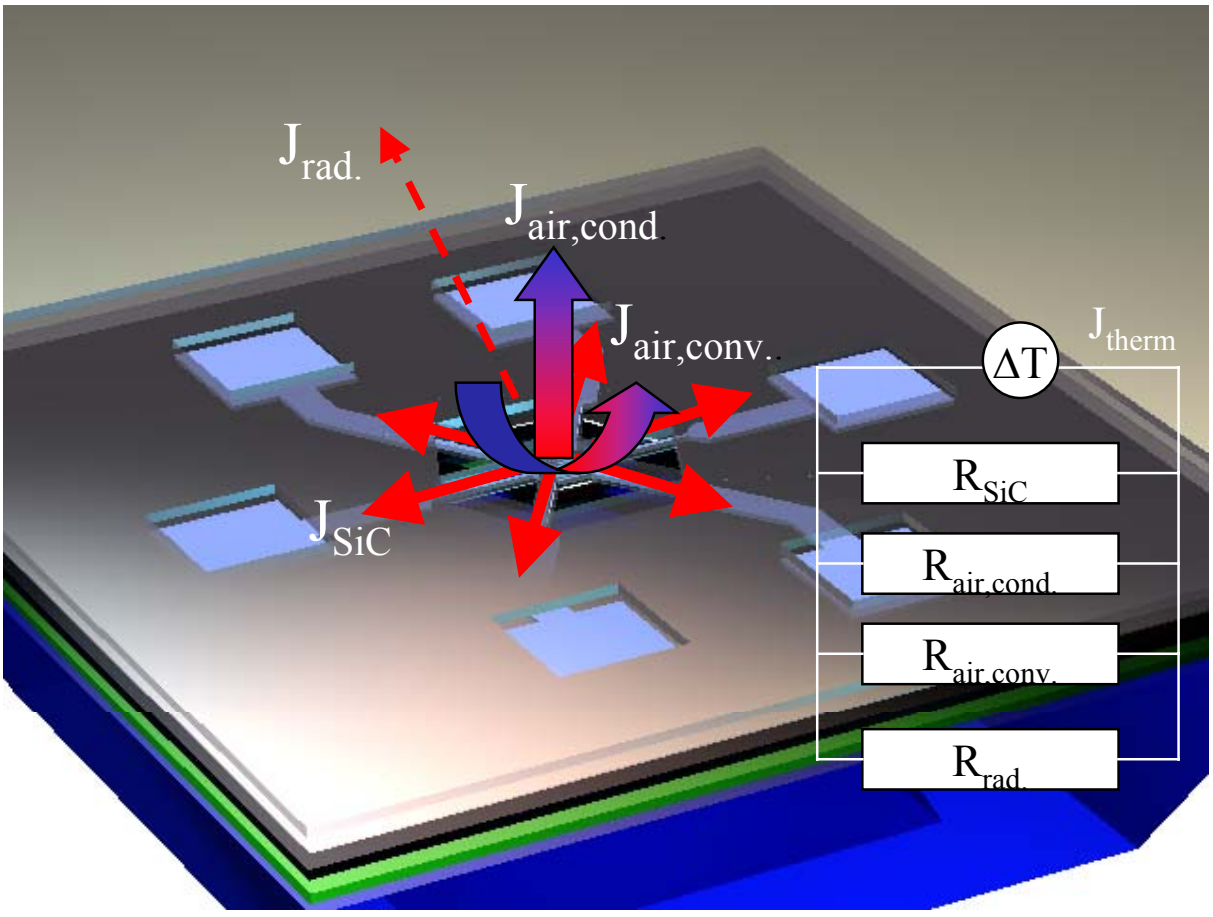

Fig.5.1: Heat flow from the heater to the surroundings through conduction, convection and radiation and equivalent thermal resistor network

Conduction

Conduction of heat occurs across the supporting micro bridges and through the surrounding ambient air. The governing equation for this effect is the general equation of heat conduction:

$$\dot{T} = \frac{\lambda}{\rho c} \operatorname{div} \operatorname{grad} T = \frac{\lambda}{\rho c} \Delta T \qquad (5.2)$$

When a heat source (e.g. an electrical heater or a chemical reaction) is included in the problem one has to add a heat source density η (heat / volume) [5.4]:

$$\dot{T} = \frac{\lambda}{\rho c} - \left(\operatorname{div}(j) + \eta\right) = \frac{\lambda}{\rho c} \Delta T + \frac{1}{\rho c} \eta \qquad (5.3)$$

which, in the stationary case, simplifies to the expression:

$$\Delta T = -\frac{\eta}{\lambda}. \qquad (T, \eta = f(\mathbf{r}, t)) \qquad (5.4)$$

Hence the temperature potential follows the same equations as an electrostatic potential. This is very useful when looking at thermal models in a more abstract way without detailed calculation of the thermal behaviour. E.g. the temperature distribution in a thermal insulator around a small heat source is identical to the electric potential of a point charge and the temperature distribution around a straight heating tube ($T \propto \ln r$) is identical to the electric potential of a charged wire (grad $E \propto \ln r$).

These differential equations (5.2-5.4) govern the effects of thermal conduction of the device. Since, due to the geometrical complexity, a complete analytical solution is not possible, numerical methods (Finite Element Analysis) are used, as will be described later (chapter 5.).

Of chief interest is the device power consumption, i.e. the power necessary to heat the micro hotplate to a Temperature T. The heat losses by conduction are:

$$P = \int j dA = -\int \lambda \, \mathrm{grad} T \, dA \qquad (5.5)$$

Conduction losses appear through the supporting material (SiC micro bridges) as well as the surrounding air. The micro bridges have a constant cross-sectional area of A = b·h = 10 μm^2, (20 μm^2, 40μm^2) and can be described as a one-dimensional problem [5.3]:

$$P = -\lambda A \frac{dT}{dx} \qquad (5.6)$$

Since there are six micro bridges with Au-leads on them, the total conduction through solid material equates to:

$$P_{cond,s} = 6(\lambda_{SiC} A_{bridge} \frac{\Delta T}{\Delta x} + \lambda_{Au} A_{leads} \frac{\Delta T}{\Delta x}) \qquad (5.7)$$

We can describe the air's thermal resistance using (5.6) and a spherical co-ordinate system (Fig. 5.2). The heater is thereby for simplicity seen as having a circular shape of radius r = 50 μm.

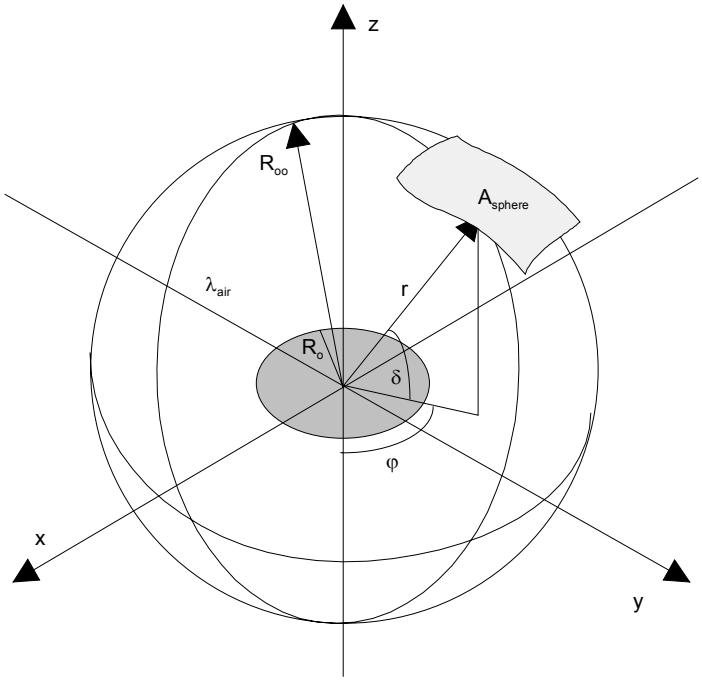

Fig. 5.2: Simplified model of micro heater as spherical heat source in a spherical co-ordinate system

$$P = \int_{R_0 r}^{R_\infty} \lambda A(r) \frac{dT}{dr} \tag{5.8}$$

$$\Leftrightarrow P = \int_{R_0 r}^{R_\infty} \lambda 4\pi r^2 \frac{dT}{dr} \tag{5.9}$$

$$\Leftrightarrow \int_{R_0}^{R_\infty} \frac{P}{4\pi\lambda} \frac{1}{r^2} dr = \int_{T_{R_0}}^{T_{R_\infty}} dT \tag{5.10}$$

$$\Leftrightarrow P_{R_0 R_\infty} = 4\pi\lambda R_0 \left(T_{R_o} - T_{R_\infty}\right) \tag{5.11}$$

Since the device will be operated as a gas sensor, variations of the thermal conductivity with gas concentration might have to be considered. Taking into

account the low concentration of the measured gases, it is justifiable to assume this effect to be negligible, since the thermal conductivity changes very little with the adding of other gases in low concentrations [5.3]. Water vapor has a different thermal conductivity than air. It is slightly lower (0,017 W/mK compared to 0,026 W/mK for air) at room temperature, equal at 200 °C (0,039 W/mK) and higher at 300 °C (0,075 W/mK compared to 0,045 W/mK for air) [3.4]. Hence, the air humidity can have a significant influence on the power losses through the air. Furthermore the vapor pressure will determine the amount of water vapor present in the air. The temperature dependence of these properties prohibits a simple analytical approximation of the influence of the air humidity on the thermal conductivity and subsequent power losses. Metal oxide gas layers do react strongly (sensitivity and drift) to humidity, thus frequently requiring the operation in a dry gas environment. Hence, as a simple approximation it is justifiable to use neglect the influence of air humidity in this model.

Inserting ΔT = 500K, r= 50 mm, l=2,6 10^{-2} W/mK, we obtain P ≈ 8,1 mW power losses through air thermal conduction.

Whilst in the stationary case we have simple temperature diffusion, the transient case is governed by the more complex Fourier equation [5.4]:

$$\frac{\partial T(x,t)}{\partial t} = \kappa \frac{\partial^2 T(x,t)}{\partial x^2} \tag{5.12}$$

$$\kappa = \frac{\lambda}{\rho \mathrm{c}} \tag{5.13}$$

and will not be looked at in further detail here. As a simple first order approximation, however one can estimate the energy required for heating the active part of the device (hotplate and IDE) using a mean thermal capacitance c as being:

$$E = \rho V c \Delta T \tag{5.14}$$

Subsequently the power required for heating the device to a temperature T in time τ is:

$$P = \frac{E}{\tau} = \frac{\rho V c \left(T - T_0\right)}{\tau}. \qquad (5.15)$$

Using typical values as ρ_{SiC}= 3.2 10^3 kg/m^3, c_{SiC}=1.2 10^3 Ws/kg K and ΔT=500K, τ=1ms V=$10^{-14}$$m^3$ gives P=19.2 mW. That is a value very close to the simulated and actual results as we will see later (chapter 7.). The 1 ms was chosen to account for pulsed operation. In this case heater time constants of about 1 ms are desirable, furthermore, this gives an estimate for the maximum power required: longer time constants will mean less power consumption.

Convection

Convection is the transportation of heat through macroscopic motion of particles in a "fluid". The static and the transient case are discussed separately. While the theoretical basis lays in the Fourier and Navier-Stokes equations, which explain the physical effects of fluids in motion, the thermal design engineer can approach this problem using the phenomenological convective heat transfer coefficient h [W/m^{-2} K^{-1}] [5.5][1]:

$$P = h A dT \qquad (5.16)$$

$$h=f(\text{shape}, L_c, T_w, T_a, g, \Delta\rho, \rho, \mu, \lambda, c_p) \qquad (5.17)$$

This coefficient can be determined experimentally or theoretically using the Nusselt number Nu which gives a correlation between the convective heat

[1] The choice of the heuristic h-coefficient is principally justifiable irrespective of the microscopic dimensions considered here; h is derived by looking at the buoyancy forces on an infinitesimal volume of matter in a continuum, balanced by frictional and shear forces. Geometrical dimensions thus do have an impact on the resulting h-value and thus the amount of heat transferred due to convection. Also at small dimensions, the shear forces and vorticity in boundary layers can have an impact on the resulting h, which in the case of the low viscosity of air will be negligible.

transfer coefficient h and the molecular thermal conductance λ/L_c (L_c – characteristic length of the convection cells).

$$h = Nu\ \lambda / L_c \qquad (5.18)$$

For a horizontal plate problem like the micro hotplate, Nu is given by [5.3]:

$$Nu = [(Nu_l)^{10} + (Nu_t)^{10}]^{1/10} \qquad (5.19)$$

with

$$Nu_l = \frac{1.4}{\ln\left(1 + 1.677 / \left(C_l Ra^{1/4}\right)\right)} \qquad (5.20)$$

$$Nu_t = 0.14\ Ra^{1/3} \qquad (5.21)$$

and

$$C_l = \frac{0.671}{\left[1 + \left(\frac{0.492}{Pr}\right)^{9/16}\right]^{4/9}} \qquad (5.22)$$

Pr is the Prandtl number, a fluid property defined by

$$Pr = \nu / \kappa \quad \text{(kinematic viscosity / thermal diffusivity).} \qquad (5.23)$$

For air $\nu = 1.43\ 10^{-5}$ m^2/s and $\kappa = 2.24\ 10^{-5}$ m^2/s giving Pr = 0.71 and subsequently $C_l = 0.515$.

Ra is the Rayleigh number, a measure for the convective instability of the system given by [5.4]

$$Ra = \frac{\alpha \Delta T g l^3}{\nu \kappa}\ . \qquad (5.24)$$

For air, assuming an ideal gas:

$V \sim T$ (p=const.) (5.25)

Thus the cubic thermal expansion coefficient is:

$\alpha_{air} = 1/273\ K^{-1}$ (5.26)

Inserting typical values (α_{air} = 1/298 K^{-1}, ΔT=500 K, g=9.81 ms^{-2}, l=10^{-4} m^2, ν=1.43 10^{-5} m^2s^{-1}, κ=2.24 10^{-5} m^2s^{-1}) we obtain Ra = 5.12 10^{-2} and Nu = 0.68 giving us h = 543.9 $Wm^{-2}K^{-1}$ in the static case.

At 500 °C heater operating temperature we would – as maximum value - thus expect thermal losses due to convection of about:

$P = h\ A\ dT = 543{,}9\ Wm^{-2}K^{-1}\ 10^{-8}\ m^2\ 500\ K \approx 2.7\ mW.$ (5.27)

The losses are comparably small, but must not be neglected, since depending on the heater version used, they can amount to about 6% of the total losses.

For the discussion of the transient case a new model, explaining the devices characteristics in a simple way can be made. The effective size of the heat source and the space above it are the geometrical factors influencing convective effects. This model describes the phenomenon as a diffusion problem and shows that with increasing frequency the effective diffusion length l, determining whether convection will occur at all, will decrease.

When looking at heated surfaces in a continuum, it is possible to split the flow into two regions: a boundary layer, in which the effects of viscosity and heat transfer are important and an outer region (freestream) at which the flow is effectively inviscid and at uniform temperature (Fig. 5.3) [5.5].

[2] In this model, the effective length or size of the convection cells is determined by the lateral size of the hotplate, assuming infite free space above it.

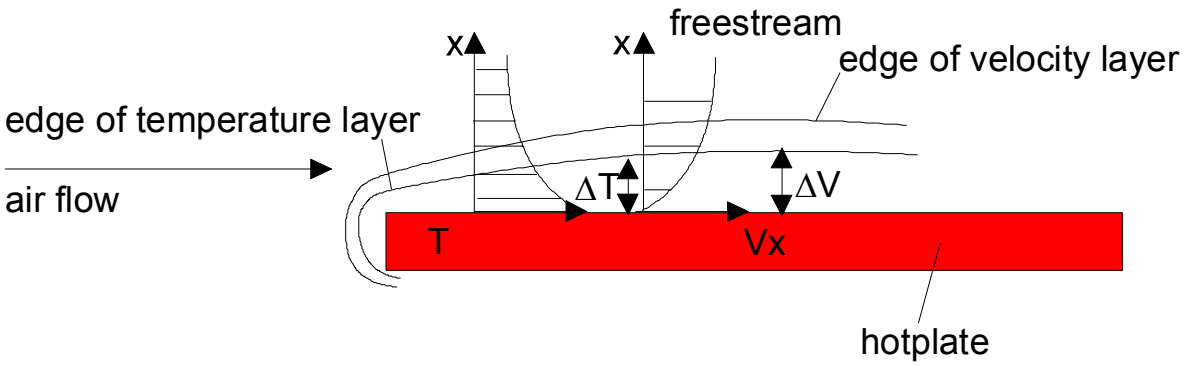

Fig. 5.3: temperature and velocity (Vx) boundary layer on a heated surface with external air flow.

Assuming no external air flow, we expect a general convective behaviour as pictured in Fig. 5.4. The heated surface causes an upwards air stream possibly leading to convection rolls due to the cooling of the air at some distance to the hot surface. The hot air generated at the bottom side of the hotplate escapes at the sides of the hotplate and is pulled towards the upwards air stream. Considering the horizontal (Vx) and vertical (Vy) air velocities due to free convection, we receive a harmonic motion, depending on Rayleigh number Ra.

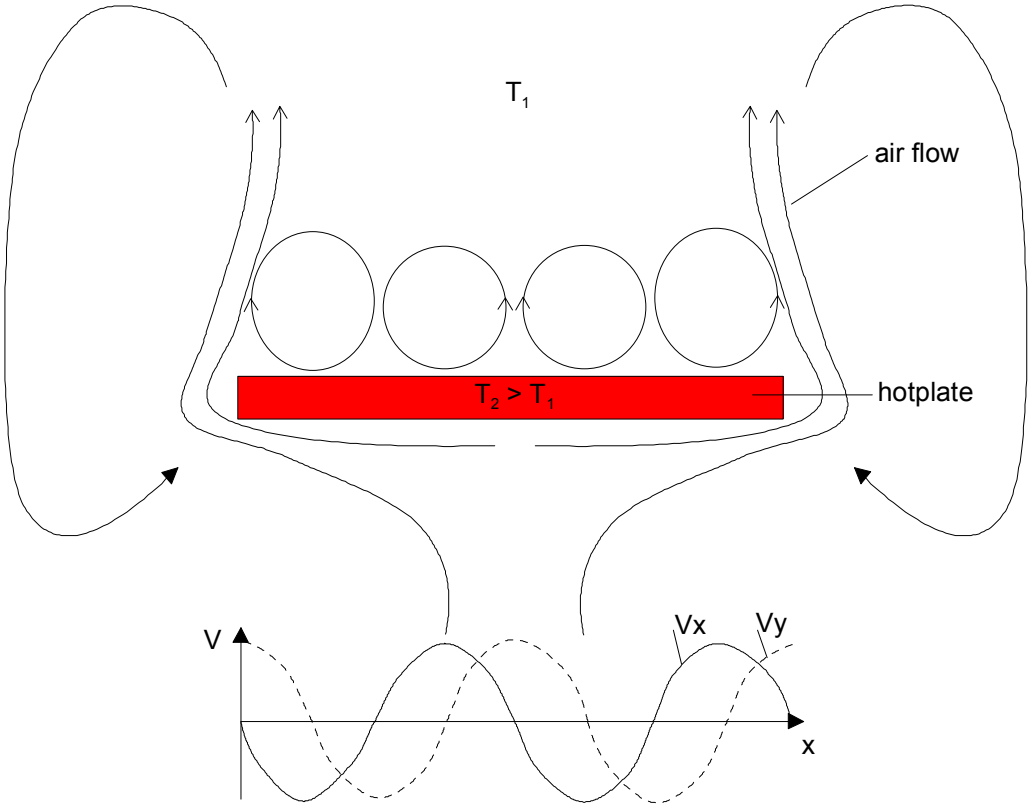

Fig. 5.4: Possible schematic air flow and air flow velocity profile due to a temperature gradient from a heated surface to the surrounding air.

In the transient case convection does not play a significant role as can be seen from the following simple approach. The transient case is important when the heater is pulsed in a millisecond time frame with a square signal. Approximating the square wave by its first order harmonic is justifiable since we are approaching the problem from the lower frequency end. We will see that convection plays a decreasing role with increasing heater frequency.

As a first approximation we can reduce the problem to a one-dimensional linear harmonic problem of a heated horizontal plate with sinusodial excitation (Fig.5.5).

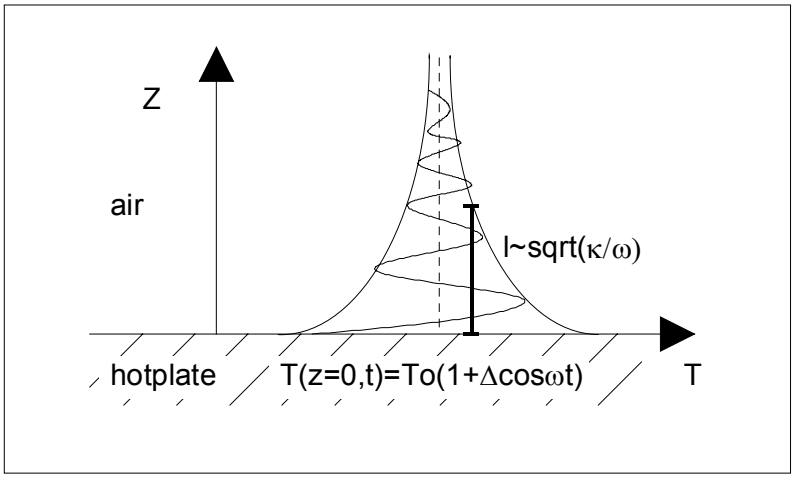

Fig. 5.5: Temperature diffusion into the continuum (air) above the hotplate under sinusodial excitation (heating). T(z,t) follows a harmonic behaviour enclosed by an exponential decay. The thermal skin effect yields the penetration depth l $\propto$ sqrt(κ/ω) at a drop of the temperature amplitude to 1/e. (Δ - Temperature-amplitude at the surface of the hotplate, ω - excitation frequency, κ - thermal diffusivity).

Origin of any convective motion is a temperature diffusion process carrying the heat by conduction through the continuum as described by the general heat conduction equation. If the temperature and temperature gradient reaches a certain level, convection, i.e. the transport of particles carrying a certain thermal energy, will start.

Using the aforementioned parallelity of the differential equations governing electrical field and thermal problems the Skin-effect one can define an effective length of penetration of temperature into the continuum[3] by

$$l = \sqrt{\frac{\kappa}{\omega}} \qquad (5.28)$$

[3] Starting from the fourier equation $\frac{\delta T(r,t)}{\delta t} = \kappa \Delta T(r,t)$, we obtain a solution of the form T_{nromed}=[1-erf(u/2)], with $u = \sqrt{\frac{\kappa}{\omega}}$, $\mathrm{erf}(z) = \frac{2}{\sqrt{\pi}} \int_0^z e^{-\varsigma^2} d\varsigma$; u (or "l" as denoted above in (5.28)) is thus the diffusion depth of the temperature field as a function of frequency and thermal diffusivity.

A simple model can be applied by assuming the convection to take place between two plates of different temperature with the first plate being the hotplate, the second one being an imaginary plate placed at the position of the effective penetration length. If convection would take place, Bénard-cells would build up between the two plates (Fig. 5.6).

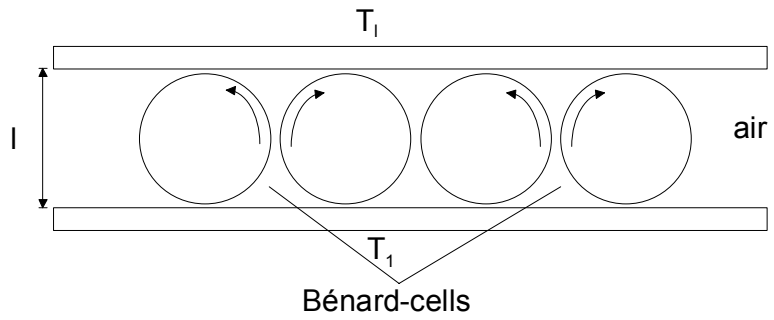

Fig. 5.6: Convective cells (Bénard-cells) between two horizontal plates at different temperatures (T_l, T_1). The medium between the two plates follows a barrel roll type motion.

The criterion for convective motion to take place is given by comparing the Stoke's friction with the buoyancy forces acting upon a particle in the continuum [5.5]. This comparison yields the Rayleigh number Ra. From experimental data one has determined that Ra must remain smaller than 1708 in order to prevent convective instability. At very high values of Ra, the Bénard rolls can develop into three-dimensional hexagonal convective cells. Ra can be described in terms of the characteristic length l, which in this case is the distance between the horizontal heated plates, ergo the effective penetration depth l of the temperature field, which leads to:

$$Ra = \frac{\alpha g l^3}{\kappa \nu} \Delta T \,, \tag{5.29}$$

using equation (5.28):

$$\Leftrightarrow \mathrm{Ra} = \frac{\alpha \mathrm{g} \left(\frac{\kappa}{\omega} \right)^{3/2}}{\kappa \nu} \Delta \mathrm{T} \tag{5.30}$$

Using $(\kappa / \nu) \approx 1$ for air:

$$\mathrm{Ra} = \frac{\alpha g}{\nu^{1/2}} \left(\frac{\kappa}{\nu} \right)^{1/2} \frac{1}{\nu^{1/2}} \frac{\Delta T}{\omega^{3/2}} \neq f(\kappa) \qquad (5.31)$$

Surprisingly, as a first approximation, in air the criterion for instability is "independent" of the thermal conductivity (or diffusivity) κ, since $\kappa_{air}/\nu_{air} \approx 1$. Using equation (5.30) and inserting values α = 1/273 K, g = 9.81 m/s^2, κ_{air} =2.24·10 $^{-5}$ m/s^2, ν_{air} = 1.43·10^{-5} m/s^2, ΔT=500 K we obtain values for Ra far below the critical Ra number Ra_c = 1708 (Table 5.1). At very high Ra numbers, chaos (Ra≈10^5-10^6) and later soft (Ra≈10^7) and hard turbulence can be expected. Solving equation (5.30) for Ra=1708 yields the critical frequency for convective instability (2.7 s) Hence, no convection occurs in the transient case of a pulsed operation with heating periods smaller 1200 ms.

Table 5.1: Rayleigh numbers and effective temperature penetration depths as result of sinusodial heating of the micro hotplate with period τ of 2 ms, 20 ms, 200 ms and 2735 ms

τ / ms	**ω / s^{-1}**	**l / m**	**Ra**
2	3141	8.44 10^{-5}	3.37 10^{-2}
20	314.1	2.67 10^{-4}	1.067
200	31.41	8.44 10^{-4}	33.72
2735	2.297	6.73 10^{-4}	1708

This justifies neglecting free convection when examining the transient heater behaviour. Hence, the simulation model will have to include convection in the static operation mode, only.

There obviously seems a discrepancy since the static and the dynamic case Ra values do not converge. This can be explained as follows: in the static case mode, we have "open space" above a limited size (!) heater and the geometrical dimensions of the heater are assumed to be the determining factor for the convection cell size. The small dimensions of the hotplate lead to small

convective cells and a small Ra and therefore only the longitudinal part of Nu contributes to the total Nu-number. Due to the fact that Nu also depends on the dimensions, the effect on the convection coefficient is partially being cancelled. The static model leads to an actual estimate of the h-coefficient.

In the dynamic model, we define the convection cell size through the effective penetration depth of the temperature field above an infinitely extended heated surface (for simplicity reasons). I.e. we are forcing convection to occur through a given temperature difference (i.e. potential) leading to bigger effective convection cell sizes and bigger Ra numbers. In order for these to occur, the experimentally determined Ra number for this particular model of 1708 has to be exceeded, otherwise these convection cells will not occur. The resulting Ra number could however not be used directly to determine a resulting h-coefficient. Solving the transient case without the simplifications made, would prohibit a simple analytical solution of the problem and be beyond the scope of this analytical model. The dynamic model purely gives an estimate whether convection will occur or not.

Radiation

Power losses by radiation follow the Stefan-Boltzmann law [5.2]

$$P = \sigma \varepsilon A T^4 \qquad (5.32)$$

Using $A_{heater} = 2 \cdot 10^{-8}$ m^2, and $\sigma = 5.7 \cdot 10^{-8}$ Wm^{-2}K^{-4} (Stefan-Boltzmann constant) we obtain even for a material emissivity $\varepsilon = 1$ (black body), which in fact will be around $\varepsilon = 0.3$ and $T = 1000$ K, which would be beyond the heaters' specification, power losses of the order of 1 mW. This justifies neglecting radiation losses in all further examinations in this work.

5.1.2 Summary

Summarising, we obtain the following equation for the power losses occurring in the system:

$$P = P_{cond,bridge} + P_{cond,air} + P_{conv} \tag{5.33}$$

$$P = 6\,k_{brige} A \frac{\Delta T}{\Delta x} + 4\pi k r_{heater} \Delta T + h_{air} A \Delta T \tag{5.34}$$

For a first order approximation of the power consumption versus heater temperature we can evaluate equation (5.34) for k_{bridge}=150 $Wm^{-1}K^{-1}$, A_{bridge}=20 μm^2, ΔT=500 K, Δx=150 µm, k=0.02 $Wm^{-1}K^{-1}$, r=50µm and h_{air}=543,9 $Wm^{-2}K^{-1}$. At 500 K above room temperature we thus expect a total power consumption of the heater of 35 mW (about 8 mW of which are air conduction losses and about 2.7 mW are static convection losses). This is equivalent to a heater efficiency of 14 k/mW.

Three main results were obtained from modelling the device. First of all, the feasibility of such a device is shown. Secondly, a rough estimate of the device behaviour was gained. Finally, and almost more importantly, the effects to be considered in the analytical model could be clarified prior to simulation. Simplifications were checked for their validity.

So, we are expecting a device with a power consumption of around 40 mW for temperatures around 500 °C and time constants for heating in the millisecond range. Radiation effects can be neglected. Convection effects should be noticeable but not be of significant importance for the total power consumption of the device.

5.2 Thermal simulations

The thermal behaviour of the device is controlled by thermal conduction through the supporting bridges and the surrounding air. As seen in chapter 5.1.1, radiation losses can be neglected. Convective effects are included in the simulation model using a mean coefficient of convection h_m, but as we will see below, they have little effect on the total power consumption of the device. Preliminary simulations, which will not be described in detail here, were made to estimate the necessary amount of accuracy of the model. These helped limit the geometrical model to a diaphragm without considering the bulk silicon part, since the expected temperatures at the cold end of the micro bridges are close to room temperature even at 500 °C heater temperature. No elevated temperature was therefore expected at the edge of the diaphragm where the bulk silicon starts: an assumption justified by the succeeding simulations and measurements.

5.2.1 Material properties and boundary conditions

As mentioned before, the model symmetry allows the reduction of the problem to a quarter of a membrane. Its symmetry planes lay in (x=0,y, z) and (x,y=0,z), boundary conditions (T=0K) are given at the outer edges of the model (x=500μm, y, z) and (x, y=500 μm, z). This boundary condition (Neumann's condition) is compulsory for the transient problem [5.6] we will discuss later in this work. The infinite space above and below the sensor is modelled using "infinite elements" in Ansys.

Simulations of the current density in the heater, which we will later look at in more detail, expect a uniform current density distribution and subsequently a uniform power density across the heater. A uniform power density is thus used as heat source in the model where the heater is situated.

The material properties used in the thermal FEA are summarised in table 5.2

Table 5.2: Material properties used in the Finite Element Analysis (T=20 °C, [5.7..5.10])

Material	**λ / W m^{-1} K^{-1}**	**C_P / J kg^{-1} K^{-1}**	**ρ / kg m^{-3}**
SiC	220	$1.2 \cdot 10^3$	3200
SiO_2	1.4	$0.8 \cdot 10^3$	2200
Si_3N_4	20	$0.75 \cdot 10^3$	3100
HfB_2	42	$0.25 \cdot 10^3$	11200
Au	312	$0.129 \cdot 10^3$	19290
Air	$2.6 \cdot 10^{-2}$	$1.005 \cdot 10^3$	1.2

Except for SiC, temperature independent material values were used. This is justifiable, since SiC constitutes by far the largest proportion of the material used for the hotplate and supporting beams. Furthermore, its thermal conductivity is much higher than for the other materials involved, such that variations in material properties due to temperature changes are insignificant. For SiC however, temperature dependant values for the thermal conductivity were used. Work done by our research partners has investigated the thermal conductivity of polycrystalline 3C-SiC layers [5.8] using the identical material (in composition and thickness) as used in our micro heater. The data obtained there (table 5.3) was used in the FEA of the micro heater.

Table 5.3: Minimum, maximum and mean thermal conductivity of 3C-SiC thin films as used in the FEA

T / K	λ / W m^{-1} K^{-1}		
	Minimum	**Medium**	**Maximum**
373	190	220	255
423	175	210	238
473	162	195	222
523	150	180	208
573	142	170	195
623	128	155	175
673	115	140	158
723	100	130	138
773	90	110	122

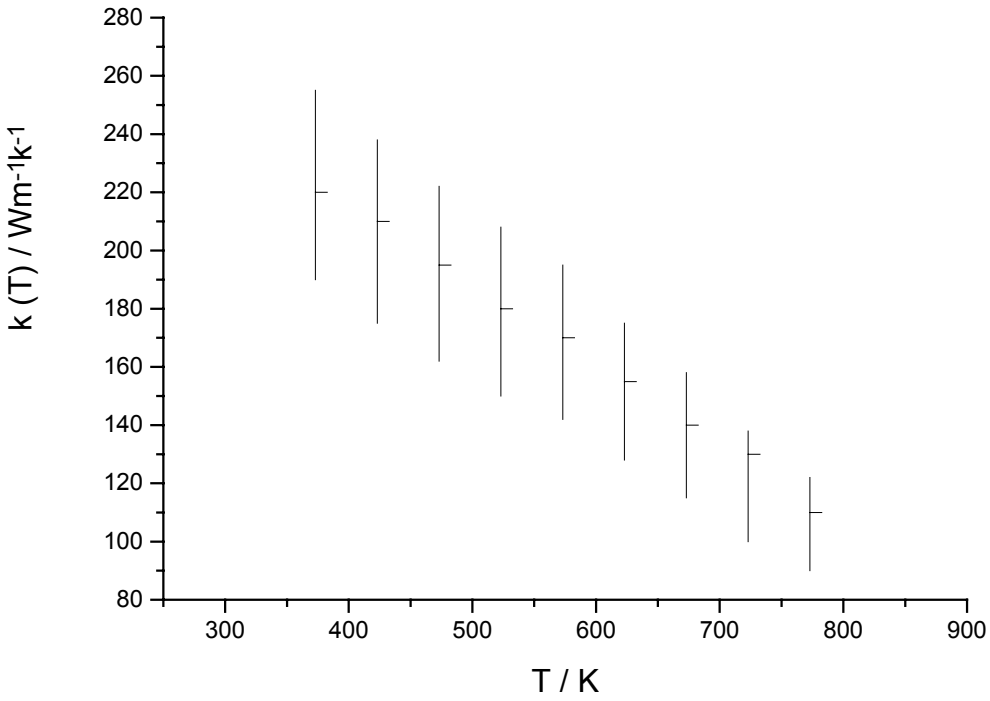

Fig. 5.7: Thermal conductivity of 1 µm thick 3C-SiC LPCVD thin films as function of temperature (mean values and error bars) [5.8]

5.2.2 Mesh generation

The parameters for mesh generation, which will not be stated here in detail, are set such that the mesh is the finest where the heater is situated (Fig. 5.6) in order to receive sufficient information on the temperature distribution on the heater and IDE. Also, mathematical singularities at the edges and interfaces to the metal contacts can be prevented this way. At the outer edge of the membrane a far wider mesh can be used, since the parameter gradients expected there are small (i.e. no large variations in T, σ, ε).

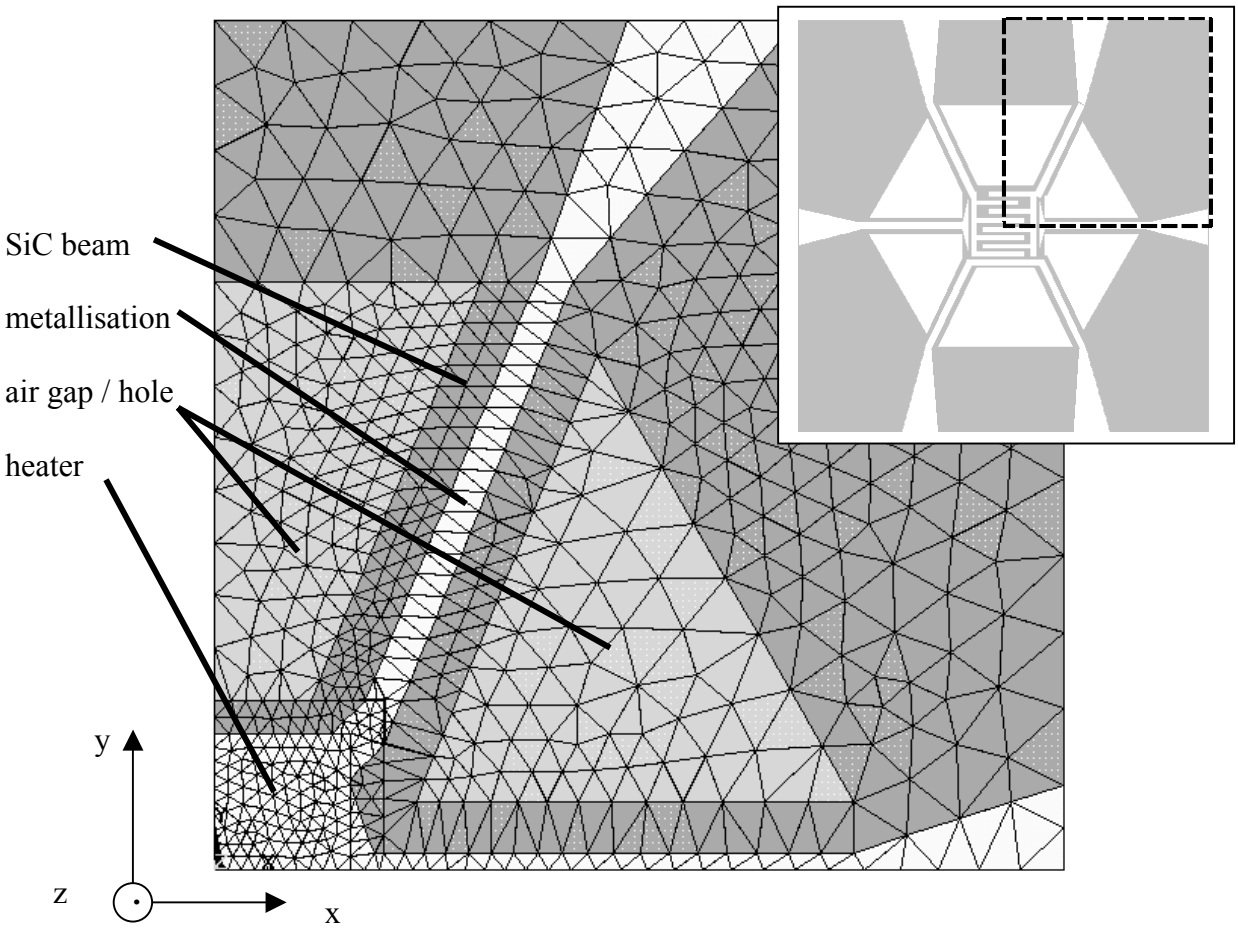

Fig. 5.8: 2D-view of the 3D-heater model with 40 µm bridge width and 150 µm bridge length and generated mesh

5.2.3 Temperature distribution across the micro hotplate

The temperature distribution on the heated diaphragm and the temperature gradient across the micro bridges are mainly controlled by the bridge diameter and length, i.e. the thermal resistance of the supporting bridges. The relative temperature distribution is, independent of the actual temperature very similar in all cases. As an example, typical distributions for three different bridge widths are given in Fig. 5.9, Fig. 5.10 and Fig. 5.11.

Upon first look there seems to be a similarity between the temperature profile along the bridges and in air. This effect is being pronounced by the hexagonal structure geometry. In fact, as expected, the temperature decreases much more rapidly in air than along the bridges (e.g. at 50 μm from the membrane the temperature along the bridges is at about 500 °C, whereas in air it is only about 200 °C (10 μm bridge width)).

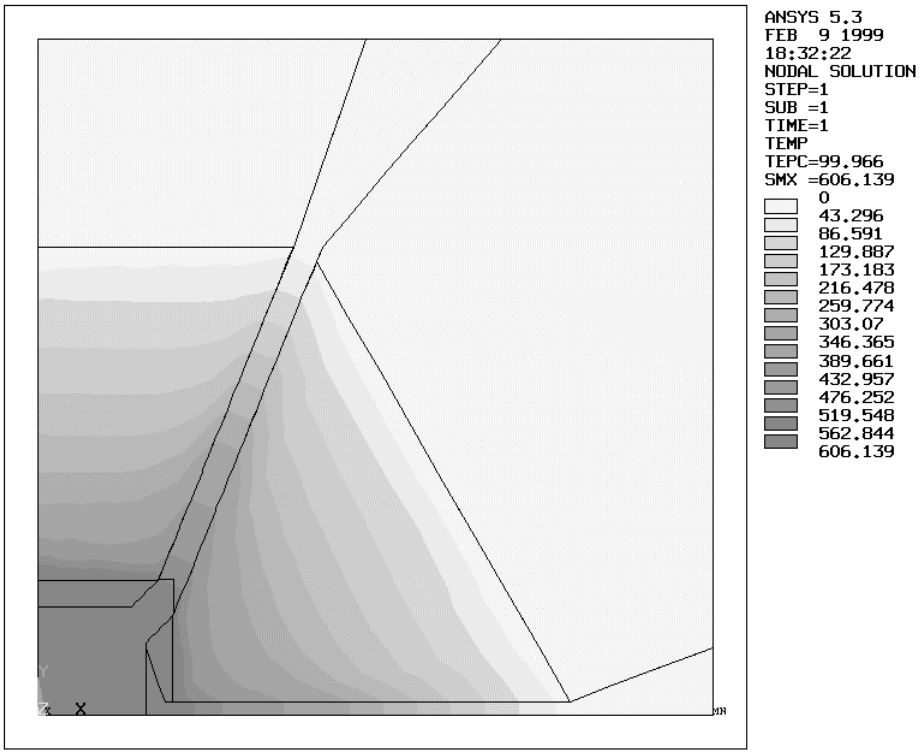

Fig. 5.9: Temperature distribution (2D-view of the 3D-heater model) on the micro hotplate with 10 μm bridge width and 150 μm bridge length (P=20mW)

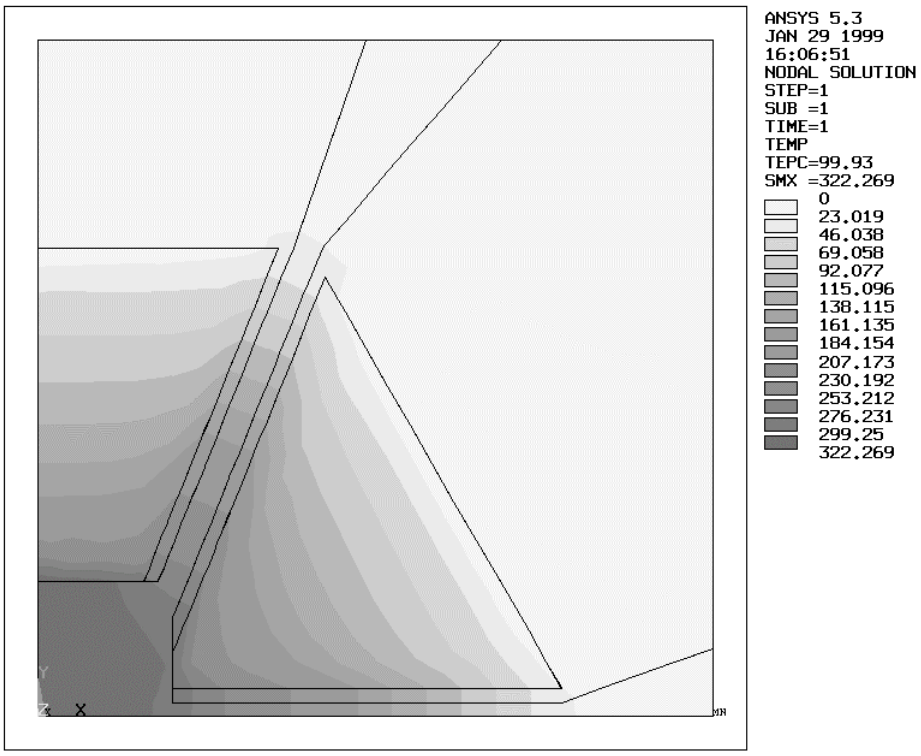

Fig. 5.10: Temperature distribution (2D-view of the 3D-heater model) on the micro hotplate with 20 µm bridge width and 150 µm bridge length (P=20mW)

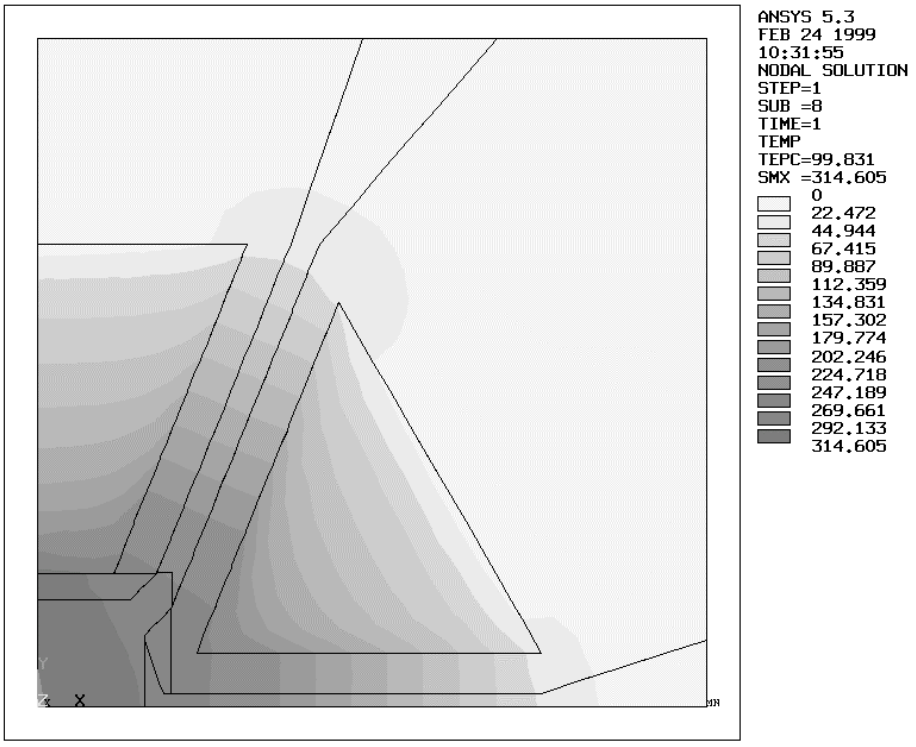

Fig. 5.11: Temperature distribution (2D-view of the 3D-heater model) on the micro hotplate with 40 µm bridge width and 150 µm bridge length (P=20mW)

The actual temperatures, however, differ considerably (Fig. 5.9, Fig. 5.10, Fig. 5.11) as will be described in more detail in (5.2.4). Evidently, the temperature drops down to nearly ambient temperature at the outer rim of the diaphragm (start of the bulk material). This is an additional justification for the simplification of the model to a membrane thereby neglecting the bulk material. One can clearly see the influence of the Au-metallisation on the temperature profile on the micro bridges.

In order to achieve a satisfying uniformity across the active area of the heater and IDE, the square membrane was compared to a circular membrane as described previously in chapter 4.

As mentioned before, the differences in the maximum heater temperature are considerable when changing the bridge width (Fig. 5.12). Apart from the maximum achievable temperature, the temperature profile and gradient is obviously effected by the bridge width. A narrower bridge - resembling a higher thermal resistance in the SiC-diaphragm - reduces the temperature gradient on the heater membrane. The wider the bridge, the more the profile approaches a parabolic shape. Clearly, an infinitely narrow bridge (or non-existing bridge, i.e. a free floating membrane) must appear as the ideal geometry when looking at the thermal aspects of the heater only.

The bridge length has an equally strong impact (Fig. 5.12, Fig. 5.13). Whereas in the version with 150 μm bridge length and 20 μm width temperatures close to 870 K (597 °C) can be achieved with 60 mW of heater power, reducing the bridge length to 100 μm results in only 720 K (447 °C) maximum temperature. In the case of the 40 μm wide bridges this results in unacceptably high power consumption when trying to reach for the specification (450-500°C, <100 mW). For this reason, despite the mechanical imponderabilities of the fragility of the 150 μm version, the 100 μm version was discarded in the later device realisation.

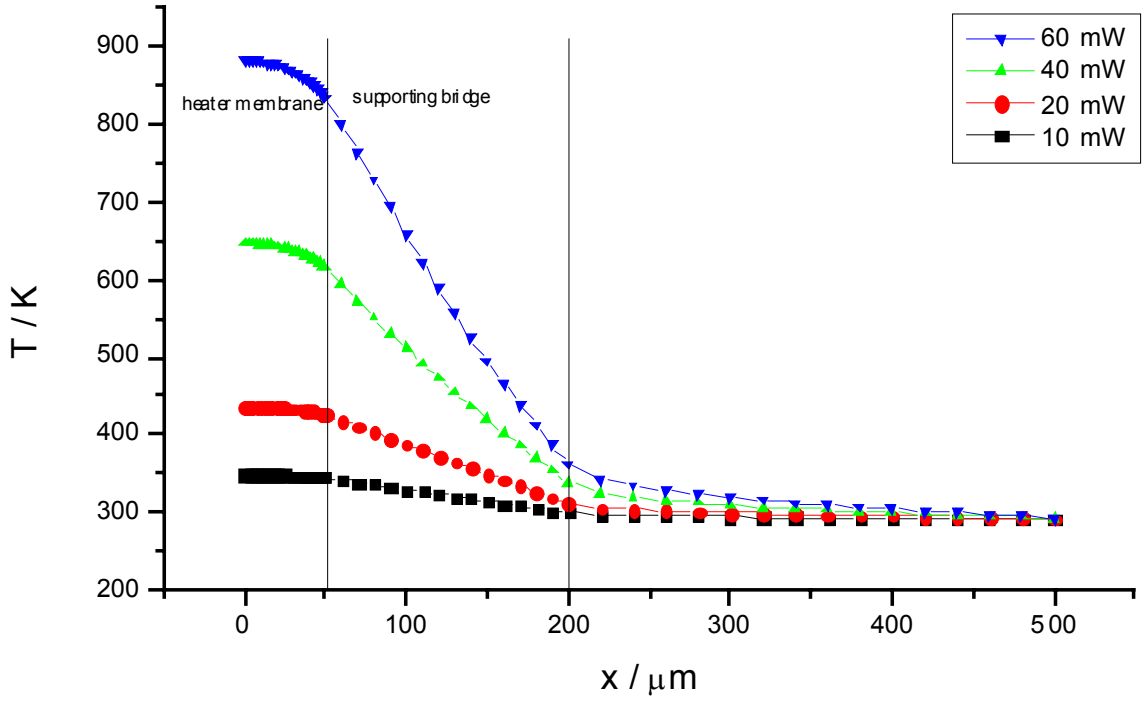

Fig. 5.12: Temperature profile from the centre of the membrane across the micro bridges to the outer edge of the membrane at various heater powers (150 µm bridge length, 20 µm bridge width)

Temperature distributions were calculated for bridge widths of 10, 20 and 40 µm and bridge lengths of 100 and 150µm, each with and without implementing convection.

Since convection plays only a minor role in the power consumption of the heater - as expected (chapter 5.1.1) -, the effect on the Temperature distribution is so miniscule that except for a slight drop in the maximum temperature of a few degrees Celsius no variation could be detected. Convection was modelled using the static model h coefficient (eq. 5.16-5.19).

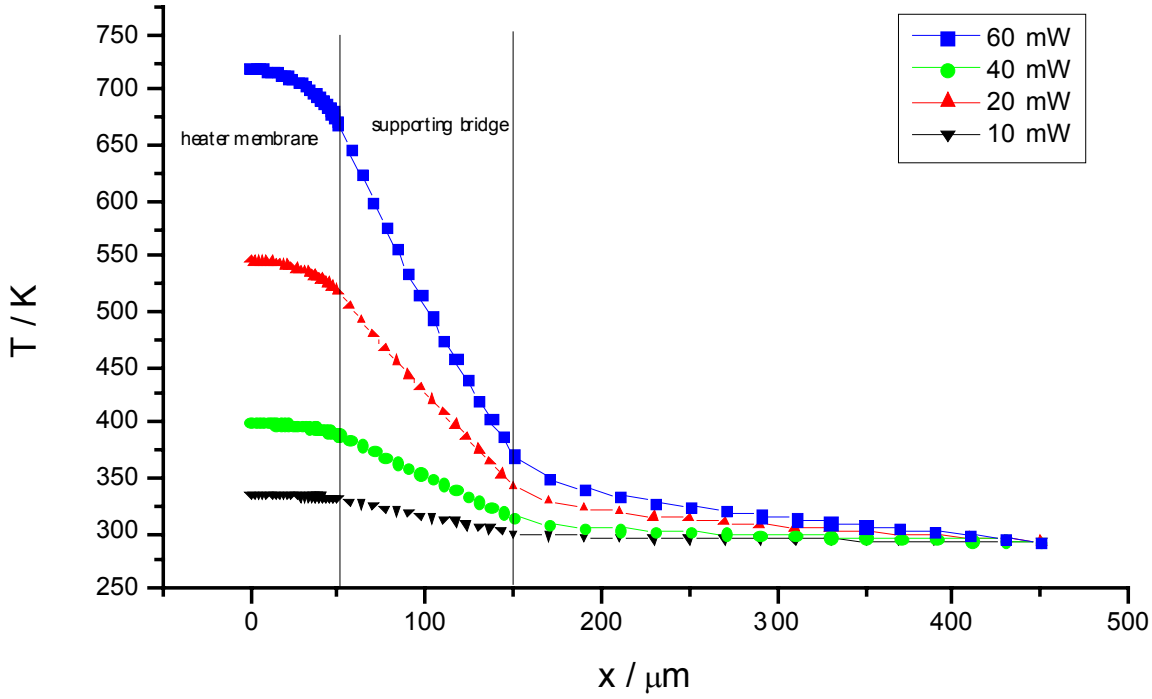

Fig. 5.13: Temperature profile from the centre of the membrane across the micro bridges to the outer edge of the membrane at various heater powers (100 µm bridge length, 20 µm bridge width)

5.2.4 Power consumption as a function of the heater temperature

The power consumption as a function of the maximum heater temperature was determined for bridge widths of 10, 20 and 40 µm and a bridge length of 150 µm. The heater version with 100 µm bridge length was discarded, since the comparably higher power losses exceeded the limitations (P<100mW) in some cases. It is not discussed in further detail here. The power consumption changes hyperbolically with the micro bridge width (Fig. 5.14). The variation in bridge width causes a variation in bridge cross-sectional area. The power losses through conduction in the bridges are inversely proportional to the cross-sectional area.

Since these play a major role in the total power consumption of the device the hyperbolic correlation is evident.

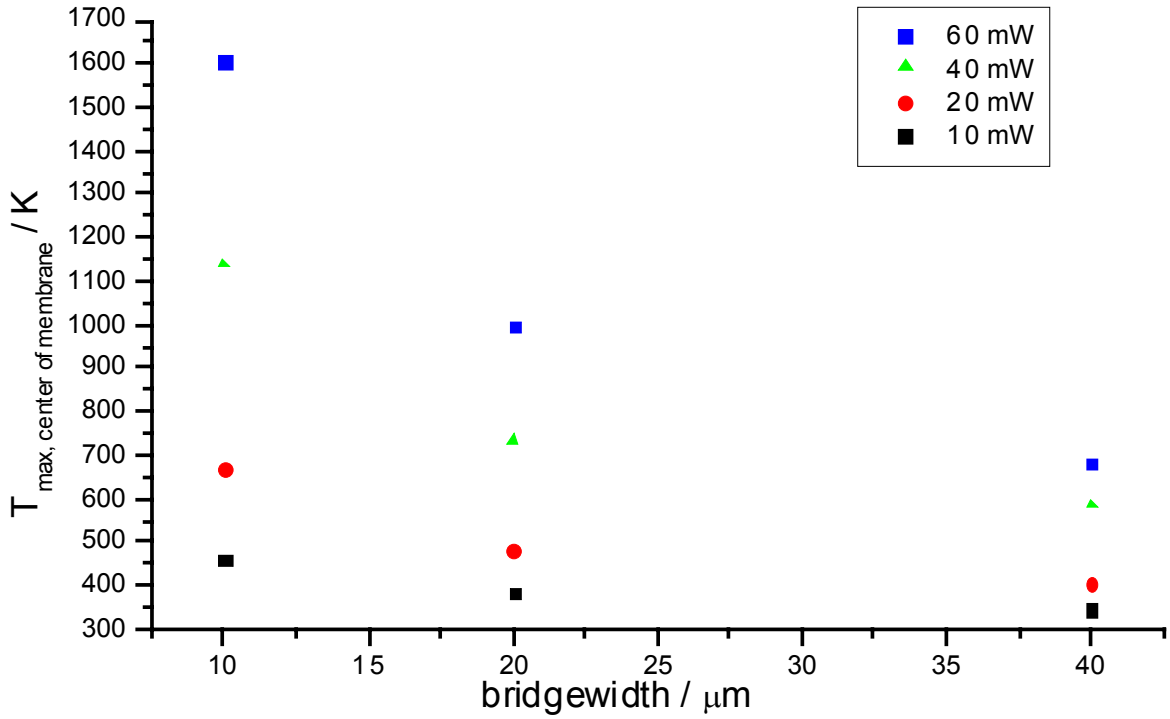

Fig.5.14: Maximum heater temperature as function of micro bridge width at various heater powers

The power dependency of the temperature (Fig. 5.15) exhibits a slight parabolic behaviour. This is caused by the decrease in thermal conductivity of the supporting micro bridges with increasing temperature (chapter 5.2.1).

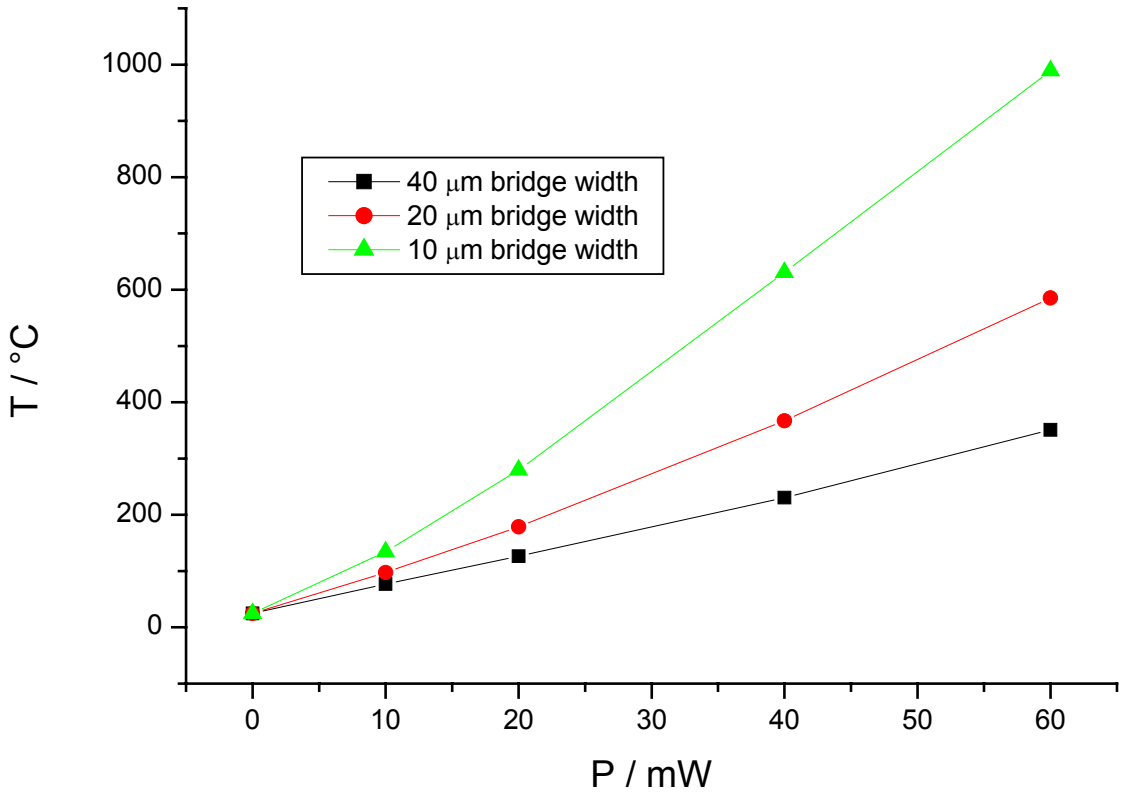

Fig.5.15: Maximum heater temperature as function of heater power at various micro bridge widths. At higher temperatures, the thermal resistance of the SiC bridges increases slightly, reducing the necessary power per degree Celsius temperature increase.

5.2.5 Transient behaviour of the micro hotplate

For the operation of the sensors in a pulsing or temperature programmed desorption mode, short response times are necessary [5.11-5.13]. Transient simulations were performed to determine and further optimise the structure. The influence of variations of the bridge width and the thickness of the consecutive layers (SiC, SiO_2) were investigated. In general, time constants of the order of 1 ms could be obtained for all cases. This behaviour exceeds the requirements set by the specifications by far.

As a first order approximation the heater can be modelled as a P-T_1 or RC-module, giving a time constant of $\tau = R \cdot C$. The transient response of the heater temperature to a square heating pulse follows:

$$T(t) = T_{max}\left(1 - e^{-\frac{t}{\tau_{on}}}\right) \qquad (5.35)$$

Cooling follows:

$$T(t) = T_{max} e^{-\frac{(t-t_0)}{\tau_{off}}} . \qquad (5.36)$$

Due to the heater geometry, the thermal resistance in longitudinal direction of the bridge dominates the thermal resistance of the total structure. With increasing bridge width, ergo increasing cross-sectional area, the thermal resistance decreases, while the effective heat capacity of the total structure $C_{eff.}=\Sigma_n c_i V_i$ is negligibly effected (with: V_i partial volumes, c_i specific heat capacity at constant pressure of each volume). The time constant must obviously decrease with increasing bridge width (Fig. 5.16, Fig. 5.17).

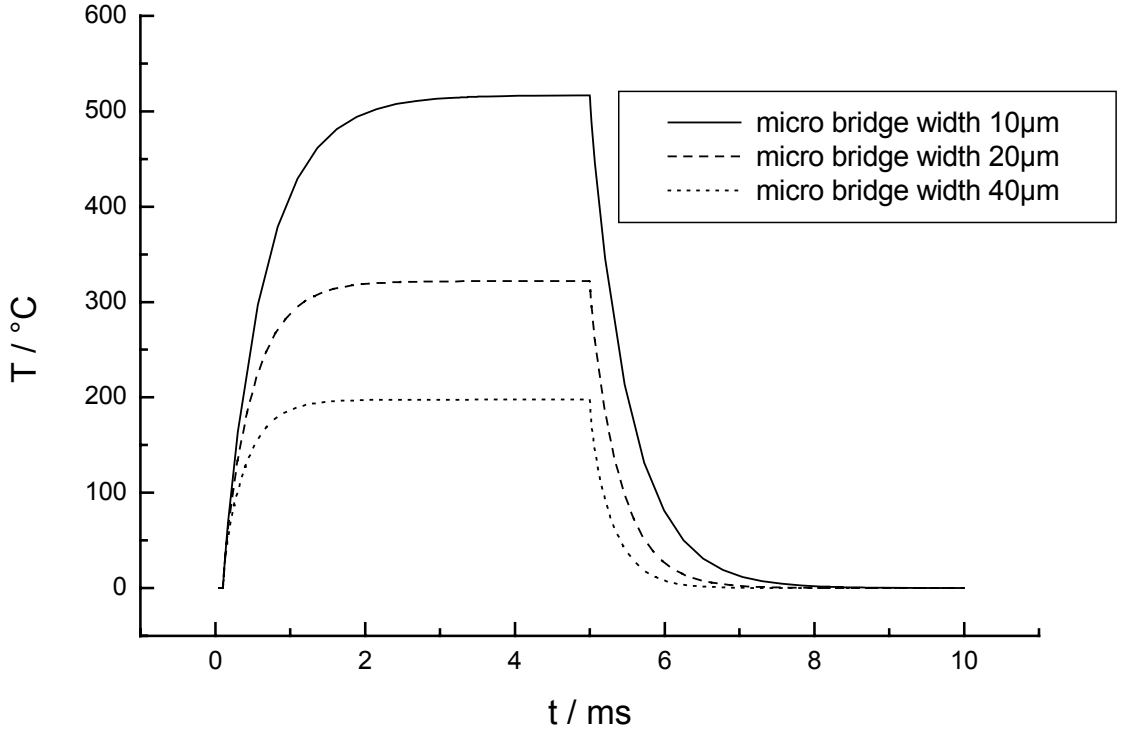

Fig. 5.16: Heater transient response to a square heat pulse of 40 mW power and 10 ms length for micro bridge widths of 10 µm, 20 µ, and 40 µm

Obviously, the maximum heater temperature increases drastically with decreasing bridge width (Fig. 5.14, chapter 5.2.3, chapter 5.2.4) in the transient case as well. The time constant τ_{on} increases slightly with decreasing bridge width (Fig. 5.17). This behaviour is clear, since due to the decreased bridge width the thermal resistance of the bridge increases, thus increasing the thermal time contant. The whole system behaves like a thermal spring-damping system. During the heating, the hotplate is at first heated quickly, but takes time to reach its steady state due to the rather "slow" heat leak through the narrow bridges to the substrate. This effect should be more noticeable when turning the hotplate off.

A heater with thinner bridge obviously reaches a higher operating temperature. In total, at constant heater power, the heater with thinner bridges reaches the

(lower) operating temperature of a wider bridge heater faster than the latter one, but continues on to a higher operating temperature (Fig. 5.16). So all in all the smaller bridge heater heats faster ($\Delta T[K]/\Delta t[s]$), but due to the higher operating temperature takes longer to reach its (higher) operating temperature compared to the wider bridge heater.

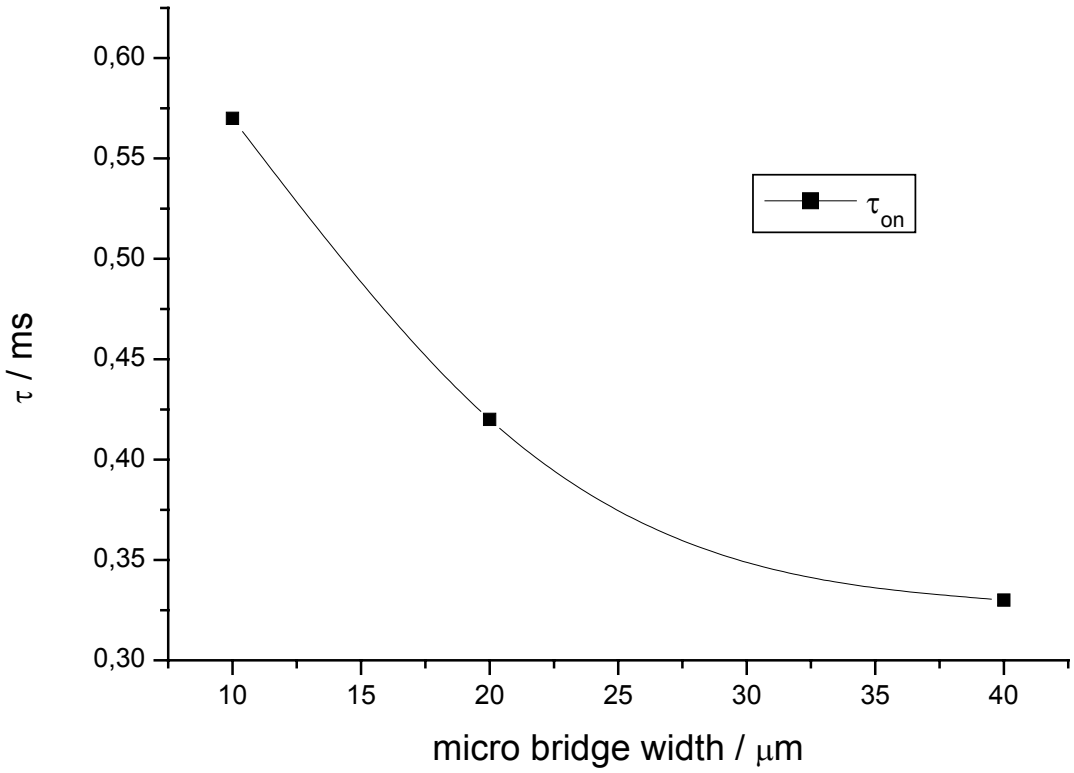

Fig.5.17: Time constant τ_{on} upon heating as function of micro bridge width b_μ at identical maximum heater temperature. A hyperbolical trend as indicated is expected, since $\tau \rightarrow \infty$ with $b_\mu \rightarrow 0$ and $\tau \rightarrow \tau_{min}$ with $b_\mu \rightarrow \infty$.

A detailed investigation of the data [5.6] suggests an influence of the thickness of the thermally insulating SiO_2 layers underneath and above the SiC layer on the transient behaviour. Their influence is, however, so small – variations amount to about ± 0,5 ms – that, considering the specifications (chapter 4), for all practical purposes it can be neglected.

For the operation in a pulsed mode, the frequency amplitude response is of interest to the prospective user. As usual for heating devices, a low pass characteristic is expected and observed. The 3dB frequency amounts to about 120 Hz. Above that, a significant decrease in heater temperature occurs with increasing power pulse frequency (Fig. 5.18).

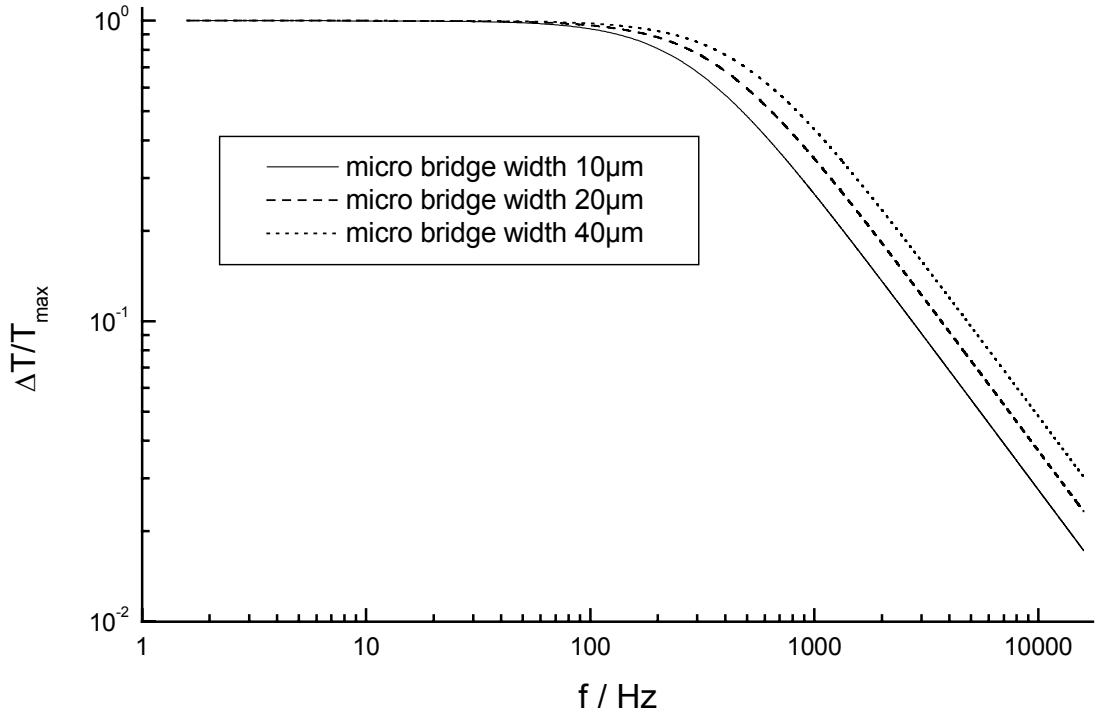

Fig. 5.18: Frequency response of micro heater at micro bridge widths of 10 µm, 20 µm and 40 µm. A low pass characteristic with 3dB frequency at 120 Hz is observed. Wider bridges reduce the time constants, thereby increasing the frequency range slightly.

The main points gained from the investigation of the heater transient thermal response are:

- The heater follows a low-pass characteristic – as expected – with response times τ_{on} and τ_{off} around 1 ms, which is far better than the set specification of $\tau_{on} < 100$ ms.

- Geometrical considerations (bridge width, oxide layer thickness) can influence the time constants. These variations can amount to 0,5 ms, which is large relative to the total time constant. Taking into account the limitations given by the specifications, no further optimisation is required.

5.2.5 Influence of thermal conductivity variations of the SiC on the obtainable heater temperature

The thermal conduction through the micro bridges is the dominating factor for the thermal behaviour of the whole device. The core part of them is made of SiC, therefore the variations in thermal conductivity of the material have to be considered. As expected, the influence of the material properties is significant (Fig. 5.19).

The bandwidth of temperatures achieved when comparing the results with lower and upper limit of the SiC thermal conductivity can reach up to 400 K in the case of the 10 μm / 150 μm bridge version at 60 mW heater power (1400 K - 1800 K). The effect, however, remains still smaller than the one from the geometrical parameters (bridge width and length).

For all practical purposes, the mean values of the SiC thermal conductivity as given in chapter 5.1.1 were used. This procedure will be justified when looking at the good agreement of the actual and simulated heater performance (chapter 7.1) and the determination of $k_{SiC}(T)$ later (chapter 7.5).

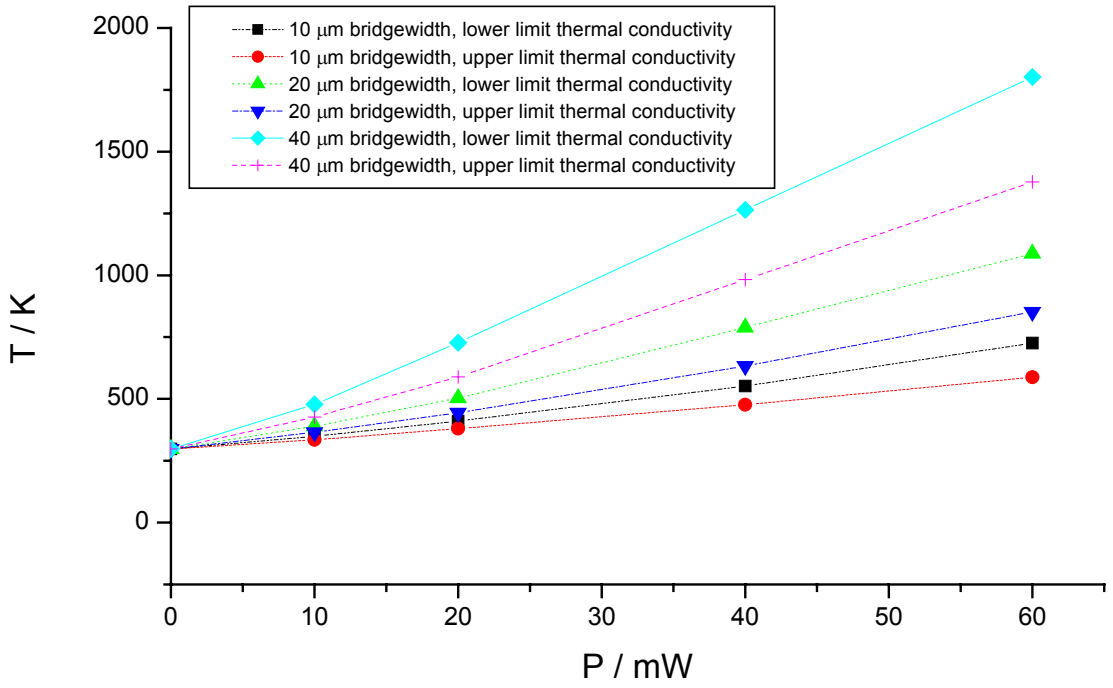

Fig.5.19: Variation of maximum heater temperature as function of heater power with varying SiC thermal conductivity

5.3 Thermo-mechanically coupled simulations

Thermally induced stress is one of the key issues of concern when improving the device stability and high temperature compatibility. Based on the temperature distributions computed using the thermal simulations, the mechanical stress in the structure could be determined. The thermally induced stress at 500 °C reaches maximum values of about 350 MPa in the bridges (compressive), thereby roughly equalling the intrinsic tensile stresses of the SiC-layer (250 MPa). A slight bow of the structure upon heating can be expected (about 5 µm in the diaphragm centre). The values given in the diagrams result from the average values of the top layer FEM elements and nodes, yielding an average value.

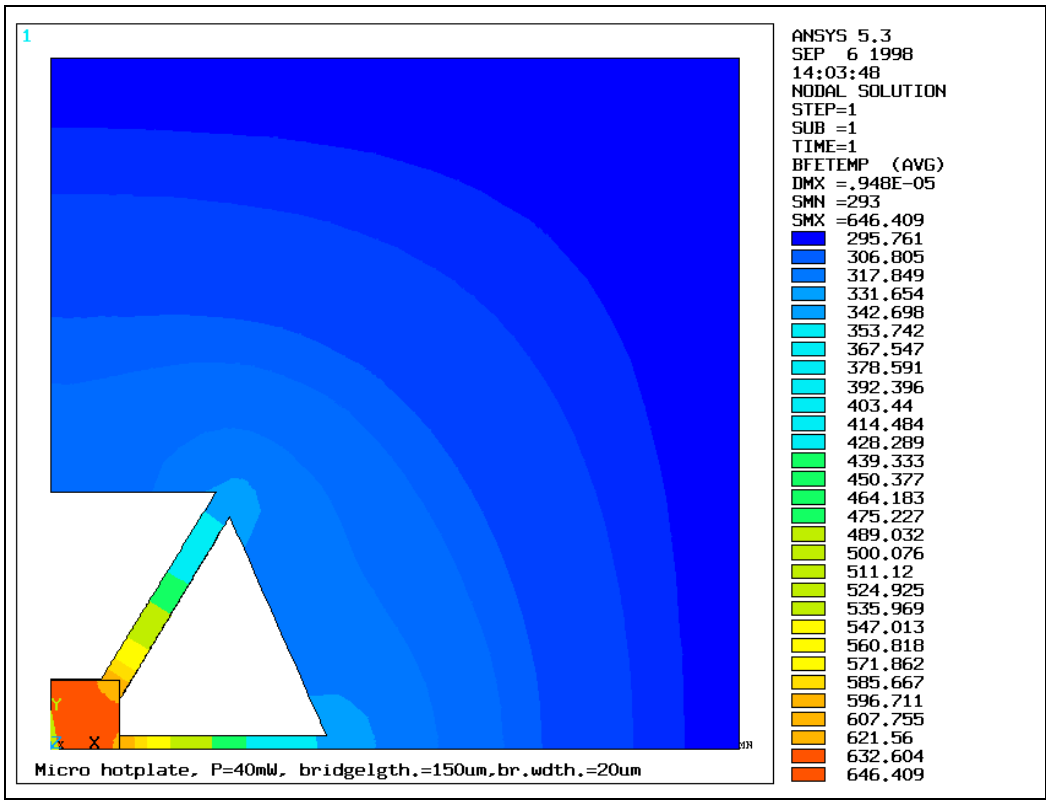

Fig.5.20: Temperature distribution (T/K) of a micro hotplate with 150 µm bridge length and 20µm bridge width at 40 mW heater power (T=646 K) (2D-view of 3D model)

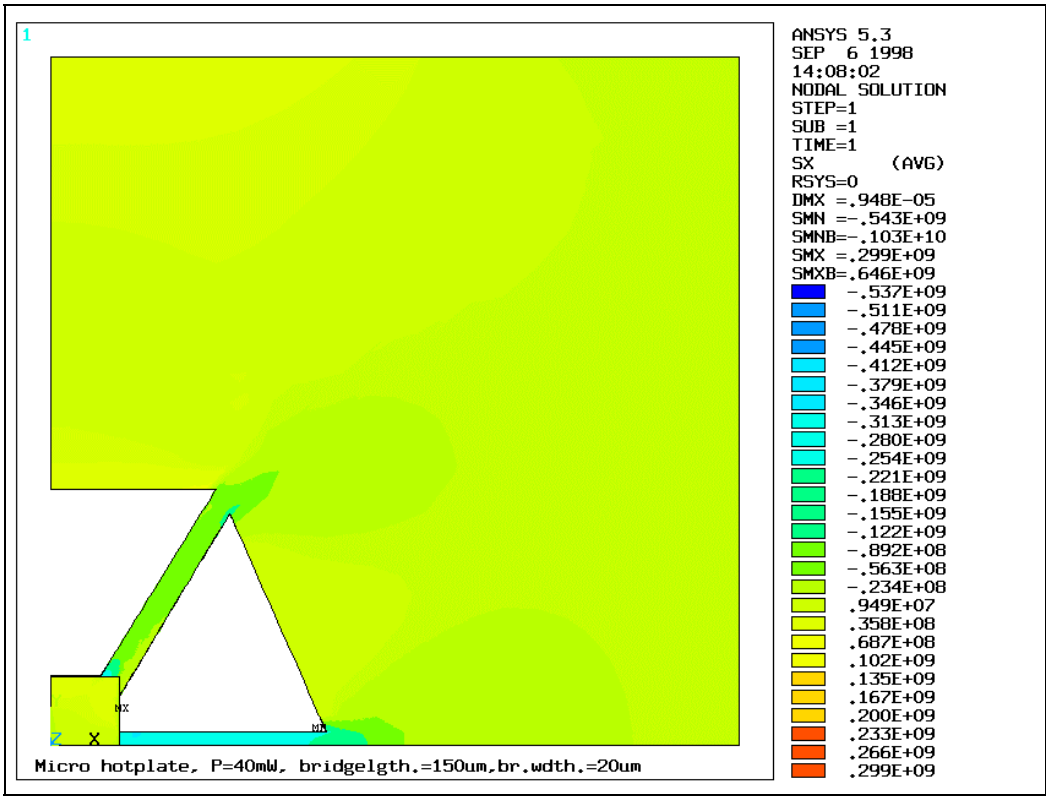

Fig.5.21: Stress distribution (σ_x/[Pa]) of a micro hotplate with 150 µm bridge length and 20µm bridge width at 40 mW heater power (T=646 K) (2D-view of 3D model)

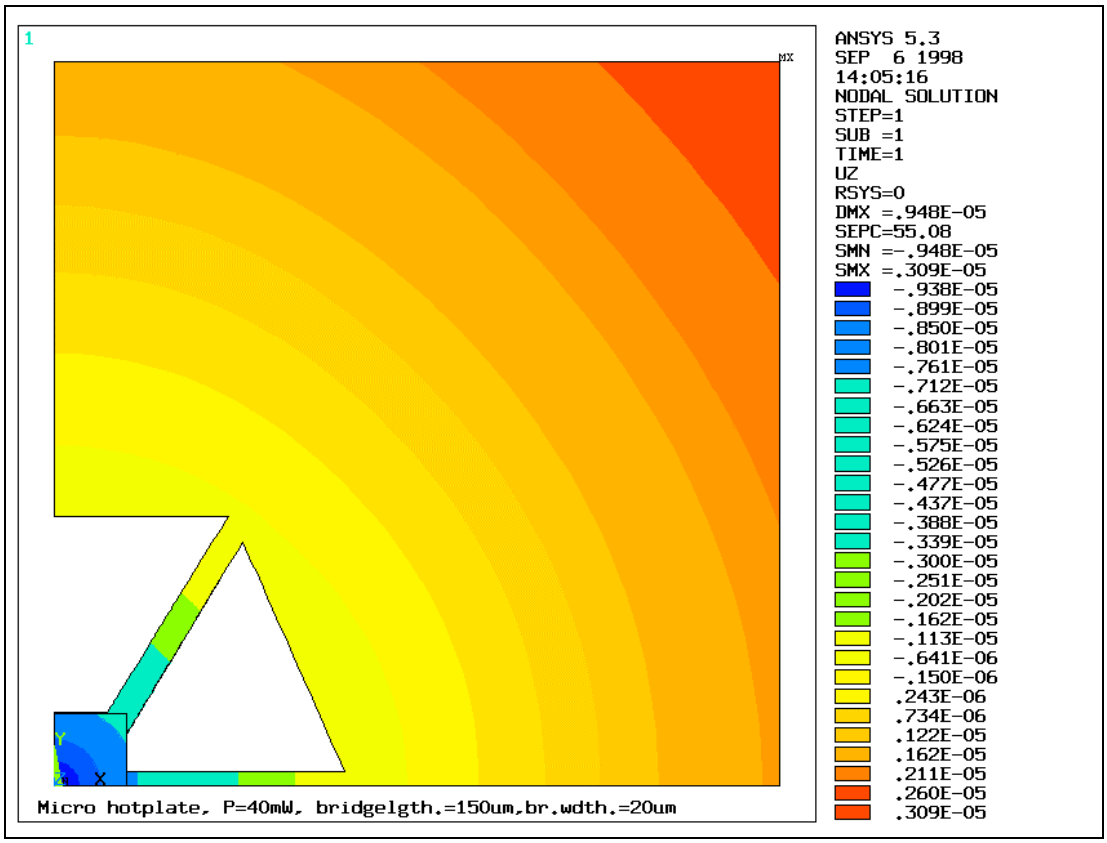

Fig.5.22: Deflection in z-direction (U_z/[m]) of a micro hotplate with 150 µm bridge length and 20µm bridge width at 40 mW heater power (T=646 K) (2D-view of 3D model)

A more detailed investigation is not necessary, since the only purpose of the thermo-mechanical FEA is to approximate the occurring stresses to prevent mechanical failure. Stresses of this magnitude are far from the mechanical limits of the SiC thin film [5.7].

5.5 Discussion and design decision

The FEA yields four main results: a general check of the suitability of the design, a check and optimisation of the device thermal, thermo-mechanical and electrical properties, a limitation of the device variations to be fabricated and an estimate of the device properties to be expected.

- The power consumption, temperature distribution and thermally induced mechanical stress is within the set specification. The thermally induced compressive stress roughly equals the expected tensile intrinsic layer stress creating a very stable situation at 400-500 °C. Mechanical failure – also in the long term – is not to be expected.
- Wide heater contact electrodes guarantee a uniform power density distribution in the heater through a uniform current density and a constant voltage gradient across the heater.
- A power consumption of 40 mW for operating temperatures around 450 °C is expected in the best case. The thermal response is of the order of one millisecond.

Based on these results the following design decision is made:

- The general structure is a micro hotplate, supported by thin beams in a larger membrane. This design allows minimum heat losses through the substrate material and the placement of multiple hotplates within one single membrane structure. Space requirements are thus minimised.
- The micro hotplate is a sandwich consisting of a SiC substrate, a resistive heater, a Si_3N_4 insulation layer and a Ti/TiWN/Au metallisation layer. The sandwich design reduces the lateral dimensions and improves the temperature uniformity across the hotplate.
- 3C-SiC is used as substrate material on a Silicon wafer allowing standard Si-bulk micromachining while offering SiC-characteristics for the active device

part. SiC is chosen despite is high thermal conductivity due to the exceptional mechanical, thermal and chemical strength allowing unprotected use in highly oxidising and aggressive environments. The 3C-Sic material also exhibits an intrinsic tensional stress roughly equalling the compressive thermal stress expected during operation. Little membrane buckling during operation and good long term stability of the mechanical structure during operation and cycling can thus be expected.

- Dimensions for the supporting beams are set by the operating temperature, power consumption and mechanical strength requirements. Whereas beams with only 100 μm length allow too much power loss through thermal conduction through the SiC, beams of 150 μm length and 10, 20 or 40 μm offer sufficient thermal resistance. All three widths will be realised in order to gain sufficient data to verify the theoretical model and to add additional safety for technological realisation.
- The resistive heater is designed as area heater, primarily for technological and processing reasons and comes in two variations: a low resistance metal thin film made from HfB_2 for battery operation and a high resistance implanted resistor in the SiC substrate for power grid and automotive operation. HfB_2 is chosen for its exceptionally high specific resistance of 253 μΩcm and its high melting point. Its low chemical strength in oxidizing environments however requires protection by a dense passivation layer. The implanted SiC heater allows operation also at high voltages without the disadvantages of the metal layer. Furthermore, no additional design change to the device has to be made. Modification from the low to the high resistance version can be made by simply replacing the metal deposition by an implantation step.
- Despite the problems to be expected when using Au metallisation layers, the Ti/TiWN/Au layer is used, since it is the only low resistance metal layer available with operating temperature limit at about 600 °C. Pt-layers as

potential competitor could not be used, since the battery operation of the device requires low heater resistances around a few ten Ohms. The contact leads to the resistors have to feature an even lower resistance. Thus, Pt is unacceptable as contact layer. Furthermore, structuring of the material is far more complex than for the Au layer.

- Interdigital electrodes for the contacting of the gas sensitive layer, contact leads for the heater and the resistive temperature sensor are realised in this one metal layer. This reduces the number and complexity of processing steps.

6. Fabrication of the sensor modules

Chapter 6 describes the fabrication of the micro hotplate gas sensor modules. Starting from a general overview of the fabrication procedures, the requirements for each part of the hotplate device are explained individually. Fig. 6.1 and Fig. 6.2 give a general overview of the processing steps.

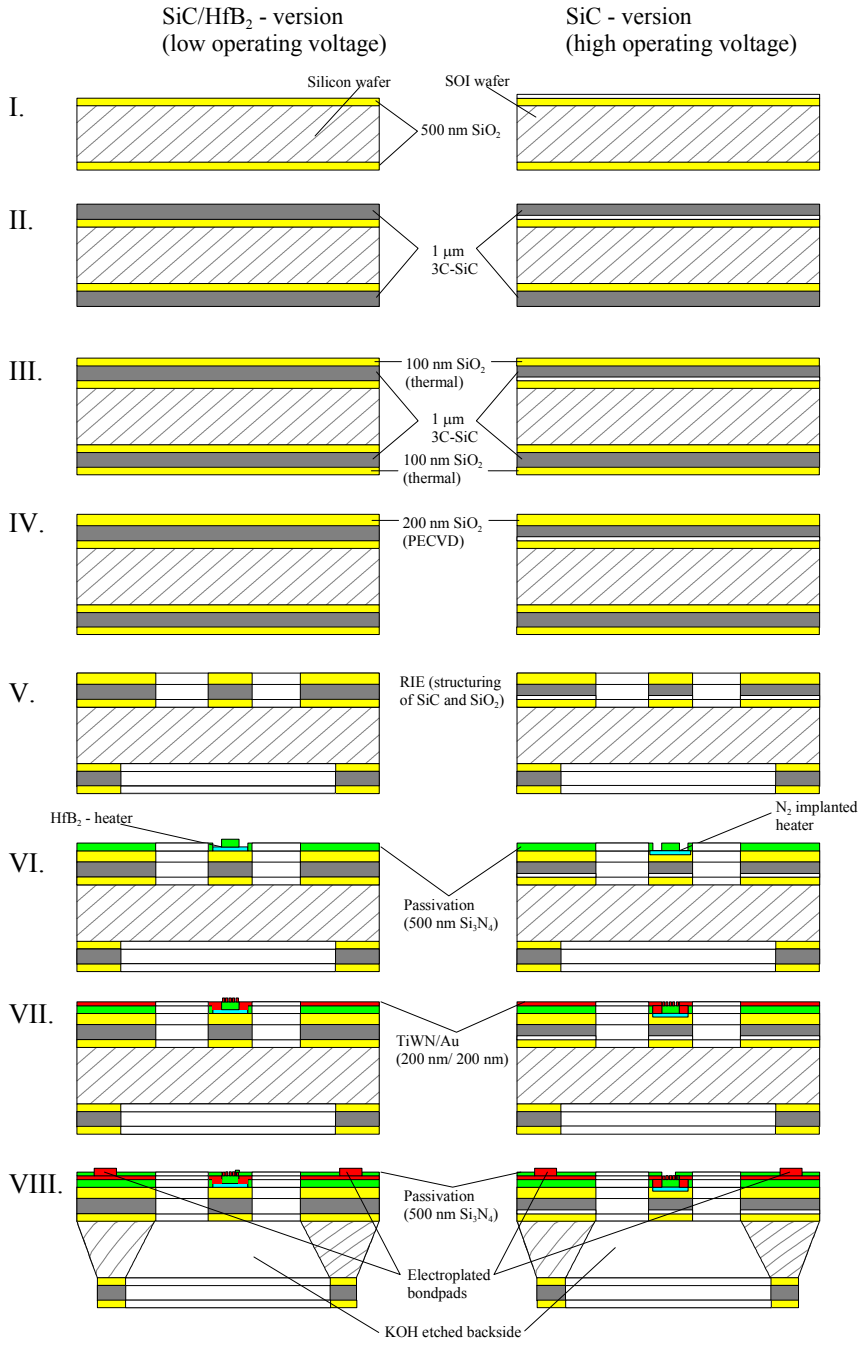

Fig.6.1: General device fabrication process outline.

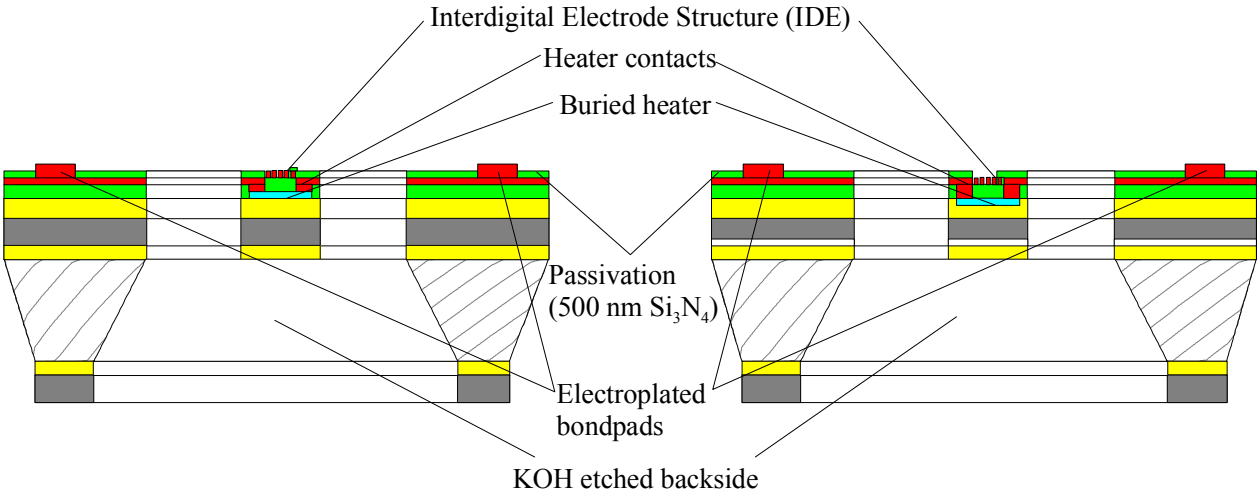

Fig. 6.2: General device fabrication outline (magnification of complete device, dimensions and aspect ratio not to scale).

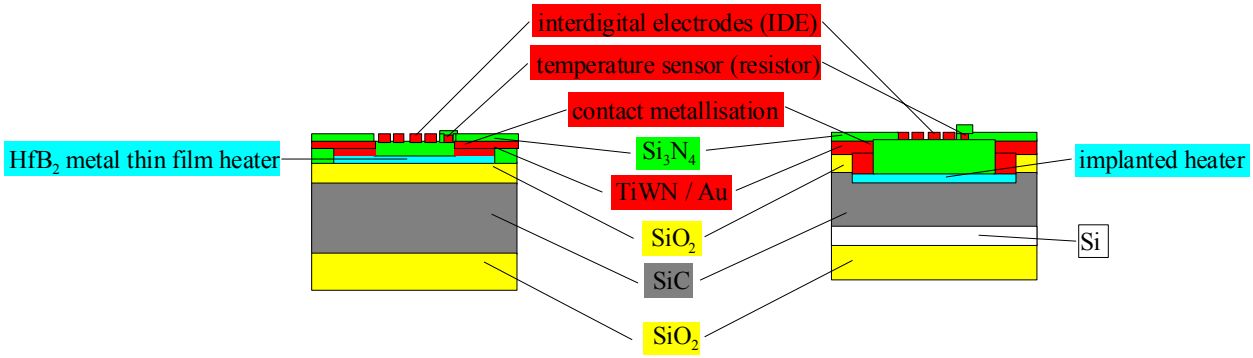

Fig. 6.3: General device fabrication outline (magnification of hotplate section, dimensions and aspect ratio not to scale).

Technological considerations (e.g. the mutual influence of the various manufacturing steps) are taken into account in every step. The fabrication procedures follow standard semiconductor processes. A complete and detailed set of process protocols describing all the fabrication steps and parameters can be found in appendix E.

The general fabrication procedure (Fig.6.1) is set up for a modular system of devices. The variation of the heater from a low voltage to a high voltage version

only requires replacement of the HfB_2 metal heater with an implantation and direct contacting of the SiC.

6.1 Supporting structure

The mechanically supporting structure also defines the geometry of the device. For the low voltage version, standard 390 µm ± 5 µm thick double-sided polished Si-wafers with 500 nm wet thermal SiO_2 are used as substrate. The wafers are n-type / P-doped with 3-5 Ωcm resistivity. The high voltage heater version requires additional doping of the SiC by ion implantation. For the implantation to show effect, a predominantly mono crystalline SiC layer is needed. Thus, SOI-substrates are used instead of the standard Si – wafers. The thin mono crystalline Si-toplayer of the SOI wafers theoretically allows the formation of a mono crystalline SiC-layer [3.26, 6.13, 6.14, 6.15]. Fabricated layers however are predominantly poly crystalline.

A 1 µm thick 3C SiC layer was deposited by LPCVD heteroepitaxy at 1100 °C. 3 sccm methylsilane diluted in 300 sccm hydrogen were used as precursor gases. Their advantage over other precursors is the low deposition temperature required reducing thermally induced damage to the Si wafer. The resulting SiC is polycrystalline and unintentionally doped (10^{17} cm^{-3}).

The electrical insulation of the SiC is achieved by growing 100 nm thermal SiO_2 on top of it (2.5 h in O_2 (3.5 l/min), 1100 °C) and reinforcing it by 200 nm PECVD SiO_2. The low oxidation rate and subsequent longer oxidation time of the SiC in comparison to the Si requires the PECVD reinforcement rather than using a thicker thermal oxide. On the one hand the low oxidation rate of the SiC (about one order of magnitude smaller than for Si) increases its durability at high temperatures. On the other hand it prevents the growing of thicker oxides, unless one uses exceptionally high temperatures (e.g. 1300 °C) with increased oxidation rates thereby causing crystal damage to the Si wafer. This must be

avoided to allow satisfactory anisotropic etching characteristics, since the KOH etches according to the crystal orientation. PECVD SiO_2 is particularly suitable to obtain thicker oxides due to the lower deposition temperatures.

This SiO_2-SiC-SiO_2 sandwich is structured using RIE. An Al-mask instead of a photoresist mask is necessary when structuring the SiC layer. The Al-mask allows etching times of up to 2 h compared to 8 min of the normally used photoresist. With typical etch rates of about 15 nm – 20 nm per minute we obtain etch times of about 1 h, which are well below the maximum 2 h possible. The use of the Al-mask requires this step to be undertaken before the deposition of succeeding layers, due to the selectivity of the required AlSi-etchants towards these layers.

This causes deep cavities in the surface of the wafer at an early processing stage. In order to achieve a satisfying quality of the succeeding steps, RIE-etching is only done through the first SiO_2, the SiC and about 300 – 350 nm of the underlying wet thermal oxide resulting in a step of about 1.5µm and leaving about 150-200 nm of SiO_2. Deep cavities produce two problems: first of all, starting at 1.7- 1.9 µm step depth, the photolithography of the succeeding layers is getting increasingly difficult and eventually impossible if high accuracy is required. The photoresist does not cover the edges properly and as a result a sort of a lense-shaped photoresist cover builds up on the heater part of the membrane. This causes optical diffraction during lithography, making the resolution of structures below 10 µm lateral size impossible. Secondly, etching right into the underlying Si is hardly a controllable process, considering the high etch rates of about 1 µm / min in Si. Furthermore, every succeeding RIE-etching process increases the hole depth further. Cavities of about 20 µm depth can result. Further lithographic processing of such samples is not possible with the required accuracy for the structural dimensions on the hotplate.

The chemical inertness of SiC hinders simple processing of the layers. For the structuring of SiC layers, a number of etching processes have been presented,

most of them involving Cl-based RIE etching. Due to the lack of suitable etching equipment and etchants for SiC layers using these Cl-based agents, a new etching process based on a standard O_2 / SF_6 process used for SiO_2 and Si_3N_4 layers was developed at TU Berlin to allow slow etching of SiC layers. The RIE of the SiC layer is done using a Vacutec RIE etcher with an O_2 / SF_6 (16 sccm / 4 sccm) plasma at 150 W and a graphite electrode to structure the SiO_2 / SiC / SiO_2 sandwich on the front side (micro bridges) and backside (etch mask for anisotropic etching) of the wafer. The graphite electrode prevents micro-masking resulting from small Al-particles [6.1]. The long etching times and high RF power required to etch the SiC layer, remove Al-particles from the Al substrate holder and chuck. These particles deposit on the SiC surface and thereby act as micro masks, preventing uniform etch rates across the substrate. The graphite electrode is being eroded as well. The graphite particles depositing on the SiC are however being etched faster than the Al mask and therefore do not mask the SiC surface.

6.2 Heater

The heater can, as mentioned before, be varied between a metal thin film heater for operating voltages around 1-2V and a semiconductor resistor made from doping the SiC in the heater region.

For the low voltage version, 200 nm HfB_2 is deposited via DC-sputtering at 700 W with 100 sccm Ar sputtering gas at 0.9 Pa process pressure on a Leybold sputtering system. The sputtering target used in our process is made from sintered HfB_2 powder with 99.5% purity.

For etching HfB_2 an H_2O:HNO_3:NH_4F (6:4:0.04) etching solution is used at room temperature. Etch rates are about 3 nm/s. A change in metal thin film colour from silver over brown to black can be observed during etching until the

HfB_2 is completely etched. This serves as colour indicator for a completed etching process.

The HfB_2 is annealed at 500 °C for 5h in N_2 atmosphere (3.5 l/min) to stabilise its electrical properties for operating temperatures up to 450 °C. A safety-distance of 200 °C is kept to the 700 °C mark for the following reason: annealing at higher temperatures can increase the layer sheet resistance (Fig.6.4) until above 700 °C bubbles build up on the layer surface eventually destroying the film by exploding and leaving craters behind (Appendix F). As can be seen in Fig. 6.4 the sheet resistance is nearly unaffected from the annealing up to 450 °C, which is more than satisfying for micro heater applications up to 450 °C. A thorough study of the HfB_2 will be necessary in order to understand the metal behaviour at these temperatures prior to setting higher annealing and operating temperatures.

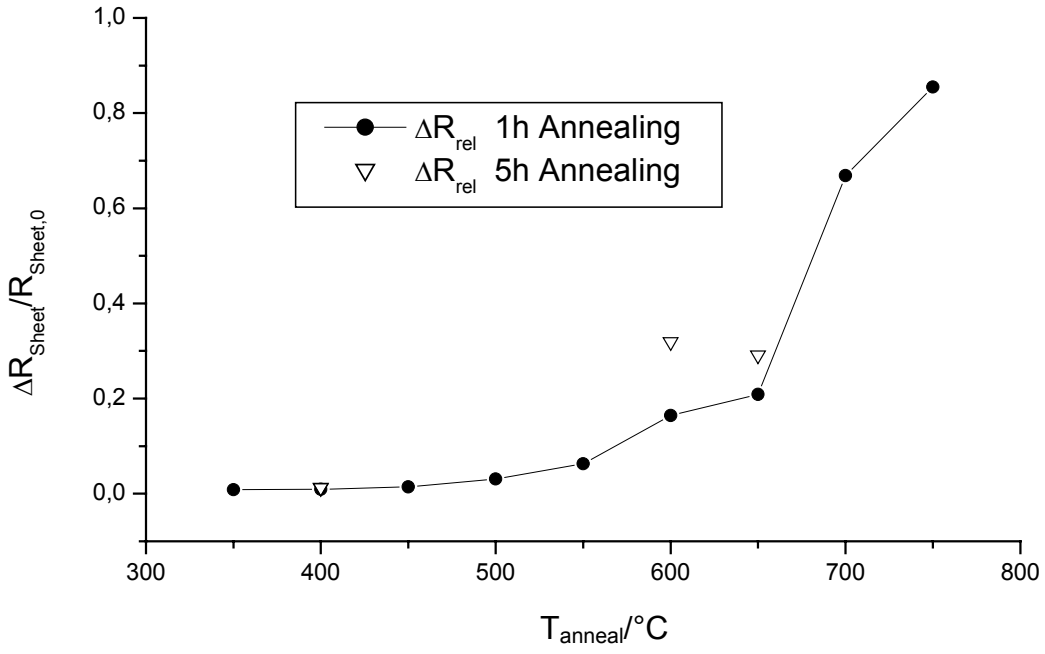

Fig. 6.4: Effect of annealing in N_2 atmosphere on sheet resistance of HfB_2 thin films (200 nm thickness)

The values obtained for 1h of annealing can be considered sufficient to justify assuming a stabilized sheet resistance up to temperatures of 450 °C, since no variation in the sheet resistance can be found between the 5 h annealing and the 1 h annealing process at 400 °C. Furthermore, usually has a much stronger impact on the underlying diffusion processes leading to change of resistivity, than time.

For the high voltage version, the SiO_2 passivation layer on top of the SiC is opened using buffered HF at 30 °C in the square heater region. A high temperature ion implantation is performed at 800 °C (dosis: $1 \cdot 10^{15}$ At/cm^{-2} , 80 keV), followed by 30 min annealing at 1100 °C in N_2 for electrical activation. A sheet resistance value of about 5 kΩ/□ is expected [6.2] and achieved (chapter 7).

6.3 Passivation

As described in the sensor concept, an insulation layer is required between heater and sensor electrodes. A 500 nm PECVD Si_3N_4 layer is deposited on top of the heater to serve as electrical insulation between heater and IDE and as passivation of the HfB_2 - layer. The Si_3N_4 has a ten times higher thermal conductivity than SiO_2 (20 Wm^{-1} K^{-1} compared to 1.4-2 Wm^{-1}K^{-1}), thereby serving as a better heat spreader underneath the IDE giving better temperature uniformity across the heater. Additionally, the higher dry etch rate of the nitride compared to the oxide facilitates easy structuring of the passivation with good etch stop on the SiO_2. RIE using an SF_6 - plasma is used to pattern the passivation layer.

6.4 Contact metallisation and electrodes

The contact metallisation system is compatible for both heater versions. It consists of a contact and diffusion barrier layer and the actual current conducting metallisation.

A 200 nm thick TiWN layer serves as contact layer and diffusion barrier between the heater and the Au-top layer. This type of layer was chosen, because this metal layer combination was the only low resistance metallisation technologically available and successfully tested at TU Berlin for temperatures of up to 650 °C [6.6].

The TiWN acts as a “stuffed” barrier where the nitrogen atoms prevent the gold from migrating through the contact layer [6.3, 6.4] as it would in a simple TiW layer. The TiWN provides an ohmic contact to the SiC in the case of the high voltage heater version. A 200 nm thick Au-layer is deposited on top of the TiWN to serve as contact to the heater and IDE electrode structure. TiWN / Au has been successfully tested as high temperature metallisation system [6.5, 6.6].

The Au-bondpads are electroplated to 1 μm thickness. The Au and the TiWN layers are successively patterned using a KJ:J_2 (potassium iodide) solution at room temperature for the Au and H_2O_2 at 45 °C for the TiWN layer. Fig. 6.5 shows the fabricated device prior to KOH etching.

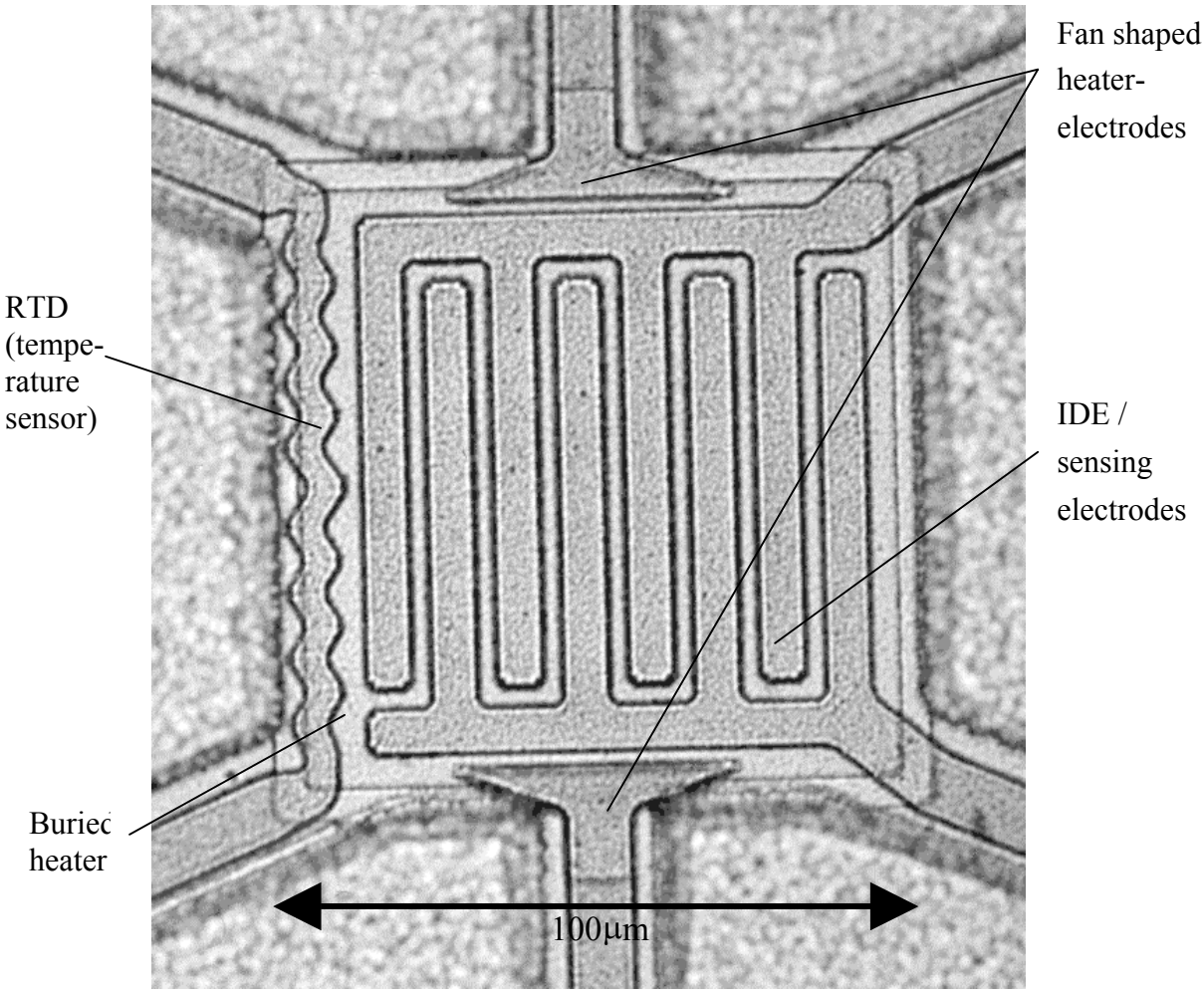

Fig.6.5: Photograph of the fabricated single micro hotplate prior to KOH etching

6.5 Secondary passivation

To protect the Au leads from aggressive ambient conditions an additional 500 nm thick PECVD Si_3N_4 layer is placed on top of the TiWN/Au metal layer. This secondary passivation is opened using RIE above the bond pad contact windows and the IDE (to allow contacting of the gas sensitive layers).

6.6 Anisotropic etching

For anisotropic etching, a glass plate is glued with wax onto the front side of the wafer to protect the wafer front side during etching. 33% KOH at 80 °C saturated with IPA (isopropyl alcohol) is used to etch the wafer. The IPA reduces convex corner undercutting, which is of vital importance to the chip shape. The SiC-membrane on the front side of the wafer serves as etch-stop for the KOH. The SiC on the backside serves as etch mask. The waxed glass plate is removed in Trichloroethylene (TCE) at 60 °C. Since the backside etch mask includes V-grooves along the sides of the chips, the wafer can be diced by breaking, releasing the complete sensors (Fig. 6.6, Fig. 6.7).

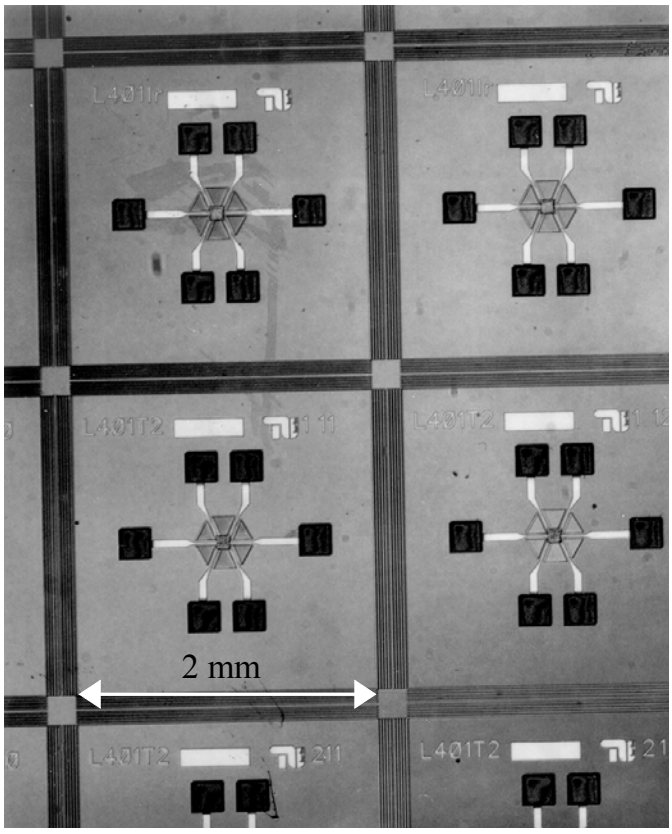

Fig. 6.6: Photograph of fabricated single micro hotplates before dicing.

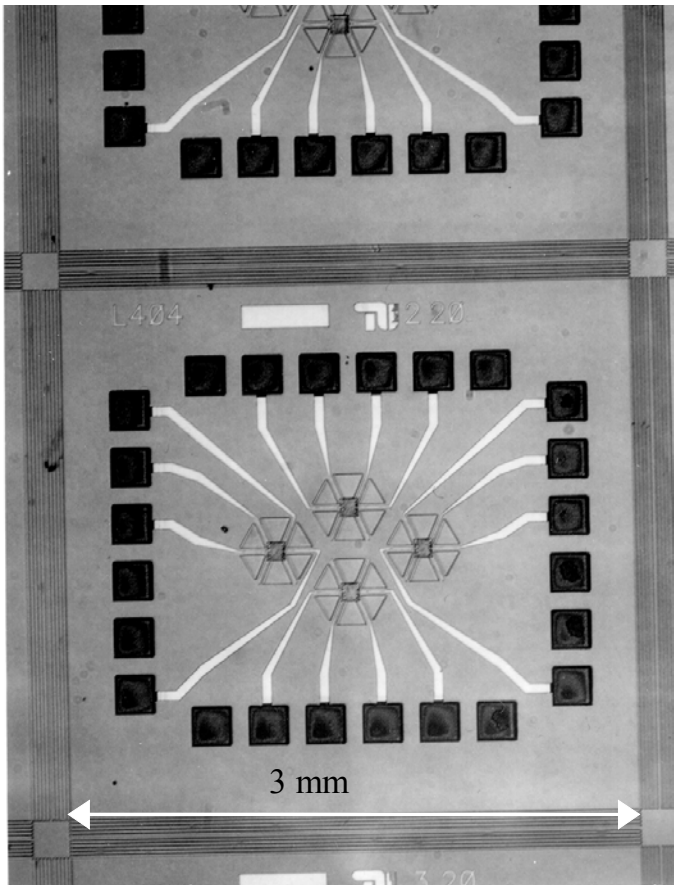

Fig. 6.7: Photograph of fabricated micro hotplate arrays before dicing.

6.7 Gas sensitive layers

Various NiO, MoO_3 and In_2O_3 layers have been tested as gas sensitive layers [6.7-6.10]. They are deposited using reactive RF-magnetron sputtering. Detailed process descriptions are given in appendix E. A shadow mask is used to protect the bondpads from contamination with the metal oxide layers during sputtering. The modular processing blocks of the device process design makes it possible to produce the shadow mask using the existing lithography masks for the structuring of the front and the back side SiC layer. By using wafers with 390 µm thickness, 500 nm SiO_2 and a 200 nm LPCVD Si_3N_4 layer instead of the SiC layer, the membrane breaks after KOH etching upon releasing. This leaves a chip identical in shape with a square hole where in the SiC device the diaphragm is situated. Placing this upside-down on top of the actual sensor gives a perfectly matched shadow mask (Fig. 6.8).

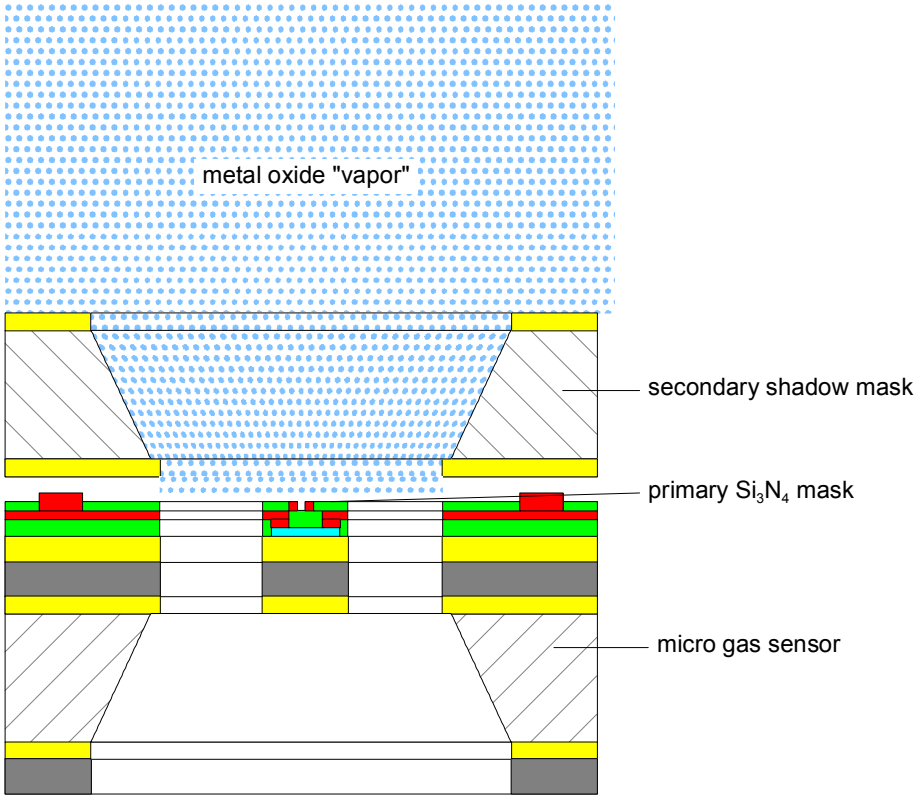

Fig. 6.8: Integrated and shadow mask during sputter deposition of gas sensitive metal oxide thin films onto the IDE

Using the secondary passivation together with the shadow mask allows alignment of the gas sensitive layer considering the IDE-dimensions of only 80 µm x 70 µm. This procedure however only allows the deposition of one type of gas sensitive layer per chip. In the case of the array chips this means that all hotplates in one chip will be covered with the same layer. I.e. in this case additional information can only be gained by modifying the operating temperature of the individual hotplates of one chip. Alternatively a delicate metal sheet shadow mask may be manufactured by laser cutting, allowing shielding of individual hotplates in one array.

Since the deposition of gas sensitive layers on array-type micro hotplate structures is extremely challenging, micro-CVD of these layers is the only viable alternative to cover individual arrays. In micro-CVD, a micro hotplate is heated and placed in a gas ambient containing the precursor gases for specific gas

sensitive CVD layers. At the required reaction temperature (which is only reached on top of the hotplate), the precursors react and deposit as gas sensitive layer. I.e this is an auto-aligning or self-lithographic process. The US National Institute of Standards and Technology NIST has taken the lead in demonstrating the viability of micro-CVD on micro hotplates.

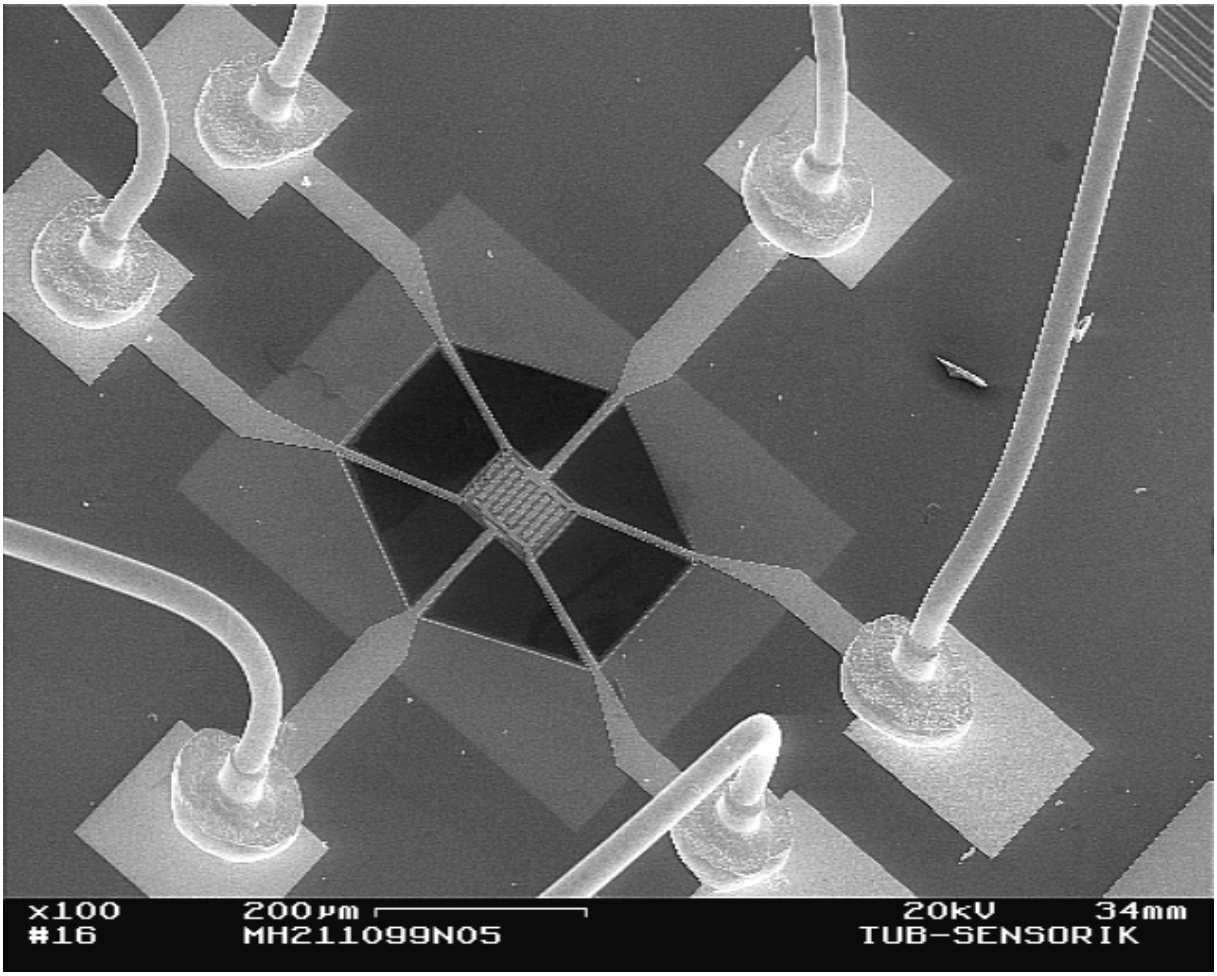

Fig. 6.9: SEM picture of a fabricated single hotplate micro gas sensor (10 µm bridge width) with Au-wire bonds

6.8 Discussion

The technological realisation of the devices uses standard Si-semiconductor processing technology wherever possible. HfB_2-thin film layers were produced using reactive RF-magnetron sputtering. At temperatures above 500 °C a

continuous increase of the sheet resistance followed by deterioration and destruction of the layer can be observed (chapter 6.2) . The HfB_2 layer is used for the fabrication of the low supply voltage heater resistor (about 10 Ω).

The surprisingly low maximum operating temperature of the HfB_2 layer allows fulfilment of the device requirements, but at this stage doesn't expand the limits of existing metal heater layers. At this stage already, limitations of the low voltage version of the device can be expected, due to the fact that the heater layer will start deteriorating above 500 °C.

Reasons can be found in the low chemical inertness of HfB_2. Suitable protective layers preventing oxidation processes at high temperatures will have to be found. For technological reasons, a Si_3N_4 passivation is used in the realisation of the device.

A high temperature N_2 – ion implantation was used to create the implanted heater resistor (about 5 kΩ) in the SiC-thin film for the high supply voltage heater version.

Si_3N_4 passivation layers electrically insulate the heater from the sensing electrode structure and passivate the substrate surface while assuring high thermal conductivity through the heater/IDE sandwich structure.

A TiWN/Au high temperature metallisation (200 nm TiWN / 200 nm Au) is chosen in both heater versions for the contacting of the heater and creation of the sensing electrodes. The reason for choosing a Au based layer is the required low resistance of the connecting leads to the heater in comparison to the heater resistance, which in the case of the HfB_2 heater is around 10 Ω. A high contact lead resistance would cause large electrical power losses and subsequent heating across the thinnest part of the leads which is on top of the supporting beams. This would inevitably result in heating of the beams (i.e. hot spots) with little power reaching the hotplate. Thus it would counteract the design effort towards low power consumption and high thermal insulation of the hotplate. Furthermore, significant experience had been gained at TU Berlin with

operating devices at high temperatures up to 650 °C using such a sandwich metal layer.

The TiWN layer acts as a stuffed diffusion barrier. The metallisation was characterized up to 650°C operating temperature. The electrodes are designed either as single electrode pair for low resistivity gas sensitive films or as IDE structure for high resistivity films.

Alternatively, six or four bondpads can be used when contacting the single device for operation, depending on whether the additional temperature sensor or the heater resistor is used for temperature control.

Essentially, at this stage already, an indication is given as to the strengths and weaknesses of the device design and material choice. As a typical failure mode, the metallisation system for the heater as well as the contact leads is limited in operating temperature, which will most likely be the failure cause for the whole device during testing.

The feasibility of the design, however, i.e. the mechanical properties of the substrate and membrane layers as well as the electrical properties of the heaters, contact leads and temperature sensors, the dimensions and geometry suggest that the required parameters for power consumption, thermo-mechanical stability, and resistance values will be on target for the finished device.

7. Characterisation of the electrical and thermal device properties

The characterisation of the electrical and thermal device properties is a necessary step to check the fulfilment of the sensor specifications, compile the data required for the device calibration and investigate the validity of the assumptions made when modelling the device. This chapter first of all includes the characterization of the integrated temperature sensor, which is used for the measurement and control of the device temperature. Secondly, the power consumption of the device as function of the heater temperature and micro hotplate geometry (micro bridges) is being determined. On the basis of this information, a comparison is made between the simulated and measured characteristics of the micro heater device.

In a further step the heater temperature and power consumption is measured as a function of ambient air pressure by placing the heater in a pressure controlled chamber. By analysing the pressure dependence of the heater temperature at constant power, the validity of the assumption of the negligibility of convection used in the model of the device can be confirmed. Based on these results, the thermal losses through the air thermal conductivity, pressure dependence of the air thermal conductivity and the thermal conductivity of the SiC beams (even as function of temperature) can be determined. It is thus possible, even to check the validity of the used thermal material data for the SiC film in the FEA-Simulation.

Thus, apart from just comparing the overall “result” of the simulated device power consumption and the measured, the correctness of the used analytical and simulation model can be proved.

Finally, the heater long term stability and maximum operating temperature under constant and pulsed mode operation is tested and failure modes are shown.

7.1 Resistance temperature coefficient (TCR) of heater and temperature sensor

The TCR of the heater and temperature sensor resistor was determined by two methods: firstly, using a four-point probe set up (Fig.7.1) with a heated vacuum chuck and a Pt100 reference resistor and secondly, by mounting them on a TO8 carrier and testing them in a temperature-controlled oven.

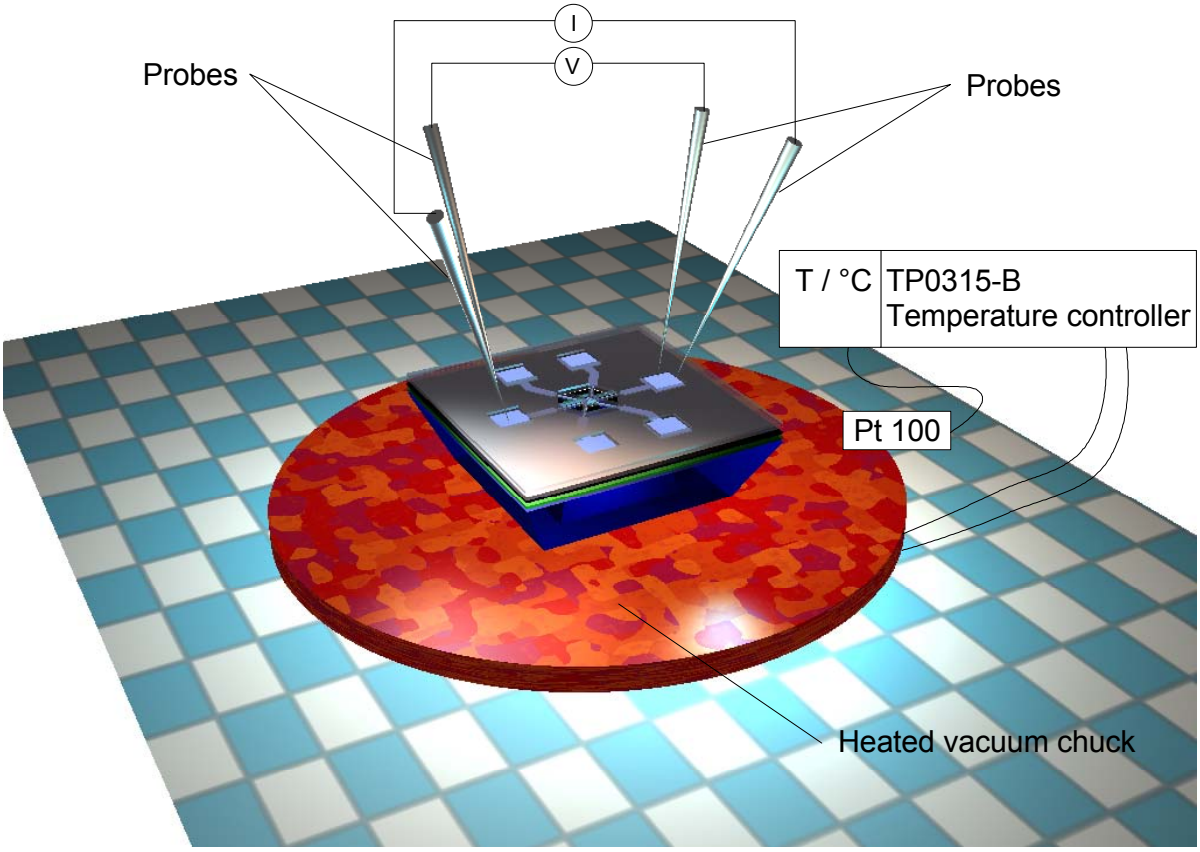

Fig. 7.1: Schematic four-point probe set-up for the calibration of the RTD- and Heater-TCR

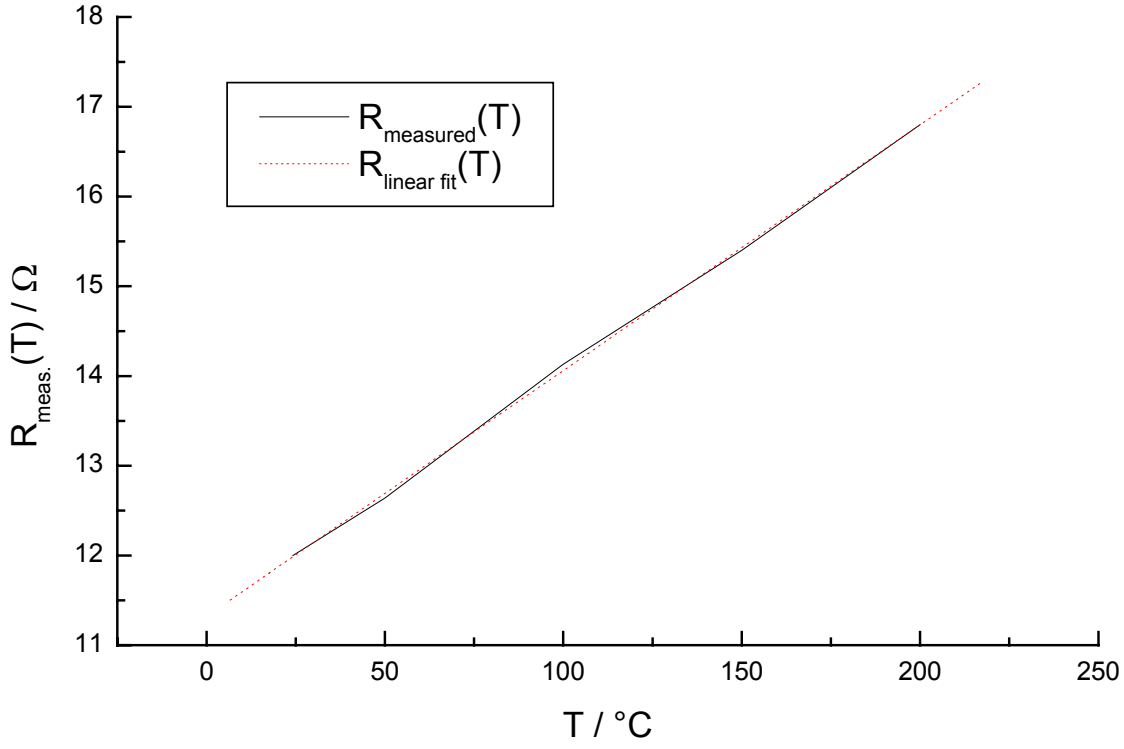

Fig. 7.2: Resistance of the temperature sensor as function of temperature compared to linear fit

As expected, we obtain a linear behaviour of the resistance as function of temperature of the metallic resistors.

Using: $R = R_{20} (1 + \alpha (\upsilon - 20\ °C)$, υ - temperature/°C (7.1)

We obtain:

$R_{20} = 9 \pm 0.78\ \Omega$ (7.2)

$\alpha_{therm} = 3.6 \times 10^{-3}\ K^{-1}$ (7.3)

for the temperature sensor and

$R_{20} = 19 \pm 1\ \Omega$ (7.4)

$\alpha_{heater,\ HfB2} = 0.96 \times 10^{-3}\ K^{-1}$ (7.5)

for the HfB_2 heater.

Both methods to determine the TCR are limited in the temperature range at about 200 °C due to the design of the hotplate and temperature oven. The high accuracy of the temperature control in combination with the excellent linearity of the temperature sensor in the measured range justified use of the obtained calibration values for the later determination and control of the heater temperature using the integrated temperature sensor. Furthermore, the functionality of the the temperature sensor was tested in a high temperature furnace up to 500 °C without measuring additional calibration curves.

For the Au temperature sensor, the contact lead resistance is similar to the actual sensor resistance. This was accounted for by determining the lead resistance by calculation from the geometrical dimensions and material properties. Furthermore, test structures were used to experimentally determine the actual material specific resistance values. During calibration in the furnace, obviously the complete structure is heated. I.e. we obtain a significant influence on the Au temperature sensor change in resistance due to the change of the lead resistance. Since both have the same material properties, the determined TCR can be taken as identical while the actual temperature sensor resistance is taken as measured value minus the lead resistance.

Based on the design of the heater and the material values for HfB_2 and Au (chapter 3.2) we would expect a resistance value of about 13 Ω (without contact resistance) for the HfB_2 heater. The remaining 6 Ohms difference between the theoretically expected and the measured value of 19 Ω could be accounted for by the contact resistance. The Au resistance temperature sensor is expected to have about 8.8 Ω resistance. The measured 9 Ω resistance are very close to this value.

Knowing the HfB_2-TCR, one can choose between operating the micro gas sensor using four contacts (IDE and heater) by measuring the heater temperature using the heater resistance itself or six contacts (IDE, heater and temperature

sensor) when using the additional temperature sensor. Furthermore, one can easily cross-check ones' results by comparing the temperatures obtained using the heater resistance or the additional temperature sensor. During the characterization of the micro hotplate heater performance, both, the heater resistance TCR as well as the additional temperature sensor were used.

An additional calibration curve was recorded for the SiC-heater resistance (Fig. 7.3). Since the SiC resistance doesn't exhibit a linear characteristic with change in temperature, no linear TCR can be given.

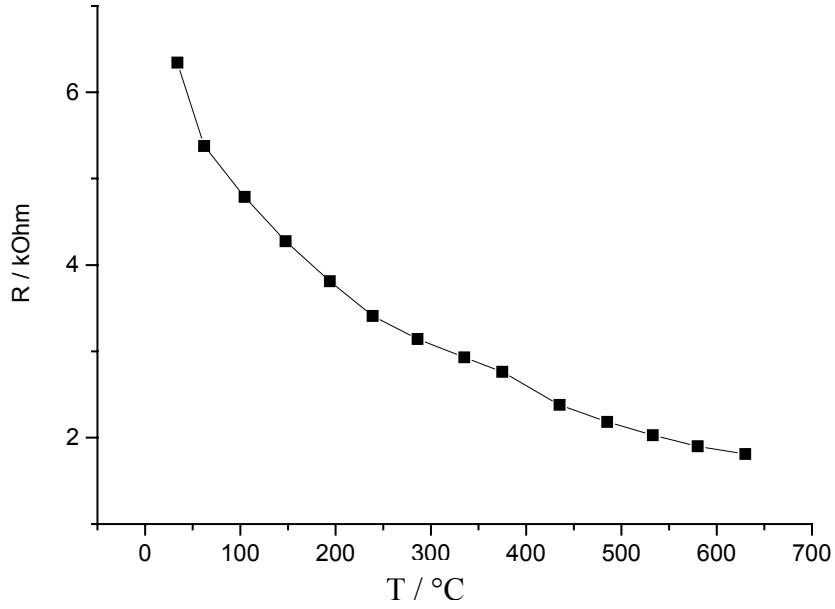

Fig. 7.3: Calibration curve R(T/°C) for SiC-heater

The calibration curve for the SiC-heater can be modelled in two ways, either by using a polynomial regression with:

$$R(T) = A + B_1 \cdot X + B_2 \cdot X^2 \quad (7.6)$$

$$A = (6.382 \pm 0.159)\ k\Omega \quad (7.7)$$

$$B_1 = (-0.0148 \pm 0.0011)\ k\Omega/K \quad (7.8)$$

$$B_2 = (1.2343 \cdot 10^{-5} \pm 0.1717 \cdot 10^{-5})\ k\Omega/K^2 \quad (7.9)$$

Or by using an NTC-approach with:

$$R(T) = R_{25°C} \cdot \exp\left(B \cdot \left(\frac{1}{T} - \frac{1}{298\,K} \right) \right) \tag{7.10}$$

$$B = (480 \pm 15)\ K. \tag{7.11}$$

The square shape of the SiC heater allows approximating the sheet resistance as being the actual heater resistance value. The resulting sheet resistance value of 6.38 kΩ/□ (room temperature) is close enough to the expected 5-6 kΩ/□ ([6.2], chapter 6.2).

7.2 Heater power consumption and maximum operating temperature

A constant current (1 mA-60 mA) source at voltages of up to 1.5 V (low voltage version) or alternatively 12 V (high voltage version) is used to operate the heater. The heater temperature was determined using the integrated temperature sensor and the heater resistance for mutual checking. The slight temperature drop at the edge of the membrane where the temperature sensor is situated (chapter 5) was accounted for. The power consumption varies with micro bridge width as expected (Fig. 7.4).

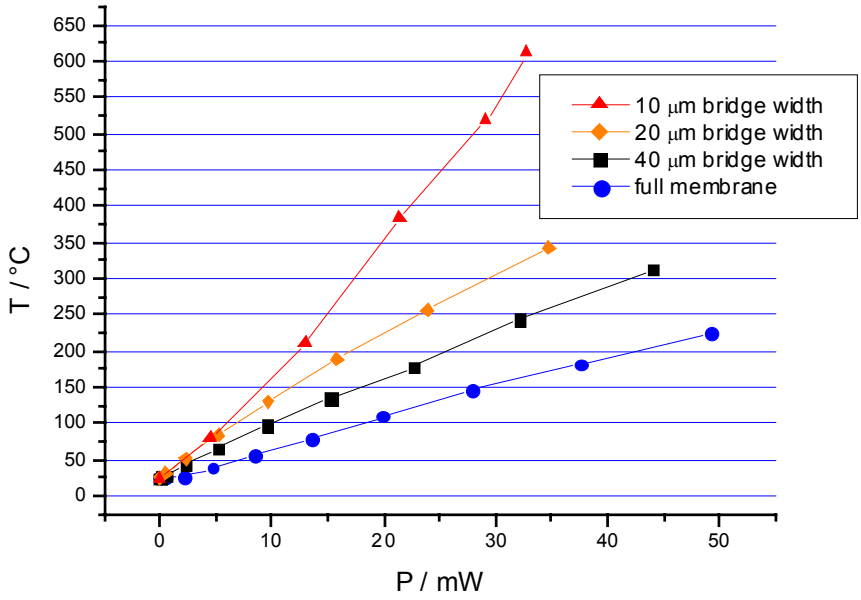

Fig. 7.4: Power consumption of micro hotplates with bridge widths of 10 µm, 20 µm, 40 µm; heater efficiencies are at: 19 K/mW, 10 K/mW, 7 K/mW, (4,5 K/mW)

Temperatures of up to 350 °C could be achieved using 35 mW of heater power using the 20 µm bridge width HfB_2 heater. At higher temperatures, deterioration of the HfB_2 heater sets in, possibly due to the high current densities. The 10 µm bridge width SiC heater version can be operated up to 650°C. At 650 °C a massive deterioration of the TiWN/Au metallisation sets in. Tests without Au-IDE proved that the heater could be operated well above 800 °C (Fig. 7.5) for several hours in air, while glowing like a light bulb. The IDE metallisation layer, however, fails as expected above 650 °C. The reason for the heater contacts, which also consist of Au/TiWN sustaining these high temperatures can be explained by the fact, that the temperature at the side of the hotplate next to the micro bridge (heat sink) is lower than at the center. Also, the design of the contact area allows some overlap of the heater and contact leading a few 10 µm onto the bridge, such that a sufficient contact area at sufficiently low temperatures (< 650 °C) exists. The key to the achievement of higher temperatures lies in new high temperature metallisation systems (e.g. Ti/TiN/Pt).

Discussion

As expected in chapter 6, the HfB_2 as well as the Au/TiWN metallisation prove to be the weak point in the device design. The technical specifications required are achieved, but the potential to break the limits of current metallisation layers is unfortunately not used.

The HfB_2 has a very high specific resistance as expected and thus allows the design of a very small square metal thin film heater with sufficiently high resistance to allow low power battery operation. Furthermore, its high resistance value allows the use of narrow and long contact leads and supporting beams of the hotplate, which lead to high thermal insulation of the hotplate and low power losses to the substrate. The values achieved lay perfectly within the designed limits. The high temperature performance of the layer is however poor compared to the expectations. As discussed in chapter 6, the low chemical stability of the HfB_2 requires a good passivation layer. Additional TaN layers [6.2] have shown to protect the HfB_2 from oxidation processes and could be an option for an improved re-design.

Pt layers could be an alternative to HfB_2, although this would require a modification of the heater geometry towards a meander shape, due to the much lower resistance value of the Pt compared to the HfB_2. A further drawback of the Pt thin film is the high effort needed for structuring of the Pt, which at TU Berlin could only be done using long time sputter etching (Pt layer sputtering was not available at TU Berlin).

State of the art Pt-based thick film devices can operate up to 900 °C. No thin film devices with comparable maximum operating temperature are however presented in literature.

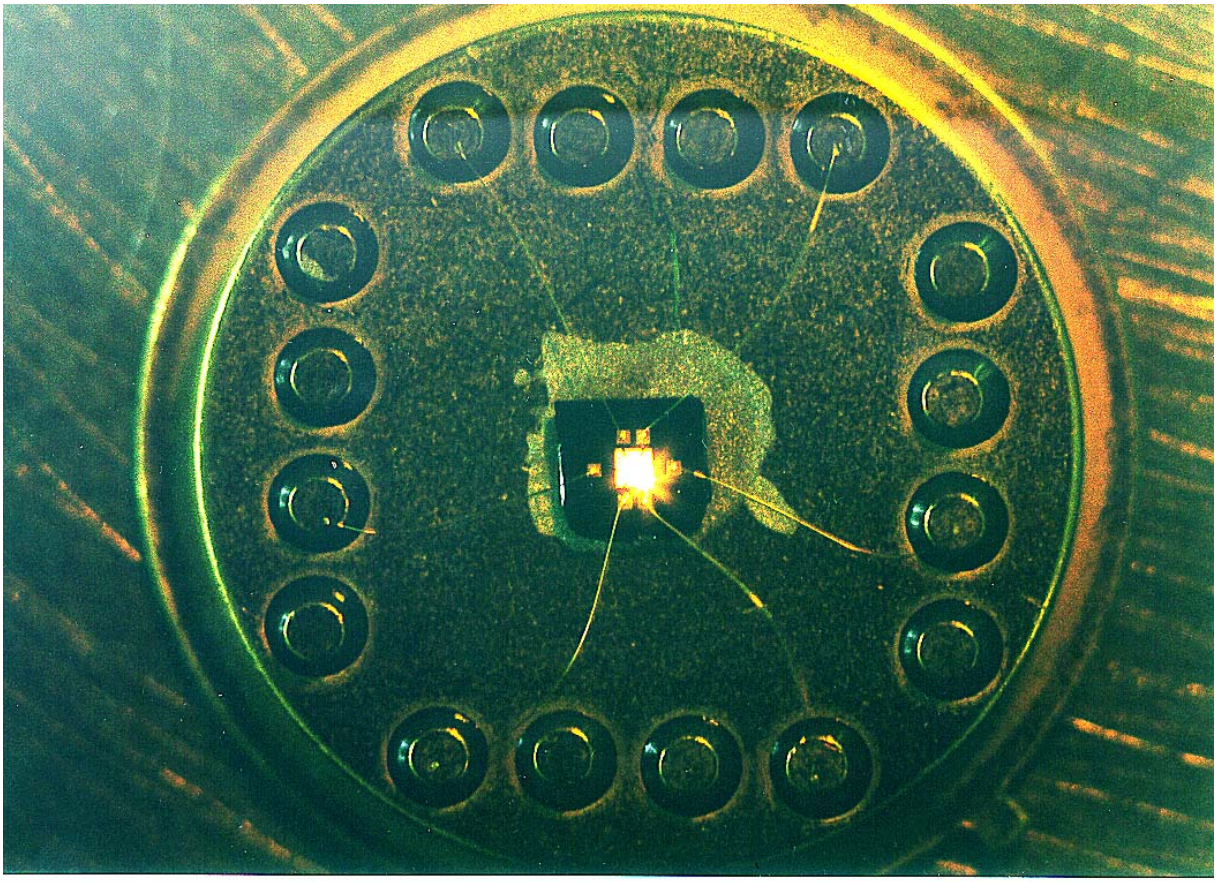

Fig. 7.5: Micro hotplate operated white glowing in air (>800 °C)

The SiC heater has the potential to work beyond 800 °C and thus to break the limits of Pt and other currently used micro hotplate heaters in thin film technology on Si substrates. Its high sheet resistance value of around 5 kΩ/□ doesn't allow for battery operation in handheld detectors, but allows operation with power grid or automotive batteries available. This heater is limited only by the temperature limits of the IDE made from the Au/TiWN layer. Usage of an alternative Pt IDE structure might enhance the limitation at 650 °C given by the Au/TiWN.

Thus, a significant improvement of the device performance, which uses more of the potential inherent in the design and material choice could be expected, when:

- Employing additional TaN protective layers for the HfB_2 heater. A thorough analysis of the HfB_2 thin film characteristics in high temperature environments will be necessary.

- Trying a meander type Pt thin film heater (despite the technology challenge this imposes) for the low voltage version of the heater, instead of the square HfB_2 heater
- Replacing the Au/TiWN IDE by a Pt IDE in order to push the limit of the high voltage SiC heater hotplate version beyond 650 °C
- Using a contact implantation rather than a direct contact of the metal to the heater for operation at temperatures beyond 800 °C. The resulting temperature gradient reduces the temperatures at the metal semiconductor contact.

7.3 Comparison of simulated and actual heater temperature

In order to check the validity of the assumptions made when modelling the device theoretically and when simulating it, the actual results and the simulations were compared. Simulations and measurements are in good agreement (Fig. 7.6, Fig. 7.7). The slight difference can be accounted for mainly by the large variation in thermal conductivity data of the SiC as used in the FEA. The actual data obtained by measurement can give a feedback on the accuracy of the thermal conductivity. A more detailed investigation of this phenomenon is given in chapter 7.5.

For simplicity, not all heater and micro bridge versions are compared here. A SiC heater version with 10 μm bridge width and an HfB2 heater version with 20 μm bridge width are selected for comparison.

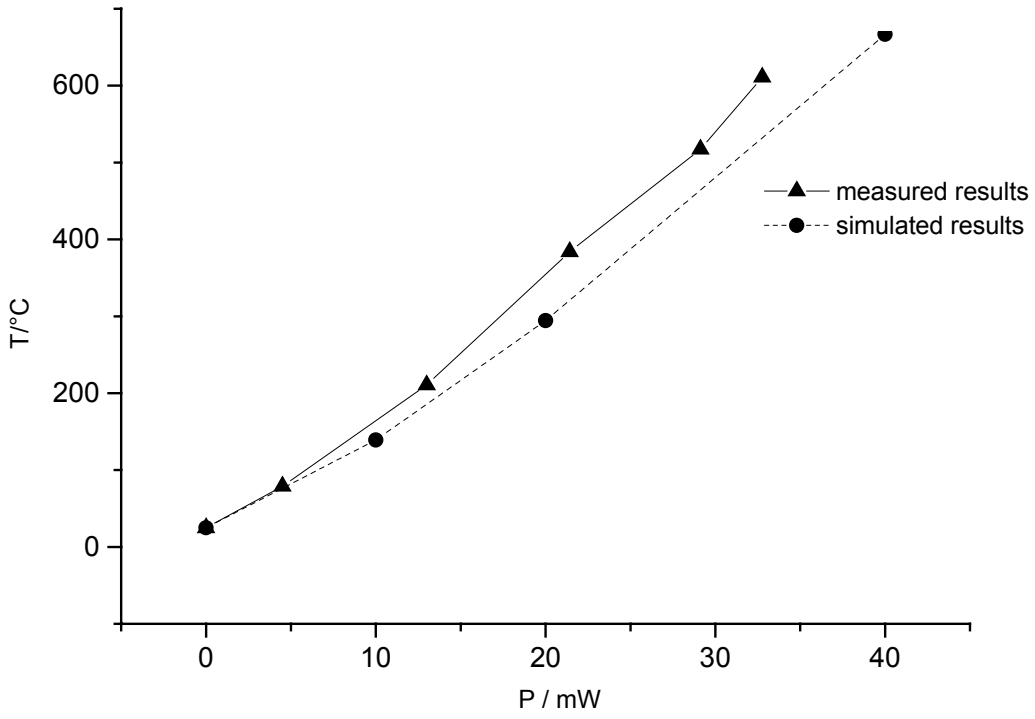

Fig.7.6: Heater temperature as function of heater power for SiC-based heater with 10 μm bridge width, heater efficiency: 16,5 K/mW (FEM), 19 K/mW (measured)

Both, the SiC version and the HfB_2 version behave almost exactly as simulated, indicating the accuracy of the used model and material properties. At lower temperatures a higher absolute accuracy can be expected due to the fact that the heater temperature at zero power consumption is governed by the ambient air temperature just like in the simulation. With growing temperature a slight difference between simulated and actual results of the same order of magnitude occurs both in the SiC and the HfB_2 version. No significant trend towards a growing or decreasing of this error could be observed.

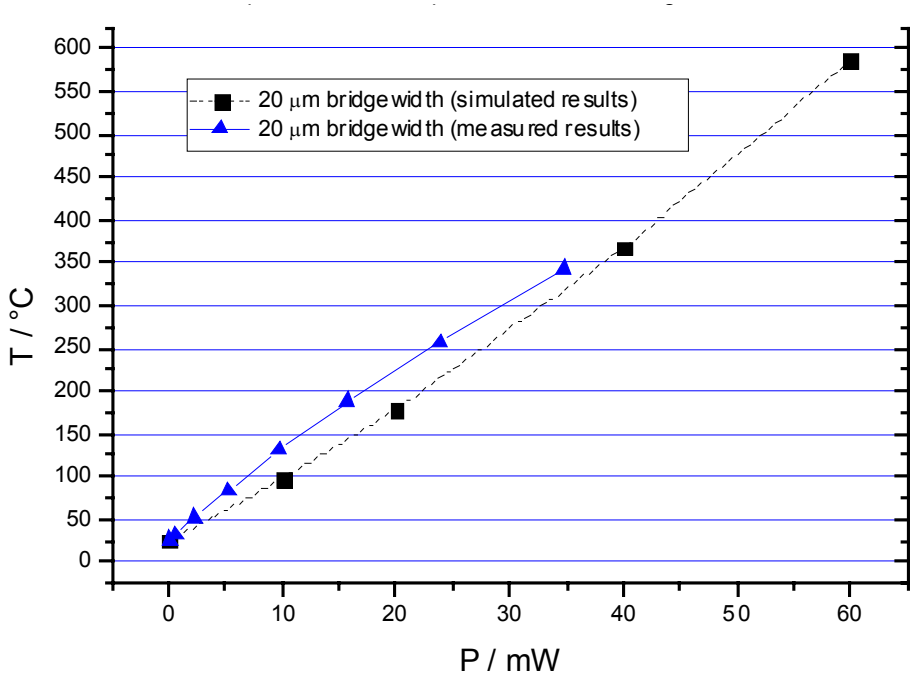

Fig.7.7: Comparison of simulated and measured heater power for low voltage heater version; heater efficiency: 10 K/mW (FEM), 10 K/mW (measured)

In both cases (SiC and HfB_2) these variations can be explained by geometrical variations in the bridge width. These are due to underetching, which results in narrower bridges and thus higher thermal resistance and lower power losses. Hence, the actual bridges are narrower than the simulated ones resulting in reduced power losses compared to the simulation.

7.4 Validity of the theoretical model: ambient air pressure dependence of heater temperature and SiC and thermal conductivity

In order to check the influence of convection and conduction through the ambient air, the heater was operated in a vacuum chamber (Fig.7.8).

The device was assembled on an NGK DIP22 carrier and put in a cryostat allowing the evacuation, cooling and heating (-180 °C – +450 °C) of the device environment. The micro heater was operated using a constant current source (i.e. approximately at constant heater power). The temperature was measured using

the integrated temperature sensor. The actual pressure could be measured using an Ionovac^{TM} detector.

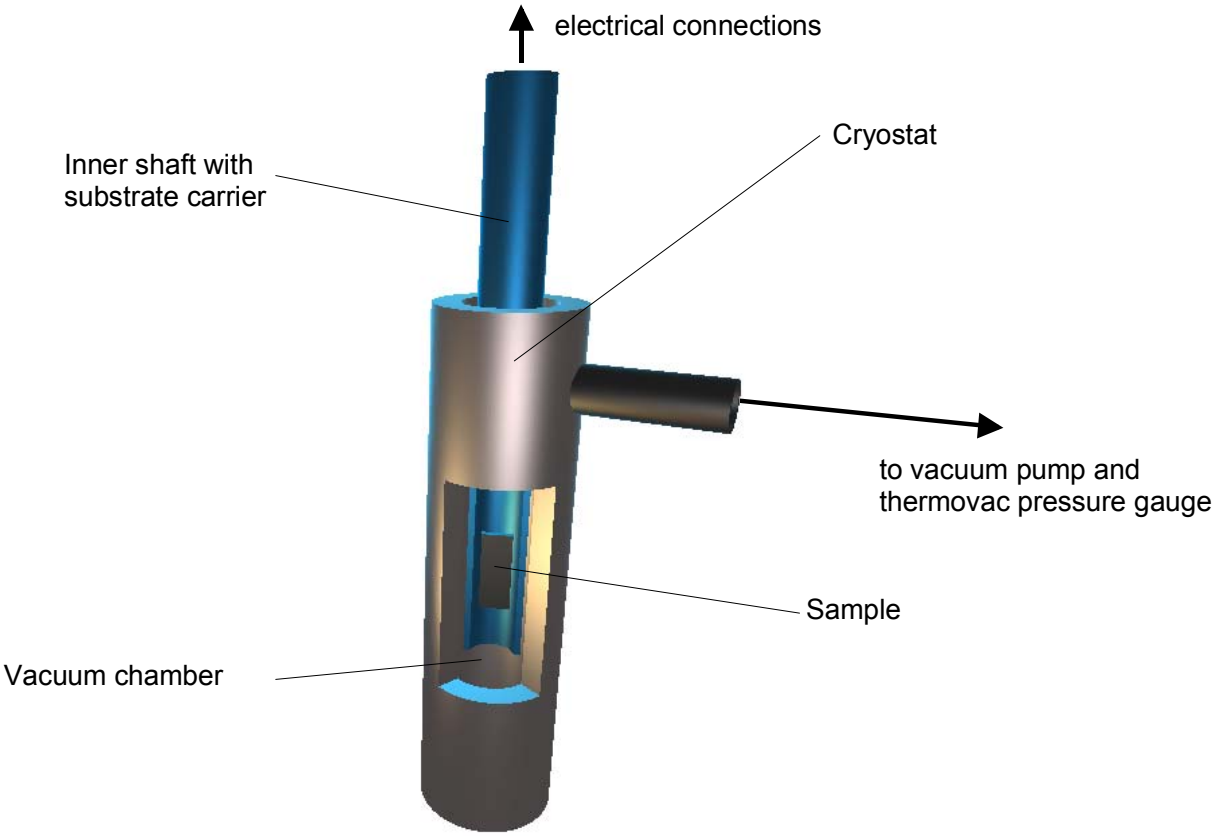

Fig. 7.8: Device operation in cryostat vacuum chamber (schematic view with open chamber for clear sight onto the sample)

The data obtained suggest two plateau-phases between 100 mbar and 1000mbar as well as below 0.1 mbar connected by a fairly linear transition (Fig.7.9). If there was significant convection, one would expect an increase in Temperature with decrease in pressure starting right below 1000 mbar. This effect clearly does not take place. Recalling that according to the analytical model only about 7.5 % of the power losses are expected to come from static convection (5.1.2), the measurements appear to confirm this assumption. At lower pressures (<10 mbar), a linear increase of the temperature with pressure is expected [5.4]. At 1 mbar …10^{-3} mbar (Knudsen-gas), the mean free path is getting larger than the container dimensions. The collisions of the molecules with the container

walls exceed the collisions in between the particles and produce the equilibrium condition described in kinetic gas theory. A saturation effect, i.e. a new plateau is thus expected.

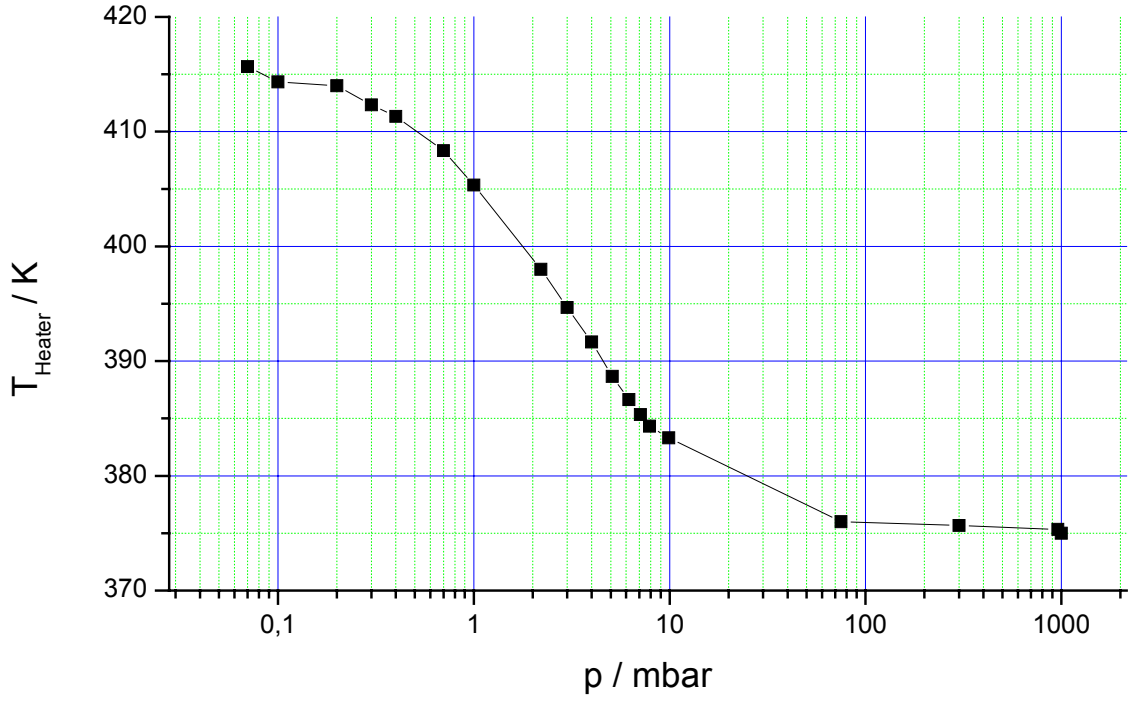

Fig. 7.9: Heater temperature as function of ambient pressure (8mW constant power consumption)

This experiment clearly gives sufficient grounds to the assumption that convection can be neglected when modelling the micro heater. Otherwise a temperature rise with decreasing pressure would be expected right below 1 bar, since a decrease in ambient pressure immediately affects convection.

In order to determine the air thermal conductivity, we first have to evaluate the thermal conductivity of the SiC micro bridges.

Thermal conductivity of supporting SiC micro bridges

As mentioned before, using a simple model, the thermal conductivity of the SiC micro bridges can be determined based on the pressure dependant heater temperature. Looking at the micro heater more closely, it can be easily used as a micro Pirani-vacuum gauge [7.1].

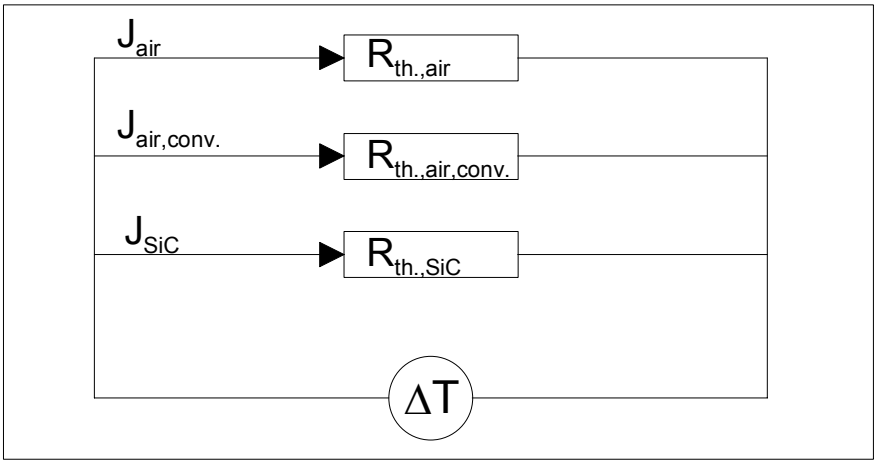

Fig. 7.10: Network of thermal resistors as simple model for thermal heater behaviour (losses through air thermal conductivity, air convection and SiC thermal conduction)

From chapter 7.4 we could see that when evacuated, convection plays an insignificant role in the heater thermal behaviour. $R_{th.,air,conv.}$, the equivalent thermal resistance of the heat loss through convection, can thus be neglected. When operating the heater in vacuum (< 0.1 mbar), it is justifiable to simplify the model network further by just considering the thermal resistance of the SiC micro bridges (i.e. losses through air thermal conduction and convection are eliminated and all losses result from the supporting SiC bridges).
The total heater power consumption thus amounts to:

$$P(T) = -k(T)A\frac{dT}{dx} \qquad (7.12)$$

Theoretically, the thermal conductivity as function of temperature follows an exponential decay ($k \sim e^{To/T}$), which is quickly replaced by a slow power law behaviour ($k \sim T^{-x}$, $1<x<2$) at higher temperatures ($T>\Theta_D$) [5.4]. The measurements of the SiC thermal conductivity presented in chapter 3 exhibit a linear behaviour with a slight parabolic term, representing the second order approximation (Taylor expansion) of the thermal conductivity behaviour.

Recalling the bandwidth (upper and lower margin) given for the temperature dependant thermal conductivity data in chapter 3 yields the following expressions for the thermal conductivity upper and lower limit, as well as its mean value as function of temperature (Tab. 5.3, Fig.5.5):

Upper limit:

$$K(T) = 344.3\frac{W}{mK} - 0.2\frac{W}{mK^2}T - 1.1\,10^{-4}\frac{W}{mK^3}T^2 \qquad (7.13)$$

Mean value:

$$K(T) = 302.5\frac{W}{mK} - 0.195\frac{W}{mK^2}T - 16.7\,10^{-5}\frac{W}{mK^3}T^2 \qquad (7.14)$$

Lower limit:

$$K(T) = 278.35\frac{W}{mK} - 0.23\frac{W}{mK^2}T - 7.36\,10^{-6}\frac{W}{mK^3}T^2 \qquad (7.15)$$

The magnitude of the parabolic term compared to the linear term justifies the modelling of the thermal conductivity with a linear expression of the type:

$$K(T) = K_0 + aT \qquad (7.16)$$

Using (7.12) we obtain

$$P(T) = \left(K_0 + aT\right)A\frac{dT}{dx} \qquad (7.17)$$

Using the device dimensions (micro bridge length dx = 150 μm, bridge cross-sectional area A = 20 μm^2, dT = ($T-T_0$)) yields:

$$P(T) = \left(K_0 + aT\right)\frac{2}{15}10^{-6}m\left(T - T_0\right) \tag{7.18}$$

$$P(T) = \frac{2}{15}10^{-6}m\left[-aT^2 + \left(k_0 + aT_0\right)T - k_0T_0\right] \tag{7.19}$$

Using this equation the variables can be found in two ways: solving a linear system of equations (7.9) or fitting a linear function to the actual data of the heater temperatures during vacuum operation and comparing the coefficients of the model function (7.17) and the obtained data (7.22).
The linear system of equations written as Matrix yields:

$$\overline{P} = C\begin{bmatrix} T_1^2 & T_1^1 & T_1^0 \\ T_2^2 & T_2^1 & T_2^0 \\ T_3^2 & T_3^1 & T_3^0 \end{bmatrix} \cdot \begin{bmatrix} -a \\ k_0 + aT_0 \\ -k_0T_0 \end{bmatrix} \tag{7.20}$$

or $\mathbf{P} = C\ \mathbf{T}\ \underline{x}$, with $C = 2/15\ 10^{-6}$ m, (7.21)

which can be solved by inverting the **T**-matrix. T_0 is set at room temperature (298 K). The measurement of the actual heater temperature in vacuum and comparing coefficients using (7.19) leads us to a relation of:

$$P(T) = -0.0156\ W + 4.8\ 10^{-5}\ (W/K)\ T + 1.3\ 10^{-8}\ (W/K^2)\ T^2 \tag{7.22}$$

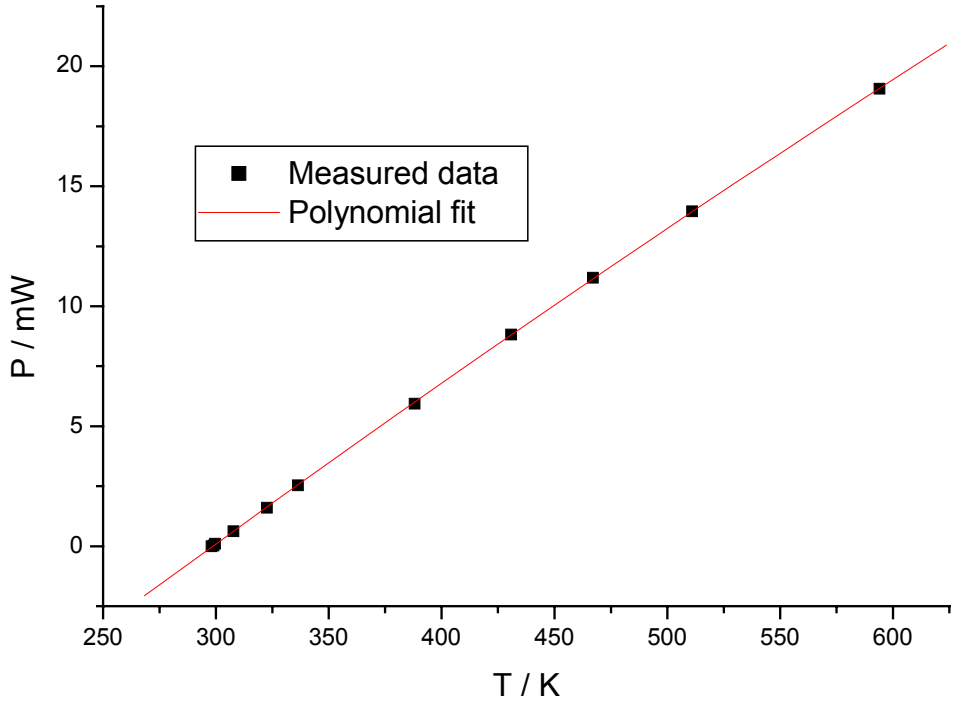

Fig. 7.11: Power consumption of heater in vacuum

Comparing the coefficients:

T^2: $2/15\ 10^{-6}$ [m] (-a) = $1.3\ 10^{-8}$ [W/K^2] (7.23)

T^1: $2/15\ 10^{-6}$ [m] (k_0+aT_0) = $4.8\ 10^{-5}$ [W/K] (7.24)

T^0: $2/15\ 10^{-6}$ [m] (-k_0T_0) = -0.0156 [W] (7.25)

leads to:

k_0 = 392 [K] (7.26)

a = -0.1 [W/mK] (7.27)

Hence we obtain:

k(T[K]) = 392 W/mK – 0.1 W/mK^2 T[K] (7.28)

Comparing these results with the data used in the simulation (7.13-7.15) a variation towards higher values of thermal conductivity can clearly be observed, which can be accounted for by a number of factors:

- Variation in micro bridge geometry. The width can vary by up to 10 % due to lithography flaws and Al-mask underetching. The SiC layer thickness varies by ± 20 % across the sample due to the deposition process. This can potentially result in more than 30% variation in bridge cross sectional area and consequently thermal resistance and losses in the micro bridge.
- Neglecting the Au-leads on top of the SiC in the model.
- Remaining power losses from insufficient vacuum, which were assumed to be zero in the model.

Considering the above stated effects and the fact that the device was never designed to be a test structure for the measurment of the SiC thermal conductivity, the results are close enough to justify the assumptions of the thermal conductivity of the SiC, made when modelling the device.

Pressure dependence of air thermal conductivity

Assuming that the change in heater temperature when evacuating the heater ambient can be accounted for simply by the lack in thermal conduction through the air, the pressure dependence of the air's thermal conductivity can be estimated.

Assuming only one type of particles with constant quantity per unit volume n and a constant temperature gradient along the x-axis, the thermal conductivity of air is given by [5.4]:

$$k_{air} = ½ \rho Cu(x_0)l, \qquad (7.28)$$

(with ρ being the mass density, $u(x_0)$ being the mean thermal velocity of the particles at x_0, C being the specific heat of the gas in J/K resulting from the thermal motion of the molecules).

k_{air} is independent of the number n of molecules per unit volume. This is clear, since ρC ~ n and from kinetic gas theory, the mean free path

$$l = \frac{1}{\sqrt{2} n \sigma_c} \tag{7.29}$$

(σ_c – effective cross sectional area of a gas atom),

and the product of n and l (as used in the above annotation) using (7.29) is:

$$l \cdot n = \frac{n}{\sqrt{2} n \sigma_c}. \tag{7.30}$$

Since k_{air} is proportional to ρ·C·l and ρ·C is proportional to n, k_{air} is proportional to l·n. Thus, using (7.30), k_{air} is independent of n. Obviously an increase in the number of particles n per unit volume increases the collision frequency between the particles, the increase in mean free path however reduces the efficiency of the collisions by the same amount. Only at very low pressures when the particle-wall collisions exceed the particle-particle collisions, we can expect an considerable change in air thermal conductivity [5.4].

Knowing the thermal conductivity of the SiC, we can now model the heater behaviour as being governed mainly by the conduction through the SiC micro bridges and the air. We thus obtain the following expression for the heater power consumption:

$$P(T,p) = -k_{SiC}(T) A \frac{dT}{dx} - 4\pi k_{air}(p) r_{heater} (T_r - T_R) \tag{7.31}$$

For further simplification, one can take into account the fact that the actual change in temperature observed when evacuating the chamber amounts to about 40 K. The medium thermal conductivity of the SiC (chapter 3.1) thus ranges

from 210 $Wm^{-1}K^{-1}$ to 220 $Wm^{-1}K^{-1}$,i.e. varying by about 10 $Wm^{-1}K^{-1}$ (≅4%) . A mean value of 215 $Wm^{-1}K^{-1}$ can be taken yielding an equation with temperature independent SiC thermal conductivity:

$$P(p)_{T\approx const.} = -\bar{k}_{SiC} A \frac{dT}{dx} - 4\pi k_{air}(p) r_{heater} (T_r - T_R) \tag{7.32}$$

solving for $k_{SiC}(p)$ ($T_R = T_0 = 298$ K):

$$k_{air}(p) = \frac{P(p) - \bar{k}_{SiC} A \frac{dT(p)}{dx}}{4\pi r (T_r(p) - T_R)} = \frac{P(p) - \bar{k}_{SiC} A \frac{1}{dx} (T(p) - T_0)}{4\pi r (T_r(p) - T_0)} \tag{7.33}$$

assuming P(p)=const. (constant heater power) (7.34)

$$k_{air}(p) = \frac{P}{4\pi r} \frac{1}{(T(p) - T_0)} - \frac{\bar{k}_{SiC} A \frac{1}{dx}}{4\pi r} \tag{7.35}$$

Recalling at the shape of the T(p)-curve (Fig. 7.9) and recalling the theoretical shape of the k(p)-curve (7.33) it is clear, that the function obtained from measuring the heater temperature as function of ambient air pressure leads to the right type of function for the air thermal conductivity as function of pressure.
A complete analytical solution is not given here, since the main objective was to prove the validity of the model.

Discussion

The theoretical model estimates the amount of power needed for heating of the device and assumes a temperature dependant SiC thermal conductivity as well as zero convection during pulsed operation and low convection during static operation of the device.

Evacuating the device leads to a heater behaviour showing no signs of decreasing convective power losses with decreasing pressure. I.e. convective losses must play an insignificant role. Further evacuating the device leads to a pressure dependant change in temperature due to the changing air thermal

conductivity (Pirani-effect). When the losses through air thermal conduction become smaller than the losses through radiation, further evacuation leads to no significant reduction in power losses and thus temperature rise.
Since in this model no relevant radiation losses can occur below heater temperatures of 1000 °C, which are never achieved, the only source for losses is through conduction through the supporting SiC micro bridges.
Thus by characterising the P(T) behaviour of the hotplate under vacuum, we can derive the SiC thermal conductivity as function of temperature. The values obtained are close enough to the ones used in the simulation, to justify assuming that not only convection doesn't play a significant role, but also, the estimated SiC thermal conductivity as function of temperature was right.
Finally, by using the SiC-thermal conductivity and the model used in Fig. 7.10 , we obtain the basic shape of the pressure dependence of the air thermal conductivity as the inverse to the measured curve of heater temperature over pressure. This coincides with the characteristics of the air thermal conductivity presented in literature. When looking at these characteristics the geometry of the device and "container" have to be considered.

Hence, not only does the actual behaviour of the micro hotplate coincide with the simulated one, which is not always the case when realising micro hotplate devices, but also the validity of the entire model is shown. Normally, the measured total power consumption is compared with the simulated one, without characterising the individual contributions from conduction, convection and radiation and it is then assumed that the model justly describes the actual device. This is the first time, a comprehensive model with individual contributions from air and substrate conduction, convection and radiation of a micro hotplate is presented and proven through characterisation.

7.5 Heater long term stability

Long term stability of the device is one of the key issues for all gas sensor devices, as previously stated (chapter 1.). The stability of the micro hotplate in terms of the mechanical and the electrical properties was investigated by operating the heater in continuous and pulsed mode in air.

Mechanically, the heater proved to be of excellent stability. Drop tests and heat pulses causing the heater membrane to move up and down by about 10 µm (rough estimate by measuring the focal plane of a microscope during heating pulses) could not destroy the membrane. The HfB_2 heater could be operated at 450°C (SiC heater: 650 °C) for up to two weeks in continuous operation mode before failure of the connecting Au/TiWN leads.

Considering the 1 ms time constant for the heater to reach its operating temperature and the time constants τ_{90} of between 10 s and 40 s [6.7,6.8,6.9] of the metal oxide layers to yield a signal when exposed to gas, a time of 1 min for one operating cycle of the gas sensor is feasible. The two weeks of operation thus would equal 20,160 cycles. If an area was tested every 10 min, this would give a lifetime of about half a year. The lifetime of an AA battery cell with 750 mAh at this operating temperature would be 25 h in continuous operation mode or 10.5 days when operated every 10 min.

The stability of the heater temperature during the two weeks of operation was investigated. The standard variation in heater temperature over this period of continuous operation at maximum operating temperature amounts to 0.64 % (Fig. 7.12, Table 7.1). A normalised scale was used in the analysis of the measured data (Fig. 7.12), since the achieved heater temperature varies between the experiments. A normalised scale allows easier comparison of the data. The initial temperature value upon switching was used for the normalisation of the temperature data.

Statistical evaluation shows that a slight drop can be observed from the initial heater temperature upon switching on of the device. This is manifested in a mean value of 99.8% of the normalised heater temperature lying slightly below the expected 100 %. The maximum temperature deviation amounts to about ± 0.53 %, which equals ± 3.325 K at 623 K (350 °C) operating temperature. The standard deviation of 0.36 % equals ±2.24 K at 623 K (350 °C) operating temperature.

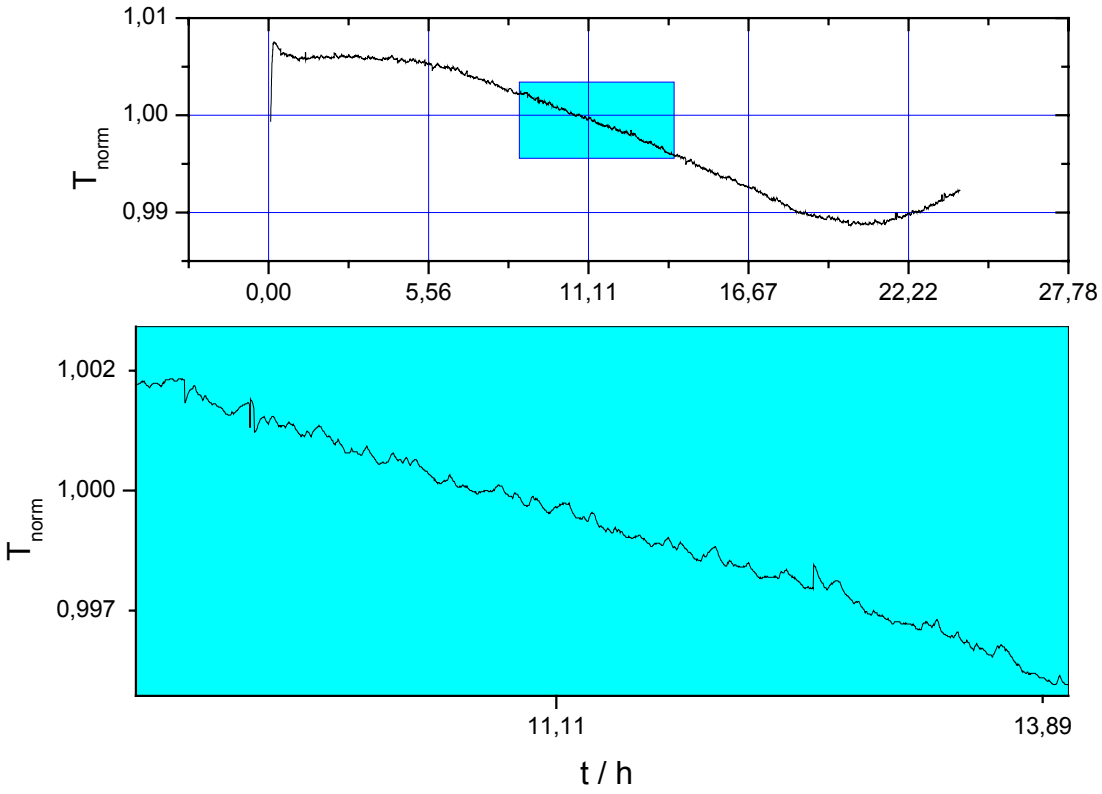

Fig. 7.12: Long term characteristic of normalised heater temperature (partial display of data: one day out of fourteen and magnified view)

Looking at the heater temperature characteristics over a weeks period, we can observe a 24 h cycle combined with a random long term drift (Fig. 7.13). This can easily be explained with the daily temperature cycles in the laboratory room.

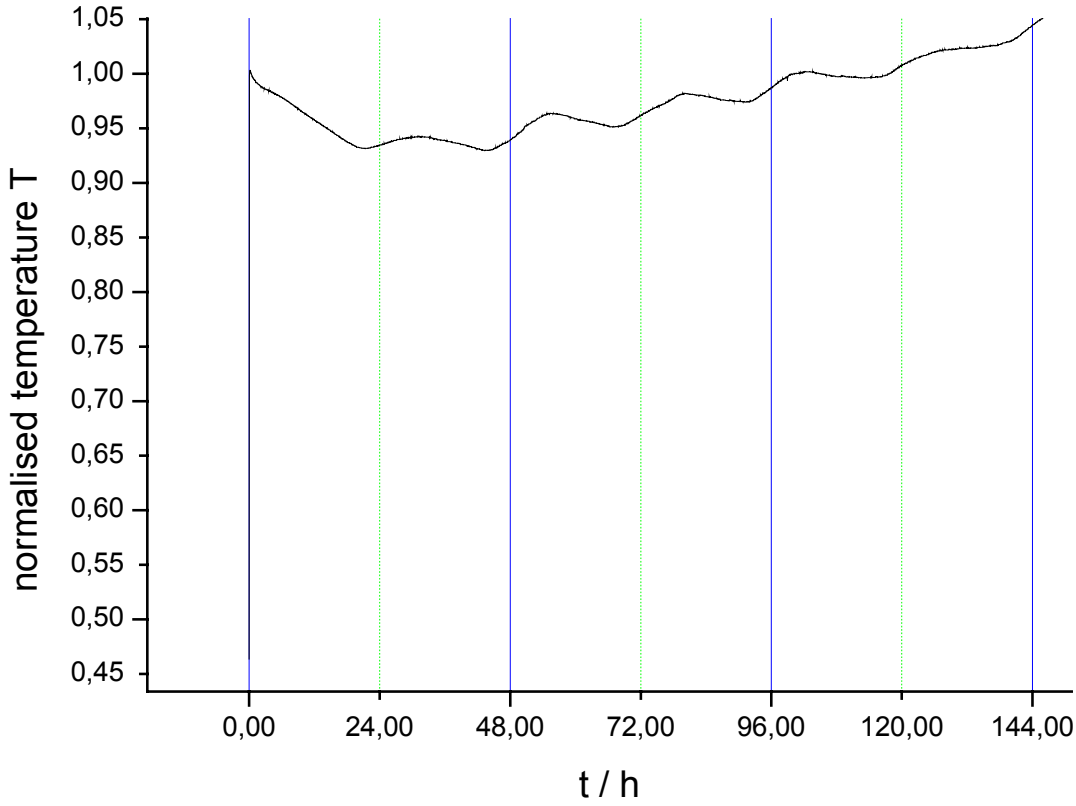

Fig. 7.13: Daily cycle in heater temperature due to ambient air temperature variations

The actual distribution of temperatures is more or less even except for two peaks, indicating mostly white thermal noise (Fig.7.14) or a cyclic transition between two temperatures (minimum and maximum).

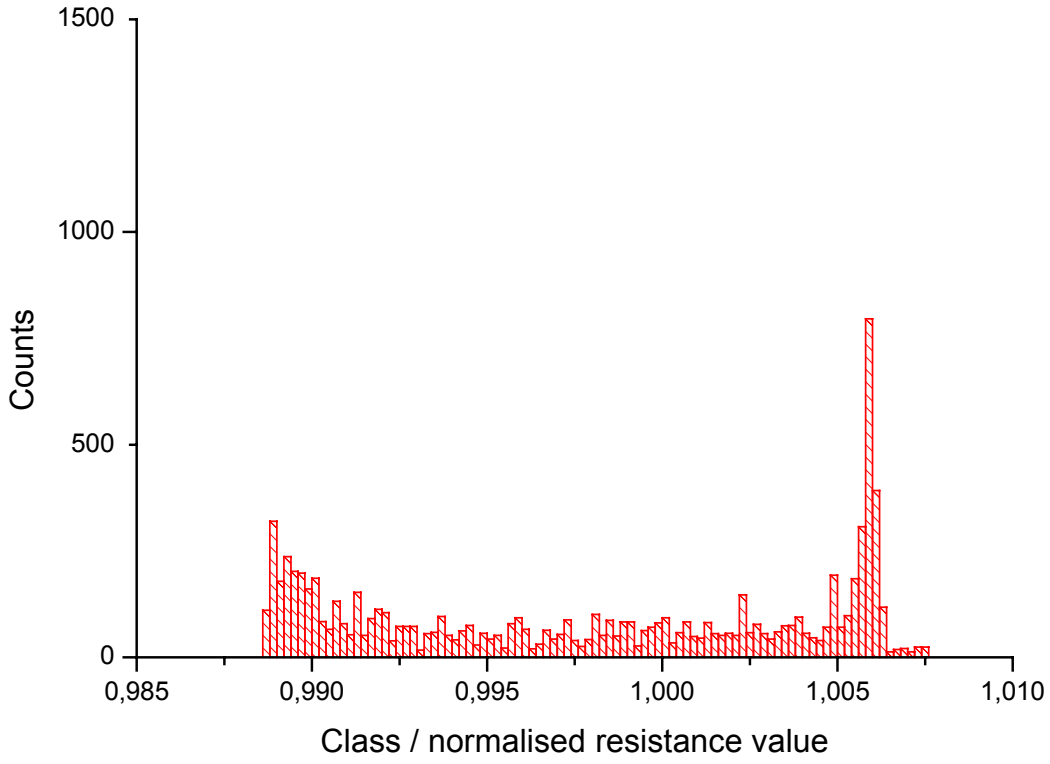

Fig. 7.14: Distribution of normalised heater temperatures. Except for two peaks the temperatures appear to be evenly distributed. This can indicate the constant transition between two temperatures (day and night) yielding constant counts for all transition temperatures and slightly higher counts for the turning points (minimum and maximum).

This observation leads us to the perspective of correlating the measured heater temperature with the room temperature or overall climate. Since, however, temperature variations of a few degrees Celsius are more than satisfying the specification, no further investigation of this behaviour was performed.

As for the mechanical and electrical stability of the doped-SiC heater version, outstanding performance at high temperatures could be found. The SiC heater could only be destroyed with application of excessively high heater powers and temperatures above 1000 °C (500 mW, 60 mA) (Fig. 7.15).

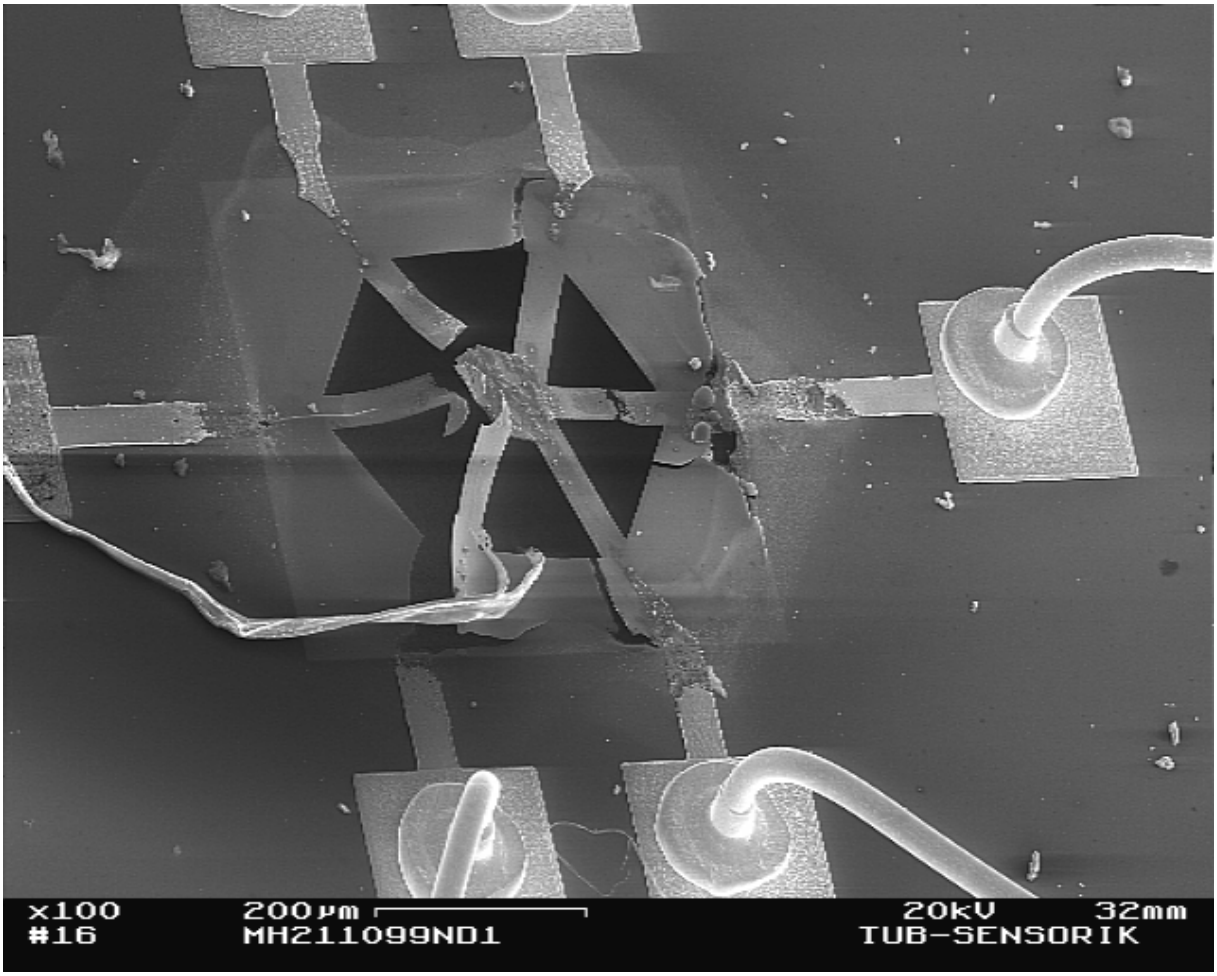

Fig. 7.15: Micro hotplate with SiC-heater after burn-out of heater due to excessively high temperature (>1000 °C) and operating current (60 mA)

One can clearly see the cracks in the SiC membrane and micro bridges and the lacking of the complete contact and IDE metallisation (small molten Au-balls on the surface (Fig. 7.16)). The operation above 650°C destroys the Au/TiWN contact and IDE metallisation.

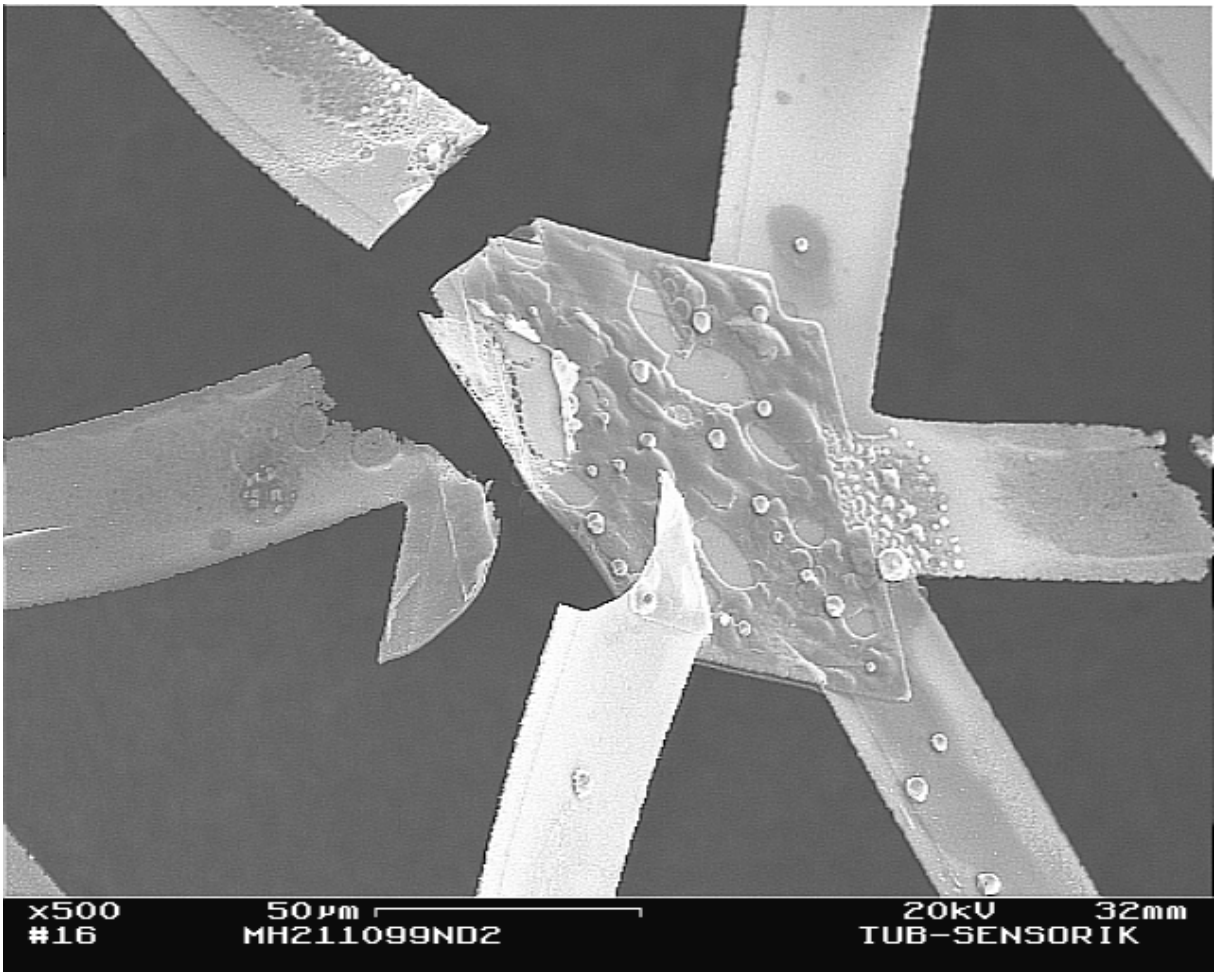

Fig. 7.16: Micro hotplate with SiC heater after burn-out. Close view with torn passivation and molten metal balls (remainders of the metallisation)

The metal starts subliming and eventually lift off at 650°C on the micro bridges. The heater itself can sustain temperatures well above 1000°C making it glow like a light bulb. This excellent material behaviour of the SiC can be accounted for by the extremely low oxidation rate of the SiC (about one tenth of Si at comparable temperatures) allowing it to sustain temperatures above 1000°C in air for days. The metallisation and IDE on top of the heater is however destroyed.

8. Discussion of heater characteristics

The chief objective of the investigations in chapter 7 was to characterise the device properties and to check the validity of the assumptions and models made when designing the device and to get the necessary data for the operation of the device as micro gas sensor.

- The power consumption of both the SiC and the HfB_2 heaters is far below the 50 mW maximum heater power allowed by the technical specifications. Thereby they also exceed the properties of state of the art devices' thermal efficiency presented in literature (~2-10 K/mW, chapter 2.3.1) by a factor of two to ten (~19 K/mW).
- The maximum operating temperatures of the heaters of 350 °C can be achieved with 35 mW of heater power (HfB_2 heater, 20 μm bridge width) and 600 °C with 32 mW (650 °C with 45 mW) of heater power (SiC heater, 10 μm bridge width). They achieve the technical specifications, but stay below the potential limits expected from the HfB_2 and the SiC material properties. Possible reasons are discussed below.
- It is the first device presented, that can be battery operated with only 1-2 V operating voltage. The HfB_2 heater has a very high resistivity and is very well suited for a square area heater in a battery operated device. It is limited, though, by the low chemical inertness of the metal layer in oxidising atmospheres and requires a better protective layer or will need to be replaced by alternative metallisations like Pt. The combination of a high specific resistance metal thin film layer (HfB_2) and very low resistance contacting leads (Au/TiWN) is necessary, in order to realise a square heater with a resistance of about 20 Ω which can be operated at 1-2 V operating voltage of a small battery in a portable device. The contacting leads obviously have to have a much lower resistance than the heater, in order not to cause further power losses. They also need to prevent heating of the micro bridges, which

constitute the bottle neck for the supply current (narrow leads, long distance of 150 μm). The choice of material combinations that can be used in MEMS devices for these purposes is limited. Thus, an improvement of the metallisation layer is of utmost importance in further developments. A very low resistivity high temperature metallisation is needed. Maybe a combination of alloy of Pt and Au/TiWN could be a first step towards such a new layer.

- The temperature on chip can be measured using the integrated temperature sensor or the heater resistance itself. A linear TCR of 3.6 10^{-3} K^{-1} (RTD) and 0.96 10^{-3} K^{-1} (HfB_2) is measured.
- The SiC heater could be operated well above 800 °C, but is limited at 650 °C by the temperature limitations of the Au/TiWN metal layer constituting the IDE structure on top of the heater. Modified metallisation layers for the IDE (e.g. Pt) may help further increase the maximum operation temperature. The drawback of this solution is that the number of metal layers and processing steps used for the device increases. The SiC heater resistance as function of temperature was determined up to 650 °C operating temperature. An approximate NTC-behaviour is observed.
- The micro hotplate power consumption fits closely to the simulated data. Variations can be accounted for by processing tolerances during etching leading to varying SiC micro bridge dimensions. Not only does the overall power consumption measured agree with the simulated data, but also does the characterisation of the individual contributing parts from conduction through air and substrate, convection and radiation mirror the behaviour expected from the theoretical model. The SiC thermal conductivity was determined and the convection and radiation effects proven to be negligible. The general characteristics of the air thermal conductivity at low pressures as function of temperature agrees with the behaviour expected from the Pirani-

effect. Thus, for the first time, a comprehensive thermal model of a micro hotplate was presented and proven.

- The long term stability tests show a standard variation of the heater temperature during continuous operation of about 0.36 % of the normalised operating temperature right until failure. This is very helpful when operating the device until its lifetime limit, since no additional compensation electronics e.g. for drifting is needed. The maximum lifetime of the devices was around two weeks of continuous operation at maximum power. In literature, little data about proper long term stability studies of micro hotplate devices was found. The maximum operating times found in literature were around 50 h [2.34]. The device presented here exceeds these limits and the technical specifications by far. Nevertheless, the potential expected when using SiC is not used. Operating times of only two weeks rather suggest the use as a one-way device. The short thermal response time of the micro hotplate allows pulsing of the micro hotplate during operation. Assuming a heater response time of about 1 ms and a gas sensitive response of about 30 s, operation cycles of 1 min for testing of a gas concentration are reasonable. Hence the lifetime of device could be strongly influenced by the cycle frequency and length. For reasons of power efficiency in the application of these devices in handheld gas detectors, the sensors are switched on for measuring, only. It is therefore reasonable to say that the device lifetime is sufficient for a start, but will have to be improved. The reason for the device failure once again lays in the Au/TiWN metallisation of the contacting leads across the micro bridges. Continuous operation at 650 °C leads to sublimation and eventually lift-off of the metal layer. New improved low resistance metallisation layers have to be found. It may be reasonable trying a combination of Pt with the Au/TiWN layer in order to increase high temperature stability.

9 Gas sensors based on the new micro hotplate

"One tends to be overoptimistic in the short run and underoptimistic in the long run, because we can only extrapolate linearly and progress is always an exponential curve. Sooner or later the exponential curve crosses the linear extrapolation", A.C. Clarke

Obviously a micro heater with outstanding properties when it comes to power consumption and electrical and mechanical stability, opens up a wide field of possible applications wherever a thermal actuation principle is needed in microsystems technology. The device presented in this work is designed for the application as a metal oxide gas sensor with integrated micro hotplate.
The small size and new materials used made this a formidable task not without technological challenges.

The first part of this paragraph explains the fabrication procedures of turning the micro hotplate into a micro gas sensor and the assembly as a "ready-to-use" sensor on a standard TO-8 package with self-adhesive hydrophobic/oliophobic Teflon™ membrane. The second part gives an example of an NO_2 sensor fabricated using In_2O_3 thin films and the micro hotplate.

9.1 Fabrication and assembly

The gas-sensitive metal oxide layers used are deposited using reactive RF-magnetron sputtering. In order to deposit the layer on the IDE only, the remaining part of the device has to be covered during sputtering. For this purpose a dual-mask is being used. As previously mentioned a Si_3N_4 PECVD layer acts as secondary passivation and masks all parts of the device except for the bondpads and the IDE. This primary mask protects the surface during

sputtering and sensor operation. A secondary shadow mask (chapter 6.) is required to protect the bondpads during sputtering, since at this stage, the passivation is opened for Au-wire bonding.

After sputter deposition and the subsequent annealing steps, the chips are glued onto a TO8 package using epoxy resin followed by a curing step (90°C, 1h) and Au-wire bonding (Fig. 9.2). A stainless steel cap with a centred hole is used to protect the sensor from mechanical damage. Teflon based self-adhesive hydrophobic and oliophobic membranes can be glued into the cap for further protection of the sensor in harsh environments (Fig. 9.1, Fig. 9.2). Obviously this increases the sensor response time upon exposure to test gases.

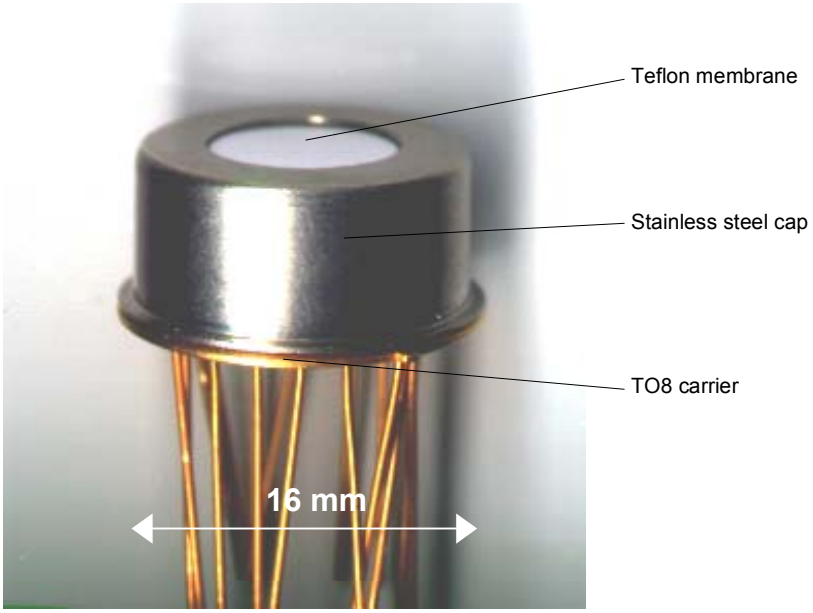

Fig. 9.1: Micro gas sensor chip mounted on TO8-carrier with stainless steel cap and hydrophobic/oliophobic Teflon membrane for industrial field tests

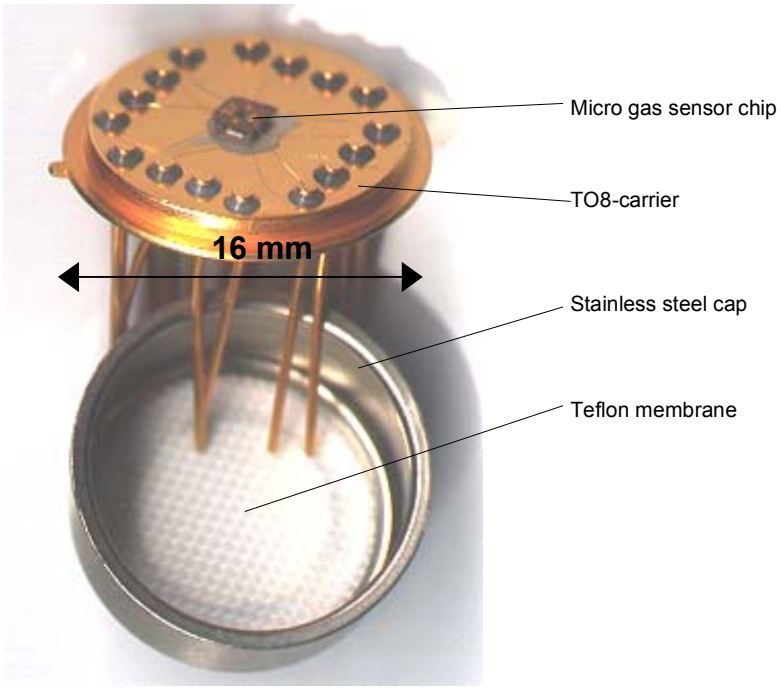

Fig. 9.2: Micro gas sensor chip mounted on TO8-carrier (stainless steel cap opened, chip visible)

9.2 An NO_2 micro gas sensor

NO_2 is a toxic gas occurring in a large variety of industrial and combustion processes. Its maximum workplace concentration (MAK) according to German law is set at 5 ppm [1.2]. In earlier work [6.10] the suitability of In_2O_3 layers for the detection of NO_2 in the MAK-range has been shown.

The In_2O_3 thin films are deposited on the IDE using reactive RF-magnetron sputtering. A particular set of sputtering parameters (P=100 W, 20 % O_2 80 % Ar) produces a 120 nm thick In_2O_3 thin film with (211) texture. These layers feature a superior quality concerning the NO_2 sensitivity compared to the normally (111) textured films [6.10]. The sensor chip is mounted on a TO8 carrier. Contacting is done using Au-wire bonding.

Measurements of the sensor response under defined gas atmosphere (5, 10, 20, 30 ppm NO_2 in synthetic air) were performed using a computer controlled gas mixing and measurement system. Exposure to NO_2 causes an increase in layer

conductivity at 300 °C operating temperature. Sensitivity, and reproducibility in the German maximum workplace concentration range (MAK = 5 ppm) are good (Fig. 9.3). The response time (τ_{50} =50s) needs further improvement.

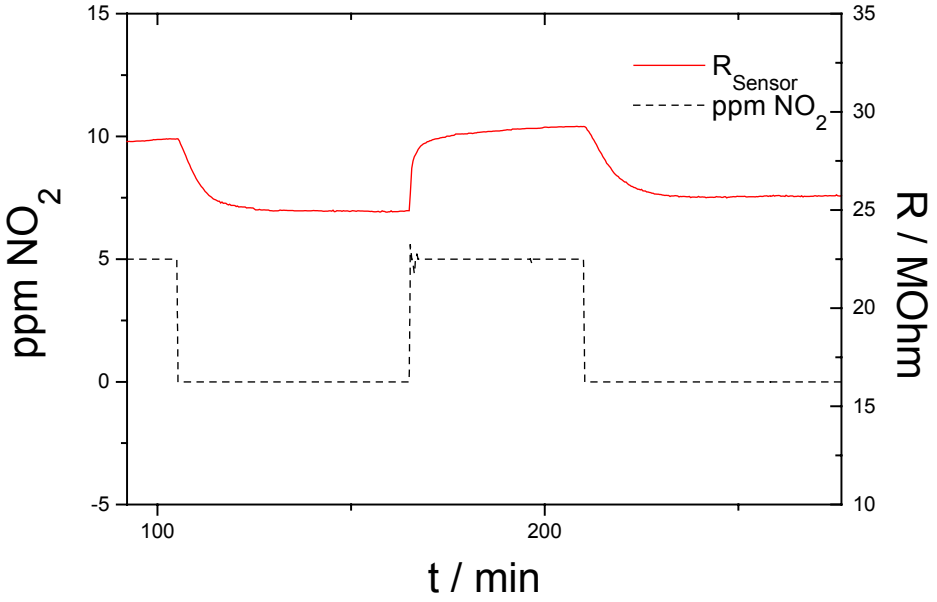

Fig. 9.3: Sensor response to 5 ppm NO_2 at 300 °C (20 mW heater power). An In_20_3 thin film layer of 120 nm thickness is being used as gas sensitive layer.

9.3 Discussion

An NO_2 sensor for the application in the MAK range was demonstrated to show the functioning of the micro hotplate as a gas sensor. Using standard TO8 carriers and protective stainless steel caps with exchangeable Teflon membranes, a device demonstrating technical feasibility was shown. The sensor power consumption (25 mW) is very low thereby exceeding the requirements (100mW) by far. Since the main focus of this work lays in the demonstration of the modular micro hotplate system and its applicability as a micro gas-sensor, no further details [6.11, 6.12] about the sensor characteristics are given here.

10 Conclusions and outlook

“Never fall in love with your own airship”, U. Eco

The following chapter discusses the task, achievements and drawbacks as well as potential future development of the new SiC/HfB_2 based micro hotplate gas sensor.

The past decade has seen a market breakthrough of metal oxide based micro gas sensors. Their advantage lies in their simplicity and modularity: various metal oxide thin films for the detection of a variety of different gases can be used on the same principle detecting device. The low selectivity of the gas sensitive layers, the fairly high power consumption and the fairly short long term stability of these devices are their main drawbacks. One of the keys to success of these devices is the existence of a micro scale, low power, battery compatible and high temperature compatible micro hotplate gas sensor module.

This work introduces and demonstrates the first ultra low power micro hotplate gas sensor module suitable for battery operation in handheld gas detecting devices.

The goal of this work was to overcome the limits of state of the art micro hotplates and of currently used materials and technology. Thus, to reduce the sensor power consumption and size, improve the long-term stability in aggressive environments and offer maximum flexibility in its application, while keeping the development expenses low. For this purpose a new device, which can be used in battery operated handheld gas detectors with very low power consumption was developed. Table 10.1 compares the achieved device properties with the specifications set in chapter 2.

Tab. 10.1: Comparison of specified and actual device properties

		Specified	Actual	
Property		**Quantitiy**		**Unit**
Heater efficiency		> 9	6,8..19	K / mW
Power consumptino as gas sensor		< 50	20	mW
			(300 °C)	
Operating temperature range		RT..T..450	450	°C
		(650)	(650)	
Thermal time constant τ_{on}		< 100	< 0.6	ms
			(FEM)	
Heater stability at maximum temperature		>> 50	Ca. 290	h
Time constant of gas sensitive response		< 30	50	s
Dimensions	single heater chip	≤ 2 x 2	2 x 2	mm^2
	hotplate	≤ 100 x 100	80 x 80	μm^2
	array heater chip	-	3 x 3	mm^2
			(4 hotplates)	
Operating voltage		1-2	1-2	V
		12-24	12-24	V
Electrode structure / geometry		Flexible/IDE	IDE with 1, 2 or 4 finger pairs	
Array integration		on-chip	on-chip	
			(integrated in membrane)	

Summarizing, the following results were obtained:

- For the first time, SiC and HfB_2 were employed in the design and demonstration of a micro hotplate device to overcome the weaknesses in long term stability of devices in corrosive high temperature environments. The new material combination was introduced to MEMS technology for micro heater and hotplate applications along with the development of the new material processing technology. A modular concept of processing blocks for micro hotplate devices was presented, allowing the production of devices operated at 1-2 V or 12-24 V with the modification of only one major processing step. Thus a wider range of applications can be covered using the same core device. The development costs could potentially be reduced considerably and therefore lower the market entrance barriers for

these devices, hindered only by the high price of the SiC material. A completely new material combination is used. It is the first micro hotplate device fabricated using SiC and the first micro hotplate using an HfB_2 metal thin film heater. Based on standard MEMS processes, the necessary deposition and structuring processes (sputtering, RIE etching, wet etching) were introduced at TU Berlin or optimised for the use in the new device. SiC has excellent mechanical, chemical and high temperature strength as substrate and heater material. This also shows in the extremely high operating temperature of the SiC hotplate version of >800°C. HfB_2 has a high melting point, but requires protection from oxidising agents. These materials bring about a huge potential for the fabrication of ultra high temperature micro hotplates. It is the first device using this material combination rather than standard MEMS materials like e.g. Si_3N_4.

- Processing technology for 3D structuring of MEMS devices was expanded. The device presented here is the first front etched and backside bulk micromachined “spider-type” micro hotplate. The power losses through air and substrate on the backside of the hotplate can therefore be reduced to a minimum. The design allows integration of several hotplates within one single membrane. It is the first device with a “punctured” membrane i.e with holes for further thermal insulation of the hotplate. The design allows the modification from a low resistance metal thin film heater to a high resistance implanted heater by altering only one processing step during fabrication.
- The actual hotplate shares the position as smallest device presented in literature together with only a few other devices. Optimised design has for the first time allowed the integration of heater, temperature detector and an adjustable electrode structure for the use of a wide range of sensitive materials on a hotplate only 100 μm x 100 μm in size with an 80 μm x 80 μm heater. The array version of the hotplate is the smallest array hotplate

device presented in literature. The reduction in size is important for the reduction of power consumption, response time and chip area and thus cost for production and operation

- The device features the lowest power consumption (or highest thermal efficiency: up to 19 K/mW for the SiC version) of all devices presented in literature (2-10 K/mW). The technical specifications of 100 mW maximum heater power consumption are being exceeded. The resulting power consumption of between 15 and 35 mW depending on the required operating temperature is, however, still fairly large for operation with standard 750 mAh AAA-cells in handheld devices. Further reduction in size or alternative approaches towards the operation modes will have to help further reduce the power consumption.
- It is the first device designed and tested for battery operation with only 1-2 V operating voltage. This requirement leads to a very low heater resistance of 10-20 Ω, in order to allow sufficient current flow and heater power to be generated. The small size of the hotplate in combination with the requirement of high temperature uniformity on the hotplate lead to a square shaped area heater. Thus, a metallisation with very high resistivity and high temperature compatibility is needed. HfB_2 satisfies these requirements; its drawbacks are discussed below. Furthermore, a low resistance heater needs a very low resistance contact metallisation layer, in order to prevent power losses in the connecting leads. Inherent in the hotplate design, the micro bridges supporting the hotplate constitute the bottle neck for the current flow to the heater. Au is the only metallisation available featuring a low enough resistivity to prevent power losses and subsequent heating of the bridges instead of the hotplate. This metallisation also has to be high temperature compatible. Au/TiWN has proven to be a working contact metallisation up to 650 °C and is used in

the device. Unfortunately, this sets the upper limit of operation for the hotplate.

- The device fulfils the maximum temperature requirements of the technical specifications (450 °C), but in the HfB_2 version fails to exceed the state of the art presented in literature. The SiC version is limited at 650 °C by the operating temperature of the IDE metallisation. The potential for very high temperatures expected from the material properties is not used.
- Theoretical modelling and FEA were used for the optimisation of the device's static and transient thermal, thermo-mechanical and electrical properties and to prevent mechanical failure at high temperatures. For the first time a comprehensive analytical model of the thermal characteristics is presented, taking into account static and transient convection and air thermal conduction effects. The model serves as feasibility test for the general design as well as for the reduction of the degrees of freedom in the simulation model. The analytical approximation also yields a first order check on the simulation results.
- The simulation data gives power efficiencies of between 5 K / mW and 20 K / mW depending on the heater version (micro bridge length and width). Mechanically, a balance between the thermally induced compressive stress (200-300 MPa at 500 °C) and the built-in tensile intrinsic stress of the SiC-layers (250 MPa) could be reached at maximum operating temperature. The enormous material capabilities of the SiC membrane also allowed the placement of several heater and micro bridge structures in one SiC membrane of 1 μm thickness. Electrical simulations were used optimised the contact electrode geometry for the heater to assure a constant power density distribution across the heater.
- Actual measurements and simulations, as well as the theoretical modelling are in good agreement. Using the device as a micro Pirani vacuum gauge, it was possible to prove the validity of the assumptions made in the

analytical model (convective and conduction effects) and determine the silicon carbide thermal conductivity. Thus, not only could the overall thermal and power performance of the device be compared with the simulated data, but also could the contributions from convection and air and SiC conduction be determined to be in agreement with the theoretical model.

- An NO_2 micro gas sensor was demonstrated using the micro hotplate with reactively sputtered In_2O_3 thin films. It features the lowest power consumption (20 mW) known in literature for a metal oxide gas sensor. A dual-masking system using an on-chip passivation layer and a shadow mask shields the device surface during sputter coating of the IDE. The sensor chip was assembled on a TO8 carrier. A stainless steel cap with an exchangeable hydrophobic or oliophobic membrane was used as protective cover. The sensor showed good sensitivity and signal reproducibility in the NO_2 MAK-range of 5 ppm. Whilst the power consumption is surprisingly low, the response time is only moderately fast (τ_{50}=50 s) and needs further improvement.

In some aspects, like e.g. battery operation, power consumption and material combination, the limits of state of the art technology were clearly exceeded. The maximum operating temperature and stability however will require further research and development. The core weakness lays in the HfB_2 protection and the Au/TiWN contact metallisation. The device opens up new possibilities for future devices based on new materials and design concepts and can be considered a milestone and basis for the development of next generation micro hotplates.

Summarising briefly, MEMS technology was expanded by introducing a new set of materials with high temperature and chemical resistance for micro hotplate applications along with the new material processing technology. Based upon

this, a captivating new concept for a new micro hotplate with ultra-low power consumption and high temperature compatibility was demonstrated. Its characteristics exceed state of the art solutions from industry and research. With little variation in the fabrication process a wide variety of devices can be produced thereby reducing the development cost for each subsequent device. Some weaknesses of previously demonstrated devices could be prevented.

Future work will have to focus on two main issues. The metallisation layers and their failure modes will have to be studied and their temperature compatibility improved. For industrial use, a sensor re-design focussing more on production compatibility than testing the technological limits will either have to improve upon the resolution of the used lithographic and etching technologies or slightly increase the sensor size in order to simplify the sensor fabrication.

11. References

Chapter 1

[1.1] Nexus! task force, “Market analyis for microsystems 1996-2002”, Nexus-Emsto /FhG-ISIT, Nobbe & Partner, Wuppertal, pp. 70-71, 1998.

[1.2] TRGS 901 “Begründungen und Erläuterungen zu Grenzwerten in der Luft am Arbeitsplatz.”, Teil II, BArBl. 4/1999.

[1.3] S. Hansen, U. Vogt, B. Baumbach, Auswertung stationärer meteorologischer - lufthygienischer Messungen im Plangebiet „Stuttgart 21“, Untersuchungen zur Umwelt “Stuttgart 21” Heft 16, Landeshauptstadt Stuttgart, Amt für Umweltschutz, Abt. Stadtklimatologie, 1999.

[1.4] M. A. Arnold, T. J. Ostler, Anal. Chem. 58, pp.220, 1986.

[1.5] J. Frank, „Grundlagen eines neuartigen, bifunktionalen Gassensorsystems zur umfassenden Raumluftüberwachung durch Kombination halbleitender Metalloxide und IR-Absorbtion“, Dissertation, Technische Universität Ilmenau, 1999.

[1.6] N. Tagushi, Jpn. Patent 45-38200 (1962).

Chapter 2

[2.1] J. Janata, „Principles of Chemical Sensors“, Kluwer Academic/Plenum Publishers, New York, 1990.

[2.2] K Bodenhöfer, A. Hierlemann, G. Noetzel, U. Weimar, W. Göpel, “Performances of Mass-Sensitive Devices for Gas Sensing: Thickness Shear Mode and Surface Acoustic Wave Transducers”, Anal. Chem. 1996, 68, 2210-2218

[2.3] A.W. Adamson, A.P. Gast, “Physical Chemistry of Surfaces”,John Wiley & Sons, pp., 1997.

[2.4] Giesler,T.,Meyer, J.-U., Kunz, R. and Ruf, H.H., "Sensing in Biological Microsystems with Flexural Plate Wave Sensors", Microsystem Technology for Chemical and Biological Microreactors, Mainz (Rheinland-Pfalz), 20.2.-21.2.1995.

[2.5] Pyun, J.C., Beutel, H., Meyer, J.-U. and Ruf, H.H.: „Development of a Biosensor for E. Coli Based on a Flexural Plate Wave (FPW) Transducer“, Biosens. Bioelectron. 13, 839-845 (1998).

[2.6] S. Middelhoek et. al., “Silicon Sensors”, Meas. Sci. Technol. 6, pp. 1641-1658, 1995.

[2.7] G. G. Guilbault, “Applications of quartz crystal microbalances in analytical chemistry”, Methods and Phenomena, Vol. 7, Elsevier, Amsterdam 1984.

[2.8] P.T. Moseley, B.C. Tofield, „Solid-state gas sensors“, IOP Publishing Ltd. Bristol, 1987.

[2.9] K. Saji, “Characteristics of limiting current-type oxygen sensor”, J. Electrochem. Soc. 124, pp.2430, 1987.

[2.10] N. Yamazoe et. al., Surf. Sci., 86, pp. 335, 1979.

[2.11] D. Mutschall, “Herstellung und Charakterisierung von NiO- und MoO_3-Dünnschichten für Anwendungen in der Gas-Mikrosensorik“, Dissertation, Technische Universität Berlin, 1997.

[2.12] R. W. Cattrall, “Chemical Sensors”, Oxford Chemistry Primers, Oxford University Press, 1997.

[2.13] W. Göpel, “Chemical and biochemical sensors, a comprehensive survey, Part I”, VCH, Weinheim, 1991.

[2.14] W. Göpel, “Chemical and biochemical sensors, a comprehensive survey, Part II”, VCH, Weinheim, 1992.

[2.15] P. Kofstad, “Nonstoichiometry, Diffusion and Electrical Conductivity in Binary Metal oxides”, Robert E. Krieger Publishing Company, Inc., Malabar, USA, 1983.

[2.16] V. Demarne, R. Sanjinés, “Thin Film Semiconducting Metal Oxide Gas Sensors”, Gas Sensors, G. Sberveglieri (ed.), Kluwer Academic Publishers, Dordrecht, The Netherlands, 1992, pp.89-106.

[2.17] V. L. Bonc-Bruevic, S.G. Kalasnikov, „Halbleiterphysik“, Deutscher Verlag der Wissenschaften, Berlin 1982.

[2.18] M. Fleischer: „Präparation und Charakterisierung von Ga_2O_3 Dünnschichten, Untersuchung der gassensitiven elektrischen Leitfähigkeitseigenschaften“, Technische Universität München, Dissertation, 1992.

[2.19] A. Bielanski, J. Haber, “Oxygen in catalysis on transition metal oxides”, Catal. Rev.-Sci. Eng., Vol.19, pp.1-41, 1979.

[2.20] C. Kohl: “Surface Processes in the Detection of Reducing Gases with SnO_2 based devices”, Sensors and Actuators 18 (1989), pp.71-113.

[2.21] M. J. Madou, S. R. Morrison, “Chemical Sensing with Solid State Devices”, Academic Press, London, San Diego, 1989.

[2.22] W. Göpel, “Solid State Chemical Sensors: Atomistic Models and Research Trends”, Sensors and Actuators 16 (1989), pp. 167-193.

[2.23] W. Göpel, “Chemisorbtion and Charge Transfer at ionic semiconductor surfaces: implications in designing gas sensors”, Prog. Surf. Sci., Vol. 20, pp. 9-103, 1985.

[2.24] P.B. Weisz, “Effects of electronic charge transfer between adsorbate and solid on chemisorbtion and catalysis”, Surf. Sci., Vol. 277, pp. 429-441, 1992.

[2.25] A.W. Adamson, A.P. Gast, “Physical Chemistry of Surfaces”,John Wiley & Sons, pp., 1997.

[2.26] C. Xu, J. Tamaki, N. Miura, N. Yamazoe, "Grain size effects on gas sensitivity of porous SnO_2-based elements", Sensors and Actuators B, Vol.3, pp. 147-155, 1991.

[2.27] J. Maier, W. Göpel, "Investigations of the bulk defect chemistry of poly crystalline tin (IV) oxide", journal of solid state chemistry, 72 (1988), pp.293-302.

[2.28] S. Matsubara, S. Kaneko, S. Morimoto, S. Shimizu, T. Ishihara, Y. Takita, "A practical capacitive type CO_2 sensor using CeO_2 $BaCO_3$ CuO ceramics", Sensors and Actuators B65, pp.128-132, 2000.

[2.29] I. Simon, N. Bârsan, M. Bauer, U. Weimar, "Micromachined metal oxide gas sensors: opportunities to improve sensor performance", Sensors and Actuators B: Chemical, Vol. 73 (1) , pp. 1-26, 2001.

[2.30] D. Briand, A. Krauss, B. van der Schoot, U. Weimar, N. Barsan, W. Gopel, N.F. de Rooij, "Design and fabrication of high-temperature micro-hotplates for drop-coated gas sensors", Sensors and Actuators B68, pp.223-233, 2000.

[2.31] T. Takada, H. Shiozawa, H. Kobayashi, H. Tanjou, Y. Matsubara, "Miniaturized hot wire type semiconductor gas sensor operated with a battery", The 6^{th} international meeting on chemical sensors, Gaithersburg, 1996.

[2.32] S. M. Sze, "Physics of Semiconductor Devices",p. 852, John Wiley and Sons, 1981.

[2.33] V. Guidi, G Cardinali, L. Don, G. Faglia, M. Ferroni, G. Martinelli, P. Nelli, G. Sberveglieri, "Thin-film gas sensor implemented on a low-power consumption micromachined silicon structure", Sensors and Actuators B 49, pp.88-92, 1998.

[2.34] W. Hellmich et. al., "A selective and highly sensitive CO sensor based on RGTO – SnO_2 films deposited onto Si-micromachined structure", Proc.

Second Asia Conference on Chemical Sensors (EACCS`95), Xi'an, China, pp.137-141, 1995.

[2.35] J.S. Suehle, R.E. Cavicchi, M Gaitan, S. Semancik, "Tin oxide gas sensor fabricated using CMOS micro-hotplates and in-situ processing", IEEE Electron Device Letters, Vol.14, No. 3, pp. 118-120, 1993.

[2.36] F. Dimeo Jr., S. Semancik, R.E. Cavicchi, G.E. Poirier, "Heteroepitaxy of conducting oxides on silicon using oxide buffer layers", The 6th international meeting on chemical sensors, Proceedings, Gaithersburg, 1996.

[2.37] S. Semancik, R.E. Cavicchi, K.G. Kreider, J.S. Suehle, P. Chaparala, "Selected-area deposition of multiple active films for conductometric microsensor arrays", Transducers'95, Eurosensors IX, Proceedings, Stockholm, Sweden, pp. 831-834, 1995.

[2.38] S. Fung, Z. Tang, P. Chan, J. Sin, P. Cheung, "Thermal analysis and design of a micro-hotplate for integrated gas sensor applications", Transducers'95, Eurosensors IX, Proceedings, Stockholm, Sweden, pp. 818-821, 1995.

[2.39] T. Takada, H. Shiozawa, H. Kobayashi, H. Tanjou, Y. Matsubara, "Miniaturized hot wire type semiconductor gas sensor operated with a battery", The 6th international meeting on chemical sensors, Gaithersburg, 1996.

[2.40] D.-D. Lee, W.-Y. Chung, T.-H. Kim, J.-M. Baek, "Low power micro gas sensor", Transducers`95, Eurosensors IX, Proceedings, Stockholm, Sweden, pp. 827-830, 1995.

[2.41] A. Götz, I. Gràcia, C. Cané, E. Lora-Tamayo, "Thermal and mechanical aspects for designing micromachined low-power gas sensors", J. Micromech. Microeng. 7, pp. 247-249, 1997.

[2.42] D.T.W. Wong, P.C.H. Chen, L. Sheng, J.K.O. Sin, “Thermal modeling of micro hotplates for integrated sensor applications”, IEEE Hongkong electron Devices Meeting, Proceedings, pp. 149-152, 1997.

[2.43] R.E. Cavicchi, J.S. Suehle, K.G. Kreider, M. Gaitan, P. Chaparala, “Optimized temperature-pulse sequences for the enhancement of chemically specific patterns from micro-hotplate gas sensors”, Sensors and Actuators B33, pp. 142-146, 1996.

[2.44] M. Zanini et. al., “Fabrication and properties of a Si-based high sensitivity microcalorimetric gas sensor”, Sensors and Actuators A, pp. 187-192, 1995.

[2.45] R.P. Manginell et. al., “Selective, pulsed CVD of platinum on microfilament gas sensors”, Tech. Digest 1996 Sol.-State Sensor and Actuator Workshop, Hilton Head, Sc, pp. 53-56, 1996.

[2.46] R.E. Cavicchi et. al., “Pulsed desorption kinetics using micromechanical, micromachined hotplate arrays”, J. Vac. Sci. Technol. A12(4), Jul/Aug 1994, pp. 2549-2553, 1994.

[2.47] C. Rossi, P. Temple-Boyer, D. Estève, “Realization and performance of thin SiO_2/Si_3N_4 membrane for microheater applications”, Sensors and Actuators A64, pp. 241-245, 1998.

[2.48] A. Pike, J.W. Gardner, “Thermal modelling and characterisation of micropower chemoresistive silicon sensors”, Sensors and Actuators B45, pp. 19-26, 1997.

[2.49] C.Rossi, E. Scheid, D. Estève, “Theoretical and experimental study of silicon micromachined microheater with dielectric stacked membranes”, Sensors and Actuators A 63, pp. 183-189, 1997.

[2.50] M. Dumitrescu et. al., Thermal simulation of surface micromachined polysilicon hot plates of low power consumption”, Proceedings of Eurosensors XI, Warsaw, September 21-24, pp. 743, 1997.

[2.51] J.W. Gardner, J.A. Covington, F. Udrea, T. Dogaru, C-C Lu, W. Milne, "SOI-based micro-hotplate microcalorimeter gas sensor with integrated BiCMOS transducer", Digest of Technical Papers, Tranducers '01, Munich, June 10-14, pp. 1688-1691, 2001.

[2.52] B. Banchapakesan, R. Cavicchi, S. Semancik, D. L. DeVoe, "Nanoscale manipulation and control of tin oxide nanostructures on large area arrays of microhotplates", Digest of Technical Papers, Transducers '03, Boston, June 9-12, pp. 119-122.

Chapter 3

[3.1] H. O. da Frota, H. Panepucci, A. Cruz-Orea, E. A. R. Coss, "Optical and conductivity measurements on MoO_3:H", Sol.State Com. Vol. 49, pp. 921-923, 1984.

[3.2] V. A. Ioffe, I. B. Patrina, E. V. Zelenetskaya, V. P. Mikheeva, "Charge compensation of impurities and electrical properties of MoO_3", Phys. Stat. Sol., Vol. 66, pp. 535-543, 1969.

[3.3] R. Paul, "Elektronische Halbleiterbauelemente", p.523, B. G. Teubner, Stuttgart, 1992.

[3.4] R.C. West et. al. (editors), "CRC Handbook of Chemistry and Physics", CRC Press, Boca Raton, Florida, 1987.

[3.5] D. Schneider and M. D. Tucker, "Non-destructive characterization and evaluation of thin films by laser-induced ultrasonic surface waves", Thin Solid Films Vol. 290-291, pp. 305-311, (1996).

[3.6] IEEE,Micro Electro Mechanical Systems Workshop,Feb 1990, Napa Vally,California, p.174, 1990.

[3.7] Osamu Tabata, Ken Kawahata, Susumu Sugiyama and Isemi Igarashi, "Mechanical property measurements of thin films using load-deflection of

composite rectangular membranes", Sensors and actuators, Vol. 20, pp. 135-141, (1989).

[3.8] IEEE Transactions on electron devices,Vol.ED25,No.10,Oct1978, p.1249

[3.9] M. T. Kim, "Influence of substrates on the elastic reaction of films for the microindentation tests", Thin Solid Films, Vol. 283, pp. 12-16, (1996).

[3.10] IEEE Micro Electro Mechanical Systems Workshop,Feb 1993, Florida, p.25.

[3.11] IEEE,Micro Electro Mechanical Systems Workshop,Feb 1990, Napa Vally,California, p.175.

[3.12] NASA TPSX-Program, Internet Database (http://asm.arc.nasa.gov/tpsx/tpsxhome.shtml), 1999.

[3.13] K.E. Petersen, Proc. of the IEEE 70, 420 (1982).

[3.14] A. W. van Herwaarden, P. M. Sarro, J. Vac. Sci. Technol. A 5, 2454 (1987).

[3.15] A. W. van Herwaarden, P. M. Sarro, Sensors and Actuators 14, 259 (1988).

[3.16] NASA TPSX-Program, Internet Database, K&K Associates Materials Database, (http://asm.arc.nasa.gov/cgi-bin/tpsx/unrestrict/V2/tpsx-frame.pl), 1999.

[3.17] P.M. Sarro, Proc. Transducers '99, Silicon Carbide as a New MEMS Technology (1999).

[3.18] P.Krause, E. Obermeier, A. Wehl, "A micromachined single-chip inkjet printhead", Sensors & Actuators A53, 405-409, 1996.

[3.19] Landolt-Börnstein, New Series III/17a, Diamond, pp. 132-142, 1985.

[3.20] J. A. Powell et. al., "Recent development in SiC (USA)", Springer Proceedings in Physics 34 – Amorphous and Crystalline Silicon Carbide, edited by G.L. Harris and C.Y.-W. Yang, Springer Verlag Berlin, Heidelberg, 2-12, 1989.

[3.21] Landolt-Börnstein, New Series III/17a, "Diamond", pp. 36-42, 1985.

[3.22] Landolt-Börnstein, New Series III/17c, “Silicon Carbide”, pp. 403-416, 1985.

[3.23] David R. Lyde (editor in chief), “CRC Handbook of Chemistry and Physics”, CRC Press, Boca Raton, Florida, 1998.

[3.24] P.T.B Shaffer, “Non-electronic applications of SiC”, pp. 343-351, 1973.

[3.25] Proceedings of IEEE,Vol 70,No.5,May 1982, p.421

[3.26] W. Reichert, “Doping by Nitrogen Implantation and Characterization of Heteroepitaxial 3C-SiC Thin Films on Si and SOI Substrates”, Dissertation, Berlin, 1998.

[3.27] A. J. Fleischmann et. Al., „Poly crystalline silicon carbide for surface micromachining“, Proc. IEEE-MEMS, San Diego, CA, Feb 11-15, 1996, pp.234-238

[3.28] Y. Onuma et al.., „Preparation of Poly Crystalline SiC thin films by reactive sputtering process“, Proc. Int. Conf. on SiC and Related Materials, Washington, DC, USA, 1993, pp. 133-136.

[3.29] Kamimura et al., „Preparation of poly crystalline SiC thin films and its application to resistive sensors“, Proc. Int. Conf. on SiC and Related Materials, Kyoto, Japan, 1995, pp. 825-828.

[3.30] L. Tong. Et al., „Amorphous SiC films by PECVD“, Proc. IEEE-MEMS, Fort Lauderdale, FL, USA, Feb 7-10, 1993, pp. 242-247.

[3.31] A. Klump at el., „Amorphous SiC and its application in silicon micromachining“, Sens & Act A 41-42, pp. 310-316, 1994.

[3.32] A. F. Flannery et al., „PECVD SiC as a chemically resistant material for micromachined transducers“, Sensors and Actuators A 70, pp. 48-55, 1998.

[3.33] P.M. Sarro et al., „Low-stress PECVD SiC thin films for IC-compatible microstructures“, Sensors and Actuators A 67, pp. 175-180,1998.

[3.34] D. R. Lide, “CRC Handbook of Chemistry and Physics”, 79th edition, pp. 4-13, 1998-1999.

Chapter 4

[4.1] C. Scheibe, “Design und Realisierung eines kapazitiven Gassensorelementes mit integrierter Heizung für Betriebstemperaturen bis 450 °C“, Dissertation, Technische Universität Berlin, 1995.

[4.2] P. W. Atkins, „Physical Chemistry“, pp. 739-740, Oxford University Press 1992.

Chapter 5

[5.1] Ansys Release 5.3, Manual, 1997.

[5.2] H. Vogel, “Gerthsen Physik”, Kapitel 5 (Wärmelehre), 19. Auflage, Springer Verlag 1997.

[5.3] Eric. C. Guyer (Editor in chief), “Handbook of Applied Thermal Design”, McGraw Hill, 1988.

[5.4] E. Guyon, J.-P. Hulin, L. Petit, “Hydrodynamik”, Vieweg & Sohn Verlagsgesellschaft Braunschweig/Wiesbaden, 1997.

[5.5] P. H. Oosthuizen, D. Naylor, “Introduction to Convective Heat Transfer Analysis”, McGraw Hill, 1999.

[5.6] S. Ganzlin, “Untersuchung des thermisch-transienten Verhaltens eines Mikroheizers auf Siliziumkarbidbasis”, Diplomarbeit, Technische Universität Berlin, 1999.

[5.7] D. R. Lide, “CRC Handbook of Chemistry and Physics”, 79th edition, pp. 6-175, 1998-1999.

[5.8] C. Lyons et al., „A High-Speed Mass Flow Sensor with Heated Silicon Carbide Bridges“, IEEE, 1998.

[5.9] M. Kasper, “Entwurf und Simulation Mikroelektronischer Aufbauten”, Skript zur Vorlesung, Technische Universität Berlin, 1997.

[5.10] H. Kuchling, “Taschenbuch der Physik”, Verlag H. Deutsch, Thun und Frankfurt/M., 1988.

[5.11] R.E. Cavicchi et. al, “Optimized temperature-pulse sequences for the enhancement of chemically specific response patterns from micro-hotplate gas sensors”, Sensors & Actuators B33, pp. 152-146, 1996

[5.12] R.E. Cavicchi et. al., “Pulsed desorption kinetics using micromachined micro hotplate arrays”, J. Vac. Sci. Technol. A12 (4), Jul/Aug 1994, pp. 2549-2553, 1994.

[5.13] H. Mayer, “Sensor-Arrays mit Metalloxid-Gassensoren zur Gaserkennung und Konzentrationsbestimmung in Echtzeit”, Technisches Messen 65 (1998), 2, pp. 58-71, 1998.

Chapter 6

[6.1] W. Reichert, D. Stefan, E. Obermeier, W. Wondrak, “Fabrication of smooth β-SiC surfaces by reactive ion etching using a graphite electrode”, Materials Sience and Engineering B46, pp. 190-194, 1997.

[6.2] W. Reichert, “Doping by Nitrogen Implantation and Characterization of Heteroepitaxial 3C-SiC Thin Films on Si and SOI Substrates”, Dissertation, Berlin, 1998.

[6.3] G. Engelmann, O. Ehrmann, J. Simon, H. Reichl, “Development of a fine pitch bumbing process”, 1990.

[6.4] O. Ehrmann, G. Engelmann, J. Simon, H. Reichl, “A bumbing technology for reduced pitch”, ITAB’90, Proceedings, pp.41 – 48, 1990.

[6.5] Joseph S. Shor, Richard A. Weber, L. G. Provost, David Goldstein, Anthony D. Kurtz, “High Temperature Ohmic Contact Metallizations for n-type 3C-SiC”, J. Electrochem. Soc., Vol. 141, No.2, February 1994, pp. 579-581, 1994.

[6.6] R. Ziermann et al., „A High Temperature Pressure Sensor with ß-SiC Piezoresistors on SOI Substrates", Transducers 97, Chicago, Illinois, USA, June 16 - 19, Digest of Technical Papers, pp. 1411 – 1414, 1997.

[6.7] C. Imawan, F. Solzbacher, H. Steffes, E. Obermeier, "Modified NiO thin films using Ti-overlayers for H_2 sensing", Eurosensors XIII, The Hague, The Netherlands, September 12-15, Proceedings, pp. 137 – 140, 1999.

[6.8] C. Imawan, F. Solzbacher, H. Steffes, E. Obermeier, "Improvement of gas sensing properties of MoO3 thin films using Ti – Overlayers for the application in NH3 gas sensors", Transducers '99 - 10th International Conference on Solid-State Sensors & Actuators, Sendai, Japan, June 7-10, Digest of Technical Papers, pp. 1686 – 1689, 1999.

[6.9] H. Steffes, C. Imawan, F. Solzbacher, E. Obermeier, "Reactively RF-Sputtered In_2O_3 Thin Films for the Detection of NO_2", Eurosensors XIII, The Hague, The Netherlands, September 12-15, Proceedings, pp. 871 – 874, 1999.

[6.10] F. Solzbacher, D. Mutschall, E. Obermeier, "Au-Modified NiO Thinfilms for Applications in H2S-Gassensors", Sensor '99 - 9th Int'l Trade Fair and Conference for Sensors / Transducers & Systems, Nürnberg, Germany, May 18-20, Sensor '99 Proceedings I, 1999, B 3.2, pp. 165-169, 1999.

[6.11] F. Solzbacher, C. Imawan, H. Steffes, E. Obermeier, M. Eickhoff, "*A new SiC/HfB_2 based low power NO_2-sensor",* Sensors and Actuators, B 77, pp. 111-115, 2001.

[6.12] F. Solzbacher, C. Imawan, H. Steffes, E. Obermeier, M. Eickhoff*, "A highly stable SiC based micro hotplate NO_2 gas sensor",* Sensors and Actuator, B 78, pp. 216-220, 2001.

[6.13] S. Nishino, J.A. Powell, H.A. Will, "Production of large-area single-crystal wafers of cubis SiC for semiconductor devices", Appl. Pys. Lett. 42(5), 460 (1983).

[6.14]HOYA Corporation, R&D Center, Tokyo, Japan, Specification sheet for 3C-SiC film on 6-inch Si wafer, (1996).

[6.15]G. Krötz, C. Wagner, W. Legner, H. Sonntag, H. Möller, G. Müller, „Micromachining applications of heteroepitaxially grown β-SiC layers on silicon", Inst. Phys. Conf. Ser. No. 142, (1996), pp. 829-832.

Chapter 7

[7.1] P. K. Wenig, J.-S. Shie, „Micro-Pirani Vacuum Gauge", Rev. Sci. Intrum. 65 (2), Feb. 1994.

Appendix A: Ansys 5.3 simulation source code: thermal and thermo-mechanical simulations

```
/batch
!------------------------------------------------------------------          !
!Simulation: SiCOI - Heaterarray                    15.4.98                  !
!Simulation of temperature distribution and power losses                     !
!Membrane dimensions:      1000 um x 1000 um x 1 um                          !
!Heater membrane size:     100 um x 100 um                                   !
!Heater temperature:  773 K                                                  !
!Load steps:                        1                                       !
!-----------------------------------------------------------------------     !
!
!Optionen
/clear
/view,-1, -1, 1
/angle, 1, 60, zs
/Pnum, kp, 1
/psf, pres, ,2
/erase
/units,si
/Prep7
/title,Micro hotplate, P=10mW bridgelgth.=150um,br.wdth=40um
!Materialkonstanten
twp = 293               !Arbeitstemperatur
tab = 773               !Heizertemperatur
!
!Elementtypes
ET,1,70
mptemp,,373,423,473,523,573,623,673,723,773
mpdata,kxx,1,,220,210,195,180,170,155,140,130,110
mp,c,1,1200
mp,dens,1,3200

mp,kxx,2,2
mp,c,2,800
mp,dens,2,2200

!Sensorgeometrie
!
hml=100E-6
hmw=100E-6
mt=1E-6
bl=150E-6
bw=40E-6
lt=1E-6

omw=300E-6
oml=300E-6

!l=hmw/2+bl+omw
```

```
dx=150E-6
dy=150E-6

!Heizer
p=0.01
hdens=p/(hml*hmw*mt)
hfm=p/(hml*hmw)
hflux=p/(bw*mt)
!
k,1,0,0,0
k,2,hmw/2,0,0
k,3,hmw/2,hml/2,0
k,4,0,hml/2,0
k,5,0,0,mt
k,49,0,0,mt+lt
k,6,hmw/2,0,mt
k,51,hmw/2,0,mt+lt
k,7,hmw/2,hml/2,mt
k,54,hmw/2,hml/2,mt+lt
k,8,0,hml/2,mt
k,56,0,hml/2,mt+lt

k,9,hmw/2+bl,0,0
k,10,hmw/2+bl,bw/2,0
k,11,hmw/2,bw/2,0
k,12,hmw/2+bl,0,mt
k,13,hmw/2+bl,bw/2,mt
k,14,hmw/2,bw/2,mt
k,52,hmw/2,bw/2,mt+lt
dx=bw/2*1.4
dy=dx

k,15,hmw/2-dx,0,0
k,16,hmw/2-dx,bw/2,0
k,17,hmw/2-dx,0,mt
k,50,hmw/2-dx,0,mt+lt
k,18,hmw/2-dx,bw/2,mt
k,59,hmw/2-dx,bw/2,mt+lt

k,19,hmw/2-dx,hml/2-dy,0
k,20,hmw/2-dx,hml/2,0
k,21,hmw/2-dx,hml/2-dy,mt
k,60,hmw/2-dx,hml/2-dy,mt+lt
k,22,hmw/2-dx,hml/2,mt
k,55,hmw/2-dx,hml/2,mt+lt

k,23,0,hml/2-dy,0
k,24,0,hml/2-dy,mt
k,57,0,hml/2-dy,mt+lt

k,25,0,bw/2,0
```

```
k,26,0,bw/2,mt
k,58,0,bw/2,mt+lt

k,27,hmw/2,hml/2-dy,0
k,28,(hmw+bl)*0.5+bw/2*0.5,(hmw/2+bl)*0.886-bw/2*0.886,0
k,29,(hmw+bl)*0.5+bw/2*0.5,(hmw/2+bl)*0.886-bw/2*0.886,mt
k,30,hmw/2,hml/2-dy,mt
k,53,hmw/2,hml/2-dy,mt+lt

k,31,(hmw+bl)*0.5-bw/2*0.5,(hmw/2+bl)*0.886+bw/2*0.886,0
k,32,(hmw+bl)*0.5-bw/2*0.5,(hmw/2+bl)*0.886+bw/2*0.886,mt

k,33,(hmw+bl)*0.5,(hmw/2+bl)*0.886,0
k,34,(hmw+bl)*0.5,(hmw/2+bl)*0.886,mt

k,35,0,(hmw/2+bl)*0.886+bw/2*0.886,0
k,36,0,(hmw/2+bl)*0.886+bw/2*0.886,mt

k,37,0,hml/2+bl+oml,0
k,38,0,hml/2+bl+oml,mt

k,39,(hmw/2+bl+omw)+bw/(2*sin(60)),hml/2+bl+oml,0
k,40,(hmw/2+bl+omw)+bw/(2*sin(60)),hml/2+bl+oml,mt

k,41,(hmw/2+bl+omw),hml/2+bl+oml,0
k,42,(hmw/2+bl+omw),hml/2+bl+oml,mt

k,43,(hmw/2+bl+omw),hml/2+bl+oml+bw/(2*cos(60)),0
k,44,(hmw/2+bl+omw),hml/2+bl+oml+bw/(2*cos(60)),mt

k,45,hmw/2+bl+omw,bw/2,0
k,46,hmw/2+bl+omw,bw/2,mt

K,47,hmw/2+bl+omw,0,0
K,48,hmw/2+bl+omw,0,mt

V,1,15,16,25,5,17,18,26
V,15,2,11,16,17,6,14,18
V,16,11,27,19,18,14,30,21
V,25,16,19,23,26,18,21,24
V,19,27,3,20,21,30,7,22
V,23,19,20,4,24,21,22,8
save
V,2,9,10,11,6,12,13,14
V,27,28,33,3,30,29,34,7
V,3,33,31,20,7,34,32,22
V,9,47,45,10,12,48,46,13
V,10,45,43,28,13,46,44,29
V,28,43,41,33,29,44,42,34
V,33,41,39,31,34,42,40,32
V,31,39,37,35,32,40,38,36
```

```
save
V,5,17,18,26,49,50,59,58
V,17,6,14,18,50,51,52,59
V,18,14,30,21,59,52,53,60
V,26,18,21,24,58,59,60,57
V,21,30,7,22,60,53,54,55
V,24,21,22,8,57,60,55,56

save
allsel
vglue,all
vsel,s,,,1,14
mat,1
type,1
vmesh,all
!vsel,all
!vatt,1,,1
!vmesh,all
!nummrg,all
vsel,s,,,14,20
mat,2
type,1

vmesh,all
wsort,,,RMS
waves,rms
finish
save

/solu
/nerr,
tunif,twp
nsel,s,loc,x,hmw/2+bl+omw
d,all,temp,twp
!f,all,heat,-hflux/4
!f,all,heat,hflux/4
nsel,s,loc,y,hml/2+bl+oml
d,all,temp,twp
!f,all,heat,-hflux/4
!f,all,heat,hflux/4
nsel,all
nsel,s,loc,x,0,hmw/2
nsel,r,loc,y,0,hml/2
nsel,r,loc,z,0,mt
!f,all,heat,hfm
bf,all,hgen,hdens
!nsel,r,loc,z,0
!d,all,temp,twp
allsel
nsel,s,loc,z,mt+lt
sf,all,conv,1270
```

```
nsel,s,loc,z,mt
nsel,r,loc,x,hmw/2,hmw/2+bl+omw
nsel,r,loc,y,hml/2,hml/2+bl+oml
sf,all,conv,20
nsel,s,loc,z,0
sf,all,conv,20
allsel
antype,static
lswrite
save
lssolve,1,1,1
finish

/exit
/prep7
etchg

mp,alpx,1,4.65E-6
mp,nuxy,1,0.16
mp,ex,1,440E9

mp,alpx,2,0.5E-6
mp,nuxy,2,0.14
mp,ex,2,70E9
finish

/solu
ldread,temp,,,,,,rth
nsel,s,loc,x,0

d,all,ux,0
nsel,s,loc,y,0
d,all,uy,0
!nsel,s,loc,x,hmw/2+bl+omw
!sf,all,pres,-250E6
!nsel,s,loc,y,hml/2+bl+oml
!sf,all,pres,-250E6
nsel,all
save
solve
finish
```

Appendix B: Ansys 5.3 simulation source code: thermal and thermo-mechanical simulations (II)

```
/batch
!-------------------------------------------------------------          !
!Simulation: SiCOI - Heaterarray                 15.4.98               !
!Simulation of temperature distribution and power losses               !
!Membrane dimensions:      1000 um x 1000 um x 1 um                    !
!Heater membrane size:     100 um x 100 um                             !
!Heater temperature:  773 K                                            !
!Load steps:                        1                                  !
!-------------------------------------------------------------------    !
!
!Optionen
/clear
/view,-1, -1, 1
/angle, 1, 60, zs
/Pnum, kp, 1
/psf, pres, ,2
/erase
/units,si
/Prep7
/title,Micro hotplate, P=10mW bridgelgth.=100um,br.wdth=40um
!Materialkonstanten
twp = 293               !Arbeitstemperatur
tab = 773               !Heizertemperatur
!
!Elementtypes
ET,1,70
mptemp,,373,423,473,523,573,623,673,723,773
mpdata,kxx,1,,220,210,195,180,170,155,140,130,110
mp,c,1,1200
mp,dens,1,3200

mp,kxx,2,2
mp,c,2,800
mp,dens,2,2200

!Sensorgeometrie
!
hml=100E-6
hmw=100E-6
mt=1E-6
bl=100E-6
bw=40E-6
lt=1E-6

omw=300E-6
oml=300E-6
```

```
!l=hmw/2+bl+omw
dx=150E-6
dy=150E-6

!Heizer
p=0.01
hdens=p/(hml*hmw*mt)
hfm=p/(hml*hmw)
hflux=p/(bw*mt)
!
k,1,0,0,0
k,2,hmw/2,0,0
k,3,hmw/2,hml/2,0
k,4,0,hml/2,0
k,5,0,0,mt
k,49,0,0,mt+lt
k,6,hmw/2,0,mt
k,51,hmw/2,0,mt+lt
k,7,hmw/2,hml/2,mt
k,54,hmw/2,hml/2,mt+lt
k,8,0,hml/2,mt
k,56,0,hml/2,mt+lt

k,9,hmw/2+bl,0,0
k,10,hmw/2+bl,bw/2,0
k,11,hmw/2,bw/2,0
k,12,hmw/2+bl,0,mt
k,13,hmw/2+bl,bw/2,mt
k,14,hmw/2,bw/2,mt
k,52,hmw/2,bw/2,mt+lt
dx=bw/2*1.4
dy=dx

k,15,hmw/2-dx,0,0
k,16,hmw/2-dx,bw/2,0
k,17,hmw/2-dx,0,mt
k,50,hmw/2-dx,0,mt+lt
k,18,hmw/2-dx,bw/2,mt
k,59,hmw/2-dx,bw/2,mt+lt

k,19,hmw/2-dx,hml/2-dy,0
k,20,hmw/2-dx,hml/2,0
k,21,hmw/2-dx,hml/2-dy,mt
k,60,hmw/2-dx,hml/2-dy,mt+lt
k,22,hmw/2-dx,hml/2,mt
k,55,hmw/2-dx,hml/2,mt+lt

k,23,0,hml/2-dy,0
k,24,0,hml/2-dy,mt
k,57,0,hml/2-dy,mt+lt
```

```
k,25,0,bw/2,0
k,26,0,bw/2,mt
k,58,0,bw/2,mt+lt

k,27,hmw/2,hml/2-dy,0
k,28,(hmw+bl)*0.5+bw/2*0.5,(hmw/2+bl)*0.886-bw/2*0.886,0
k,29,(hmw+bl)*0.5+bw/2*0.5,(hmw/2+bl)*0.886-bw/2*0.886,mt
k,30,hmw/2,hml/2-dy,mt
k,53,hmw/2,hml/2-dy,mt+lt

k,31,(hmw+bl)*0.5-bw/2*0.5,(hmw/2+bl)*0.886+bw/2*0.886,0
k,32,(hmw+bl)*0.5-bw/2*0.5,(hmw/2+bl)*0.886+bw/2*0.886,mt

k,33,(hmw+bl)*0.5,(hmw/2+bl)*0.886,0
k,34,(hmw+bl)*0.5,(hmw/2+bl)*0.886,mt

k,35,0,(hmw/2+bl)*0.886+bw/2*0.886,0
k,36,0,(hmw/2+bl)*0.886+bw/2*0.886,mt

k,37,0,hml/2+bl+oml,0
k,38,0,hml/2+bl+oml,mt

k,39,(hmw/2+bl+omw)+bw/(2*sin(60)),hml/2+bl+oml,0
k,40,(hmw/2+bl+omw)+bw/(2*sin(60)),hml/2+bl+oml,mt

k,41,(hmw/2+bl+omw),hml/2+bl+oml,0
k,42,(hmw/2+bl+omw),hml/2+bl+oml,mt

k,43,(hmw/2+bl+omw),hml/2+bl+oml+bw/(2*cos(60)),0
k,44,(hmw/2+bl+omw),hml/2+bl+oml+bw/(2*cos(60)),mt

k,45,hmw/2+bl+omw,bw/2,0
k,46,hmw/2+bl+omw,bw/2,mt

K,47,hmw/2+bl+omw,0,0
K,48,hmw/2+bl+omw,0,mt

V,1,15,16,25,5,17,18,26
V,15,2,11,16,17,6,14,18
V,16,11,27,19,18,14,30,21
V,25,16,19,23,26,18,21,24
V,19,27,3,20,21,30,7,22
V,23,19,20,4,24,21,22,8
save
V,2,9,10,11,6,12,13,14
V,27,28,33,3,30,29,34,7
V,3,33,31,20,7,34,32,22
V,9,47,45,10,12,48,46,13
V,10,45,43,28,13,46,44,29
V,28,43,41,33,29,44,42,34
V,33,41,39,31,34,42,40,32
```

```
V,31,39,37,35,32,40,38,36
save
V,5,17,18,26,49,50,59,58
V,17,6,14,18,50,51,52,59
V,18,14,30,21,59,52,53,60
V,26,18,21,24,58,59,60,57
V,21,30,7,22,60,53,54,55
V,24,21,22,8,57,60,55,56

save
allsel
vglue,all
vsel,s,,,1,14
mat,1
type,1
vmesh,all
!vsel,all
!vatt,1,,1
!vmesh,all
!nummrg,all
vsel,s,,,14,20
mat,2
type,1

vmesh,all
wsort,,,RMS
waves,rms
finish
save

/solu
/nerr,
tunif,twp
nsel,s,loc,x,hmw/2+bl+omw
d,all,temp,twp
!f,all,heat,-hflux/4
!f,all,heat,hflux/4
nsel,s,loc,y,hml/2+bl+oml
d,all,temp,twp
!f,all,heat,-hflux/4
!f,all,heat,hflux/4
nsel,all
nsel,s,loc,x,0,hmw/2
nsel,r,loc,y,0,hml/2
nsel,r,loc,z,0,mt
!f,all,heat,hfm
bf,all,hgen,hdens
!nsel,r,loc,z,0
!d,all,temp,twp
allsel
nsel,s,loc,z,mt+lt
```

```
sf,all,conv,1270
nsel,s,loc,z,mt
nsel,r,loc,x,hmw/2,hmw/2+bl+omw
nsel,r,loc,y,hml/2,hml/2+bl+oml
sf,all,conv,20
nsel,s,loc,z,0
sf,all,conv,20
allsel
antype,static
lswrite
save
lssolve,1,1,1
finish

/exit
/prep7
etchg

mp,alpx,1,4.65E-6
mp,nuxy,1,0.16
mp,ex,1,440E9

mp,alpx,2,0.5E-6
mp,nuxy,2,0.14
mp,ex,2,70E9
finish

/solu
ldread,temp,,,,,,rth
nsel,s,loc,x,0

d,all,ux,0
nsel,s,loc,y,0
d,all,uy,0
!nsel,s,loc,x,hmw/2+bl+omw
!sf,all,pres,-250E6
!nsel,s,loc,y,hml/2+bl+oml
!sf,all,pres,-250E6
nsel,all
save
solve
finish
```

Appendix C: List of main performed simulations (effects considered are checked with an "X")

No.	Type of simulation	Bridge length / μm	Bridge width / μm	Power cons. / mW	Convection	Thermal conduction through air	File name
1	thermal	100	10	10			h10110n
2	thermal	100	10	20			h10120n
3	thermal	100	10	40			h10140n
4	thermal	100	10	60			h10160n
5	thermal	100	20	10			h10210n
6	thermal	100	20	20			h10220n
7	thermal	100	20	40			h10240n
8	thermal	100	20	60			h10260n
9	thermal	100	40	10			h10410n
10	thermal	100	40	20			h10420n
11	thermal	100	40	40			h10440n
12	thermal	100	40	60			h10460n
13	thermal	100	10	10	X		h15110
14	thermal	100	10	20	X		h15120
15	thermal	100	10	40	X		h15140
16	thermal	100	10	60	X		h15160
17	thermal	100	20	10	X		h15210
18	thermal	100	20	20	X		h15220
19	thermal	100	20	40	X		h15240
20	thermal	100	20	60	X		h15260
21	thermal	100	40	10	X		h15410
22	thermal	100	40	20	X		h15420
23	thermal	100	40	40	X		h15440
24	thermal	100	40	60	X		h15460
25	thermal	150	10	10			h15110n
26	thermal	150	10	20			h15120n
27	thermal	150	10	40			h15140n
28	thermal	150	10	60			h15160n
29	thermal	150	20	10			h15210n
30	thermal	150	20	20			h15220n
31	thermal	150	20	40			h15240n
32	thermal	150	20	60			h15260n
33	thermal	150	40	10			h15410n
34	thermal	150	40	20			h15420n
35	thermal	150	40	40			h15440n
36	thermal	150	40	60			h15460n
37	thermal	150	10	10	X		h15110
38	thermal	150	10	20	X		h15120
39	thermal	150	10	40	X		h15140
40	thermal	150	10	60	X		h15160
41	thermal	150	20	10	X		h15210
42	thermal	150	20	20	X		h15220
43	thermal	150	20	40	X		h15240

No.	Type of simulation	Bridge length / μm	Bridge width / μm	Power cons. / mW	Convection	Thermal conduction through air	File name
44	thermal	150	20	60	X		h15260
45	thermal	150	40	10	X		h15410
46	thermal	150	40	20	X		h15420
47	thermal	150	40	40	X		h15440
48	thermal	150	40	60	X		h15460
49	thermal	100	10	10	X	X	l15110
50	thermal	100	10	20	X	X	l15120
51	thermal	100	10	40	X	X	l15140
52	thermal	100	10	60	X	X	l15160
53	thermal	100	20	10	X	X	l15210
54	thermal	100	20	20	X	X	l15220
55	thermal	100	20	40	X	X	l15240
56	thermal	100	20	60	X	X	l15260
57	thermal	100	40	10	X	X	l15410
58	thermal	100	40	20	X	X	l15420
59	thermal	100	40	40	X	X	l15440
60	thermal	100	40	60	X	X	l15460
61	thermal	150	10	10	X	X	l15110
62	thermal	150	10	20	X	X	l15120
63	thermal	150	10	40	X	X	l15140
64	thermal	150	10	60	X	X	l15160
65	thermal	150	20	10	X	X	l15210
66	thermal	150	20	20	X	X	l15220
67	thermal	150	20	40	X	X	l15240
68	thermal	150	20	60	X	X	l15260
69	thermal	150	40	10	X	X	l15410
70	thermal	150	40	20	X	X	l15420
71	thermal	150	40	40	X	X	l15440
72	thermal	150	40	60	X	X	l15460
73	thermo-mechanical	100	10	10			h10110n
74	thermo-mechanical	100	10	20			h10120n
75	thermo-mechanical	100	10	40			h10140n
76	thermo-mechanical	100	10	60			h10160n
77	thermo-mechanical	100	20	10			h10210n
78	thermo-mechanical	100	20	20			h10220n
79	thermo-mechanical	100	20	40			h10240n
80	thermo-mechanical	100	20	60			h10260n
81	thermo-mechanical	100	40	10			h10410n

No.	Type of simulation	Bridge length / μm	Bridge width / μm	Power cons. / mW	Convection	Thermal conduction through air	File name
82	thermo-mechanical	100	40	20			h10420n
83	thermo-mechanical	100	40	40			h10440n
84	thermo-mechanical	100	40	60			h10460n
85	thermo-mechanical	100	10	10	X		h15110
86	thermo-mechanical	100	10	20	X		h15120
87	thermo-mechanical	100	10	40	X		h15140
88	thermo-mechanical	100	10	60	X		h15160
89	thermo-mechanical	100	20	10	X		h15210
90	thermo-mechanical	100	20	20	X		h15220
91	thermo-mechanical	100	20	40	X		h15240
92	thermo-mechanical	100	20	60	X		h15260
93	thermo-mechanical	100	40	10	X		h15410
94	thermo-mechanical	100	40	20	X		h15420
95	thermo-mechanical	100	40	40	X		h15440
96	thermo-mechanical	100	40	60	X		h15460
97	thermo-mechanical	150	10	10			h15110n
98	thermo-mechanical	150	10	20			h15120n
99	thermo-mechanical	150	10	40			h15140n
100	thermo-mechanical	150	10	60			h15160n
101	thermo-mechanical	150	20	10			h15210n
102	thermo-mechanical	150	20	20			h15220n
103	thermo-mechanical	150	20	40			h15240n
104	thermo-mechanical	150	20	60			h15260n
105	thermo-	150	40	10			h15410n

No.	Type of simulation	Bridge length / μm	Bridge width / μm	Power cons. / mW	Convection	Thermal conduction through air	File name
106	mechanical thermo-mechanical	150	40	20			h15420n
107	thermo-mechanical	150	40	40			h15440n
108	thermo-mechanical	150	40	60			h15460n
109	thermo-mechanical	150	10	10	X		h15110
110	thermo-mechanical	150	10	20	X		h15120
111	thermo-mechanical	150	10	40	X		h15140
112	thermo-mechanical	150	10	60	X		h15160
113	thermo-mechanical	150	20	10	X		h15210
114	thermo-mechanical	150	20	20	X		h15220
115	thermo-mechanical	150	20	40	X		h15240
116	thermo-mechanical	150	20	60	X		h15260
117	thermo-mechanical	150	40	10	X		h15410
118	thermo-mechanical	150	40	20	X		h15420
119	thermo-mechanical	150	40	40	X		h15440
120	thermo-mechanical	150	40	60	X		h15460
121	thermo-mechanical	100	10	10	X	X	l15110
122	thermo-mechanical	100	10	20	X	X	l15120
123	thermo-mechanical	100	10	40	X	X	l15140
124	thermo-mechanical	100	10	60	X	X	l15160
125	thermo-mechanical	100	20	10	X	X	l15210
126	thermo-mechanical	100	20	20	X	X	l15220
127	thermo-mechanical	100	20	40	X	X	l15240
128	thermo-mechanical	100	20	60	X	X	l15260

No.	Type of simulation	Bridge length / μm	Bridge width / μm	Power cons. / mW	Convection	Thermal conduction through air	File name
129	thermo-mechanical	100	40	10	X	X	l15410
130	thermo-mechanical	100	40	20	X	X	l15420
131	thermo-mechanical	100	40	40	X	X	l15440
132	thermo-mechanical	100	40	60	X	X	l15460
134	thermo-mechanical	150	10	10	X	X	l15110
135	thermo-mechanical	150	10	20	X	X	l15120
135	thermo-mechanical	150	10	40	X	X	l15140
136	thermo-mechanical	150	10	60	X	X	l15160
137	thermo-mechanical	150	20	10	X	X	l15210
138	thermo-mechanical	150	20	20	X	X	l15220
139	thermo-mechanical	150	20	40	X	X	l15240
140	thermo-mechanical	150	20	60	X	X	l15260
141	thermo-mechanical	150	40	10	X	X	l15410
142	thermo-mechanical	150	40	20	X	X	l15420
143	Thermo-mechanical	150	40	40	X	X	l15440
144	Thermo-mechanical	150	40	60	X	X	l15460
145	Thermal, Small λ	150	10	10	X	X	Hl15110
146	Thermal, Small λ	150	10	20	X	X	Hl15120
147	Thermal, Small λ	150	10	40	X	X	Hl15140
148	Thermal, Small λ	150	10	60	X	X	Hl15160
149	Thermal, Small λ	150	20	10	X	X	Hl15210
150	Thermal, Small λ	150	20	20	X	X	Hl15220
151	Thermal, Small λ	150	20	40	X	X	Hl15240
152	Thermal,	150	20	60	X	X	Hl15260

No.	Type of simulation	Bridge length / μm	Bridge width / μm	Power cons. / mW	Convection	Thermal conduction through air	File name
153	Small λ Thermal,	150	40	10	X	X	Hl15410
154	Small λ Thermal,	150	40	20	X	X	Hl15420
155	Small λ Thermal,	150	40	40	X	X	Hl15440
156	Small λ Thermal,	150	40	60	X	X	Hl15460
157	Small λ Thermal,	150	10	10	X	X	Hh15110
158	Large λ Thermal,	150	10	20	X	X	Hh15120
159	Large λ Thermal,	150	10	40	X	X	Hh15140
160	Large λ Thermal,	150	10	60	X	X	Hh15160
161	Large λ Thermal,	150	20	10	X	X	Hh15210
162	Large λ Thermal,	150	20	20	X	X	Hh15220
163	Large λ Thermal,	150	20	40	X	X	Hh15240
164	Large λ Thermal,	150	20	60	X	X	Hh15260
165	Large λ Thermal,	150	40	10	X	X	Hh15410
166	Large λ Thermal,	150	40	20	X	X	Hh15420
167	Large λ Thermal,	150	40	40	X	X	Hh15440
168	Large λ Thermal,	150	40	60	X	X	Hh15460
	Large λ						

Appendix D: Ansys 5.3 simulation source code: electrical simulations

```
/batch
/prep7
/title, electrical model of micro hotplate with high resistance

et,1,67,,,0

res=10E-2

mp,rsvx,1,res
mp,rsvy,1,res

u0=24
u1=0
lm=100E-6
bm=100E-6
ls=150E-6
bs=10E-6

k,1,0,0
k,2,bm,0
k,3,bm,lm
k,4,0,lm

k,5,bm,(lm-bs)/2
k,6,bm+ls,(lm-bs)/2
k,7,bm+ls,(lm+bs)/2
k,8,bm,(lm+bs)/2

k,9,0,(lm-bs)/2
k,10,-ls,(lm-bs)/2
k,11,-ls,(lm+bs)/2
k,12,0,(lm+bs)/2
save
k,13,bm+ls*0.5,lm+ls*0.886
k,14,bm+ls*0.5+0.886*bs,lm+ls*0.886-0.5*bs
k,15,bm,lm-0.7*bs
k,16,bm-0.7*bs,lm
k,17,bm+ls*0.5-0.886*bs,lm+ls*0.886+0.5*bs

k,20,bm+ls*0.5,-ls*0.886
k,22,bm+ls*0.5+0.886*bs,-ls*0.886+0.5*bs
k,21,bm,0.7*bs
k,18,bm-0.7*bs,0
k,19,bm+ls*0.5-0.886*bs,-ls*0.886-0.5*bs

k,25,-ls*0.5,-ls*0.886
k,24,-ls*0.5-0.886*bs,-ls*0.886+0.5*bs
```

```
k,23,0,0.7*bs
k,27,0.7*bs,0
k,26,-ls*0.5+0.886*bs,-ls*0.886-0.5*bs

k,30,-ls*0.5,lm+ls*0.886
k,31,-ls*0.5-0.886*bs,lm+ls*0.886-0.5*bs
k,32,0,lm-0.7*bs
k,28,0.7*bs,lm
k,29,-ls*0.5+0.886*bs,lm+ls*0.886+0.5*bs

save
a,1,2,3,4
a,5,6,7,8
a,9,10,11,12
a,3,15,14,13
a,3,13,17,16
save
a,18,19,20,2
a,2,20,22,21
a,1,25,26,27
a,23,24,25,1

a,4,28,29,30
a,30,31,32,4
!aglue,all
nummrg,all
esize,5e-6
save
!aglue,all
nummrg,all

allsel
amesh,all

!nsel,s,loc,x,0,2e-6
!nsel,r,loc,y,(lm-bs)/2,(lm+bs)/2

!cp,1,volt,all

!allsel

!nsel,s,loc,x,bm-2e-6,bm
!nsel,r,loc,y,(lm-bs)/2,(lm+bs)/2

!cp,2,volt,all

allsel
wsort,,,,rms
waves,rms
finish
```

```
/solu

antype,static

nsel,s,loc,x,0,2e-6
nsel,r,loc,y,(lm-bs)/2,(lm+bs)/2

d,all,volt,u1

allsel

nsel,s,loc,x,bm-2e-6,bm
nsel,r,loc,y,(lm-bs)/2,(lm+bs)/2

d,all,volt,u0

allsel

nsel,s,loc,x,lm+ls
d,all,volt,u1

allsel

nsel,s,loc,x,-ls,-ls
d,all,volt,u1

allsel

lsel,s,,,15,,,1
d,all,volt,u1
allsel
lsel,s,,,17,,,1
d,all,volt,u1
allsel
lsel,s,,,21,,,1
d,all,volt,u1
allsel
lsel,s,,,24,,,1
d,all,volt,u1
allsel
lsel,s,,,28,,,1
d,all,volt,u1
allsel
lsel,s,,,32,,,1
d,all,volt,u1
allsel
lsel,s,,,36,,,1
d,all,volt,u1
allsel
lsel,s,,,38,,,1
d,all,volt,u1
```

```
allsel

save
lswrite

lssolve,1,1,1
save
```

-Prozeßprotokoll LEGUAN Mikroheizer-

Hochohmige SiC - Variante

ProtokollNummer
10/99

Wafer

Okmetic	771/40393		50	Test	100 mm <100>
Substrat:	390 µm n/P	3-5 Ωcm			
Oberflächen:	poliert/poliert				

Nr.	Prozeßschritt	Teilschritte	Parameter	Werte	Bemerkungen, Datum - Unterschrift
1.0.	**Eingangs-Reinigung**	H_2SO_4 / H_2O_2	Temperatur [°C]: Zeit [min.]:	120 7	rechtes Becken
		Leitwertspülen			
		Rinser Dryer	99s / 111s / 222s		
2.0.	**Oxidation**	**Oxidation** feucht soll: **500 nm ± 2 nm**	Prozeßname: Prozeßtemperatur [°C]: Prozeßzeit [min]: Rohr-Nr.: Fahrt Nr.: Abstand der Wafer bei Ox.:	FOX1000 1000 1h 26m 1B4	
		Messung Oxiddicke	n (Ellipsometer): Programm (MPV):	45	

	Links			Mitte-Links			Mitte Rechts			Rechts		
	W.-Nr. L:	W.-Nr. M:	W.-Nr. R:	W.-Nr. L:	W.-Nr. M:	W.-Nr. R:	W.-Nr. L:	W.-Nr. M:	W.-Nr. R:	W.-Nr. L:	W.-Nr. M:	W.-Nr. R:
d [nm]												
δ [nm]												
Min												
Max												

Nr.	Prozeßschritt	Teilschritte	Parameter	Werte	Bemerkungen, Datum - Unterschrift
3.0.	**Fototechnik**	**Belacken: EATON**	Fotolack: Prozeßname:	AZ 1514 PSXi 5000	Prebake 30 min 100°C im Ofen
"SiC- Strukt. FS"		**Belichten: MA 150** Maske: SiC-Strukt. FS Justiermarke: 1	Programm: Belichtungszeit [s]: Lichtleistung 405nm [mW/cm²]: Anzeige CL2:	3 8 250 20	
		Entwickeln	manuell im Entwicklerbecken	1m 30s	kontinuierlich schwenken
		Inspektion	Strukturbreite Maske: (Steg im Justierkreuz) Strukturbreite Lack: bei Abweichung > 0.3µm neue Fototechnik	10µm	
4.0.	**Strukturierung Oxid**	**Ätzen PECVD Oxid** - (VACUTEC)	Prozeßname: Prozeßzeit: SF_6-Fluß [sccm]: Druck [mTorr]: Leistung [W]:	Nitrid-Etch 4 m 20 150 150	Strukturen ca. 120 nm in das Oxid Ätzen, um bei den Schnipseln Vorder- und Rückseite justieren zu können.
		Inspektion	Ätzrate PE- Oxid:		
5.0.	**Lack entfernen**	**Remover 1**	Prozeßzeit [min]:	5	
		Remover 2	Prozeßzeit [min]:	2,5	
		Leitwertspülen			
		Rinser Dryer	99 / 111 / 222 s		
		Inspektion	Mikroskop (Dunkelfeld)		bei Resten: Veraschen 2 min in Vacutec
6.0.	**Fototechnik**	**Belacken: EATON** Rückseite	Fotolack: Prozeßname:	AZ 1514 PSXi 5000	Prebake 30 min 100 °C im Ofen

Nr. Prozeßschritt	Teilschritte	Parameter	Werte	Bemerkungen, Datum - Unterschrift
"SiC-Strukt. BS" Rückseite	**Belichten: MA 25** Maske RS: SiC-Strukt. BS Maske VS: SiC-Strukt. FS Justiermarke: 1	Belichtungszeit [s]: Lichtleistung 405nm [mW/cm²]: Anzeige CL2: Belichtungsabstand: eingetragene Waferdicke:	18 350 50 µm 500 µm	
	Entwickeln	manuell im Entwicklerbecken	1m 30s	kontinuierlich schwenken
	Inspektion	Strukturbreite Maske: (Steg im Justierkreuz) Strukturbreite Lack: bei Abweichung > 0.3 µm neue Fototechnik	10µm	
7.0. Strukturierung Oxid	**Ätzen PECVD Oxid** - (VACUTEC)	Prozeßname: Prozeßzeit: SF_6-Fluß [sccm]: Druck [mTorr]: Leistung [W]:	Nitrid-Etch 4 m 20 150 150	Strukturen ca. 120 nm in das Oxid Ätzen, um bei den Schnipseln Vorder- und Rückseite justieren zu können.
	Inspektion	Ätzrate PE-Oxid: Ätzrate PE-Nitrid:		
8.0. Lack	**Remover 1**	Prozeßzeit [min]:	5	
entfernen	**Remover 2**	Prozeßzeit [min]:	2,5	
	Leitwertspülen			
	Rinser Dryer	99 / 111 / 222 s		
	Inspektion	Mikroskop (Dunkelfeld)		bei Resten: Veraschen 2 min in Vacutec
9.0. Wafer sägen	**Folie aufkleben**	Folienseite (VS: Vorderseite; RS: Rückseite)	VS	

Nr.	Prozeßschritt	Teilschritte	Parameter	Werte	Bemerkungen, Datum - Unterschrift
		Sägen	Programm: Sägeblatt: Sägeblatthalterung [mm]: Sägegeschw.: Step 1 [µm]: Step 2 [µm]: Wasserdruck:	 Si 15 40.000 20.000 reduziert	Hier werden die Wafer in $2 \times 4\ cm^2$ große Schnipsel zur SiC-Beschichtung gesägt Testfelder möglichst an Sägekante. Darauf achten, daß auf allen Schnipseln genügend Justierkreuze sind.
		Reinigen und Trocknen	manuell		Mit Spritzpistole und N_2-Pistole.
		Folie abziehen			
		Inspektion	Partikel Ausbrüche		
10.0. Verpacken		**Proben verpacken**	Stoßsicherheit prüfen		Verschicken an Martin Eyckhoff
11.0. LPCVD-SiC		**LPCVD-SiC-Abscheidung** soll: **1000 nm**	Prozeßname: Prozeßtemperatur [°C]: Prozeßzeit [min, sec]: Rohr-Nr.: Fahrt Nr.: Abstand der Wafer bei Prozeß:	 1200	Polykristalline / amorphe 3C-SiC-Schichten werden bei DaimlerChrysler München abgeschieden (Martin Eyckhoff).
		Messung Nitriddicke	n (Ellipsometer): Programm (MPV):		

		Links			**Mitte**			**Rechts**		
		W.-Nr. L:	W.-Nr. M:	W.-Nr. R:	W.-Nr. L:	W.-Nr. M:	W.-Nr. R:	W.-Nr. L:	W.-Nr. M:	W.-Nr. R:
	d [nm]									

Nr.	Prozeßschritt	Teilschritte	Parameter	Werte	Bemerkungen, Datum - Unterschrift

	δ [nm]									
	Min									
	Max									

12.0. Oxidation	**Oxidation** trocken soll: 100 nm ± 2 nm	Prozeßname: Prozeßtemperatur [°C]: Prozeßzeit [min]: Rohr-Nr.: 3.5 l / min N_2 (Aufheizen) 3.6 l / min O_2 (Oxidation) 3.5 l / min (Abkühlen)	 1100 2h 30m	Oxidation im kleinen Temperrohr (Etage 2).
	Messung Oxiddicke	n (Ellipsometer): Programm (MPV):		
13.0.Oxidmaske	**PECVD-SiO_2-Abscheidung** (VACUTEC) Dicke soll: **400 nm**	Temperatur [°C] Prozeßname: Oxid Prozeßzeit: SiH_4-Fluß [sccm]: N_2O -Fluß [sccm]: N_2 -Fluß [sccm]: RF-Leistung: Druck [mTorr]	350 Oxid 350°C 50 1.5 600 350 10 800	
	Inspektion	Partikel		

Nr. Prozeßschritt	Teilschritte	Parameter	Werte	Bemerkungen, Datum - Unterschrift
14.0. Fototechnik	**Belacken: manuell**	Fotolack: Zeit 1 / s Umdrehungen 1 / rpm Zeit 2 / s: Umdrehungen 2 / rpm	AZ 1514 10 1000 20 3000	Randentlackung manuell, Prebake in liegendem Teflon-Carrier im Ofen (35 min, 100 °C).
"Passopen SiO_2 "	**Belichten: MA 4** Maske: Passopen SiO_2 Justiermarke: 2	Programm: Belichtungszeit [s]: Lichtleistung 405nm [mW/cm²]: Anzeige CL2:	10	Sägefolie auf dem Chuck aufkleben, Schlitze mit Skalpell dort ziehen, wo die Proben liegen, damit das Vakuum angezogen werden kann. Leicht überbelichten.
	Entwickeln	manuell im Tauchbad	1m 30s	Spülen und Trocknen manuell mit Spritz- und N_2-Pistole. Postbake in flach liegendem Teflon-Carrier im Ofen (125°C, 35 min).
	Inspektion	Strukturbreite Maske: (Steg im Justierkreuz) Strukturbreite Lack: bei Abweichung > 0.3 µm neue Fototechnik	10 µm	
15.0. Oxid ätzen	**Ammoniumfl. - Tauchbad**	aktuelle Ätzrate [nm/min]: Temperatur [°C]: Zeit: [min]	 32 °C 4	Ätzrate überprüfen Oxid über dem SiC komplett entfernen.
	Leitwertspülen	manuell		Hydrophobietest
16.0. Lack	**Remover 1**	Prozeßzeit [min]:	5	alternativ eigenes Removerbad auf Heizplatte (65 °C, 8 m)
entfernen	**Remover 2**	Prozeßzeit [min]:	2,5	
	Leitwertspülen	manuell		Spülen und Trocknen manuell mit Spritz- und N_2-Pistole.
	Inspektion	Mikroskop (Dunkelfeld)		bei Resten: Veraschen 2 min in Vacutec

Nr. Prozeßschritt	Teilschritte	Parameter	Werte	Bemerkungen, Datum - Unterschrift
17.0. Hoch-temperatur-Implantation	**Implantation: N** Energie [keV]: **80** Dosis [At/cm^2]: 1E15 Temperatur [°C]: 800	Prozeßname: Maske: Lack Strom [µA]:		Reinigung in H_2SO_4 / H_2O_2 Lackentfernung notwendig Implantation im FZ Rossendorf (Dr.)
18.0. Sputtern Al	**Sputtern Al** **MRC** soll: **(1,2 ±0,1) µm**	Prozeßname: DC-Power [kW]: Argon-Druck [mTorr]: Vorsputtern [s]: Scan-Speed [cm/min]: Anzahl der Scans:	3 7 15 30 18 4	Sputtern der Al-Maske für das SiC-Ätzen. Hierzu spezielle Halterung für Schnipsel an der dafür vorgesehenen Palette der MRC befestigen.
19.0. Fototechnik	**Belacken: manuell**	Fotolack: Zeit 1 / s Umdrehungen 1 / rpm Zeit 2 / s: Umdrehungen 2 / rpm	AZ 1514 10 1000 20 3000	Randentlackung manuell, Prebake in liegendem Teflon-Carrier im Ofen (35 min, 100 °C).
"SiC-Strukt. FS"	**Belichten: MA 4** Maske: SiC-Strukt. FS Justiermarke: 1	Programm: Belichtungszeit [s]: Lichtleistung 405nm [mW/cm^2]: Anzeige CL2:	8	Sägefolie auf dem Chuck aufkleben, Schlitze mit Skalpell dort ziehen, wo die Proben liegen, damit das Vakuum angezogen werden kann.
	Entwickeln	manuell im Tauchbad	1m 30s	Spülen und Trocknen manuell mit Spritz- und N_2-Pistole. Postbake in flach liegendem Teflon-Carrier im Ofen (125°C, 35 min).
	Inspektion	Strukturbreite Maske: (Steg im Justierkreuz) Strukturbreite Lack: bei Abweichung > 0,3 µm neue Fototechnik	10 µm	

Nr.	Prozeßschritt	Teilschritte	Parameter	Werte	Bemerkungen, Datum - Unterschrift
20.0.	**Al - Strukturierung**	**Ätzen Aluminium** (Tauchbad)	Temperatur: Ätzzeit: (Badbewegung ein)	40°C	Strukturieren der Al-Maske
		Leitwertspülen	manuell		Spülen und Trocknen manuell mit Spritz- und N_2-Pistole.
		Dip in der Poly-Ätze	Temperatur: Ätzzeit (ca. 5 s):	RT	ggf. weglassen.
		Leitwertspülen			Spülen und Trocknen manuell mit Spritz- und N_2-Pistole.
		Inspektion	Breite Al Steg: (Steg Justierkreuz)		
21.0.	**Lack entfernen**	**Remover 1**	Prozeßzeit [min]:	5	alternativ eigenes Removerbad auf Heizplatte (65 °C, 8 m)
		Remover 2	Prozeßzeit [min]:	2,5	
		Leitwertspülen	manuell		Spülen und Trocknen manuell mit Spritz- und N_2-Pistole.
		Inspektion	Mikroskop (Dunkelfeld)		bei Resten: Veraschen 2 min in Vacutec

Nr.	Prozeßschritt	Teilschritte	Parameter	Werte	Bemerkungen, Datum - Unterschrift
22.0.	**Strukturierung SiC**	**Ätzen SiC** - (VACUTEC)	Prozeßname: Prozeßzeit: O_2-Fluß [sccm]: SF_6-Fluß [sccm]: Druck [mTorr]: Leistung [W]:	SiC 100% 45 + 30 m 20 4 150 200	Zuvor Dicke der Al-Maske mit dem Tencor / Dektak nachmessen. 45 min Ätzen und dann Ätzrate prüfen. Ätzzeit für das Nachätzen einstellen (ca. 30 min). Hierbei sollen 300 nm Oxid, 1000 nm SiC sowie ca. 300 nm des darunter liegenden Feuchtoxides geätzt werden. NICHT bis in das Si ätzen(!), da die hohe Ätzrate tiefe Gruben verursacht, die eine gute Fototechnik unmöglich machen. Al-Elektrode ersetzen durch Graphit-Elektrode. VORSICHT, sehr zerbrechlich, also nicht den Schraubenzieher ansetzen! Nach Benutzung Rückbau und Wegräumen der Graphit-Elektrode.
23.0.	**Sputtern Al Rückseite**	**Sputtern Al** **MRC** soll: **(1,2 ±0,1) µm**	Prozeßname: DC-Power [kW]: Argon-Druck [mTorr]: Vorsputtern [s]: Scan-Speed [cm/min]: Anzahl der Scans:	3 7 15 30 18 4	Sputtern der Al-Maske für das SiC-Ätzen. Hierzu spezielle Halterung für Schnipsel an der dafür vorgesehenen Palette der MRC befestigen.
24.0.	**Fototechnik**	**Belacken: manuell**	Fotolack: Zeit 1 / s Umdrehungen 1 / rpm Zeit 2 / s: Umdrehungen 2 / rpm	AZ 1514 10 1000 20 3000	Randentlackung manuell, Prebake in liegendem Teflon-Carrier im Ofen (35 min, 100 °C).

Nr. Prozeßschritt	Teilschritte	Parameter	Werte	Bemerkungen, Datum - Unterschrift
"SiC-Strukt. BS"	**Belichten: MA 4** Maske: SiC-BS Justiermarke: 1	Programm: Belichtungszeit [s]: Lichtleistung 405nm [mW/cm²]: Anzeige CL2:	8	Sägefolie auf dem Chuck aufkleben, Schlitze mit Skalpell dort ziehen, wo die Proben liegen, damit das Vakuum angezogen werden kann.
	Entwickeln	manuell im Tauchbad	1m 30s	Spülen und Trocknen manuell mit Spritz- und N_2-Pistole. Postbake in flach liegendem Teflon-Carrier im Ofen (125°C, 35 min).
	Inspektion	Strukturbreite Maske: (Steg im Justierkreuz) Strukturbreite Lack: bei Abweichung > 0.3 µm neue Fototechnik	10 µm	
25.0. Al - Strukturierung	**Ätzen Aluminium** (Tauchbad)	Temperatur: Ätzzeit: (Badbewegung ein)	40°C	
	Leitwertspülen	manuell		Spülen und Trocknen manuell mit Spritz- und N_2-Pistole.
	Inspektion	Breite Al Steg: (Steg Justierkreuz)		
26.0. Lack	**Remover 1**	Prozeßzeit [min]:	5	alternativ eigenes Removerbad auf Heizplatte (65 °C, 8 m)
entfernen	**Remover 2**	Prozeßzeit [min]:	2,5	
	Leitwertspülen	manuell		
	Inspektion	Mikroskop (Dunkelfeld)		bei Resten: Veraschen 2 min in Vacutec

Nr. Prozeßschritt	Teilschritte	Parameter	Werte	Bemerkungen, Datum - Unterschrift
27.0. Strukturierung SiC	**Ätzen SiC** - (VACUTEC)	Prozeßname: Prozeßzeit: O_2-Fluß [sccm]: SF_6-Fluß [sccm]: Druck [mTorr]: Leistung [W]:	SiC 100% 45 + 30 m 20 4 150 200	Zuvor Dicke der Al-Maske mit dem Tencor / Dektak nachmessen. 45 min Ätzen und dann Ätzrate prüfen. Ätzzeit für das Nachätzen einstellen (ca. 30 min). Hierbei soll durch 300 nm Oxid, 1000 nm SiC und 500 nm des darunter liegenden Feuchtoxides bis knapp in das Si geätzt werden. Al-Elektrode ersetzen durch Graphit-Elektrode. VORSICHT, sehr zerbrechlich, also nicht den Schraubenzieher ansetzen! Nach Benutzung Rückbau und Wegräumen der Graphit-Elektrode.
	Inspektion	Ätzrate SiC:		
28.0.Passivierung	**PECVD-Si_3N_4-Abscheidung** (VACUTEC) Dicke soll: **500nm**	Temperatur [°C] Prozeßname: Nitrid Prozeßzeit: SiH_4-Fluß [sccm]: NH_3-Fluß [sccm]: N_2-Fluß [sccm]: RF-Leistung: Druck [mTorr]	350 Nitrid 350°C 50 5.3 3.0 450 10 800	
	Inspektion	Partikel		

Nr. Prozeßschritt	Teilschritte	Parameter	Werte	Bemerkungen, Datum - Unterschrift
29.0. Fototechnik	**Belacken: manuell**	Fotolack: Zeit 1 / s Umdrehungen 1 / rpm Zeit 2 / s: Umdrehungen 2 / rpm	AZ 1514 10 1000 20 3000	Randentlackung manuell, Prebake in liegendem Teflon-Carrier im Ofen (35 min, 100 °C).
"PSG Strukt."	**Belichten: MA 4** Maske: PSG Strukt. Justiermarke: 4	Programm: Belichtungszeit [s]: Lichtleistung 405nm [mW/cm²]: Anzeige CL2:	8	Sägefolie auf dem Chuck aufkleben, Schlitze mit Skalpell dort ziehen, wo die Proben liegen, damit das Vakuum angezogen werden kann.
	Entwickeln	manuell im Tauchbad	1m 30s	Spülen und Trocknen manuell mit Spritz- und N_2-Pistole. Postbake in flach liegendem Teflon-Carrier im Ofen (125°C, 35 min).
	Inspektion	Strukturbreite Maske: (Steg im Justierkreuz) Strukturbreite Lack: bei Abweichung > 0.3 µm neue Fototechnik	10 µm	
30.0. Strukturierung Passivierung	**Ätzen PECVD Nitrid-** (VACUTEC)	Prozeßname: Prozeßzeit: SF_6-Fluß [sccm]: Druck [mTorr]: Leistung [W]:	Nitrid-Etch 1m 15s 20 150 150	Ätzrate überprüfen
	Inspektion	Ätzrate PE-Oxid: Ätzrate PE-Nitrid:		
31.0. Lack	**Remover 1**	Prozeßzeit [min]:	5	alternativ eigenes Removerbad auf Heizplatte (65 °C, 8 m)
entfernen	**Remover 2**	Prozeßzeit [min]:	2,5	
	Leitwertspülen			

Nr.	Prozeßschritt	Teilschritte	Parameter	Werte	Bemerkungen, Datum - Unterschrift
29.0.	**Fototechnik**	**Belacken: manuell**	Fotolack: Zeit 1 / s Umdrehungen 1 / rpm Zeit 2 / s: Umdrehungen 2 / rpm	AZ 1514 10 1000 20 3000	Randentlackung manuell, Prebake in liegendem Teflon-Carrier im Ofen (35 min, 100 °C).
	"PSG Strukt."	**Belichten: MA 4** Maske: PSG Strukt. Justiermarke: 4	Programm: Belichtungszeit [s]: Lichtleistung 405nm [mW/cm²]: Anzeige CL2:	8	Sägefolie auf dem Chuck aufkleben, Schlitze mit Skalpell dort ziehen, wo die Proben liegen, damit das Vakuum angezogen werden kann.
		Entwickeln	manuell im Tauchbad	1m 30s	Spülen und Trocknen manuell mit Spritz- und N_2-Pistole. Postbake in flach liegendem Teflon-Carrier im Ofen (125°C, 35 min).
		Inspektion	Strukturbreite Maske: (Steg im Justierkreuz) Strukturbreite Lack: bei Abweichung > 0.3µm neue Fototechnik	10 µm	
30.0.	**Strukturierung Passivierung**	**Ätzen PECVD Nitrid-** (VACUTEC)	Prozeßname: Prozeßzeit: SF_6-Fluß [sccm]: Druck [mTorr]: Leistung [W]:	Nitrid-Etch 1m 15s 20 150 150	Ätzrate überprüfen
		Inspektion	Ätzrate PE-Oxid: Ätzrate PE-Nitrid:		
31.0.	**Lack**	**Remover 1**	Prozeßzeit [min]:	5	alternativ eigenes Removerbad auf Heizplatte (65 °C, 8 m)
	entfernen	**Remover 2**	Prozeßzeit [min]:	2,5	
		Leitwertspülen			

Nr. Prozeßschritt	Teilschritte	Parameter	Werte	Bemerkungen, Datum - Unterschrift
	Entwickeln	manuell im Tauchbad	1m 30s	Spülen und Trocknen manuell mit Spritz- und N_2-Pistole. Postbake in flach liegendem Teflon-Carrier im Ofen (125°C, 35 min).
	Inspektion	Strukturbreite Maske: (Steg im Justierkreuz) Strukturbreite Lack: bei Abweichung > 0.3 µm neue Fototechnik	10 µm	
34.0. Galvanik Au	**Galvanik Au**	Temperatur: Fläche: Stromstärke [mA]: Zeit:	60°C	
	Inspektion	Dicke (Tencor) Mitte Ra: Underplating:	Rand	
35.0. Lack	**Remover 1**	Prozeßzeit [min]:	5	alternativ eigenes Removerbad auf Heizplatte (65 °C, 8 m)
entfernen	**Remover 2**	Prozeßzeit [min]:	2,5	
	Leitwertspülen			
	Rinser Dryer	99 / 111 / 222 s		
	Inspektion	Mikroskop (Dunkelfeld)		bei Resten: Veraschen 2 min in Vacutec
36.0. Fototechnik	**Belacken: manuell**	Fotolack: Zeit 1 / s Umdrehungen 1 / rpm Zeit 2 / s: Umdrehungen 2 / rpm	AZ 1514 10 1000 20 3000	Randentlackung manuell, Prebake in liegendem Teflon-Carrier im Ofen (35 min, 100 °C).

Nr. Prozeßschritt	Teilschritte	Parameter	Werte	Bemerkungen, Datum - Unterschrift
"Au/TiWN Neu"	**Belichten: MA 4** Maske: Au/TiWN Neu Justiermarke: 5	Programm: Belichtungszeit [s]: Lichtleistung 405nm [mW/cm²]: Anzeige CL2:	10	Sägefolie auf dem Chuck aufkleben, Schlitze mit Skalpell dort ziehen, wo die Proben liegen, damit das Vakuum angezogen werden kann. Leicht überbelichten.
	Entwickeln	manuell im Tauchbad	1m 30s	Spülen und Trocknen manuell mit Spritz- und N_2-Pistole. Postbake in flach liegendem Teflon-Carrier im Ofen (125°C, 35 min).
	Inspektion	Strukturbreite Maske: (Steg im Justierkreuz) Strukturbreite Lack: bei Abweichung > 0.3 µm neue Fototechnik	10 µm	
37.0. Strukturierung TiWN - Au	**Gold ätzen in JKJ_2 -Ätze**	Temperatur: Ätzzeit:	21 °C	leicht schwenken
	Inspektion	Unterätzung Lack:		
	TiWN ätzen in H_2O	Temperatur: Ätzzeit:	40°C	leicht schwenken
	Inspektion	Unterätzung:		
38.0. Lack entfernen	**Remover 1**	Prozeßzeit [min]:	5	alternativ eigenes Removerbad auf Heizplatte (65 °C, 8 m)
	Remover 2	Prozeßzeit [min]:	2,5	
	Leitwertspülen			
	Inspektion	Mikroskop (Dunkelfeld)		bei Resten: Veraschen 2 min in Vacutec

Nr. Prozeßschritt	Teilschritte	Parameter	Werte	Bemerkungen, Datum - Unterschrift
39.0.Passivierung	**PECVD-Si_3N_4-Abscheidung** (VACUTEC) Dicke soll: **600nm**	Temperatur [°C] Prozeßname: Nitrid Prozeßzeit: SiH_4-Fluß [sccm]: NH_3-Fluß [sccm]: N_2-Fluß [sccm]: RF-Leistung: Druck [mTorr]	350 Nitrid 350°C 70 5.3 3.0 450 10 800	Testschnipsel zur Dickenbestimmung mit in die Anlage legen.
	Inspektion	Partikel		
40.0. Fototechnik	**Belacken: manuell**	Fotolack: Zeit 1 / s Umdrehungen 1 / rpm Zeit 2 / s: Umdrehungen 2 / rpm	AZ 1514 10 1000 20 3000	Randentlackung manuell, Prebake in liegendem Teflon-Carrier im Ofen (35 min, 100 °C).
"Pass. Neu	**Belichten: MA 4** Maske: Pass.Neu Justiermarke: 7	Programm: Belichtungszeit [s]: Lichtleistung 405nm [mW/cm²]: Anzeige CL2:	10	Sägefolie auf dem Chuck aufkleben, Schlitze mit Skalpell dort ziehen, wo die Proben liegen, damit das Vakuum angezogen werden kann. Leicht überbelichten.
	Entwickeln	manuell im Tauchbad	1m 30s	Spülen und Trocknen manuell mit Spritz- und N_2-Pistole. Postbake in flach liegendem Teflon-Carrier im Ofen (125°C, 35 min).
	Inspektion	Strukturbreite Maske: (Steg im Justierkreuz) Strukturbreite Lack: bei Abweichung > 0.3 µm neue Fototechnik	10 µm	

Nr. Prozeßschritt	Teilschritte	Parameter	Werte	Bemerkungen, Datum - Unterschrift
41.0. Strukturierung Passivierung	**Ätzen PECVD-Nitrid** (VACUTEC)	Prozeßname: Prozeßzeit: SF_6-Fluß [sccm]: Druck [mTorr]: Leistung [W]:	Nitrid-Etch 1m 15s 20 150 150	Ätzrate überprüfen mit Hilfe des bei der Abscheidung beschichteten Testschnipsels.
	Inspektion	Ätzrate PE-Oxid: Ätzrate PE-Nitrid:		
42.0. Lack	**Remover 1**	Prozeßzeit [min]:	5	alternativ eigenes Removerbad auf Heizplatte (65 °C, 8 m)
entfernen	**Remover 2**	Prozeßzeit [min]:	2,5	
	Leitwertspülen			
	Rinser Dryer	99 / 111 / 222 s		
	Inspektion	Mikroskop (Dunkelfeld)		bei Resten: Veraschen 2 min in Vacutec
43.0. Anisotropes	**Aufwachsen**	Wachsart:	Tabletten (altes)	Viertel-Glaswafer für Schnipsel verwenden.
Ätzen	**Oxid entfernen**	Ammoniumfluorid (32 °C) Ätzzeit:	 90 s	(speziell angesetzte Lsg. verwenden - nicht Prozeßbecken in der Ätztechnik verwenden!)
	Spülen in DI-Wasser (mit Hand)	Transport zur KOH in DI Wasser Vorwärmen in DI-Wasser		
	KOH / IPA-Ätzen	Becken: T[°C] ρ g/cm^3] bei 20 °C vermutliche Ätzzeit: rein [Uhrzeit]:	IPA 80 6h 30m	auf Zeit ätzen, nachmessen nach 3h und 6h.

Nr. Prozeßschritt	Teilschritte	Parameter	Werte	Bemerkungen, Datum - Unterschrift
	erste Kontrolle spülen, trocknen, Messen	raus 1 [Uhrzeit]: Ätztiefe (Stahl) [µm]: rein 2 [Uhrzeit]:		
	zweite Kontrolle spülen, trocknen, Messen	raus 2 [Uhrzeit]: Ätztiefe (Stahl) [µm]: rein 3 [Uhrzeit]:		
	dritte Kontrolle spülen, trocknen, Messen	raus 3 [Uhrzeit]: Ätztiefe (Stahl) [µm]:		
	Inspektion	Gesamtätzzeit: Ätzrate: Unterätzung:		
	Spülen in DI-Wasser **Trocknen (N_2)**	(mit Hand)		
	Wachs entfernen	abwachsen 2 X in TCE spülen Trocknen (N_2)		ggf. in Carot'scher Lösung nachreinigen (H_2SO_4 / H_2O_2)
	Inspektion	defekte Membranen defekte Strukt. Vorderseite		markieren in den einzelnen Wafermap
44.0. Chips vereinzeln	**Vereinzeln**	Brechen der Chips		
	Inspektion	Partikel Ausbrüche		

Prozeßprotokoll LEGUAN Mikroheizer-

Niederohmige HfB_2 - Variante

Protokollnummer	Wafer							
10/99		Okmetic	771/40393		50	Test	100 mm	<100>
		Substrat:	390 µm	n/P	3-5 Ωcm			
		Oberflächen:	poliert/poliert					

Nr.	Prozeßschritt	Teilschritte	Parameter	Werte	Bemerkungen, Datum - Unterschrift
1.0.	Eingangs-	H_2SO_4 / H_2O_2	Temperatur [°C]: Zeit [min.]:	120 7	rechtes Becken
	Reinigung	Leitwertspülen			
		Rinser Dryer	99s / 111s / 222s		
2.0.	Oxidation	Oxidation feucht soll: 500 nm ± 2 nm	Prozeßname: Prozeßtemperatur [°C]: Prozeßzeit [min]: Rohr-Nr.: Fahrt Nr.: Abstand der Wafer bei Ox.:	FOX1000 1000 1h 26m 1B4	
		Messung Oxiddicke	n (Ellipsometer): Programm (MPV):	45	

		Links			Mitte-Links			Mitte Rechts			Rechts		
		W.-Nr. L:	W.-Nr. M:	W.-Nr. R:	W.-Nr. L:	W.-Nr. M:	W.-Nr. R:	W.-Nr. L:	W.-Nr. M:	W.-Nr. R:	W.-Nr. L:	W.-Nr. M:	W.-Nr. R:
	d [nm]												
	δ [nm]												
	Min												
	Max												

Nr. Prozeßschritt	Teilschritte	Parameter	Werte	Bemerkungen, Datum - Unterschrift
3.0. Fototechnik	**Belacken: EATON**	Fotolack: Prozeßname:	AZ 1514 PSXi 5000	Prebake 30 min 100°C im Ofen
"SiC- Strukt. FS"	**Belichten: MA 150** Maske: SiC-Strukt. FS Justiermarke: 1	Programm: Belichtungszeit [s]: Lichtleistung 405nm [mW/cm²]: Anzeige CL2:	3 8 250 20	
	Entwickeln	manuell im Entwicklerbecken	1m 30s	kontinuierlich schwenken
	Inspektion	Strukturbreite Maske: (Steg im Justierkreuz) Strukturbreite Lack: bei Abweichung > 0.3µm neue Fototechnik	10µm	
4.0. Strukturierung Oxid	**Ätzen PECVD Oxid** - (VACUTEC)	Prozeßname: Prozeßzeit: SF_6-Fluß [sccm]: Druck [mTorr]: Leistung [W]:	Nitrid-Etch 4 m 20 150 150	Strukturen ca. 120 nm in das Oxid Ätzen, um bei den Schnipseln Vorder- und Rückseite justieren zu können.
	Inspektion	Ätzrate PE-Oxid:		
5.0. Lack	**Remover 1**	Prozeßzeit [min]:	5	
entfernen	**Remover 2**	Prozeßzeit [min]:	2,5	
	Leitwertspülen			
	Rinser Dryer	99 / 111 / 222 s		
	Inspektion	Mikroskop (Dunkelfeld)		bei Resten: Veraschen 2 min in Vacutec
6.0. Fototechnik	**Belacken: EATON** Rückseite	Fotolack: Prozeßname:	AZ 1514 PSXi 5000	Prebake 30 min 100 °C im Ofen

Nr. Prozeßschritt	Teilschritte	Parameter	Werte	Bemerkungen, Datum - Unterschrift
"SiC-Strukt. BS" Rückseite	**Belichten: MA 25** Maske RS: SiC-Strukt. BS Maske VS: SiC-Strukt. FS Justiermarke: 1	Belichtungszeit [s]: Lichtleistung 405nm [mW/cm²]: Anzeige CL2: Belichtungsabstand: eingetragene Waferdicke:	18 350 50 µm 500 µm	
	Entwickeln	manuell im Entwicklerbecken	1m 30s	kontinuierlich schwenken
	Inspektion	Strukturbreite Maske: (Steg im Justierkreuz) Strukturbreite Lack: bei Abweichung > 0.3µm neue Fotolechnik	10µm	
7.0. Strukturierung Oxid	**Ätzen PECVD Oxid** - (VACUTEC)	Prozeßname: Prozeßzeit: SF_6-Fluß [sccm]: Druck [mTorr]: Leistung [W]:	Nitrid-Etch 4 m 20 150 150	Strukturen ca. 120 nm in das Oxid Ätzen, um bei den Schnipseln Vorder- und Rückseite justieren zu können.
	Inspektion	Ätzrate PE-Oxid: Ätzrate PE-Nitrid:		
8.0. Lack	**Remover 1**	Prozeßzeit [min]:	5	
entfernen	**Remover 2**	Prozeßzeit [min]:	2,5	
	Leitwertspülen			
	Rinser Dryer	99 / 111 / 222 s		
	Inspektion	Mikroskop (Dunkelfeld)		bei Resten: Veraschen 2 min in Vacutec
9.0. Wafer sägen	**Folie aufkleben**	Folienseite (VS: Vorderseite; RS: Rückseite)	VS	

Nr.	Prozeßschritt	Teilschritte	Parameter	Werte	Bemerkungen, Datum - Unterschrift
		Sägen	Programm: Sägeblatt: Sägeblatthalterung [mm]: Sägegeschw.: Step 1 [µm]: Step 2 [µm]: Wasserdruck:	 Si 15 40.000 20.000 reduziert	Hier werden die Wafer in 2 x 4 cm^2 große Schnipsel zur SiC-Beschichtung gesägt Testfelder möglichst an Sägekante. Darauf achten, daß auf allen Schnipseln genügend Justierkreuze sind.
		Reinigen und Trocknen	manuell		Mit Spritzpistole und N_2-Pistole.
		Folie abziehen			
		Inspektion	Partikel Ausbrüche		
10.0. Verpacken		**Proben verpacken**	Stoßsicherheit prüfen		Verschicken an Martin Eyckhoff
11.0. LPCVD-SiC		**LPCVD-SiC-Abscheidung** soll: **1000 nm**	Prozeßname: Prozeßtemperatur [°C]: Prozeßzeit [min, sec]: Rohr-Nr.: Fahrt Nr.: Abstand der Wafer bei Prozeß:	 1200	Polykristalline / amorphe 3C-SiC-Schichten werden bei DaimlerChrysler München abgeschieden (Martin Eyckhoff).
		Messung Nitriddicke	n (Ellipsometer): Programm (MPV):		

		Links			**Mitte**			**Rechts**		
		W.-Nr. L:	W.-Nr. M:	W.-Nr. R:	W.-Nr. L:	W.-Nr. M:	W.-Nr. R:	W.-Nr. L:	W.-Nr. M:	W.-Nr. R:
	d [nm]									

Nr.	Prozeßschritt	Teilschritte	Parameter	Werte	Bemerkungen, Datum - Unterschrift
		δ [nm]			
		Min			
		Max			
12.0. Oxidation		**Oxidation** trocken soll: 100 nm ± 2 nm	Prozeßname: Prozeßtemperatur [°C]: Prozeßzeit [min]: Rohr-Nr.: 3.5 l / min N_2 (Aufheizen) 3.6 l / min O_2 (Oxidation) 3.5 l / min (Abkühlen)	 1100 2h 30m	Oxidation im kleinen Temperrohr (Etage 2).
		Messung Oxiddicke	n (Ellipsometer): Programm (MPV):		
13.0.Passivierung		**PECVD-SiO_2-Abscheidung** (VACUTEC) Dicke soll: **200 nm**	Temperatur [°C] Prozeßname: Oxid Prozeßzeit: SiH_4-Fluß [sccm]: N_2O -Fluß [sccm]: N_2 -Fluß [sccm]: RF-Leistung: Druck [mTorr]	350 Oxid 350°C 14 1.5 600 350 10 800	
		Inspektion	Partikel		

Nr. Prozeßschritt	Teilschritte	Parameter	Werte	Bemerkungen, Datum - Unterschrift
14.0. Sputtern Al	**Sputtern Al** **MRC** soll: **(1,2 ±0,1) µm**	Prozeßname: DC-Power [kW]: Argon-Druck [mTorr]: Vorsputtern [s]: Scan-Speed [cm/min]: Anzahl der Scans:	3 7 15 30 18 4	Sputtern der Al-Maske für das SiC-Ätzen. Hierzu spezielle Halterung für Schnipsel an der dafür vorgesehenen Palette der MRC befestigen.
15.0. Fototechnik	**Belacken: manuell**	Fotolack: Zeit 1 / s Umdrehungen 1 / rpm Zeit 2 / s: Umdrehungen 2 / rpm	AZ 1514 10 1000 20 3000	Randentlackung manuell, Prebake in liegendem Teflon-Carrier im Ofen (35 min, 100 °C).
"SiC-Strukt. FS"	**Belichten: MA 4** Maske: SiC-Strukt. FS Justiermarke: 1	Programm: Belichtungszeit [s]: Lichtleistung 405nm [mW/cm²]: Anzeige CL2:	8	Sägefolie auf dem Chuck aufkleben, Schlitze mit Skalpell dort ziehen, wo die Proben liegen, damit das Vakuum angezogen werden kann.
	Entwickeln	manuell im Tauchbad	1m 30s	Spülen und Trocknen manuell mit Spritz- und N_2-Pistole. Postbake in flach liegendem Teflon-Carrier im Ofen (125°C, 35 min).
	Inspektion	Strukturbreite Maske: (Steg im Justierkreuz) Strukturbreite Lack: bei Abweichung > 0.3 µm neue Fototechnik	10 µm	
16.0. Al - Strukturierung	**Ätzen Aluminium** (Tauchbad)	Temperatur: Ätzzeit: (Badbewegung ein)	40°C	Strukturieren der Al-Maske
	Leitwertspülen	manuell		Spülen und Trocknen manuell mit Spritz- und N_2-Pistole.

Nr. Prozeßschritt	Teilschritte	Parameter	Werte	Bemerkungen, Datum - Unterschrift
	Dip in der Poly-Ätze	Temperatur: Ätzzeit (ca. 5 s):	RT	ggf. weglassen.
	Leitwertspülen			Spülen und Trocknen manuell mit Spritz- und N_2-Pistole.
	Inspektion	Breite Al Steg: (Steg Justierkreuz)		
17.0. Lack	**Remover 1**	Prozeßzeit [min]:	5	alternativ eigenes Removerbad auf Heizplatte (65 °C, 8 m)
entfernen	**Remover 2**	Prozeßzeit [min]:	2,5	
	Leitwertspülen	manuell		Spülen und Trocknen manuell mit Spritz- und N_2-Pistole.
	Inspektion	Mikroskop (Dunkelfeld)		bei Resten: Veraschen 2 min in Vacutec
18.0. Strukturierung SiC	**Ätzen SiC** - (VACUTEC)	Prozeßname: Prozeßzeit: O_2-Fluß [sccm]: SF_6-Fluß [sccm]: Druck [mTorr]: Leistung [W]:	SiC 100% 45 + 30 m 20 4 150 200	Zuvor Dicke der Al-Maske mit dem Tencor / Dektak nachmessen. 45 min Ätzen und dann Ätzrate prüfen. Ätzzeit für das Nachätzen einstellen (ca. 30 min). Hierbei sollen 300 nm Oxid, 1000 nm SiC sowie ca. 300 nm des darunter liegenden Feuchtoxides geätzt werden. NICHT bis in das Si ätzen(!), da die hohe Ätzrate tiefe Gruben verursacht, die eine gute Fototechnik unmöglich machen. Al-Elektrode ersetzen durch Graphit-Elektrode. VORSICHT, sehr zerbrechlich, also nicht den Schraubenzieher ansetzen! Nach Benutzung Rückbau und Wegräumen der Graphit-Elektrode.

Nr. Prozeßschritt	Teilschritte	Parameter	Werte	Bemerkungen, Datum - Unterschrift
19.0. Sputtern Al Rückseite	**Sputtern Al MRC** soll: **(1,2 ±0,1) µm**	Prozeßname: DC-Power [kW]: Argon-Druck [mTorr]: Vorsputtern [s]: Scan-Speed [cm/min]: Anzahl der Scans:	3 7 15 30 18 4	Sputtern der Al-Maske für das SiC-Ätzen. Hierzu spezielle Halterung für Schnipsel an der dafür vorgesehenen Palette der MRC befestigen.
20.0. Fototechnik	**Belacken: manuell**	Fotolack: Zeit 1 / s Umdrehungen 1 / rpm Zeit 2 / s: Umdrehungen 2 / rpm	AZ 1514 10 1000 20 3000	Randentlackung manuell, Prebake in liegendem Teflon-Carrier im Ofen (35 min, 100 °C).
"SiC-Strukt. BS"	**Belichten: MA 4** Maske: SiC-BS Justiermarke: 1	Programm: Belichtungszeit [s]: Lichtleistung 405nm [mW/cm²]: Anzeige CL2:	 8	Sägefolie auf dem Chuck aufkleben, Schlitze mit Skalpell dort ziehen, wo die Proben liegen, damit das Vakuum angezogen werden kann.
	Entwickeln	manuell im Tauchbad	1m 30s	Spülen und Trocknen manuell mit Spritz- und N_2-Pistole. Postbake in flach liegendem Teflon-Carrier im Ofen (125°C, 35 min).
	Inspektion	Strukturbreite Maske: (Steg im Justierkreuz) Strukturbreite Lack: bei Abweichung > 0,3 µm neue Fototechnik	10 µm	
21.0. Al - Strukturierung	**Ätzen Aluminium** (Tauchbad)	Temperatur: Ätzzeit: (Badbewegung ein)	40°C	
	Leitwertspülen	manuell		Spülen und Trocknen manuell mit Spritz- und N_2-Pistole.

Nr. Prozeßschritt	Teilschritte	Parameter	Werte	Bemerkungen, Datum - Unterschrift
	Inspektion	Breite Al Steg: (Steg Justierkreuz)		
22.0. Lack	**Remover 1**	Prozeßzeit [min]:	5	alternativ eigenes Removerbad auf Heizplatte (65 °C, 8 m)
entfernen	**Remover 2**	Prozeßzeit [min]:	2,5	
	Leitwertspülen	manuell		
	Inspektion	Mikroskop (Dunkelfeld)		bei Resten: Veraschen 2 min in Vacutec
23.0. Strukturierung SiC	**Ätzen SiC** - (VACUTEC)	Prozeßname: Prozeßzeit: O_2-Fluß [sccm]: SF_6-Fluß [sccm]: Druck [mTorr]: Leistung [W]:	SiC 100% 45 + 30 m 20 4 150 200	Zuvor Dicke der Al-Maske mit dem Tencor / Dektak nachmessen. 45 min Ätzen und dann Ätzrate prüfen. Ätzzeit für das Nachätzen einstellen (ca. 30 min). Hierbei soll durch 300 nm Oxid, 1000 nm SiC und 500 nm des darunter liegenden Feuchtoxides bis knapp in das Si geätzt werden. Al-Elektrode ersetzen durch Graphit-Elektrode. VORSICHT, sehr zerbrechlich, also nicht den Schraubenzieher ansetzen! Nach Benutzung Rückbau und Wegräumen der Graphit-Elektrode.
	Inspektion	Ätzrate SiC:		
24.0. Sputtern HfB_2	**Sputtern HfB_2** Leybold Soll-Schichtdicke: 180nm	Prozeßname: DC-Power [kW]: Argon-Druck [mTorr]: Rücksputtern [s]: Anzahl der Umdrehungen [vpm]: Prozeßzeit [min]:	HfB_2/36 7 180 26	Nach dem Sputtern der HfB_2-Schicht möglichst schnelles Weiterprozessieren, da sich sonst eine schwer zu strukturierende Hafnia-Schicht (HfO) bildet.

Nr. Prozeßschritt	Teilschritte	Parameter	Werte	Bemerkungen, Datum - Unterschrift
	Inspektion	Sichtkontrolle Krümel Schichtdicke: Vierspitzenmeßplatz Prog. 4 Flächenwiderstand [Ω / □]	 12.5	
25.0. Fototechnik	**Belacken: manuell**	Fotolack: Zeit 1 / s Umdrehungen 1 / rpm Zeit 2 / s: Umdrehungen 2 / rpm	AZ 1514 10 1000 20 3000	Randentlackung manuell, Prebake in liegendem Teflon-Carrier im Ofen (35 min, 100 °C).
"HfB_2 Strukt."	**Belichten: MA 4** Maske: HfB_2 Strukt. Justiermarke: 3	Programm: Belichtungszeit [s]: Lichtleistung 405nm [mW/cm²]: Anzeige CL2:	 8	Sägefolie auf dem Chuck aufkleben, Schlitze mit Skalpell dort ziehen, wo die Proben liegen, damit das Vakuum angezogen werden kann.
	Entwickeln	manuell im Tauchbad	1m 30s	Spülen und Trocknen manuell mit Spritz- und N_2-Pistole. Postbake in flach liegendem Teflon-Carrier im Ofen (125°C, 35 min).
	Inspektion	Strukturbreite Maske: (Steg im Justierkreuz) Strukturbreite Lack: bei Abweichung > 0.3 µm neue Fototechnik	10 µm	
26.0. Strukturierung HfB_2	**HfB_2 ätzen** 6 : 4 : 0.04 H_2O:HNO_3:NH_4F	Temperatur: Ätzzeit:	21 °C 90 s	leicht schwenken. HfB_2 verfärbt sich von silber über braun zu schwarz, bis das darunter liegende SiC sichtbar wird. Bei Ätzzeiten über 120 s Ätze wechseln. Beim Ansetzen immer zuerst das Wasser (!), dann die Säuren. Vor Gebrauch Abkühlen auf RT abwarten.

Nr. Prozeßschritt	Teilschritte	Parameter	Werte	Bemerkungen, Datum - Unterschrift
	Inspektion	Unterätzung Lack:		
27.0. Lack	**Remover 1**	Prozeßzeit [min]:	5	alternativ eigenes Removerbad auf Heizplatte (65 °C, 8 m)
entfernen	**Remover 2**	Prozeßzeit [min]:	2,5	
	Leitwertspülen	manuell		
	Inspektion	Mikroskop (Dunkelfeld)		bei Resten: Veraschen 2 min in Vacutec
28.0. N_2-Tempern	**Tempern im Rohr**	Temperrohr:	500°C	Stabilisierungstemperung des Heizers.
	Etage 2	T:	5 h	
		N_2: 3.5 l/min		
	Inspektion			
29.0.Passivierung	**PECVD-Si_3N_4-Abscheidung** (VACUTEC)	Temperatur [°C]	350	
		Prozeßname:	Nitrid	
	Nitrid		350°C	
	Dicke soll:	Prozeßzeit:	50	
	500nm	SiH_4-Fluß [sccm]:	5.3	
		NH_3-Fluß [sccm]:	3.0	
		N_2-Fluß [sccm]:	450	
		RF-Leistung:	10	
		Druck [mTorr]	800	
	Inspektion	Partikel		

Nr. Prozeßschritt	Teilschritte	Parameter	Werte	Bemerkungen, Datum - Unterschrift
30.0. Fototechnik	**Belacken: manuell**	Fotolack: Zeit 1 / s Umdrehungen 1 / rpm Zeit 2 / s: Umdrehungen 2 / rpm	AZ 1514 10 1000 20 3000	Randentlackung manuell, Prebake in liegendem Teflon-Carrier im Ofen (35 min, 100 °C).
"PSG Strukt."	**Belichten: MA 4** Maske: PSG Strukt. Justiermarke: 4	Programm: Belichtungszeit [s]: Lichtleistung 405nm [mW/cm²]: Anzeige CL2:	8	Sägefolie auf dem Chuck aufkleben, Schlitze mit Skalpell dort ziehen, wo die Proben liegen, damit das Vakuum angezogen werden kann.
	Entwickeln	manuell im Tauchbad	1m 30s	Spülen und Trocknen manuell mit Spritz- und N_2-Pistole. Postbake in flach liegendem Teflon-Carrier im Ofen (125°C, 35 min).
	Inspektion	Strukturbreite Maske: (Steg im Justierkreuz) Strukturbreite Lack: bei Abweichung > 0.3µm neue Fototechnik	10 µm	
31.0. Strukturierung Passivierung	**Ätzen PECVD Nitrid-** (VACUTEC)	Prozeßname: Prozeßzeit: SF_6-Fluß [sccm]: Druck [mTorr]: Leistung [W]:	Nitrid-Etch 1m 15s 20 150 150	Ätzrate überprüfen
	Inspektion	Ätzrate PE-Oxid: Ätzrate PE-Nitrid:		
32.0. Lack	**Remover 1**	Prozeßzeit [min]:	5	alternativ eigenes Removerbad auf Heizplatte (65 °C, 8 m)
entfernen	**Remover 2**	Prozeßzeit [min]:	2,5	
	Leitwertspülen			

Nr. Prozeßschritt	Teilschritte	Parameter	Werte	Bemerkungen, Datum - Unterschrift
	Inspektion	Mikroskop (Dunkelfeld)		bei Resten: Veraschen 2 min in Vacutec
33.0. Sputtern TiWN-Au	**Sputtern TiWn- Au** Leybold Soll-Schichtdicke: 230nm / 200 nm	Prozeßname: DC-Power [kW]: Argon-Druck [mTorr]: Rücksputtern [s]: TiWN Anzahl der Umdrehungen [vpm]: Prozeßzeit [min]: Au Anzahl der Umdrehungen [vpm]: Prozeßzeit [min]:	B	TiWN in Leybold Z660 der Aufbau und Verbindungstechnik (Claudia Meinherz). Zugangsberechtigt: Florian Solzbacher. Lichtschranke überbrücken.
	Inspektion	Sichtkontrolle Krümel Schichtdicke: Vierspitzenmeßplatz Prog. 4 Flächenwiderstand [Ω]		
34.0. Fototechnik	**Belacken: manuell**	Fotolack: Zeit 1 / s Umdrehungen 1 / rpm Zeit 2 / s: Umdrehungen 2 / rpm	AZ 1514 10 1000 20 3000	Randentlackung manuell, Prebake in liegendem Teflon-Carrier im Ofen (35 min, 100 °C).
"Galv."	**Belichten: MA 4** Maske: Galv. Justiermarke: 6	Programm: Belichtungszeit [s]: Lichtleistung 405nm [mW/cm²]: Anzeige CL2:	10	Sägefolie auf dem Chuck aufkleben, Schlitze mit Skalpell dort ziehen, wo die Proben liegen, damit das Vakuum angezogen werden kann. Leicht überbelichten.

Nr. Prozeßschritt	Teilschritte	Parameter	Werte	Bemerkungen, Datum - Unterschrift
	Entwickeln	manuell im Tauchbad	1m 30s	Spülen und Trocknen manuell mit Spritz- und N_2-Pistole. Postbake in flach liegendem Teflon-Carrier im Ofen (125°C, 35 min).
	Inspektion	Strukturbreite Maske: (Steg im Justierkreuz) Strukturbreite Lack: bei Abweichung > 0.3µm neue Fototechnik	10 µm	
35.0. Galvanik Au	**Galvanik Au**	Temperatur: Fläche: Stromstärke [mA]: Zeit:	60°C	
	Inspektion	Dicke (Tencor) Mitte Ra: Underplating:	Rand	
36.0. Lack	**Remover 1**	Prozeßzeit [min]:	5	alternativ eigenes Removerbad auf Heizplatte (65 °C, 8 m)
entfernen	**Remover 2**	Prozeßzeit [min]:	2,5	
	Leitwertspülen			
	Rinser Dryer	99 / 111 / 222 s		
	Inspektion	Mikroskop (Dunkelfeld)		bei Resten: Veraschen 2 min in Vacutec
37.0. Fototechnik	**Belacken: manuell**	Fotolack: Zeit 1 / s Umdrehungen 1 / rpm Zeit 2 / s: Umdrehungen 2 / rpm	AZ 1514 10 1000 20 3000	Randentlackung manuell, Prebake in liegendem Teflon-Carrier im Ofen (35 min, 100 °C).

Nr. Prozeßschritt	Teilschritte	Parameter	Werte	Bemerkungen, Datum - Unterschrift
"Au/TiWN Neu"	**Belichten: MA 4** Maske: Au/TiWN Neu Justiermarke: 5	Programm: Belichtungszeit [s]: Lichtleistung 405nm [mW/cm²]: Anzeige CL2:	10	Sägefolie auf dem Chuck aufkleben, Schlitze mit Skalpell dort ziehen, wo die Proben liegen, damit das Vakuum angezogen werden kann. Leicht überbelichten.
	Entwickeln	manuell im Tauchbad	1m 30s	Spülen und Trocknen manuell mit Spritz- und N_2-Pistole. Postbake in flach liegendem Teflon-Carrier im Ofen (125°C, 35 min).
	Inspektion	Strukturbreite Maske: (Steg im Justierkreuz) Strukturbreite Lack: bei Abweichung > 0.3µm neue Fotolechnik	10 µm	
38.0. Strukturierung	**Gold ätzen in JKJ_2 -Ätze**	Temperatur: Ätzzeit:	21 °C	leicht schwenken
TiWN - Au	**Inspektion**	Unterätzung Lack:		
	TiWN ätzen in H_2O	Temperatur: Ätzzeit:	40°C	leicht schwenken
	Inspektion	Unterätzung:		
39.0. Lack	**Remover 1**	Prozeßzeit [min]:	5	alternativ eigenes Removerbad auf Heizplatte (65 °C, 8 m)
entfernen	**Remover 2**	Prozeßzeit [min]:	2,5	
	Leitwertspülen			
	Inspektion	Mikroskop (Dunkelfeld)		bei Resten: Veraschen 2 min in Vacutec

Nr. Prozeßschritt	Teilschritte	Parameter	Werte	Bemerkungen, Datum - Unterschrift
40.0.Passivierung	**PECVD-Si_3N_4-Abscheidung** (VACUTEC) Dicke soll: **600m**	Temperatur [°C] Prozeßname: Nitrid Prozeßzeit: SiH_4-Fluß [sccm]: NH_3-Fluß [sccm]: N_2-Fluß [sccm]: RF-Leistung: Druck [mTorr]	350 Nitrid 350°C 70 5.3 3.0 450 10 800	Testschnipsel zur Dickenbestimmung mit in die Anlage legen.
	Inspektion	Partikel		
41.0. Fototechnik	**Belacken: manuell**	Fotolack: Zeit 1 / s Umdrehungen 1 / rpm Zeit 2 / s: Umdrehungen 2 / rpm	AZ 1514 10 1000 20 3000	Randentlackung manuell, Prebake in liegendem Teflon-Carrier im Ofen (35 min, 100 °C).
"Pass. Neu	**Belichten: MA 4** Maske: Pass. Neu Justiermarke: 7	Programm: Belichtungszeit [s]: Lichtleistung 405nm [mW/cm²]: Anzeige CL2:	 10	Sägefolie auf dem Chuck aufkleben, Schlitze mit Skalpell dort ziehen, wo die Proben liegen, damit das Vakuum angezogen werden kann. Leicht überbelichten.
	Entwickeln	manuell im Tauchbad	1m 30s	Spülen und Trocknen manuell mit Spritz- und N_2-Pistole. Postbake in flach liegendem Teflon-Carrier im Ofen (125°C, 35 min).
	Inspektion	Strukturbreite Maske: (Steg im Justierkreuz) Strukturbreite Lack: bei Abweichung > 0.3µm neue Fototechnik	10 µm	

Nr. Prozeßschritt	Teilschritte	Parameter	Werte	Bemerkungen, Datum - Unterschrift
42.0. Strukturierung Passivierung	**Ätzen PECVD-Nitrid** (VACUTEC)	Prozeßname: Prozeßzeit: SF_6-Fluß [sccm]: Druck [mTorr]: Leistung [W]:	Nitrid-Etch 1m 15s 20 150 150	Ätzrate überprüfen mit Hilfe des bei der Abscheidung beschichteten Testschnipsels.
	Inspektion	Ätzrate PE-Oxid: Ätzrate PE-Nitrid:		
43.0. Lack	**Remover 1**	Prozeßzeit [min]:	5	alternativ eigenes Removerbad auf Heizplatte (65 °C, 8 m)
entfernen	**Remover 2**	Prozeßzeit [min]:	2,5	
	Leitwertspülen			
	Rinser Dryer	99 / 111 / 222 s		
	Inspektion	Mikroskop (Dunkelfeld)		bei Resten: Veraschen 2 min in Vacutec
44.0. Anisotropes	**Aufwachsen**	Wachsart:	Tabletten (altes)	Viertel-Glaswafer für Schnipsel verwenden.
Ätzen	**Oxid entfernen**	Ammoniumfluorid (32 °C) Ätzzeit:	 90 s	(speziell angesetzte Lsg. verwenden - nicht Prozeßbecken in der Ätztechnik verwenden!)
	Spülen in DI-Wasser (mit Hand)	Transport zur KOH in DI-Wasser Vorwärmen in DI-Wasser		
	KOH / IPA-Ätzen	Becken: T[°C] ρ g/cm^3] bei 20 °C vermutliche Ätzzeit: rein [Uhrzeit]:	IPA 80 6h 30m	auf Zeit ätzen, nachmessen nach 3h und 6h.

Nr. Prozeßschritt	Teilschritte	Parameter	Werte	Bemerkungen, Datum - Unterschrift
	erste Kontrolle spülen, trocknen, Messen	raus 1 [Uhrzeit]: Ätztiefe (Stahl) [µm]: rein 2 [Uhrzeit]:		
	zweite Kontrolle spülen, trocknen, Messen	raus 2 [Uhrzeit]: Ätztiefe (Stahl) [µm]: rein 3 [Uhrzeit]:		
	dritte Kontrolle spülen, trocknen, Messen	raus 3 [Uhrzeit]: Ätztiefe (Stahl) [µm]:		
	Inspektion	Gesamtätzzeit: Ätzrate: Unterätzung:		
	Spülen in DI-Wasser **Trocknen (N_2)**	(mit Hand)		
	Wachs entfernen	abwachsen 2 X in TCE spülen Trocknen (N_2)		ggf. in Carot'scher Lösung nachreinigen (H_2SO_4 / H_2O_2)
	Inspektion	defekte Membranen defekte Strukt. Vorderseite		markieren in den einzelnen Wafermap
45.0. Chips vereinzeln	**Vereinzeln**	Brechen der Chips		
	Inspektion	Partikel Ausbrüche		

Appendix F: Effect of high temperature thermal annealing on HfB_2 thin film layers calculations

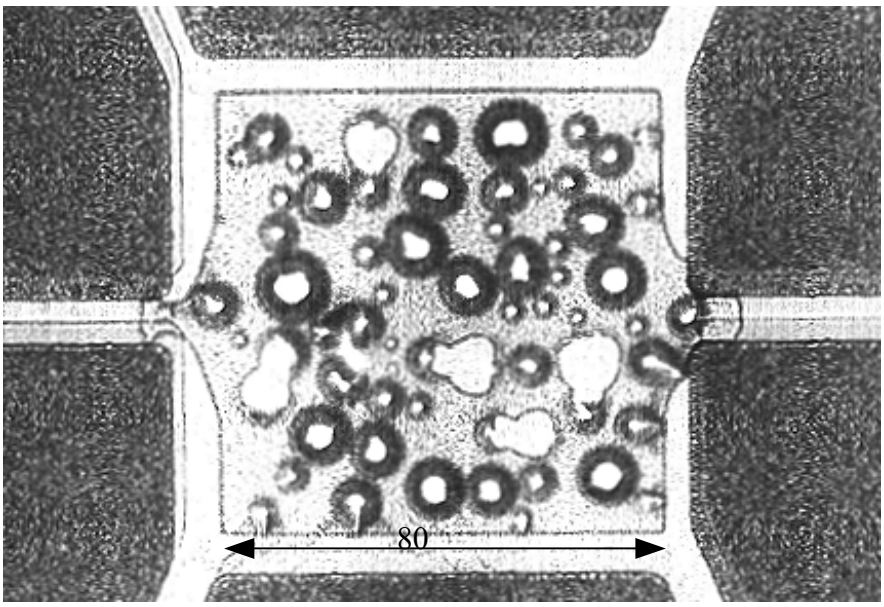

Fig.F.1: Bubbles on a 200 nm thick HfB_2 thin film after annealing in N_2 for 5 h at 750°C. Bubbles are up to 1 μm high.

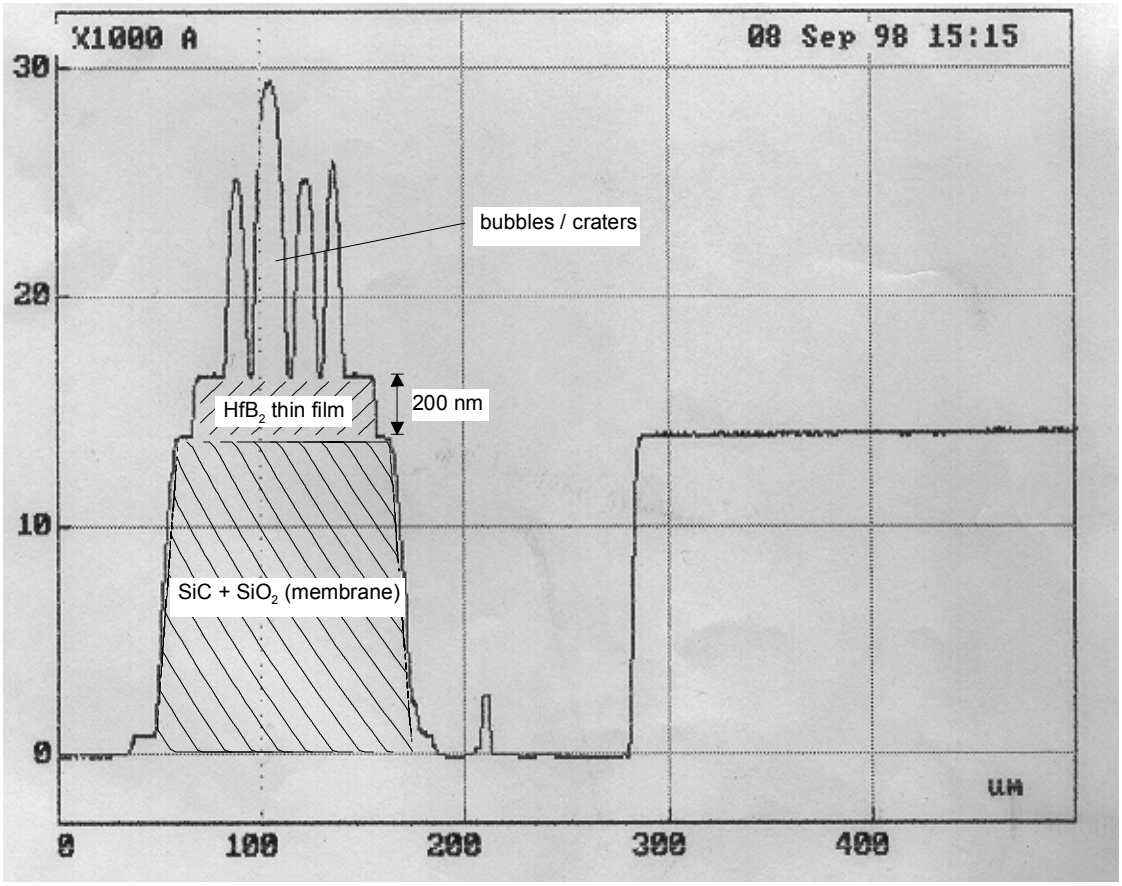

Fig.F.2: Height profile of bubbles in HfB_2 thin film after annealing in N_2 for 5 h at 750°C

A likely reason for this effect might be the building of a Hafnia (HfO_2) layer on top of the HfB_2, which features a considerably higher specific resistance and a different thermal expansion coefficient. The Hafnia layer builds up naturally on top of the HfB_2 in air[3.28]. Even when annealing in N_2, some O_2 might propagate further into the HfB_2. The increase in specific resistance as well as the chipping-off of the metal thin film from the surface of the wafer could thus be explained. A possible explanation for the building of bubbles might be that the HfO_2 acts as a diffusion barrier, preventing a gaseous species (target impurities) appearing upon heating the thin film from escaping, thereby “blowing up” the film, eventually leading to a destruction of the film. Hafnium is also known to absorb H_2 very strongly at 700°C to form $HfH_{1.86}$ [6.2]. Since the annealing was done in pure N_2 this effect is however not too likely to be connected to the appearance of the bubbles. This effect was not studied in further detail, since the device specifications were limited to 500°C operating temperature (low voltage version).